Tectonostratigraphy, Structural Styles, and Hydrocarbon Prospectivity of the Rifted-Passive Margins of the Southern Gulf of Mexico and the Atlantic Margin of Morocco

by
Md Nahidul Hasan

A dissertation submitted to the Department of Earth and Atmospheric Sciences,
College of Natural Sciences and Mathematics
in partial fulfillment of the requirements for the degree of

DOCTOR OF PHILOSOPHY

in Geology

Chair of Committee: Paul Mann

Committee Member: Jonny Wu

Committee Member: Donald Van Nieuwenhuise

Committee Member: Clara Rodriguez

University of Houston
December 2022

DEDICATION

To my wife, Liza, for accompanying me on this long journey and for all her patience and support.

To mom and dad for all their personal and financial sacrifices that got me to where I am now.

ACKNOWLEDGMENTS

I thank Dr. Paul Mann, my research advisor and committee chair, for his guidance and supervision throughout my graduate career at the University of Houston. His support for my research progress as a PhD student has been continuous since my first day at the University of Houston in August 2019. I greatly appreciate the financial support provided to me by Dr. Mann and the Conjugate Basins, Tectonics, and Hydrocarbons (CBTH) consortium that funded my employment over the past three years as a CBTH research assistant. I also appreciate the additional financial support for my study provided to me by the Houston Endowment Recruitment Fellowship of the University of Houston.

Special thanks go to Dr. Jonny Wu, Dr. Donald Van Nieuwenhuise, and Dr. Clara Rodriguez for their service on my committee and for contributing their time and expertise to improve my research products. A special thanks to Andrew Pepper (This !s Petroleum Systems LLC, Fredericksburg, Texas), who introduced me to thermal stress modeling and was always able to take the time to answer my questions.

I thank Dr. Jeniffer Masy and Robert Sorley of Geoex MCG for kindly providing their excellent geophysical datasets in the southern Gulf of Mexico and along the Atlantic margin of Morocco, without which this study would not have been possible. I would also like to thank the software providers to the Department of Earth and Atmospheric Sciences and to the CBTH project whose software made this work possible: Schlumberger (Petrel), Petroleum Experts Inc. (MOVE), Seequent (Oasis Montage), and Zetaware Inc. (Genesis and Trinity).

I thank the many past and present students and researchers of the CBTH group, especially Mei Liu, Nawaz Bugti, Lei Sun, Jack Kenning, Kenneth Shipper, and Sean Romito, who shared numerous insights in our weekly group meetings and individual work sessions. I also thank Charles Bondurant and Ahmed Afifi, who were my mentor and line manager for my summer internship at BP in the summer of 2022 and who entrusted me with a large exploration project in the Gulf of Mexico and provided me the necessary support and encouragement to complete the study in the three-month window. Lastly, I thank all my family and friends back home whose many years of support and love have allowed me to complete this dissertation.

ABSTRACT

This dissertation addresses the tectonic evolution, structural style, source rock maturity, and hydrocarbon prospectivity of rifted-passive margins of the Gulf of Mexico (GOM) and circum-Atlantic and western Indian Oceans. **Chapter 2** compiles information from my own study of the southern GOM with previously published information on the structural evolution and similarities of deepwater passive margin foldbelts (PMFBs) of the Gulf of Mexico, Atlantic Ocean, and western Indian Ocean. Comparison of the thirteen passive margin foldbelts from these margins shows that their shared structural characteristics are driven by gravitational forces resulting from thermal subsidence, onshore cratonic uplift, tectonic oversteepening of the margin, and deltaic depositional loading.

Chapter 3 focuses on the tectonic evolution of the Campeche salt basin in the southern Gulf of Mexico and integrates shipborne magnetic data with 28,612 km of pre-stack, depth-migrated, 2D seismic data to reconstruct the geometry of the top of the Paleozoic crystalline basement. This mapping better defined the 400-km-long and 40-55-km-wide outer marginal trough, which formed adjacent to the late Jurassic oceanic crust and acts to channel the downslope flow of gravitationally-driven salt of the Campeche PMFB. In **Chapter 4**, I conducted thermal stress modeling along the Campeche salt basin to better understand the spatial variation of present-day maturation of the potential source rocks and their expelled petroleum volume. My 1D and map-based modeling demonstrate that the more deeply buried, late Jurassic source rocks matured in the late Paleogene to early Neogene and are currently expelling oils into the water column as known from natural oil surface seeps. **Chapter 5** uses the same mapping approach as Chapter 4 to describe an elongate, 80-150-km-wide marginal rift that overlies the zone of continental necking and parallels the modern coastline of Morocco. 1D and map-based thermal maturity modeling show that Jurassic source rocks of the marginal rift are mature for petroleum expulsion along a 400-km length of this rift. Late Cretaceous uplift and erosion of the margin documented in IODP wells are related to Africa-Eurasia convergence across northern Africa and provide an explanation for the observed immaturity of Cretaceous source rocks.

TABLE OF CONTENTS

LIST OF TABLES

LIST OF FIGURES

CHAPTER 1: INTRODUCTION TO THIS DISSERTATION

1.1 History and development of this dissertation

I grew up in Tongi, Gazipur, a small city near Dhaka, the capital of Bangladesh. Although I came from a family of modest educational and economic background, my mother believed that education was the best way to positively change the lives of her children. Because of the low cost of government-subsidized education in Bangladesh, I was able to become the first member of my family to graduate with a BSc and one-year MSc in Geological Sciences from Jahangirnagar University in Dhaka. Following my graduation in 2017, I moved to the United States to pursue my Master of Science (MSc) degree in Geology at Southern Illinois University Carbondale (SIUC), where I worked as a teaching assistant for introductory geology classes for undergraduate students. For my MSc thesis in SIUC, I worked with my thesis supervisor, Dr. Sally Potter-McIntyre, on the subsurface seismic characterization of an oil-producing field in Kansas using 2D seismic and well-log data (Hasan, 2021). I published the results of this thesis in the Journal of Midcontinent Geoscience in 2021 (Hasan et al., 2021).

Following the completion of my MSc and my graduation from SIUC in 2019, I contacted Dr. Paul Mann at the University of Houston, who encouraged me to visit the CBTH group and the University of Houston in March 2019. After this visit, I applied and was accepted as a graduate research assistant in geology in the Department of Earth and Atmospheric Sciences, where I was supported by Dr. Mann's CBTH project in the fall semester of 2019. Based on my previous academic record as an undergraduate and MS student in Bangladesh and as an MSc student at SIUC and with the recommendation of Dr. Mann, I was awarded the Houston Endowment Recruitment Fellowship from the University of Houston that supplemented by CBTH research assistant salary for the duration of my PhD study.

Dr. Mann proposed the Campeche salt basin in the southern Gulf of Mexico as my PhD study area as a follow-up to the work of a previous PhD student with the CBTH project, Jack Kenning, who graduated in 2020. Dr. Mann and I visited with Robert Sorley and Jennifer Masy of Geoex MCG in August 2019 to request the geophysical dataset of their Maximus survey, which included 28,612 line-km of seismic reflection data covering the entire Campeche margin. After beginning the mapping of the grid, I focused my study on the regional structural variation of the Campeche salt basin that could best be explained as a passive margin foldbelt (Padilla y Sánchez, 2007; Pindell and Miranda, 2011; Rivera et al., 2011). This initial mapping study of the Campeche salt basin and its tectonic origin was submitted to the journal *Marine and Petroleum Geology* in February 2021. It was revised and accepted in August 2021.

As I mapped the entire seismic grid for this first project and chapter of this project, I transitioned to a regional thermal maturity model of the basin in collaboration with Andrew Pepper (This !s Petroleum Systems LLC, Fredericksburg, Texas) and Dr. Mann. For this study, the method was based on the concept of thermal stress (Pepper and Corvi, 1995) that differed from the traditional methods of thermal modeling based on vitrinite reflectance which had been used in a previous study by Jack Kenning as part of his PhD study (Kenning and Mann, 2020a). My thermal stress-based modeling study was submitted to the journal *Marine and Petroleum Geology* in August 2022 and was revised and accepted in October 2022.

In 2021, Dr. Mann and I were invited to contribute a chapter on passive margin foldbelt in a volume entitled *Deepwater Sedimentary Systems: Science, Discovery, and Applications*, that was edited by John Rotzien, Cindy Yielding, Richard Sears, Javier Hernandez-Molina, and Octavian Catuneanu. Dr. Rotzien is an adjunct professor at the University of Houston. Dr. Mann suggested I take the lead on writing this paper as I had proposed a similar passive margin foldbelt model for the Campeche salt basin in Chapter 3 of this dissertation (Hasan and Mann, 2021). In this book chapter, I focused on the similarities and hydrocarbon potential of thirteen passive margin foldbelts in the Gulf of Mexico, offshore Atlantic, and East African margins that had been identified by previous workers or by previous CBTH studies of these rifted-passive margins.

As a fourth chapter, Dr. Mann suggested that I follow-up on the CBTH-supported MS work of Benjamin Miller (Miller, 2021), who had made gravity models for the marginal rift of northern Morocco based on a Geoex MCG seismic and ship-based gravity dataset provided to him by Robert Sorley and Jeniffer Masy. Dr. Mann and I again met with Robert Sorley and Jeniffer Masy of Geoex MCG, where I also obtained access to this same offshore Morocco survey. I incorporated the gravity modeling of Benjamin Miller and completed a 1D and map-based basin model based on the modeling principles described in Chapter 4 during the fall semester of 2022.

During the summer of 2022, I was a summer intern at BP Americas in Houston, where I worked on a Jurassic prospect description in the northeastern Gulf of Mexico. Following the internship, I was offered a full-time position in September 2022 and will begin working as a geologist with BP on January 17, 2023. In September 2022, I was approved for permanent residency in the United States based on the contribution of my PhD research to the US economy and national interests.

In addition to the research described above, I was a member of the AAPG Wildcatters student organization for three years at UH. I served as its treasurer for the 2020-2021 academic year.

During the course of my PhD program, I presented my research at many national and international conferences, either in-person or virtually. Professional interactions gained from these meetings were important for continuously improving the quality of my research. The presentations and meetings attended are summarized below.

In addition to the research awards listed below, I received the Outstanding Graduate Work in Geology Award from the EAS Department in 2021 and 2022 based on my high CGPA and research progress.

Table 1.1 Conference and meeting presentations given throughout PhD.

Event	Title	Awards	Presentation date
Houston Geological Society Robert E. Sheriff Lecture, Univ. of Houston	Structural and stratigraphic history of the deepwater Campeche and Yucatan sub-basins, southern Gulf of Mexico		November 11, 2019
AAPG ACE Annual Convention and Exhibition, Houston, Texas	Explaining differing styles of salt deformation in the Campeche and Yucatan salt basins, southern Gulf of Mexico	2^{nd} place student poster presentation competition ($1500)	September 30, 2020
Gulf Coast Association of Geological Societies conference (Geogulf 2020), Louisiana, Texas	Deformation of the Campeche salt province, southeastern Gulf of Mexico, interpreted within the structural framework of a passive margin foldbelt	3rd place poster presentation (tie), Gordon I. Atwater Award	October 2, 2020
Houston Geological Society Robert E. Sheriff Lecture, University of Houston	Explaining structural styles of the Campeche salt province, southwestern Gulf of Mexico, within the		November 9, 2020

	framework of a passive margin fold belt		
AAPG Virtual Research Symposium: Mexican Basins, Virtual	Relating structural style of the Campeche salt basin, southwestern Gulf of Mexico, to subtle, northward dip variations in its underlying basement		November 19, 2020
AGU Fall Meeting, Virtual	Basement controls on the downdip transport direction and internal salt structures of the Campeche passive margin foldbelt, southeastern Gulf of Mexico		December 15, 2020
UH EAS 34th Annual Student Research Conference and Alumni & Industry Open House, Univ. of Houston	Thermal maturity modeling of the Tithonian source rocks along the Campeche salt basin, southern Gulf of Mexico		April 30, 2021
IMAGE (SEG/AAPG) International Meeting for Applied Geoscience & Energy, Virtual	Rifted, continental basement morphology of the Campeche salt basin and its controls on pods of source rock maturity, southern Gulf of Mexico	Selected as one of the top 15 best student poster abstracts, but no student poster competition was offered at this meeting	September 27, 2021

IMAGE (SEG/AAPG) International Meeting for Applied Geoscience & Energy, Virtual	Mega-regional seismic mapping of the Moroccan rifted-passive margin of the Central Atlantic Ocean	No student poster competition was offered at this meeting	September 27, 2021
Gulf Coast Association of Geological Societies conference (Geogulf 2021), Austin, Texas	Regional thermal maturity modeling along the Campeche salt basin, southern Gulf of Mexico		October 28, 2021
Houston Geological Society Robert E. Sheriff Lecture, Univ. of Houston	Thermal maturity modeling along the Campeche Salt Basin, southern Gulf of Mexico		November 1, 2021
Third EAGE-HGS Conference on Latin America, Virtual	Regional source rock maturity modeling along the Campeche salt basin, southern Gulf of Mexico		November 9, 2021
PEMEX Sedimentary Basin Analysis Conference, Virtual	Structure, stratigraphy, and petroleum potential of the deepwater southern Gulf of Mexico	Invited talk by PEMEX	March 9, 2022
UH EAS 35th Annual Student Research Conference and Alumni & Industry	Estimating thermal stress and expelled hydrocarbons from Mesozoic-Cenozoic source rocks of the southern Gulf of Mexico	1st Place Presentation (Advanced PhD - $850)	April 29, 2022

Open House, Univ. of Houston			
Asociacion Mexicana de Geologos Petroleros Conferencia, Virtual	Structural evolution and petroleum potential of the Campeche and Yucatan salt basin	Invited talk	March 30, 2022
IMAGE (SEG/AAPG) International Meeting for Applied Geoscience & Energy, Houston, Texas	Tectonic history and hydrocarbon potential of the Moroccan rifted-passive margin		August 29, 2022
21st HGS-PESGB Africa Conference, Houston, Texas	Tectonic controls on source rock thermal maturity of the Atlantic rifted-passive margin of Morocco	Best student presentation ($100)	September 26, 2022

1.2 Rationale, topics, and organization of this dissertation

The overall goal of this dissertation is to improve understanding of the tectonic evolution, structural styles, source rock thermal stress, and hydrocarbon prospectivity of rifted-passive margins. The dissertation includes one chapter on passive-margin foldbelts of the Gulf of Mexico, circum-Atlantic and western Indian Ocean, two on the Campeche salt basin, and one on offshore Morocco. All of these chapters are either published in peer-reviewed book chapters or journals or are in press in journals as summarized below:

Chapter 2: **Deepwater passive margin foldbelts**. Chapter 2 has been published as: Hasan, M.N., Mann, P., 2022. Deepwater passive margin foldbelts. In: Rotzien, J., Yeilding, C., Sears, R., Hernández-Molina, F.J., Catuneanu, O., (Eds.), *Deepwater Sedimentary Systems: Science, Discovery, and Applications*, Elsevier, p. 119-147. https://doi.org/10.1016/B978-0-323-91918-0.00016-5.

Chapter 3: **Structural styles and evolution of the Campeche salt basin, southern Gulf of Mexico.** Chapter 3 has been published as: Hasan, M.N., Mann, P., 2021. Structural styles and evolution of the Campeche salt basin, southern Gulf of Mexico. *Marine and Petroleum Geology*, v. 133, n. 105313. https://doi.org/10.1016/j.marpetgeo.2021.105313.

Chapter 4**: Basin-scale estimates of thermal stress and expelled petroleum from Mesozoic-Cenozoic potential source rocks, southern Gulf of Mexico.** As of the time of submission of this dissertation, Chapter 4 is in press with the journal *Marine and Petroleum Geology*.

Chapter 5**: Controls of tectonic evolution on source rock thermal maturity of the Moroccan salt basin.** As of the time of submission of this dissertation, Chapter 5 is in review with the journal *Basin Research*.

1.2.1 Summary of Chapter 2

Deepwater passive margin foldbelts (PMFBs) are the present and future focus of exploration and production due to the abundance of undrilled structural traps, the presence of natural oil seeps, and advances in deepwater drilling technology. PMFBs are characterized by linked updip extension and downdip contraction detached over a basinward dipping layer of salt or overpressured shale. PMFBs are found on rifted- and transform-passive margins around the world, such as the Gulf of Mexico, offshore South Atlantic, and East African margins. The linked kinematic system is driven by a combination of gravitational force resulting from thermal subsidence, onshore cratonic uplift, tectonic oversteepening of the margin, and deltaic depositional loading. Symmetric detachment folds typically dominate systems associated with salt detachment, whereas shale-detached PMFBs are dominated by imbricate thrusts, fault-bend folds, and fault-propagation folds. The difference in structural style is caused by different rheology of the detachment layer.

1.2.2 Summary of Chapter 3

The late Jurassic Campeche salt basin in the southern Gulf of Mexico (GOM) forms a passive margin foldbelt of late Middle Miocene to Recent age. The Campeche salt basin is defined by a 200-km-wide updip zone of listric, normal faults of the Comalcalco and Macuspana rifts, and a coeval, 300-km-wide, downdip zone of deeper-water, salt-cored folds, detachment folds with kink bands, thrusts, and diapirs. This study integrates shipborne magnetic data with 28,612 km of pre-stack, depth-migrated, 2D seismic data to reconstruct the geometry of the top of the Paleozoic basement and base-salt topography above which the passive margin foldbelt evolved. Magnetic and basement mapping reveals that the 40-55-km-wide Campeche segment of the 400 km long GOM outer marginal trough marks the limit of the northwest-directed passive margin foldbelt. The elongated basement depression of the outer marginal trough combined with a basement step-up fault along the edge of the Jurassic oceanic crust localizes the thickest Bajocian-early Callovian salt. The outer marginal trough controls the arcuate, northwestward, and downdip path of salt flowage within the passive margin foldbelt.

1.2.3 Summary of Chapter 4

The Campeche and Yucatan salt basins remain two of the least explored areas of the Gulf of Mexico basin. This study uses a grid of 23,600 line-km pre-stack depth migrated (PSDM) 2D seismic reflection profiles, shipborne gravity data, and open-source geologic information to model the thermal stress of four potential source intervals (Oxfordian, Tithonian-centered, Cenomanian-Turonian, lower Miocene). We performed map-based and 1D thermal modeling along two margin-perpendicular transects, each consisting of five pseudo wells tied to the regional grid of seismic reflection data. My modeling takes into account thermal stress variations related to the depth of base lithosphere, crustal type and thickness, paleo-water depth, Jurassic salt thickness, and the transient heat flow effects related to recent clastic sedimentation. We predict that deeply-buried, salt-related minibasins along the outer marginal trough are mature for petroleum expulsion with deeply-buried Mesozoic source rocks within the oil window during the late Paleogene to early Neogene time. The 'lag time' required for vertical oil migration explains why oil maturation occurred in the late Paleogene to early Neogene but active oil seeps are observed today at the sea surface. I predict that oil is present in subsurface traps in the deepest part of the outer marginal trough and we calculate that the Oxfordian source interval has expelled a cumulative 20 million bbl of oil equivalent [BOE]/km2 and that the Tithonian-centered source interval has expelled 67 million bbl of oil equivalent [BOE]/km2.

1.2.4 Summary of Chapter 5

This study of the Moroccan salt basin of the Central Atlantic Ocean interprets a grid of ~8474 line-km of pre-stack, depth-migrated, 2D seismic reflection profiles, publicly-available gravity and well data, and 2D gravity models. Gravity modeling and seismic interpretation reveal a ~750 km elongate, 50-80-km-wide basement low or marginal rift that overlies the zone of the rifted continental necking domain, parallels the modern coastline of Morocco, and crosscuts the east-northeast orogenic and Mesozoic rift grain of northwestern Africa. Calibrations of downhole temperature measurements from Tantan-1 and DSDP-416 offshore wells were then used to constrain 1D and map-based thermal maturity models to understand the hydrocarbon potential of source rocks ranging in age from Triassic to Late Cretaceous. Calibration of Tantan-1 and DSDP-416 shows that the geothermal gradient in the marginal rift is 29 °C and in the oceanic crust is 23 °C. Radiogenic heat due to the granitic composition causes a higher geothermal gradient in the continental crust. Modeling shows that the absence of radiogenic heat in the oceanic crust results in relatively lower geothermal gradients and can explain the immaturity of source rocks in these deepwater areas. Deeply-buried Triassic and Jurassic source rocks are mature for petroleum generation along the southern ~400 km of the marginal rift as validated by a compilation of the locations of offshore producing wells and shows. Late Cretaceous - Base Cenozoic uplift and erosion of the margin were observed as a major angular unconformity and break in vitrinite reflectance in the offshore area. The absence of Early Cretaceous deltaic deposits is why Cretaceous source rocks have remained immature in the northern ~350 km marginal rift.

The following chapter is based on: Hasan, M.N., Mann, P., 2022. Deepwater passive margin foldbelts. In: Rotzien, J., Yeilding, C., Sears, R., Hernández-Molina, F.J., Catuneanu, O., (Eds.), Deepwater Sedimentary Systems: Science, Discovery, and Applications, Elsevier, p. 119-147. https://doi.org/10.1016/B978-0-323-91918-0.00016-5.

CHAPTER 2: DEEPWATER PASSIVE MARGIN FOLDBELTS

2.1 Introduction

2.1.1 What is a passive margin foldbelt?

Passive margin foldbelts (PMFBs) are zones of gravitational failure along low-angle detachments that result in updip, extensional structures on the shelf and slope, and downdip compressional structures in the deepwater basin (Rowan et al., 2004) (Fig. 2.1). Over the past few decades, interest has increased significantly in deepwater passive margin foldbelts primarily due to the presence of undrilled structural closures with reported natural oil seeps (Morley et al., 2011). Currently, deepwater PMFBs have become a focus of deepwater exploration with several recent giant discoveries (Zhang et al., 2017). However, PMFBs are challenging structural settings to interpret and model in the overall context of understanding deepwater sedimentary systems. This chapter addresses the traits and variability in passive margins foldbelts in selected deepwater provinces.

The term PMFB takes into account all three of these structural domains: an updip extensional domain marked by rift features, a middle transitional zone of sliding with an absence of either rifts or folds, and a downdip compressional zone marked by thrusting, folding, diapir squeezing, and salt nappe extrusion (Fig. 2.1). Counter-regional (landward-dipping) normal faults and associated rollovers can also form as local complexities produced by abrupt variations in the geometry of the detachment surface (Rowan, 2020). The variability in these structural domains plays a key role in all aspects of the upstream exploration process and evaluation of prospects in PMFB.

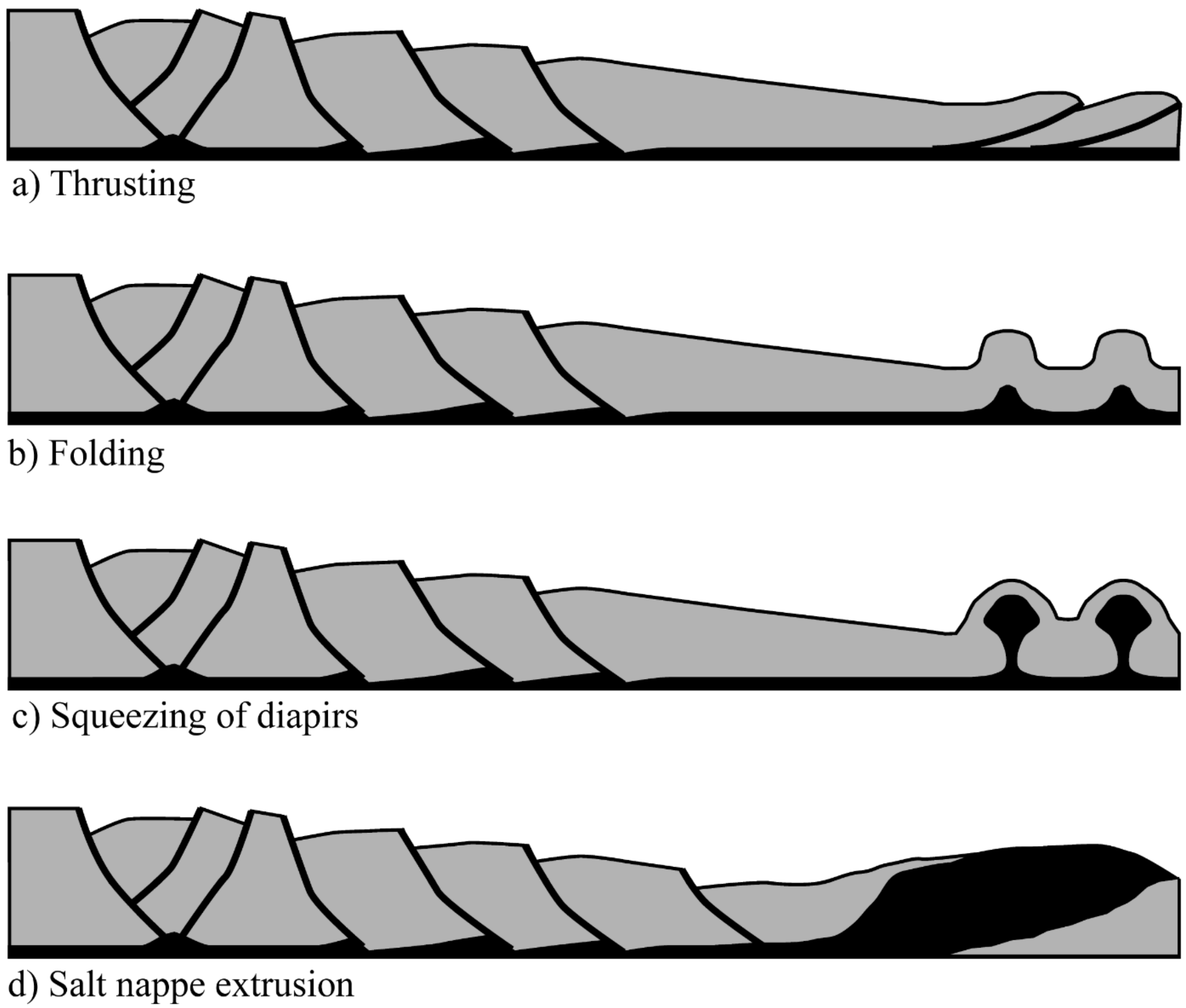

Figure 2.1: Schematic diagram showing different styles of gravitational failure detached on either salt or shale interval that result in differing structural types of passive margin foldbelts: (a) thrust-dominated shortening results in a fold-thrust belt at the base of the PMFB; (b) fold-dominated shortening with more upright folds at the base of the PMFB; (c) squeezing of pre-existing diapirs produces even higher relief, upright folds; (d) inflation of salt body resulting extrusion of a salt nappe at the base of the PMFB (modified from Rowan et al., 2004).

The width of these PMFBs can range from a few kilometers to hundreds of kilometers, as shown in the many examples described in this chapter. The driver for the detachment of PMFB is the potential energy stored in landward to seaward-sloping stratigraphic surfaces. Detachment in such settings commonly occurs along a low-friction evaporitic layer or overpressured shale.

Common mechanisms that have been previously proposed to explain the locations of PMFB include: (1) rapid sedimentary loading related to a tectonic event from the hinterland and (2) the formation of a large delta that contributes to a localized and updip zone of anomalously thick clastic sedimentation (Morley et al., 2011). Both of these settings produce oversteepening of the passive margin that is necessary to generate sufficient shear stress for failure and the resulting formation of the PMFB (Krueger and Gilbert, 2009).

2.1.2 Objectives

The objective of this chapter is to explain the structural evolution, similarities, dissimilarities, and controlling factors for the formation of shale- and salt-based, deepwater PMFB of the Gulf of Mexico, Atlantic Ocean, and western Indian Ocean. In addition to the scientific relevance, these regions are selected for many reasons, including data availability and diversity, petroleum prospectivity, and the quality of the ongoing research conducted by the Conjugate Basins, Tectonics, and Hydrocarbons industry-funded research consortium led by scientists at the University of Houston (Fig. 2.2). Examples of PMFB from other passive margins along the eastern Indian Ocean and southeastern and eastern Asia are reviewed by Morley et al. (2011).

Studied PMFB in this chapter include (Table 2.1; Fig. 2.2): (1) the Atwater-Mississippi PMFB of the US Gulf of Mexico, (2) the Perdido PMFB of the US Gulf of Mexico, (3) the Mexican Ridges PMFB of the Mexican Gulf of Mexico, (4) the Campeche PMFB of the Mexican Gulf of

Mexico, (5) the Foz do Amazonas PMFB associated with the Amazon Delta of northern Brazil, (6) the Pará-Maranhão PMFB of northern Brazil, (7) the Barreirinhas PMFB of northern Brazil, (8) the Pelotas PMFB of northern Brazil, (9) the Niger PMFB associated with the Niger Delta of Nigeria, (10) the Kwanza PMFB of Angola, (11) the Orange River PMFB of South Africa, (12) the Lamu PMFB of the Kenyan passive margin in the western Indian Ocean, and (13) the Rovuma PMFB of the Mozambique passive margin in the western Indian Ocean.

Publicly-available and dip-oriented regional cross-sections at similar vertical exaggerations are shown for each passive margin foldbelt system. These standardized maps and cross-sections allow the scientific community to address the following six questions that are key for understanding the origin, structural evolution, and deepwater hydrocarbon potential of PMFB:

(1) What are the controls on the variations in the lateral extent of the three characteristic structural domains of PMFB: the updip, extensional zone, the transitional zone, and the downdip, compressional zone?

(2) What are the controls on the dip of the underlying detachment and the bathymetric slopes, and how do these variable dips affect the observed structural styles?

(3) Are there appreciable differences in the structural styles of PMFB based on their detaching on salt versus shale horizons?

(4) What are the causes of margin oversteepening that produce margin instability and result in the formation of PMFB?

(5) How do the taper angles of PMFB compare with the taper angles of accretionary prisms in subduction settings and subaerial fold and thrust belts?

(6) How does PMFB affect the components of deepwater petroleum systems that include source rocks, reservoirs, traps, and hydrocarbon maturation?

Figure 2.2: Map of global topography (Olson et al., 2016) and bathymetry (GEBCO, 2020) showing the location and detachment type of the passive margin foldbelts of the Gulf of Mexico, Atlantic Ocean, and western Indian Ocean. The colored rectangles represent the detachment type of the passive margin foldbelts (red = PMFB with gliding on a salt detachment and yellow = PMFB with gliding on a shale detachment). Thirteen PMFB described in this chapter include: (1) Atwater-Mississippi foldbelt of the US Gulf of Mexico (GOM), (2) Perdido foldbelt of the US Gulf of Mexico, (3) Mexican Ridges foldbelt of the Mexican Gulf of Mexico, (4) Campeche salt basin of the Mexican Gulf of Mexico, (5) Foz do Amazonas Basin related to the delta of the Amazon River of northern Brazil, (6) Pará-Maranhão Basin of northern Brazil, (7) Barreirinhas Basin of northern Brazil, (8) Pelotas Basin of southern Brazil and Uruguay, (9) Niger Delta of Nigeria, (10) Kwanza Basin of Angola, (11) Orange River Basin of South Africa, (12) Lamu Basin of Kenya, and (13) Rovuma Basin of Mozambique.

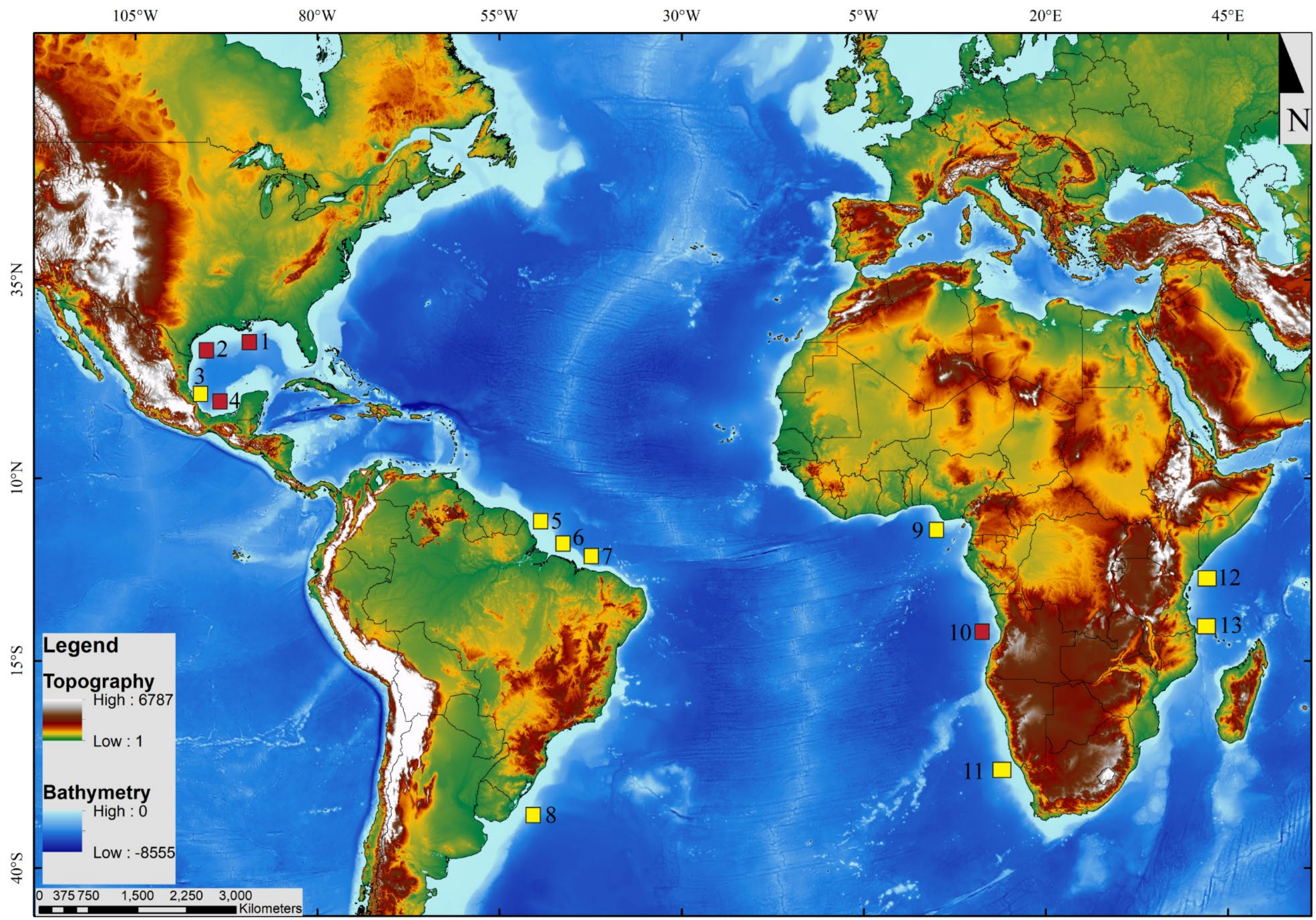
105°W
80°W
55°W
30°W
5°W
20°E
45°E
35°N
10°N
15°S
40°S
N
1
2
3
4
5
6
7
8
9
10
11
12
13
Legend
Topography
High : 6787
Low : 1
Bathymetry
High : 0
Low : -8555
0 375 750 1,500 2,250 3,000
Kilometers

2.2 Previous studies of passive margin foldbelts: Main findings and implications

Passive margin foldbelts defined by updip extension and downdip shortening along either salt or shale detachments were first identified and systematically described by Rowan et al. (2004) (Fig. 2.1). This study noted that PMFB deformation includes elements of both gravity sliding along a basinward-dipping detachment surface and gravity spreading of a sedimentary wedge along a seaward-dipping bathymetric surface. Shortening at the base of the PMFB is driven by shelf and upper slope deposition that maintains the bathymetric slope and the gravitational potential with increased basinward tilting. The system can be driven by both thermal subsidence of the adjacent oceanic crust and increased basinward tilting related to the uplift of the continental block. The net shortening amounts and deformation rates of PMFB are much lower than those observed in either subaerial fold and thrust belts or subduction-related accretionary prisms because the driving, gravitational forces of thin-skinned PMFB are much smaller than the thicker-skinned forces related to the convergence of lithospheric plates.

Rowan et al. (2004) concluded that the main control on the variation in structural styles of PMFB was whether the detachment horizon beneath the PMFB was composed of shale with frictional strength—that produces basinward-verging thrust imbricates and associated folds because of the properties of plastic shale—or salt—that produces symmetrical fold above a viscous salt sheet with no internal frictional strength.

Morley et al. (2011) produced a global review of deepwater PMFB but widened the PMFB definition to include subduction-related accretionary prisms and deformed belts formed in arc-continent and continent-continent collisional zones. For the collisional types, these authors drew examples from Southeast Asia and East Asia. Rowan et al. (2004) and Morley et al. (2011) pointed out that the largest control on the structural styles of deepwater foldbelts sensu lato was shale vs. salt detachments—rather than their diverse tectonic settings.

Other than these two global reviews, most previous studies of PMFB have focused on specific examples of PMFB, such as the Atwater-Mississippi fan foldbelt (Bouroullec et al., 2017; Bouroullec and Weimer, 2017; Peel et al., 1995), Perdido foldbelt (Fiduk et al., 1999; Trudgill et al., 1999), Mexican Ridges foldbelt (Salomón-Mora et al., 2009), Campeche salt basin (Hasan and Mann, 2021), Foz do Amazonas (Reis et al., 2016), Pará-Maranhão, and Barreirinhas Basin (Oliveira et al., 2013), Pelotas Basin (Strozyk et al., 2017), Niger Delta (Bilotti and Shaw, 2005; Wu et al., 2015; Zhang et al., 2021), Kwanza Basin (Evans and Jackson, 2020; Hudec and Jackson, 2004), Orange River Basin (de Vera et al., 2010), Lamu Basin (Cruciani et al., 2017; Cruciani and Barchi, 2016), and Rovuma Basin (Cai et al., 2020). Academic and industry studies have produced a considerable amount of high-quality and deep-penetration seismic reflection data from PMFB. Several seismic profiles and cross-sections are used in this analysis.

This chapter focusses only on the origins and evolution of PMFB from the Gulf of Mexico, the South Atlantic Ocean, and the western Indian Ocean. This chapter does not include in its analysis the more broadly defined collision-related margins of the southeast and east Asia, summarized by Morley et al. (2011).

Table 2.1: Compilation of the main characteristics of the thirteen passive margin foldbelts described in this chapter, including their geographic locations, their basin name, the detachment type, the detachment surface age, the detachment slope angle, and the bathymetric slope as measured from the seismic reflection lines and cross-sections shown in this chapter.

Geographic location	Basin name	Detachment type	Detachment surface age	Extensional domain (km)	Translational domain (km)	Compressional domain (km)	Detachment slope angle (β)	Bathymetric slope (α)
Gulf of Mexico	Atwater-Mississippi foldbelt	Salt	Middle Jurassic	260	---	150	3.5	0.9
	Perdido foldbelt	Salt	Middle Jurassic	300	---	215	5	1.5
	Mexican Ridges foldbelt	Shale	Eocene-Oligocene	65	15	120	7	2.3
	Campeche salt basin	Salt	Middle Jurassic	200	---	300	3	2.2
Offshore South America	Foz do Amazonas basin	Shale	Early Cretaceous; base Paleocene-Eocene; early Pliocene	85	---	120	3	1.1
	Pará-Maranhão basin	Shale and marls	Paleocene	13	5	15	7	1.5
	Barreirinhas basin	Shale	Late Cretaceous	40	13	13	4	2
	Pelotas basin	Shale	Paleocene-Eocene	150	20	38	2	1.9
Offshore West Africa	Niger delta	Shale	Cretaceous	190	22	85	1.5	1.4
	Kwanza basin	Salt	Early Cretaceous	200	---	160	2	2.2
	Orange River basin	Shale	Late Cretaceous	140	20	95	1	1.1
Offshore East Africa	Lamu basin	Shale	Late Cretaceous, late Oligocene	13	10	20	3	1.9
	Rovuma basin	Shale	Late Eocene	21	11	45	2	3.4

2.3 Examples of passive margin foldbelts in the Gulf of Mexico

2.3.1 Regional setting of passive margin foldbelts in the Gulf of Mexico

The Gulf of Mexico (GOM) contains several well-described examples of gravity-driven PMFB that are detached on both salt and shale horizons (Fig. 2.3). The Gulf of Mexico evolved during a two-phase opening, with the first phase of rifting from the Triassic to the Middle Jurassic, and the second phase marked by seafloor spreading during the Late Jurassic (Marton and Buffler, 1999; Pindell and Kennan, 2009; Hudec et al., 2013; Eddy et al., 2014; Nguyen and Mann, 2015).

Following Phase 1 rifting (~210–163 Ma), seawater—probably from the Pacific Ocean—filled the broad sag basin overlaying the extinct rifts of the Bajocian-early Callovian and, through repeated episodes of evaporation, formed the Louann-Campeche salt deposit as part of a single, giant salt basin (Nguyen and Mann, 2015; Steier and Mann, 2019). The progressive, counterclockwise rotation of the Yucatan continental block formed an area of Late Jurassic, post-salt oceanic crust in the deep, central part of the Gulf of Mexico that separated the southern Campeche salt basin from the Louann salt basin.

In this section, the gravity-driven tectonics and hydrocarbon potential of the Gulf of Mexico are described in four key areas (Fig. 2.3): (a) Atwater-Mississippi fan PMFB, (b) Perdido PMFB, (c) Mexican Ridges PMFB, and (d) Campeche PMFB. The basin margins of the Gulf of Mexico have undergone extensive gravitational gliding and spreading since the Middle Jurassic (Bouroullec and Weimer, 2017; Rowan et al., 2004). The major detachment layer for most of these PMFB is the Middle Jurassic salt—except in the case of the Mexican Ridges PMFB—where the detachment layer is Eocene–Oligocene shale (Peel et al., 1995; Salomón-Mora et al., 2011).

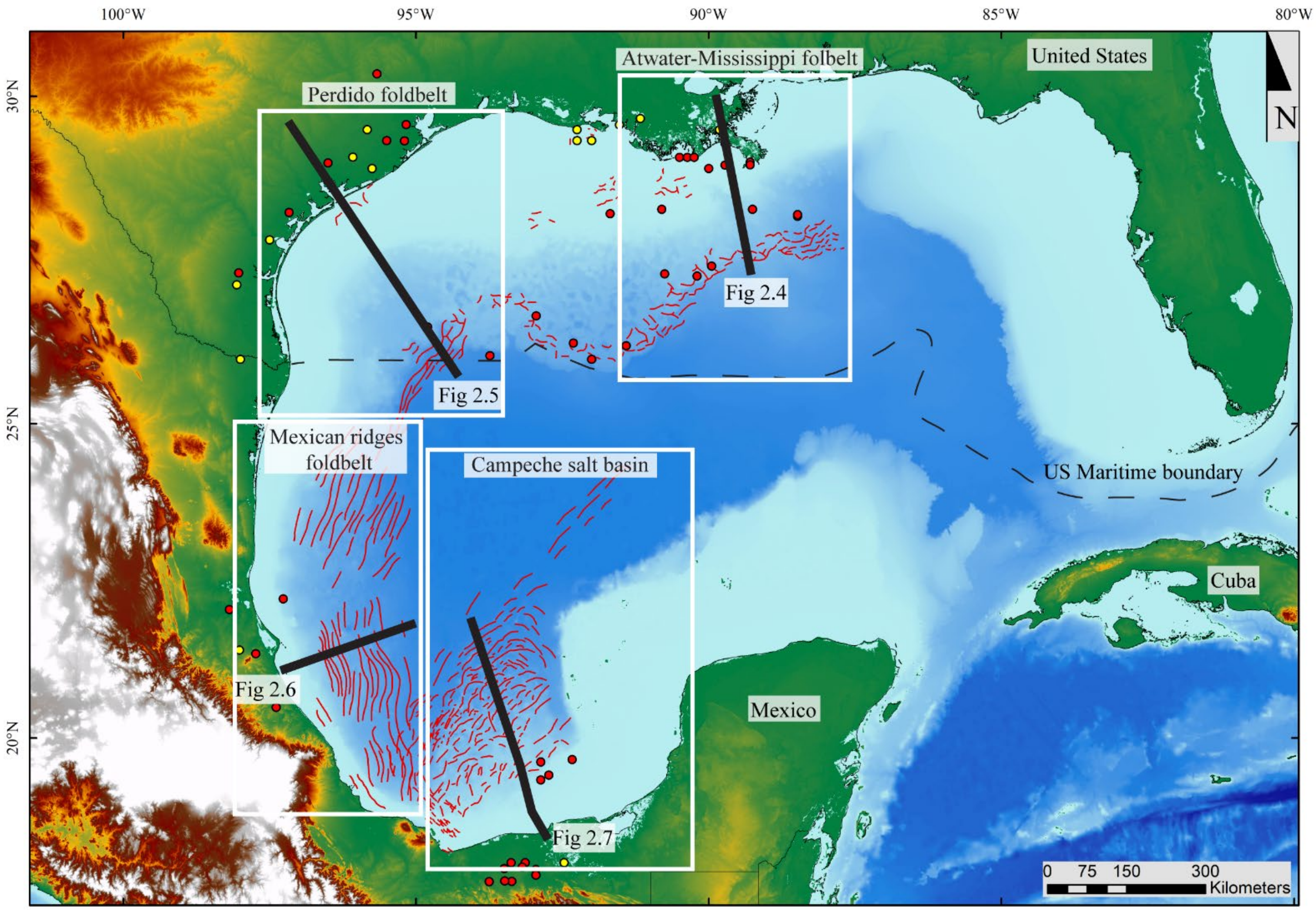

Figure 2.3: Bathymetric map of the Gulf of Mexico showing the distribution of passive margin foldbelts included in this study. PMFBs include the salt-detached Atwater-Mississippi PMFB, salt-detached Perdido PMFB, salt-detached Campeche PMFB, and shale-detached Mexican Ridges PMFB. US maritime boundary is shown by the dashed black line passive margin fold axes are shown by red lines; locations of the illustrated cross-sections are shown by the solid black lines, and the location of giant oil and gas fields are shown by the red dots (oil fields) and by the yellow dots (gas fields) (CBTH database compilation, 2020).

2.3.2 Atwater-Mississippi fan passive margin foldbelt

Structural provinces and age of formation

The Atwater-Mississippi fan and passive margin foldbelt in the northeastern US Gulf of Mexico is influenced by complex salt tectonics that controlled the formation of minibasins and salt-associated structures. The Mississippi Delta constitutes the primary sediment source to the slope and deepwater and produced a major influx of clastic deposition during the Miocene–Pliocene that shaped the present-day morphology of this PMFB. The Atwater-Mississippi fan has a Neogene stratigraphic thickness of 3000–8500 m (Bouroullec and Weimer, 2017).

Unlike other passive margins around the world where only the basal autochthonous salt level acts as the primary salt detachment, the thicker, remobilized salt in the Gulf of Mexico produces local areas where a high-level, secondary detachment and salt canopy is formed, as seen for the Atwater-Mississippi fan PMFB (Bouroullec and Weimer, 2017). The extensive allochthonous salt-feeder system is likely controlled by thick Middle Jurassic salt deposition (Hasan and Mann, 2021). The enormous Neogene sediment deposition and complex, structural variability provide numerous listric normal faults, counter-regional faults, salt-withdrawal minibasins, salt canopy, folds, and thrust structures (Fig. 2.4; Grando et al., 2009).

Regional structural profile

The northwest-southeast regional, structural cross-section of the Atwater-Mississippi PMFB (Fig. 2.4) shows a 260-km-wide extensional domain dominated by Paleogene-Early Miocene listric normal faults. The present-day shelf that is affected by the extensional domain exhibits an extensive counter-regional salt-withdrawal basin filled with Miocene–Pliocene strata.

The Middle Jurassic autochthonous salt is completely evacuated from the salt-withdrawal minibasin, forming a large salt weld (Fig. 2.4).

The compressional domain of the Atwater-Mississippi PMFB extends 150 km in the northwest-southeast direction (Fig. 2.4). The updip part of the compressional domain is dominated by relatively smaller salt bodies while the downdip to the distal end of the passive margin system contains a single, large salt canopy. The injection of secondary salt bodies into the clastic intervals constrains a Middle to Late Miocene timing for salt emplacement.

A fold-thrust belt exists beneath the salt canopy in the compressional domain with the foldbelt detaching on an underlying and autochthonous salt horizon. The total shortening across all the folds and thrusts is 10 km with its formation during the Middle to Late Miocene (Peel et al., 1995). The Middle to Late Miocene timing of the allochthonous salt emplacement, folds, and thrusts of the PMFB is linked to the influx of 4–8 km of clastic sedimentation from the Mississippi Delta.

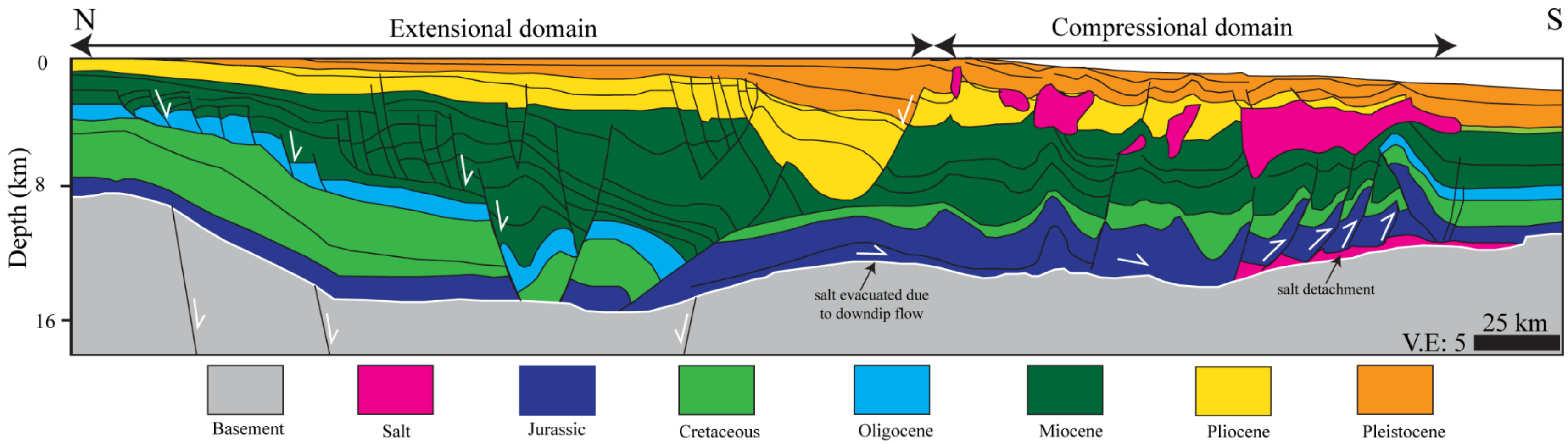

Figure 2.4: Regional northwest-to-southeast depth cross-section through the Mississippi-Atwater passive margin foldbelt of the northern US Gulf of Mexico (location of the cross-section is shown on the map in Fig. 2.3). The lateral extents of the extensional and compressional domains are indicated. The compressional structures at the toe of the slope are cored by the Louann salt of the Middle Jurassic age. The complete evacuation of Louann salt from the updip extensional domain inflates the downdip structures and, in some cases, results in an allochthonous sheet in the upper part of the section (modified from Grando et al., 2009).

Hydrocarbon potential

The hydrocarbon potential of the Atwater-Mississippi PMFB is controlled by the interaction of salt tectonics and high sedimentation in the Neogene that provides the necessary structural traps and high-quality reservoir rocks. Extensive exploration and production with major discoveries are reported in the Atwater-Mississippi passive margin foldbelt. They include Neptune, Mad Dog, Tahiti, Knotty Head, Genghis Khan, Big Foot, and Thunder Horse (Morley et al., 2011).

Bouroullec et al. (2017) compiled 87 discoveries in the Atwater-Mississippi fan foldbelt and showed that 19 fields produce from structural traps with four-way dip closures (anticlines, salt pillows, turtle structures), 52 fields have combined structural-stratigraphic traps with three-way closures (salt-flank traps, foldbelt truncation traps), and 16 fields produce from stratigraphic traps (pinch outs, channels, and valley fills). Most of the successful traps are combined structural-stratigraphic traps. Almost all of the fields produce from Oligocene to Pleistocene reservoirs (Bouroullec et al., 2017). In these fields, high-quality reservoirs are primarily turbidites deposited in basin-floor fan systems originally fed by the Mississippi Delta.

2.3.3 Perdido passive margin foldbelt

Structural provinces and age of formation

The deepwater Perdido foldbelt, northwestern Gulf of Mexico (Fig. 2.3), includes an onshore extensional system, the Port Isabel foldbelt compressional zone, and a downdip compressional zone defined by large detachment folds cored by autochthonous Middle Jurassic salt (Fig. 2.5). Updip extension of approximately 60 km suggests the downdip fold and thrust belt and salt canopy should collectively accommodate a similar amount of shortening (Trudgill et al., 1999).

Two orogenic events of the Cordilleran orogeny of the Pacific margin of North America controlled the evolution of the Perdido PMFB during the Cenozoic period (Fitz-Díaz et al., 2018): first, the Laramide orogeny during the Late Cretaceous to Eocene and second, the post-orogenic uplift of North America from the Oligocene to present-day. Both events increased the seaward tilt of the western margin of the Gulf of Mexico and the resulting denudation led to large amounts of clastic sedimentation (Hudec et al., 2019). The combination of increased tilting and sedimentation destabilized the margin and gave rise to the Perdido PMFB system during the Oligocene, with gravity-related sliding continuing to the Miocene. The onset of deltaic deposition related to the Mississippi River in the Miocene–Pliocene resulted in the depositional abandonment in the Perdido PMFB and created a stable, gravitational equilibrium (Morley et al., 2011).

The primary detachment layer of the Perdido PMFB is the Middle Jurassic Louann salt. One unique feature of Perdido is the presence of a basement step-up called the “Baha High” by Hudec et al. (2019). Buttressing against the Baha High also forms the limit of the salt canopy in the Perdido PMFB. Basinward of the salt canopy is a series of anticlines that vary in their structural profile from symmetrical to asymmetrical. These anticlines are associated with reverse faults and kink bands (Fig. 2.5).

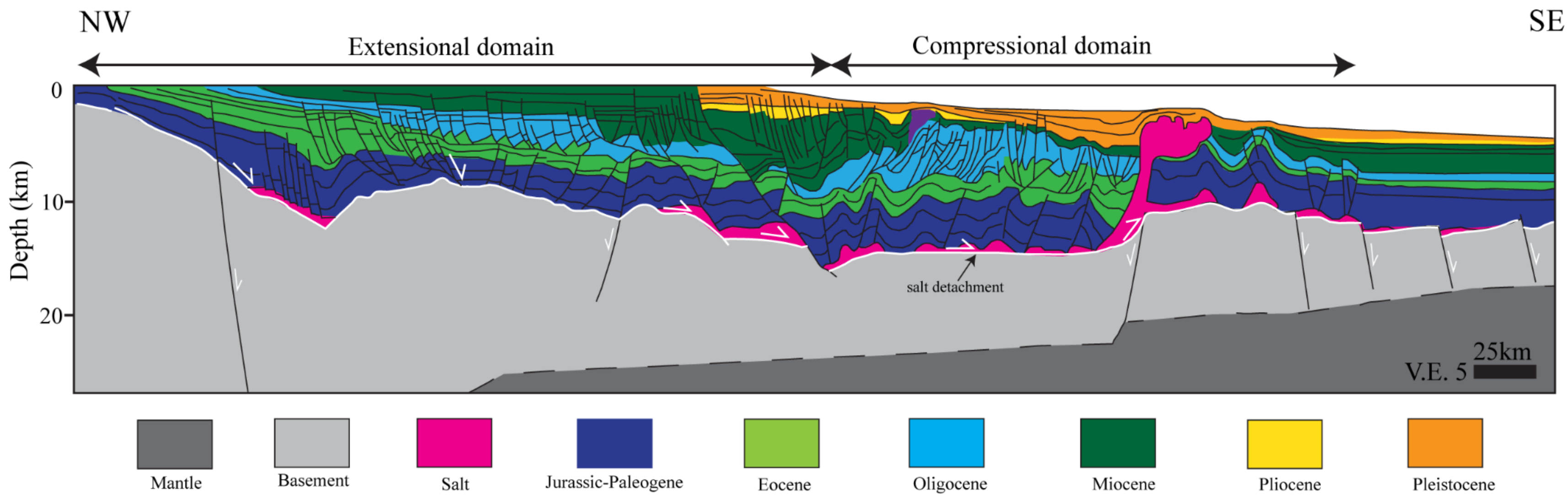

Figure 2.5: Regional, northwest-to-southeast, depth cross-section through the Perdido passive margin foldbelt in the northwestern part of the US Gulf of Mexico (location of the section is shown on the map in Fig. 2.3). The section shows the complex, stacked system of salt detachments. Numerous listric normal faults and zones of salt deflation characterize the updip extensional domain, while thrusts, salt inflation, and an upper salt canopy characterize the downdip compressional domain. Salt buttressing and emergent folds form along a basement ramp or "step-up fault" called the "Baha High" that also forms the approximate limit of the salt canopy. The Perdido foldbelt is the downdip and more external part of a more extensive belt of contraction that includes the Port Isabel foldbelt with its own salt canopy (modified from Trudgill et al., 1999; Morley et al., 2011).

Regional structural profile

The northwest-southeast dip-oriented structural cross-section of the Perdido PMFB traverses both the updip extensional and downdip compressional domains (Fig. 2.5). A 300-km-wide zone representing a thin-skinned extensional system detaches along Callovian-Bajocian salt. A secondary detachment with extensional growth faults can be observed along an Eocene horizon with a significant growth sequence during the Miocene.

The 215-km-wide downdip compressional domain is dominated by multi-level detachment structures, a salt canopy, and anticlines with reverse faults on both limbs. Thrusts and folds form multiple detachment layers in the middle part of the cross-section. The structures detaching over salt are gentle detachment folds, whereas structures detaching along Eocene shale units represent strongly shortened folds and thrusts. On the lower slope of the Perdido PMFB, the basement step-up fault (Baha High) marks the distal edge of the salt canopy.

Hydrocarbon potential

The cluster of large deepwater discoveries in the distal, downdip area of the Perdido PMFB includes BAHA, Trident, Great White, Silvertip, and Tobago. All indicate a working petroleum system (Morley et al., 2011). Seafloor oil seeps have been reported in the downdip portion of Perdido and indicate the presence of a mature source rock, which is Tithonian in age (Fiduk et al., 1999).

Maturity modeling by previous studies suggests that the Tithonian source rock passed into the peak oil window after the formation of the large structural closures. Trudgill et al. (1999) interpreted some of the structures in the Perdido area were not covered by fine-grained sediment until 10.5Ma, suggesting that seal integrity is the highest risk factor. The presence of numerous normal faults and reverse faults likely provide migration pathways.

No significant discoveries have been reported in the middle slope of the basin, such as the Port Isabel exploration area (Morley et al., 2011). Buttressed by the Baha High in the downslope direction, the stress provided by the updip extension is likely accommodated in the Port Isabel area. This observation suggests this zone is more structurally complex than the downdip compressional area (Peel et al., 1995). Thrusts and folds within the multi-detachment represent potential areas where seal failure is a key risk.

2.3.4 Mexican Ridges passive margin foldbelt

Structural provinces and age of formation

The Mexican Ridges extend over >400 km across the western Gulf of Mexico and form a Neogene passive margin foldbelt (Fig. 2.3) (Kenning and Mann, 2020a). The margin exhibits significantly different structural styles than the salt-filled northeastern and southern Gulf of Mexico. Callovian-Bajocian salt is absent in the Mexican Ridges because the area is underlain by an oceanic crust that formed during the late Jurassic after the salt deposition (Nguyen and Mann, 2015; Kenning and Mann, 2020a).

The present-day area of the Mexican Ridges remained a passive margin for much of the Mesozoic due to post-rift thermal subsidence. The Late Cretaceous to Middle Eocene Laramide orogeny shortened significant areas of eastern Mexico adjacent to the Mexican Ridges. From the Late Eocene to the Early Miocene, uplift and denudation contributed a large amount of clastic sediment to the deepwater (Salomón-Mora et al., 2009).

Progressive tilting and sediment loading resulted in gravity gliding along the Eocene–Oligocene shale detachment surface from the Middle Miocene (Morley et al., 2011; Salomón-Mora et al., 2009). The resultant passive margin foldbelt of the Mexican Ridges is characterized by a system of normal growth faults in the shelfal area known as the Quetzalcoatl extensional system, a neutral zone of shortening, and a train of folds along the continental slope (Yarbuh et al., 2018).

Regional structural profile

The southeast-to-northwest regional, structural cross-section of the Mexican Ridges PMFB traverses all elements of the PMFB that includes a 65-km-wide zone of extensional system, a 15-km-wide neutral zone of shortening, and a 120-km-wide zone of compression (Fig. 2.6).

The extensional domain is dominated by a listric normal fault system that detaches on Eocene shale. A group of synthetic-antithetic listric faults form grabens and create upper Miocene to Recent depocenters containing growth strata (Fig. 2.6). The translation zone is relatively narrow and characterized by the absence of any prominent structures related to either extension or compression.

The downdip compressional domain is dominated by a series of detachment folds that are associated with reverse faulting. Most of the reverse faulting is associated with folds that are detached on a secondary layer of the Oligocene-Miocene age (Fig. 2.6). The observation of upper Miocene to Recent growth strata in the extensional domain indicates its synchronous timing with the deepwater foldbelts in the compressional domain. However, one key study proposes a time lag in the propagation of the folding in the downdip direction (Salomón-Mora et al., 2011).

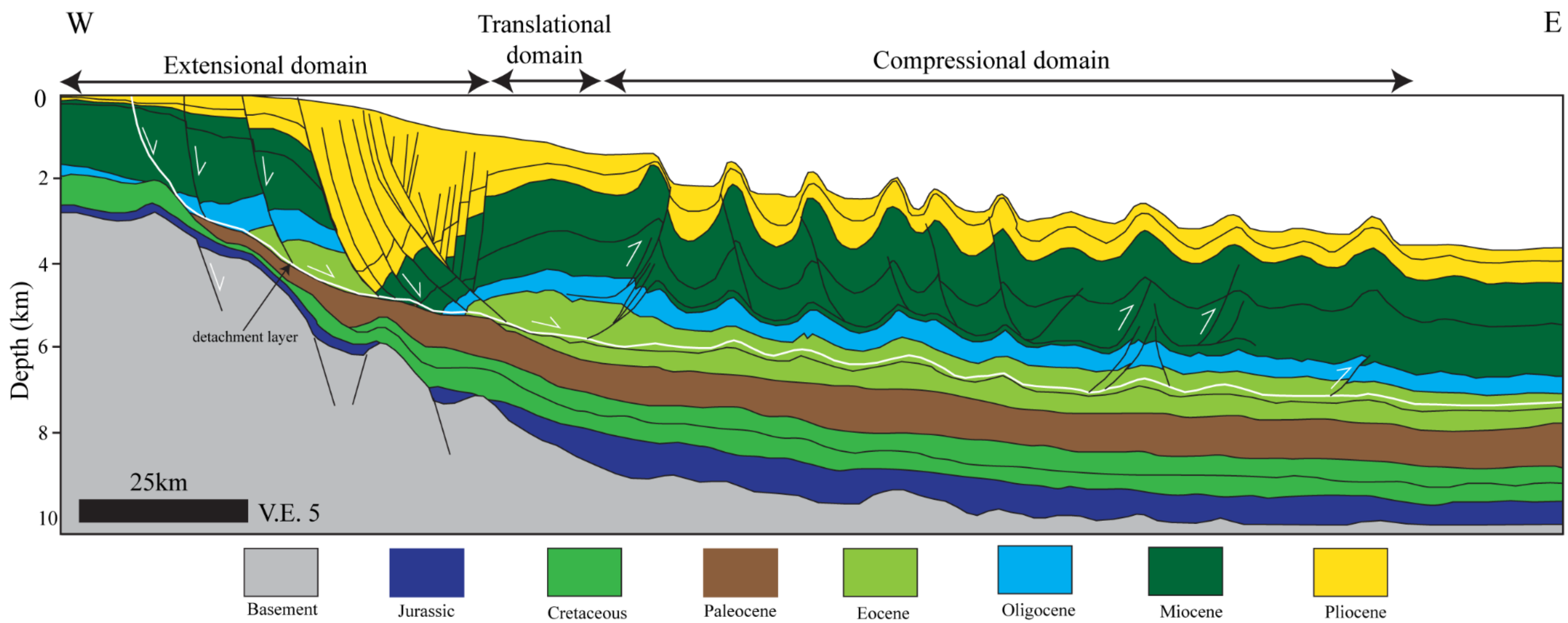

Figure 2.6: Regional, west-to-east depth cross-section through the Mexican Ridges passive margin foldbelt along the western margin of the Mexican Gulf of Mexico (location of the cross-section shown on the map in Fig. 2.3). The structural domains include the updip Quetzalcoatl extensional domain characterized by listric growth faults; a narrow translational domain characterized by a neutral zone of overlying shortening structures, and a downdip, compressional domain characterized by break thrusts and detachment folds. The slip on the updip listric normal faults and downdip folds and thrusts formed a common detachment surface that followed a shale interval of Eocene–Oligocene age (modified from Salomón-Mora et al., 2009).

Hydrocarbon potential

In the Mexican Ridges, the main structural styles are detachment folds with local reverse faults that result in four-way dip closures. The key reservoir-seal pairs are interpreted as interlayered clastic deposits representing Cenozoic turbidite fan systems (Salomón-Mora et al., 2009).

The crustal composition of the Mexican Ridges passive margin foldbelt has important implications in terms of hydrocarbon maturity (Kenning and Mann, 2020a). Oceanic crust, having a lower heat flow, may cause the source rocks to remain immature at the time of foldbelt formation in Middle Miocene to Recent, especially in the proximal, updip area with less overburden.

The presence of bottom-simulating reflectors (BSRs) has been described by previous authors and indicates a gas-mature system in the deepwater area (Kenning and Mann, 2020a). Oceanic spreading in the GOM is thought to have continued into the earliest Cretaceous (Nguyen and Mann, 2015), meaning that the most prolific Late Jurassic source rocks across the entire Gulf of Mexico may not exist above areas where oceanic crust is younger than Tithonian.

2.3.5 Campeche passive margin foldbelt

Structural provinces and age of formation

The Campeche passive margin foldbelt is defined by a 200-km-wide updip extensional zone and a coeval, 300-km-wide downdip compressional zone (Fig. 2.7). The extent of the translational zone is not obvious because numerous complex salt structures complicate the imaging, making it difficult to observe direct evidence of lateral translation.

Deformation due to passive diapirism and basinward tilting of the margin began during the Late Jurassic and Cretaceous with the formation of minor contractional structures. The Middle

Miocene Chiapanecan orogeny (related to the shallow subduction of the Cocos plate) oversteepened and destabilized the margin with updip extension along the northeast-trending Macuspana and Comalcalco rift systems (Mitra et al., 2005; Pindell and Miranda, 2011). These extensional systems detach as listric normal faults during the Middle Miocene along the underlying autochthonous salt of the Bajocian-early Callovian age. The updip extension of 20.5 km in the Comalcalco and Macuspana rifts contributed to the development of the deepwater compressional domain (Hasan and Mann, 2021).

Analysis of reflection continuity and stratal geometry in the compressional domain reveals the presence of Middle Miocene growth packages (Davison, 2020). Growth sequence and mass transport deposits in the Late Miocene to Recent indicate a major pulse of salt mobilization during this time (Hasan and Mann, 2021).

Regional structural profile

The southeast-to-northwest regional structural cross-section of the Campeche salt basin reveals three key observations: a part of the updip area is dominated by normal faults; the upslope extensional domain includes a zone of regional listric normal faults, detaching on both allochthonous salt and autochthonous salt; and several rollover structures and counterregional normal faults have formed because of extensional deformation (Fig. 2.7). Rollover anticlines associated with the listric normal faults contain up to 4–6 km of Pliocene-Recent clastic deposits.

The downdip area of compressional deformation is characterized by salt canopies, open salt-cored folds, salt diapirs, and break thrusts. The allochthonous salt bodies have coalesced in the proximal part of this domain. (Fig. 2.7).

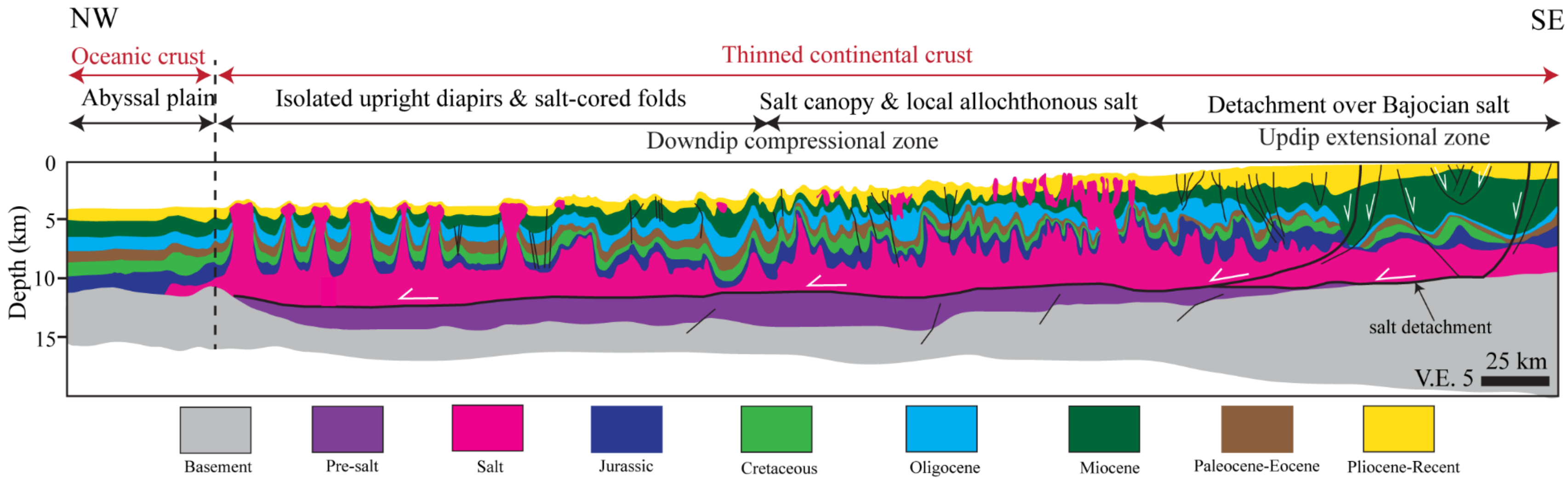

Figure 2.7: Regional, southeast-to-northwest structural cross-section across the Campeche passive margin foldbelt (location of the cross-section is shown on the map in Fig. 2.3). The lateral extent of the updip extension zone and the downdip compressional zone is shown along with the across-strike variability of structural styles and the underlying types of crust, which generally dips seaward. The updip extensional zone consists of listric normal faults that detach on both allochthonous salt remobilized during the Late Miocene and autochthonous salt of the Bajocian-early Callovian age. The downdip contractional zone consists of salt-cored folds, thrusts, autochthonous salt diapirs, allochthonous salt canopy, and detachment folds with kink bands (modified from Hasan and Mann, 2021).

Hydrocarbon potential

Hydrocarbon plays are most common in the shallow water extensional domain and the outer marginal trough due to the presence of Tithonian source rock, high-quality carbonate and clastic reservoirs, and numerous salt structures (Davison, 2020; Hasan and Mann, 2021).

Updip salt rollers and rollover anticlines provide potential traps above the sloping salt detachment (Kenning and Mann, 2020b). Numerous salt-associated undrilled structures with diverse geometries are present in the downdip compressional domain and make the trap potential the least risky element of the Campeche PMFB (Shann, 2020). Combined structural and stratigraphic traps are present along the upturned strata at the flanks of the salt diapirs (Kenning and Mann, 2020b).

Clusters of natural sea surface oil seeps from the Campeche salt basin have been described in studies of the updip extensional domain in the shallow offshore area and the downdip, deepwater compressional domain (Hasan and Mann, 2021; Kenning and Mann, 2020b). The abundance of seeps indicates a working petroleum system within the Campeche PMFB, although the presence of seeps also indicates likely seal failures related to active deformation.

The abundance of undrilled salt-associated structural traps, mature source rocks as shown by oil seeps, potential migration pathways, and opening its leases to international oil companies has made the Campeche PMFB one of the most intensively explored margins over the past several years.

2.4 Examples of passive margin foldbelts on the Atlantic margin of South America

2.4.1 Regional setting of passive margin foldbelts along South America

The continental margin of South America forms areas of either rifted-passive margins (northeastern and southwestern Brazil, Uruguay, and Argentina) or transform-rifted margins (northern Equatorial Brazil). All of these areas formed during the Late Jurassic breakup of Gondwana and resulted in the formation of the South Atlantic Ocean (Contreras et al., 2010).
The conjugate African and Brazilian margin basins are separated by oceanic crust developed along the Mid-Atlantic Ridge (Strozyk et al., 2017).

In this section, the structural evolution of the passive margin foldbelts of the four salt-free basins of Brazil are described (Fig. 2.8): (a) Foz do Amazonas, (b) Pará-Maranhão, (c) Barreirinhas, and (d) Pelotas. For all four, the essential elements and morphology of a passive margin foldbelt are present and include a detachment along overpressured shale and marl layers.

The Foz do Amazonas, Barreirinhas, and Pará-Maranhão basins are located along the steep-sloped, transform-passive margin of northern equatorial Brazil (Oliveira et al., 2013). The more gently sloped Pelotas Basin formed along the volcanic-rifted-passive margin in southern Brazil and Uruguay.

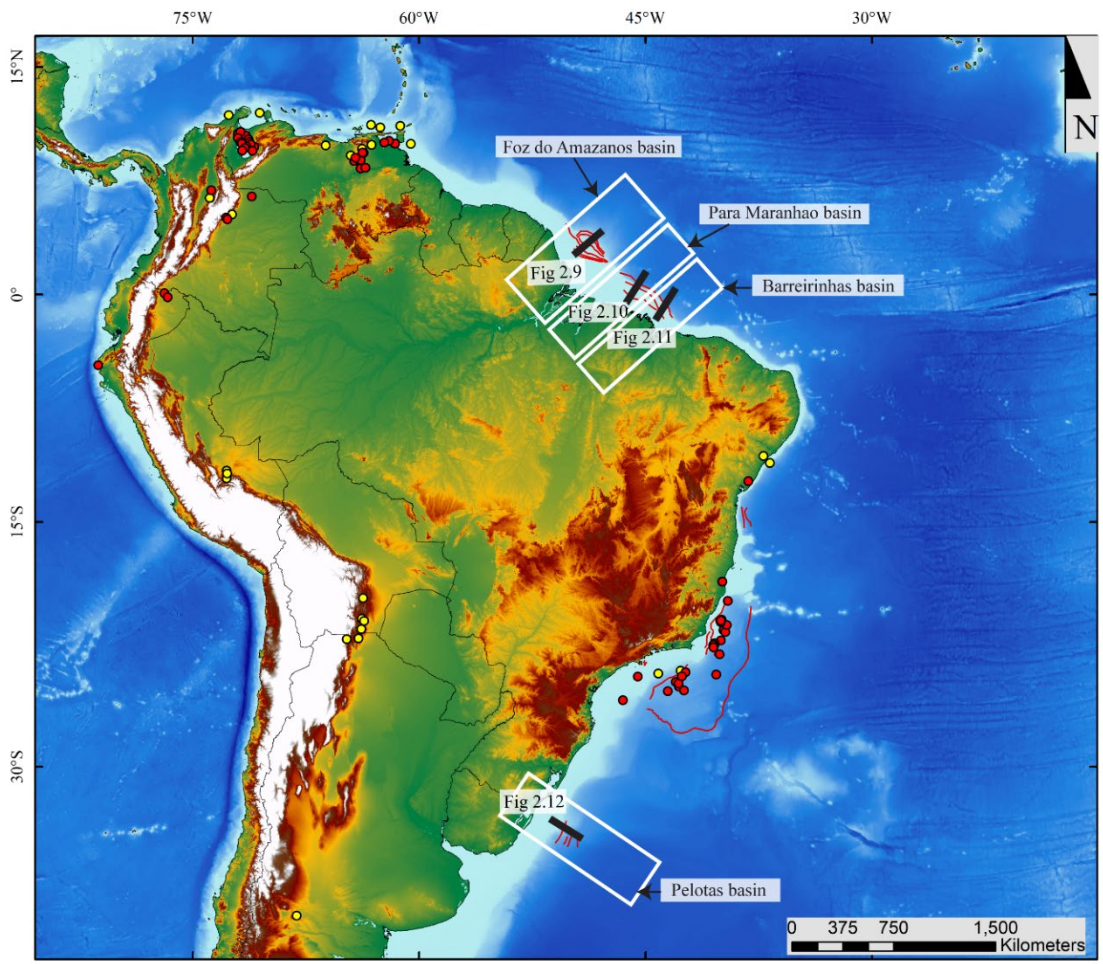

Figure 2.8: Bathymetric map of the South Atlantic passive margin of the South American continent showing the locations of four, shale-detached passive margin foldbelts: Foz do Amazonas Basin, Pará-Maranhão Basin, Barreirinhas Basin, and Pelotas Basin. Passive margin fold axes are shown by red lines, locations of the illustrated cross-sections are shown by the solid black lines, and the location of the giant oil and gas fields are shown by the red dots (oil fields) and by the yellow dots (gas fields) (CBTH database compilation, 2020).

2.4.2 Foz do Amazonas passive margin foldbelt

Structural provinces and age of formation

The Foz do Amazonas, or "Mouth of the Amazon River," Basin is the largest offshore sedimentary basin of the Brazilian Equatorial Atlantic margin. Gravitational failure along this steep-sloped, transform-passive margin basin has controlled its present-day structural styles (Reis et al., 2010).

The Foz do Amazonas Basin was controlled by its transform-related slopes, steepening, and inversion of the margin related to distant orogenic and erosional events in the Andean Mountains along the western margin of South America. Sediment supply to the Foz do Amazonas area dramatically increased during the Middle to Late Miocene due to the increased rate of Andean uplift, which deposited up to 10 km of clastics since the Middle Miocene (Reis et al., 2016). The period of rapid sedimentation oversteepened and destabilized the margin and resulted in gravitational failure and the formation of the passive margin foldbelt. The along-strike variation of sediment thickness due to this event controls the intensity and run-out distance of the gravity-driven deformation (Reis et al., 2010).

Regional structural profile

The southwest-northeast depth cross-section through Foz do Amazonas Basin shows a 85-km-wide extensional domain that is dominated by basinward-dipping listric normal faults and counter-regional, or landward-dipping, normal faults. Three detachment levels labeled as H1 (Early Cretaceous), H2 (base Paleocene-Eocene), and H3 (Early Pliocene) are indicated in the seismic profile (Fig. 2.9a). The main detachment level is the intermediate one (H2) located along the base of an overpressured, marine shale of Paleocene-Eocene age (Fig. 2.9).

A 120-km-wide compressional zone is composed of a zone of imbricated thrusts that dip landward. Each thrust fault detaches over the intermediate detachment horizon—H2 (base Paleocene-Eocene). The intensity of the landward-dipping and imbricated thrusting decreases in the landward direction (Fig. 2.9a and b).

Hydrocarbon potential

The Foz do Amazonas Basin is a frontier basin with only three deepwater wells—all of them penetrating sedimentary rocks no older than the Miocene (da Cruz et al., 2021). In the shelfal areas, Type-I source rocks of both Aptian and Cenomanian–Turonian ages have been identified along with the main reservoirs consisting of Upper Cretaceous and Cenozoic sandstone. A seismic facies analysis shows that a Late Cretaceous shale seals most of the basin (da Cruz et al., 2021). Using seismic reflection grids, direct indicators of working petroleum systems include bright spots, gas chimneys, and bottom-simulating reflectors. Two petroleum systems proposed for the Foz do Amazonas Basin include: (a) late Aptian source rocks paired with Late Cretaceous reservoir rocks (b) Cenomanian–Turonian source rocks paired with Late Cretaceous reservoirs (da Cruz et al., 2021).

There are three primary geologic risk factors in the Foz do Amazonas passive margin foldbelt. First, the downdip compressional domain is composed of active thrusts, indicating that timing and seal failure risk is high. Second, due to the lack of deepwater penetrations, the presence and quality of source rock in the basin remain speculative. Third, the abundant mass-transport complexes resulting from gravitational instabilities can act as barriers to vertical hydrocarbon migration.

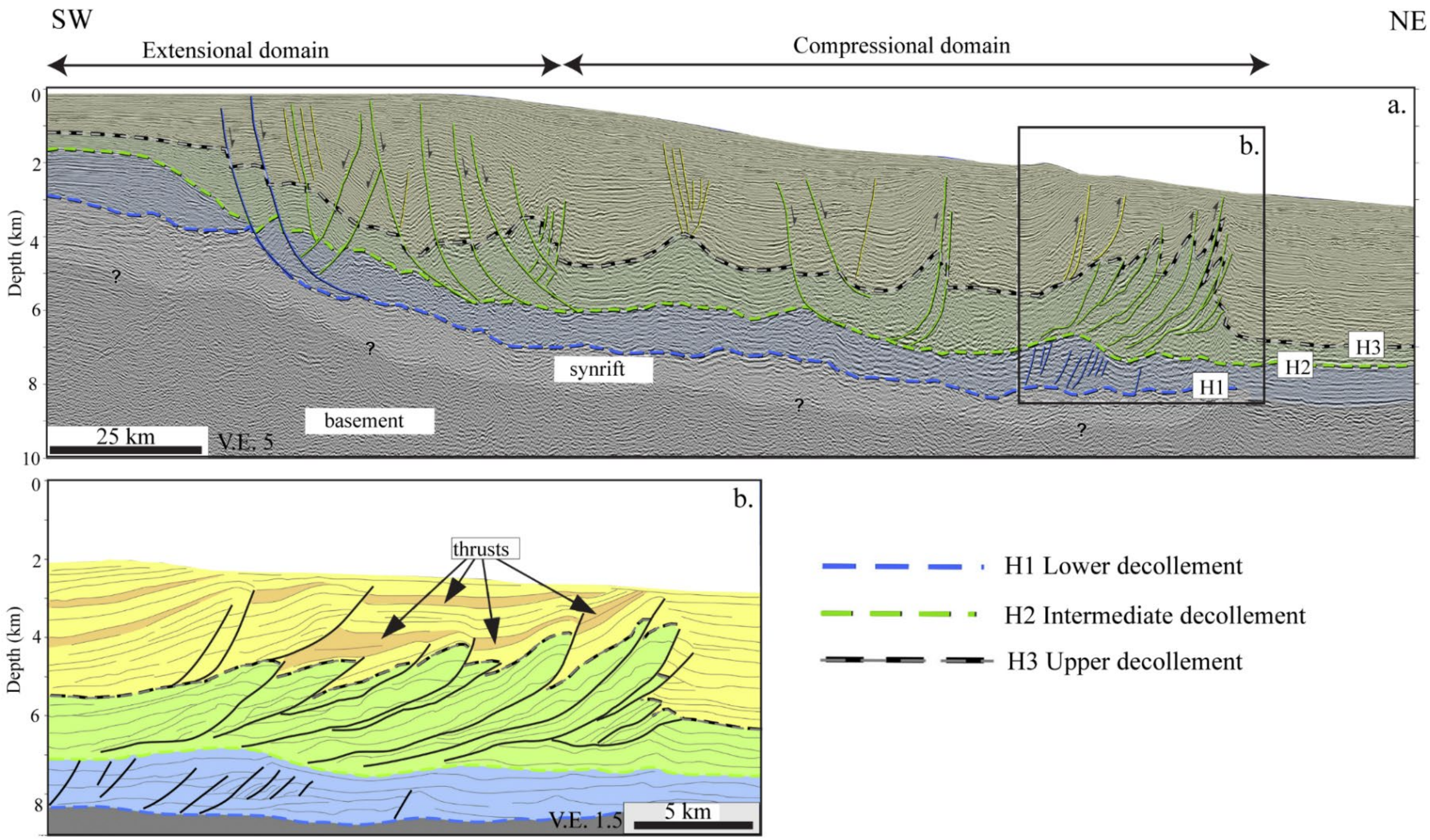

Figure 2.9: (a) Regional, southwest-to-northeast cross-section in depth through Foz do Amazonas Basin (location on Fig. 2.8) showing three detachment levels labeled as H1 (detachment along an Early Cretaceous horizon), H2 (detachment along the base Paleocene-Eocene horizon) and H3 (detachment along an Early Pliocene horizon). The main detachment level is the intermediate one (H2) located at the base of an overpressured, marine shale of the Paleocene-Eocene age. (b) Zoom of seismic section (location of the zoomed area is boxed in Fig. 2.9a) showing the downdip fold and imbricated thrust belt of the Foz do Amazonas Basin (modified from Reis et al., 2016).

2.4.3 Pará-Maranhão passive margin foldbelt

Structural provinces and age of formation

The Pará-Maranhão Basin in northeastern Brazil is located between the Foz do Amazonas Basin to the northwest and the Barreirinhas Basin to the southeast (Fig. 2.8). During the formation of the Equatorial Atlantic in the Albian, a right-lateral shear across a broad zone shaped the steep margins of both the Pará-Maranhão and Barreirinhas basins (Oliveira et al., 2013). Following this oblique opening stage, the basin subsided as a steeply-sloped passive margin. The Pará-Maranhão Basin experienced significant gravity gliding to form its passive margin foldbelt (Fig. 2.10). Cenozoic gravity gliding occurred in response to depositional loading and thermal subsidence, thereby increasing the slope gradient and causing episodic reactivation of the bounding fracture zones (Oliveira et al., 2013).

The detachment surface occurs along the top of the overpressured shale of the Paleocene age. Overpressure is related to rapid sedimentation, burial, and the development of this strong shale seal. It also signals the possible presence of underlying hydrocarbons (Oliveira et al., 2013).

Regional structural profile

The southwest-northeast structural cross-section of the Pará-Maranhão PMFB shows all three structural domains of the passive margin foldbelt: a 13-km-wide updip area of extension, a 5-km-wide zone of translation, and a 15-km-wide zone of downdip compression (Fig. 2.10). The extensional domain of the Pará-Maranhão PMFB is characterized by several large synthetic normal faults that are associated with prominent rollovers with growth strata. The thickness of growth strata can be up to 3 km (Fig. 2.10). The translational domain is relatively narrow with thrust duplexes and folding. The main detachment surface is Paleocene shale with minor marls. Imbricate thrusts dominate the downdip contractional domain without the presence of any large anticlines. The thrust structures backstep in age in the landward direction with the younger thrusts developing in the hanging wall (Fig. 2.10).

Hydrocarbon potential

Sub-commercial occurrences of light oil are reported in Cenozoic carbonate reservoirs and Upper Cretaceous turbiditic reservoirs of the offshore Pará-Maranhão Basin (Oliveira et al., 2013). However, exploration interest has increased in this area following significant hydrocarbon discoveries in deepwater plays in the conjugate African equatorial margin and French Guiana (Jubilee and Zaedyus play) (Da Silva Pellegrini and Ribeiro, 2018). Three key plays associated with shallow water shelfal prograding clinoforms and deepwater turbidites have been interpreted by Da Silva Pellegrini and Ribeiro (2018). Potential source rocks of the late Albian-early Cenomanian and Cenomanian–Turonian age have been identified in the oil maturity window from the conjugate West African margin (Da Silva Pellegrini and Ribeiro, 2018).

The rollover structures in the updip extensional domain and deepwater thrusts form traps of high exploration interest. A nominal total sediment thickness of 4 km in the updip extensional domain and 2 km in the downdip compressional domain makes source rock maturity the primary risk for the Pará-Maranhão Basin (Fig. 2.10). The imbricated thrusts in the downdip compressional domain also add the risk of breached reservoirs and few adjacent structural traps.

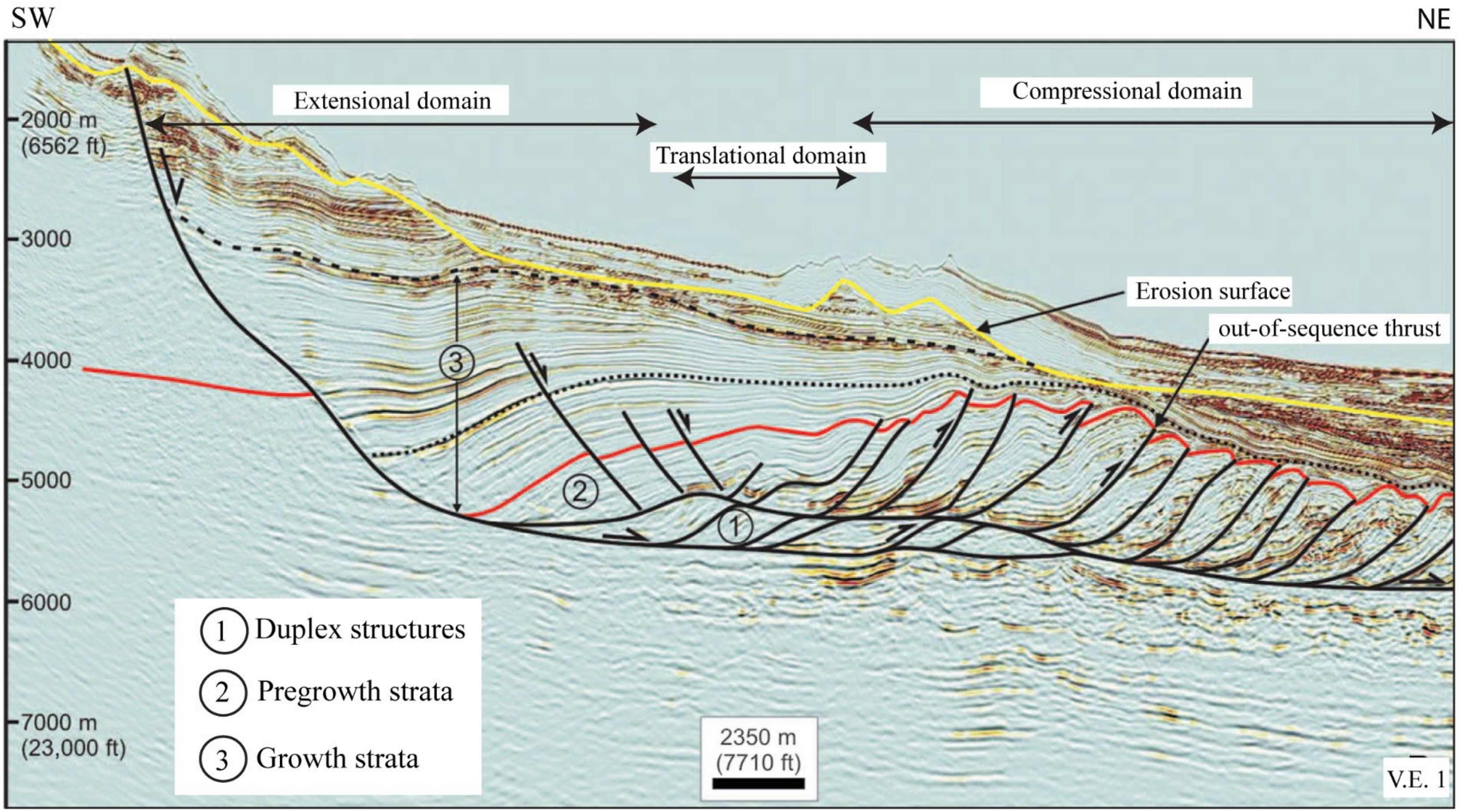

Figure 2.10: Regional, southwest-to-northeast, depth-converted, seismic reflection cross-section through Pará-Maranhão passive margin foldbelt of the northern Brazilian passive margin (location of the cross-section shown on the map in Fig. 2.8) showing the lateral extent of the three, structural domains of the PMFB: an updip, extensional domain; a midslope translational domain and a downdip compressional domain. The main listric normal fault detaches along a horizon of shale and marl of the Paleocene age. The downdip, compressional zone developed as a backstepping and landward-propagating sequence of younger thrusts developing in the hanging wall (modified from Oliveira et al., 2013).

2.4.4 Barreirinhas passive margin foldbelt

Structural provinces and age of formation

The Barreirinhas Basin comprises an area of 46,000 km^2 that is bounded to the northwest by the Foz do Amazonas Basin and to the southeast by an elevated high of the crystalline basement (Oliveira et al., 2013). The tectonic and structural evolution of the Barreirinhas Basin is similar to the Pará-Maranhão Basin. The basin contains a basal pre-rift sequence composed of Paleozoic rocks that experienced rifting from late Aptian to late Albian. A 10-km-thick sequence of post-rift sediment was deposited in the deep and ultra-deepwater (Fig. 2.11).

The passive margin foldbelt system evolved as a single detachment layer of the Late Cretaceous age and shows all three structural domains—extensional, translational, and compressional. The timing of major translation occurred during the Paleogene. A previous study reported a total shortening of 5% based on sequential structural restoration (Oliveira et al., 2013).

Regional structural profile

The southwest-northeast depth cross-section through the Barreirinhas Basin shows 5–6 km total sediment thickness in the updip extensional domain (Fig. 2.11). The extensional domain is 40-km-wide with present-day bathymetric and detachment slopes of 2° and 4°, respectively (Table 2.1). Like other passive margins, the zone is dominated by listric normal faults that detach on Late Cretaceous overpressured shale.

The 13-km-wide translational domain lacks normal faults and thrust faults. Thrust structures dominate the downdip compressional domain. The pattern of growth strata indicates that the timing of deformation is Early Paleogene. Three large thrust structures are found in the area of downdip compression (Fig. 2.11).

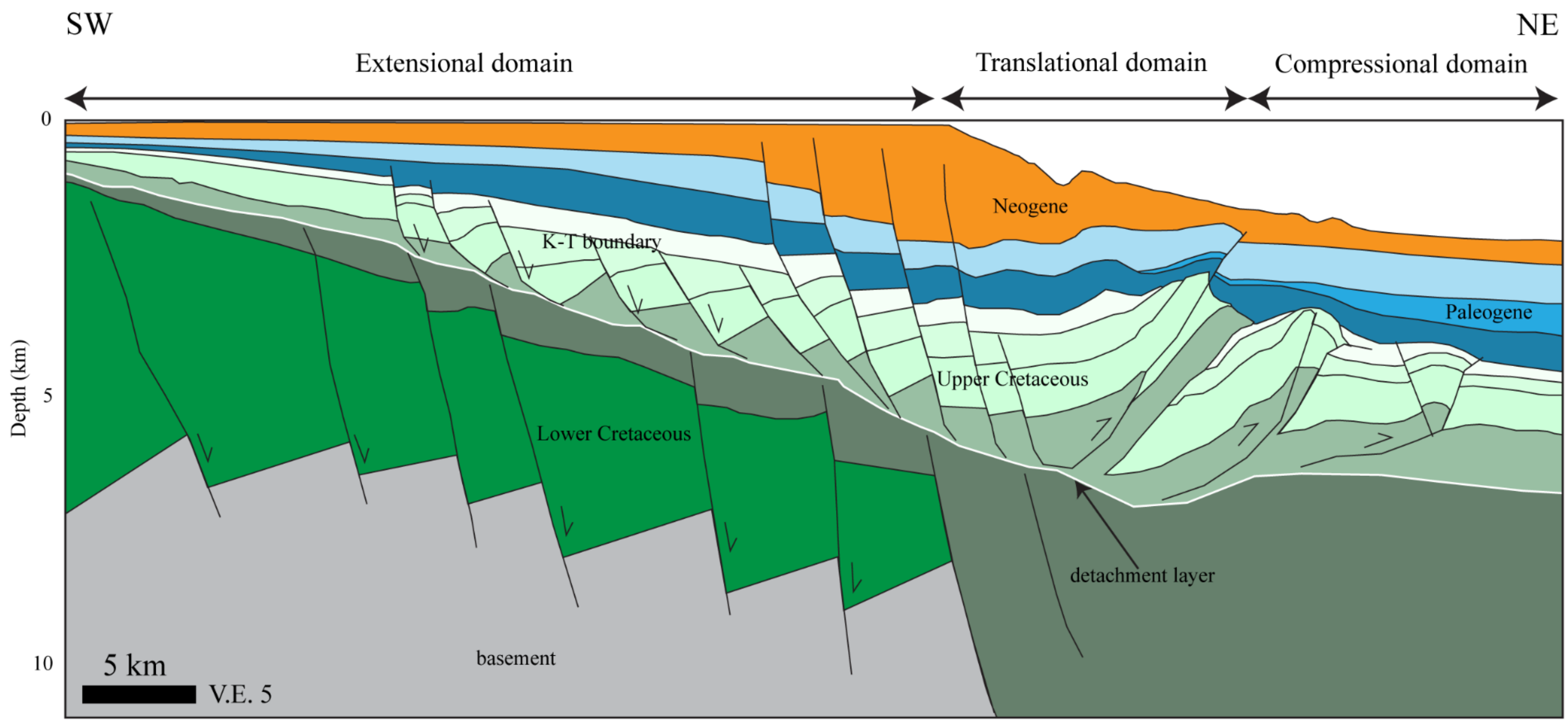

Figure 2.11: Regional, southwest-to-northeast depth cross-section through the Barreirinhas Basin of northern Brazil (location of the cross-section shown on the map in Fig. 2.8). The lateral extent of the three structural domains is shown and includes the zone of updip, listric normal faults of the extensional zone; the intermediate, midslope transitional area, and the downslope fold and thrust belt of the compressional zone. The common basal detachment for the updip listric normal faults and downdip folds and thrusts developed along a marine shale unit of late Cretaceous age (modified from Oliveira et al., 2013).

Hydrocarbon potential

The Barreirinhas passive margin foldbelt was explored in the 1960s through 1980s with only minor hydrocarbon production being established for a short period of time in some of the onshore fields (Oliveira et al., 2013). The primary Cretaceous source rock in the Barreirinhas PMFB is deeper (6–8 km) than the equivalent located in the Pará-Maranhão basin. Thicker overburden likely contributes to the source rock maturation (Da Silva Pellegrini and Ribeiro, 2018). Exploration in the Barreirinhas PMFB includes four key points. First, Early Paleogene timing of deformation in the downdip compressional resulted in the presence of structural closures during peak expulsion of source rocks. Second, the detachment surface may act as an obstacle to hydrocarbon fluid migration from deeper source rocks. Third, possible periodic reactivation of faults may cause the migration of fluids out of reservoirs. Fourth, the absence of drilled wells suggests that high-quality reservoirs and source rocks are two key geologic risks.

2.4.5 Pelotas passive margin foldbelt

Structural provinces and age of formation

The Pelotas Basin in offshore southern Brazil extends into northern Uruguay and remains a relatively underexplored basin (Fig. 2.8). The structural boundary between the Pelotas Basin and the Santos Basin to the north is the east-west-trending Florinanopolis high that is interpreted as a fracture or transfer zone (Conti et al., 2017). The main difference between the Pelotas Basin with other Brazilian passive margin foldbelts is the presence of thick magmatic wedges of seaward-dipping reflectors (SDRs) (Stica et al., 2014). The SDRs are present from the continental shelf to the lower slope of the Pelotas Basin. Unlike the Santos and Campos Basins, Aptian salt and salt-related structures are absent in the Pelotas Basin (Contreras et al., 2010). Passive margin processes dominated the post-rift, passive margin of the Pelotas Basin during the late Cretaceous and Cenozoic.

Regional structural profile

The regional northwest-southeast seismic section through the Pelotas PMFB reveals a 150-km-wide extensional zone, a 20-km-wide zone of translation, and a 38-km zone of downdip compression (Fig. 2.12). The extensional domain is significantly wider than the other two structural domains. The passive margin foldbelt detached along a Paleocene-Eocene interval of overpressured shale.

Antithetic faults accompany the thin-skinned, synthetic, and listric normal faults of the extensional domain. Minor thrusting is observed in the translational domain, and thrust structures dominate the downdip compressional domain. The thrust structures form a backstepping sequence in the landward direction. The stratal growth patterns reveal that late Neogene deformation affected the PMFB (Fig. 2.12).

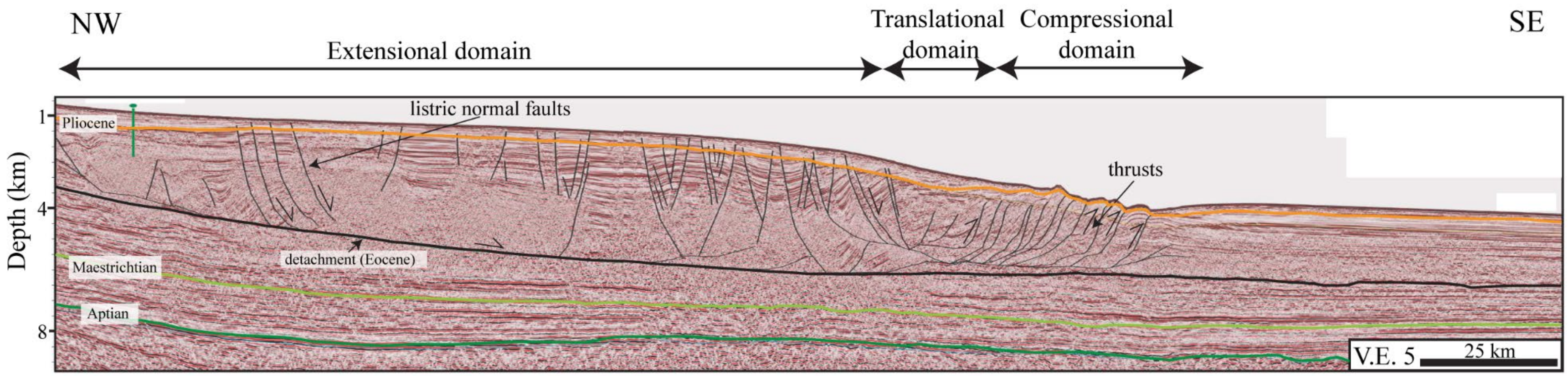

Figure 2.12: Regional, northwest-to-southeast depth cross-section based on a deep-penetration seismic reflection line through Pelotas Basin of offshore Uruguay (location of the cross-section is shown on the map in Fig. 2.8). The lateral extent of the three structural domains are shown and include the updip extensional domain that is characterized by both synthetic and antithetic listric normal faults, the transitional zone in the midslope area and the downdip, compressional zone. The underlying detachment for the normal faults occurs on a shale interval of Paleocene-Eocene age (modified from Geo Expro, 2013).

Hydrocarbon potential

The Pelotas passive margin foldbelt is a frontier basin where significant oil and gas accumulations have yet to be discovered. Favorable source, reservoir, and seal intervals have been proposed through seismic facies analysis in the pre-rift, syn-rift, and post-rift megasequences by Conti et al. (2017). The source rocks interpreted in the Uruguayan portion of the Pelotas Basin are represented by a restricted marine source rock deposited during the Permian pre-rift phase, and two marine source rocks deposited during the Aptian-Albian and Cenomanian–Turonian post-rift phase (Conti et al., 2017). Up to 7 km thickness of Cretaceous and Cenozoic post-rift clastics were deposited in the basin, including potential Paleocene and Albian source rocks. In addition, numerous oil seeps have been reported in the basin, especially in slope areas at water depths of 500–800 meters (Geo Expro, 2013).

There are two potential risks for petroleum exploration in the Pelotas passive margin foldbelt. First, the presence of seaward dipping reflectors indicates volcanic activity, which causes higher transient heat flow and possible over-maturity of source rocks. Second, the present-day deformation of the passive margin foldbelt can lead to seal integrity risk.

2.5 Examples of passive margin foldbelts along West Africa

2.5.1 Regional setting of passive margin foldbelts along West Africa

The continental margin of West Africa formed during the south-to-north progressive rifting of Gondwana and the separation of the South American and African continents. Rifting started in the south during the Late Jurassic and propagated northward (Ceraldi et al., 2017). During the syn-rift to passive margin transition, salt was deposited in the central area of the West African margin during Aptian time. The passive margin stage is dominated by regional uplift and seaward tilting of the African continent with related deposition of deepwater sedimentary intervals in submarine fan environments (Liu et al., 2008).

This section describes the structural evolution of three passive margin foldbelts of the offshore West African margin (Fig. 2.13): (1) Niger, (2) Kwanza, and (3) Orange River. The gravity tectonics in the Niger and Orange River PMFB are controlled by overpressured shale, whereas in the Kwanza Basin, deformation is controlled by salt remobilization (Morley et al., 2011; Rowan, 2020).

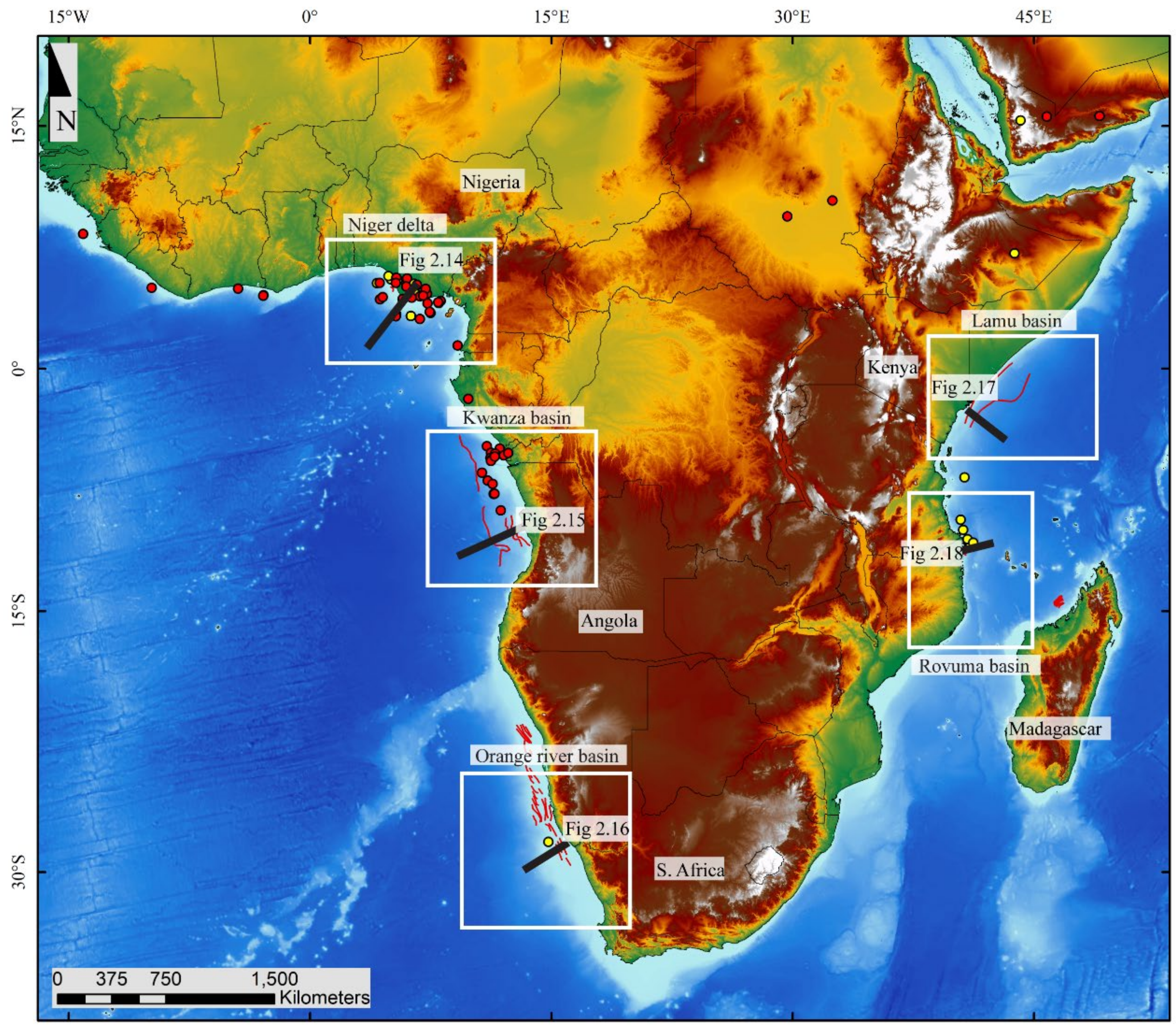

Figure 2.13: Bathymetric map of the offshore African margin showing the locations of five passive margin foldbelts formed along the passive margins of the African continent: the Niger PMFB along the Niger Delta of Nigeria; the Kwanza PMFB of Angola; the Orange River PMFB of South Africa; the Lamu Basin of Kenya; and the Rovuma Basin of Mozambique. Passive margin fold axes are shown by red lines, locations of the illustrated cross-sections are shown by the solid black lines, and the location of the giant oil and gas fields are shown by the red dots (oil fields) and by the yellow dots (gas fields) (CBTH database compilation, 2020).

2.5.2 Niger passive margin foldbelt

Structural provinces and age of formation

The Niger passive margin foldbelt is a prolific hydrocarbon province located in the Gulf of Guinea (Zhang et al., 2021). The depositional history of the Niger Delta began in the Eocene with the deposition of a clastic wedge that is 12 km thick. The Niger PMFB evolved above an overpressured shale detachment (Wu et al., 2015). The gravity system of the Niger Delta PMFB is characterized as a headward delta-top zone of extension, a midslope zone of translation, and a delta-toe zone of contraction (Steele et al., 2009; Wu et al., 2015). The distance from the updip extensional zone to the downdip contraction zone is approximately 300 km. The overpressured shale detachment layer is the Akata Formation which has a slope of 1.4°.

Regional structural profile

The regional cross-section of the passive margin foldbelt developed on the Niger Delta shows the distribution of three main structural zones: (1) a 190-km-wide zone of updip extension, (2) a 22-km-wide zone of translation, and (3) an 85-km-wide zone of downdip compression (Fig. 2.14). The updip extensional zone is characterized by both basinward and counter-regional growth faults and associated rollover depocenters. Gravity gliding along the listric normal faults creates additional accommodation in the updip extensional domain and increases the stress head in the downdip direction. The translational zone is characterized by large areas of little or no deformation interspersed with broad detachment folds above the Akata Formation (Corredor et al., 2005).

A zone of imbricate thrust structures dominates the downdip compressional domain. An older thrust system of Oligocene to Middle Miocene age has been reactivated by the deposition of Upper Miocene and Plio-Pleistocene sandstone splays. This depositional reactivation resulted in various oversteepened thrust structures that were initially shale diapirs or mobile shale-cored structures (Corredor et al., 2005; Steele et al., 2009).

Hydrocarbon potential

The Niger passive margin foldbelt ranks as one of the largest hydrocarbon provinces in the world with an estimated ultimate recovery of 40 billion barrels (Adegoke et al., 2017). Three different petroleum systems are present in the Niger PMFB: (1) Lower Cretaceous lacustrine system, (2) marine systems in Upper Cretaceous-Lower Paleocene, and (3) a Cenozoic system.

The most prolific reservoirs are found in the delta growth faults of the extensional zone and in the deepwater elements in the midslope translational zone. Hydrocarbon accumulation in the deltaic reservoirs is likely to have migrated upward from downdip areas (Steele et al., 2009). Most of the giant fields of Niger are in the translational domain (e.g., Bonga, Agbami, Akpo, N'nwa-Doro, and Erha). The prospectivity in the translational zone is due to large structural closures containing excellent channelized deepwater reservoirs and mature source rocks in the oil window.

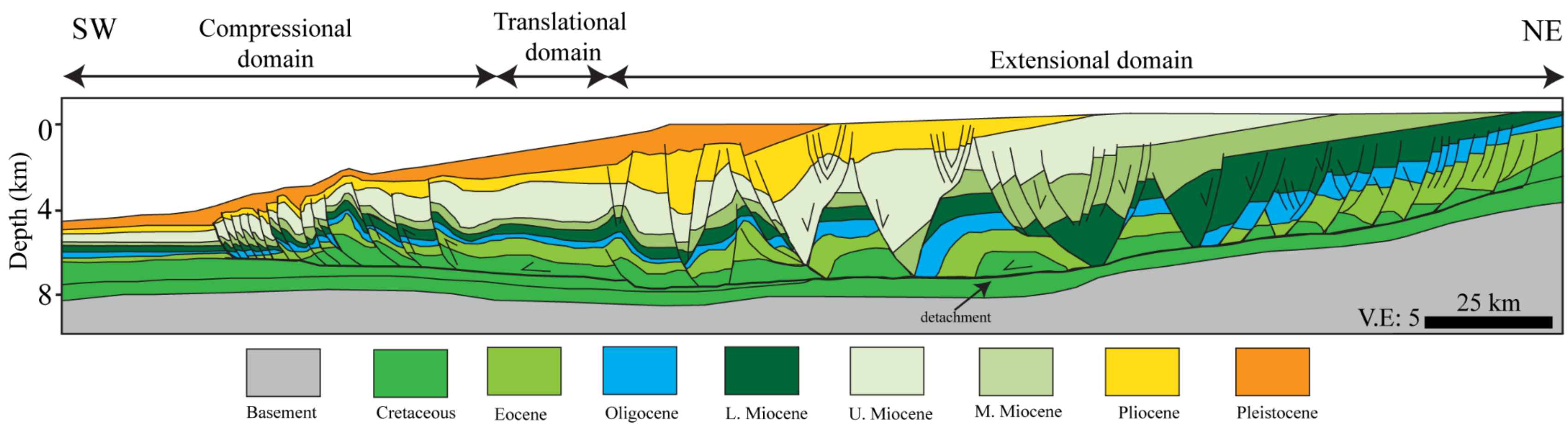

Figure 2.14: Regional, northeast-to-southwest depth cross-section through Niger passive margin foldbelt (location of the cross-section is shown on the map in Fig. 2.13). The lateral extents of the three structural zones are shown and include the updip area of delta-top extensional faults, an intermediate translational domain, and a zone of delta-toe of imbricate thrusts and folds. The underlying detachment for all three zones occurs within the Akata Formation, a prodelta marine shale of Cretaceous age (modified from Steele et al., 2009; Zhang et al., 2021).

2.5.3 Kwanza passive margin foldbelt

Structural provinces and age of formation

The Kwanza Basin formed as a salt-influenced passive margin foldbelt offshore Angola (Fig. 2.13). Rifting of the Kwanza Basin was initiated in the Early Cretaceous during the opening of the South Atlantic Ocean. A thick layer of Aptian salt was deposited shortly after rifting and its salt geometry reflects the syn-rift topography (Evans and Jackson, 2020; Hudec and Jackson, 2002). The salt accumulation is separated by a high, the Atlantic hinge zone, along which the salt is thin or absent. The basin is divided into two main parts: the western part, known as the Outer Kwanza basin, that contains a 4-km-thick interval of salt, and the eastern part, known as the Inner Kwanza basin (Morley et al., 2011).

The presence of salt, gradient of the slope, sediment loading, and onland basement uplift events control the present-day structural configuration of the Kwanza Basin. Hudec and Jackson (2004) pointed out three phases of regional uplift: early Albian, Campanian, and Miocene, which contributed to the evolution of the basin as a passive margin foldbelt.

Regional structural profile

A northeast-southwest depth cross-section shows a 200-km-wide zone of thin-skinned listric normal faults detaching over a relatively thin interval of Aptian salt. Prominent turtle structures and normal fault-bounded depocenters are located in the updip extensional domain (Fig. 2.15). The downdip compressional domain is 160 km-wide and is dominated by a large-scale salt nappe, thickened salt plateau, and squeezed diapirs. The salt nappe is approximately 100 km wide and 2–4 km thick. The Atlantic hinge zone divides the extensional and compressional domains

(Fig. 2.15). The translational domain is not easily discernible but has been interpreted by previous studies in the area of the Atlantic hinge zone (Evans and Jackson, 2020).

Hydrocarbon potential

Pre-salt reservoir targets along the South Atlantic conjugate margins have been a major focus with significant discoveries concentrated in the Santos and Campos basins offshore Brazil. Using these Brazilian discoveries as analogs, the underexplored deepwater Kwanza Basin is now emerging as a prolific pre-salt hydrocarbon basin. The ultra-deepwater well Baleia-1 was the first commercial oil discovery in 1996 in the pre-salt section of the Inner Kwanza Basin. This well encountered oil shows in a 120-meter-thick sandstone reservoir. In 2011, due to recent deepwater discoveries in Brazil, Maersk drilled the Azul-1 pre-salt discovery, shortly following the Cameia-1 discovery well (Greenhalgh et al., 2012).

Although hydrocarbon discoveries in the Outer Kwanza basin remain elusive, separate syn-rift basins divided by the Atlantic hinge zone formed the setting for pre-salt discoveries in the Inner Kwanza Basin (Hudec and Jackson, 2004). Restricted circulation during the Early Cretaceous led to the deposition of high-quality source rocks. During episodes of relative uplift and subsidence of the West African continental margin, sediment overlying the Aptian evaporites has slowly migrated down the slope to create large structural closures in the basin (Greenhalgh et al., 2012).

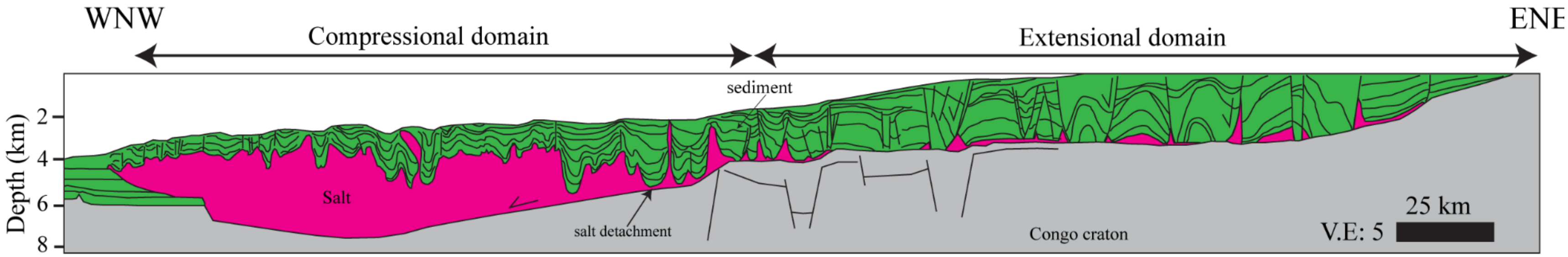

Figure 2.15: Regional, northeast-to-southwest depth cross-section through the Kwanza passive margin foldbelt, offshore Angola (location of the cross-section is shown on the map in Fig. 2.13). The two structural domains of the PMFB include the updip zone of listric normal faults detaching on Aptian salt and the downdip compressional area that includes large salt nappe of approximately 100 km in width and 2–4 km in thickness (modified from Hudec and Jackson, 2004; Evans and Jackson, 2020).

2.5.4 Orange River passive margin foldbelt

Structural provinces and age of formation

The Orange River Basin is located in offshore Namibia and South Africa and records the development of a Late Jurassic to present-day volcanic-rifted margin (Granado et al., 2009). South Atlantic rifting is marked by a Late Jurassic to Late Cretaceous syn-rift megasequences, separated from the Late Cretaceous to present-day passive margin megasequences by the breakup unconformity. The post-rift evolution of the margin is characterized by gravity-driven failure that produced the Orange River passive margin foldbelt (de Vera et al., 2010).

Gravitational failure is recorded by its updip extensional domain linked to a downdip contractional domain detaching along a thin layer of overpressured shale of the Turonian age. Sequential structural restoration shows a total extension of 24 km and a downdip shortening of 16 km (de Vera et al., 2010). The pattern of growth strata suggests that the gravity failure was short-lived, from the Coniacian to Santonian, and was likely the result of the uplift of the West African craton and sediment loading by the Orange River Delta.

Regional structural profile

The regional northeast-southwest depth cross-section through the Orange River PMFB shows the main depositional megasequences and the late Cretaceous gravity-driven PMFB (Fig. 2.16). The extensional domain is 140 km in length, the translational domain is 20 km in length, and the compressional domain is 95 km in length.

The extensional domain is characterized by typical listric normal faults that detach on the Turonian interval. The average detachment slope is 1° with a bathymetric slope of 1.1°. Growth strata in the extensional domain show thickening along individual faults. The slip timing is interpreted as Coniacian to Santonian, although later reactivation of some extensional faults is likely (de Vera et al., 2010). The translational domain is relatively short, with a downdip length of 20 km. The 95-km-wide compressional domain is characterized by numerous high-angle landward-dipping imbricate thrust faults (Fig. 2.16).

Hydrocarbon potential

Structural and stratigraphic traps in the Orange River PMFB include structural traps related to listric growth faults and stratigraphic traps related to turbidite-dominated submarine fans (Brownfield, 2016). There have been no discoveries to date in the Orange River PMFB. Hydrocarbons are likely generated from Barremian-Aptian and Cenomanian–Turonian marine Type II source rocks that are now buried by as much as 7 km of clastic, sedimentary rocks (Brownfield, 2016). Basin modeling studies have shown that the generation from Cenomanian–Turonian source rocks postdates the timing of structural deformation and therefore poses a significant risk for hydrocarbon accumulation.

Furthermore, smaller gas discoveries (Kudu, Ibhubesi, K-J1) and gas seeps in shallow water indicate gas-prone source rock in the passive margin section that immediately overlies the Cretaceous seaward-dipping reflectors (Brownfield, 2016; deVera et al., 2010). Hydrocarbons can potentially migrate into Cretaceous and Cenozoic sandstone reservoirs that include deltaic and nearshore marine sandstone, turbidite sandstone, slope truncations along the present-day shelf and paleo-shelf edge and basin-floor fan reservoirs. Structural traps include growth-fault-related structures and rotated fault blocks within the continental shelf. Cretaceous and Cenozoic mudstone and shale rocks form the primary reservoir seals (Brownfield, 2016).

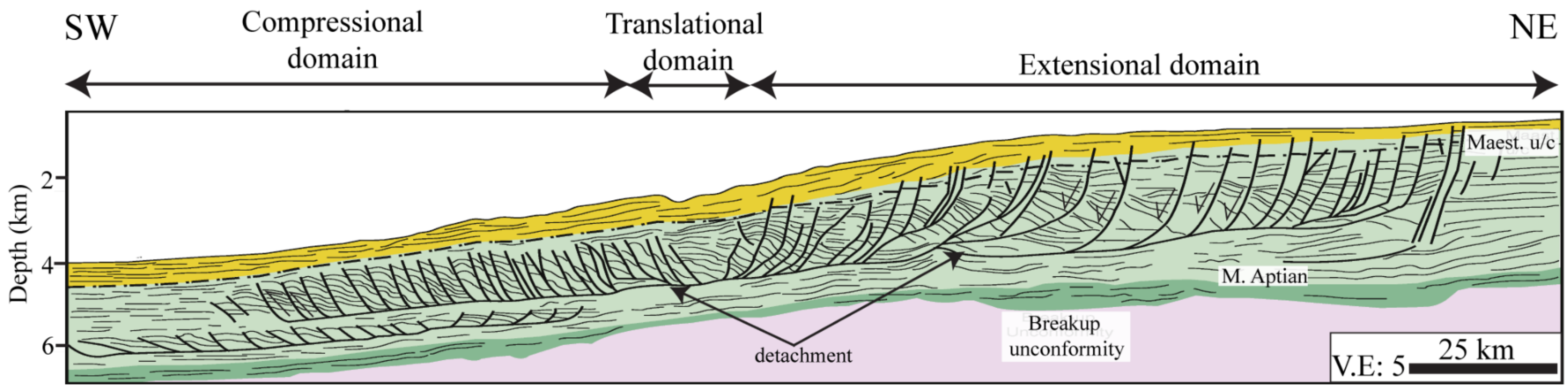

Figure 2.16: Regional, northeast-to-southwest depth cross-section through the Orange River PMFB of late Cretaceous age along the south Atlantic passive margin of South Africa (location of the cross-section is shown on the map in Fig. 2.13) The lateral extents of the three structural domains are shown with the updip extensional domain characterized by listric, normal faults; a narrow transitional zone and a downdip zone of imbricated thrust faults (modified from Grando et al., 2009; de Vera et al., 2010).

2.6 Examples of passive margin foldbelts along East Africa

2.6.1 Regional setting of passive margin foldbelts along East Africa

In this section, the structural evolution and hydrocarbon potential of two passive margin foldbelts of the offshore East African margin are described: (1) Lamu and (2) Rovuma. The offshore Lamu and Rovuma Basins are located along the passive continental margin of East Africa, stretching along the coast from Mozambique to Kenya (Fig. 2.13). The passive continental margin originated due to Karoo rifting and the Africa-Madagascar breakup during the Middle Jurassic. Seafloor spreading ceased in the Early Cretaceous around 120–130 Ma. From the Early Cretaceous onward, both regions evolved as PMFB. The initiation of the East African Rift System took place during Eocene and is believed to have contributed to the passive margin foldbelt process (Cai et al., 2020).

2.6.2 Lamu passive margin foldbelt

Structural provinces and age of formation

The passive margin foldbelt system in the Lamu Basin detached along two horizons, Late Cretaceous and Late Oligocene, which are both interpreted as overpressured shale. Although the presence of salt has been inferred, drilling of Kencan-1 and Garissa-1 and seismic facies analysis revealed that a siliciclastic unit forms the detachment level (Cai et al., 2020). Analysis of growth strata indicates that the passive margin foldbelt remained active from Late Cretaceous to Early Miocene, but almost all PMFB-related deformation occurred before the late Paleocene. Locally, a series of post-rift-related seamounts form a downslope barrier to the PMFB (Cruciani et al., 2017; Cruciani and Barchi, 2016).

Regional structural profile

The northwest-southeast depth cross-section through the Lamu passive margin foldbelt shows the presence of two overlapping foldbelts driven by gravitational processes (Fig. 2.17). The older thrust system that detaches on the Late Cretaceous interval does not clearly exhibit the main elements of a PMFB. An overlying and younger detachment on a Late Oligocene shale unit does exhibit the main elements of a PMFB, including: (1) a 13-km-wide zone of updip extension dominated by thin-skinned listric normal faults, (2) a 10-km-wide zone of translation characterized by absence of shortening and containing thick packages of Miocene-Recent sediment, and (3) a 20-km-wide zone of downdip compression expressed as multiple imbricated thrust faults detached on a basinward dipping detachment surface.

Hydrocarbon potential

The structural cross-section shows that the older and younger thrust belt, both the older and younger PMFB in the Lamu Basin formed during the Late Paleogene to Recent times. Cai et al. (2020) predict gas discoveries in the Lamu PMFB because the primary Jurassic source rock was in the oil generation window during the Late Cretaceous and was in the gas window from the Early Paleogene to Recent. Chances of gas discoveries are predicted because the gas generation window was in the Early Paleogene to Recent. Cai et al. (2020) propose two main sources of risk for hydrocarbons in the Lamu PMFB: (1) Late Cenozoic seamounts are present and may create higher-than-expected heat flow and (2) source rock quality varies along the trend of the margin.

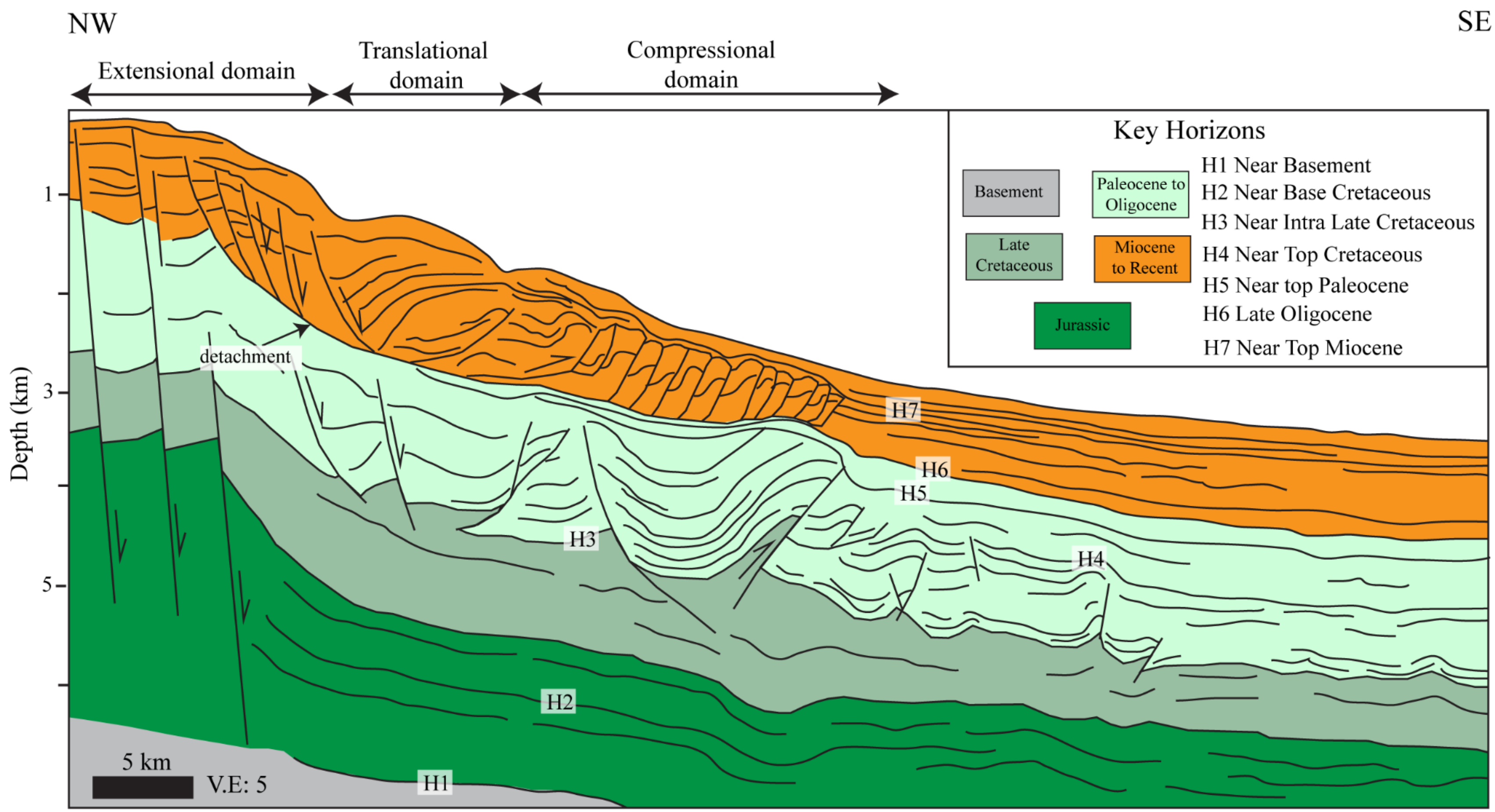

Figure 2.17: Regional, northwest-to-southeast depth cross-section through the Lamu passive margin foldbelt on the Kenyan passive margin on the western Indian Ocean (location of the cross-section is shown on the map in Fig. 2.13). The Lamu PMFB consists of a vertical stack of two thrust systems detached over basinward dipping detachment faults. The ages of the strata along the two detachment horizons are Late Cretaceous and Late Oligocene (modified from Cruciani and Barchi, 2016).

2.6.3 Rovuma passive margin foldbelt

Structural provinces and age of formation

The Rovuma passive margin foldbelt formed after the cessation of Mesozoic rifting and seafloor spreading. The downdip foldbelt developed mainly in the Oligocene and Miocene and detached along the top of a Paleocene shale horizon. An Oligo-Miocene deltaic system overlies the detachment horizon (Mahanjane and Franke, 2014).

Previous studies have proposed two principal causes for the formation of the Rovuma PMFB: (1) the progradation of the Cenozoic Rovuma Delta and (2) the uplift of the adjacent land area in eastern Africa. Both mechanisms are linked to the early development of the East African Rift System (Cai et al., 2020; Mahanjane and Franke, 2014).

Regional structural profile

The geometry of the passive margin foldbelt of the offshore Rovuma Basin comprises three domains: (a) a 21-km-wide updip extensional domain, (b) a 11-km-wide translational domain, and (c) a 45-km-wide downdip compressional domain (Fig. 2.18). In the upslope extensional domain, listric normal faults detach on Eocene mudstones that are inferred to be undercompacted and overpressured. The generation of accommodation creates a large rollover depocenter in the distal portion of the extensional and translation domains. The translation domain lacks prominent structural features and basinward-dipping thrusts faults that characterize the downdip compressional domain. Based on the ages of growth strata, the timing of deformation is post-Oligocene.

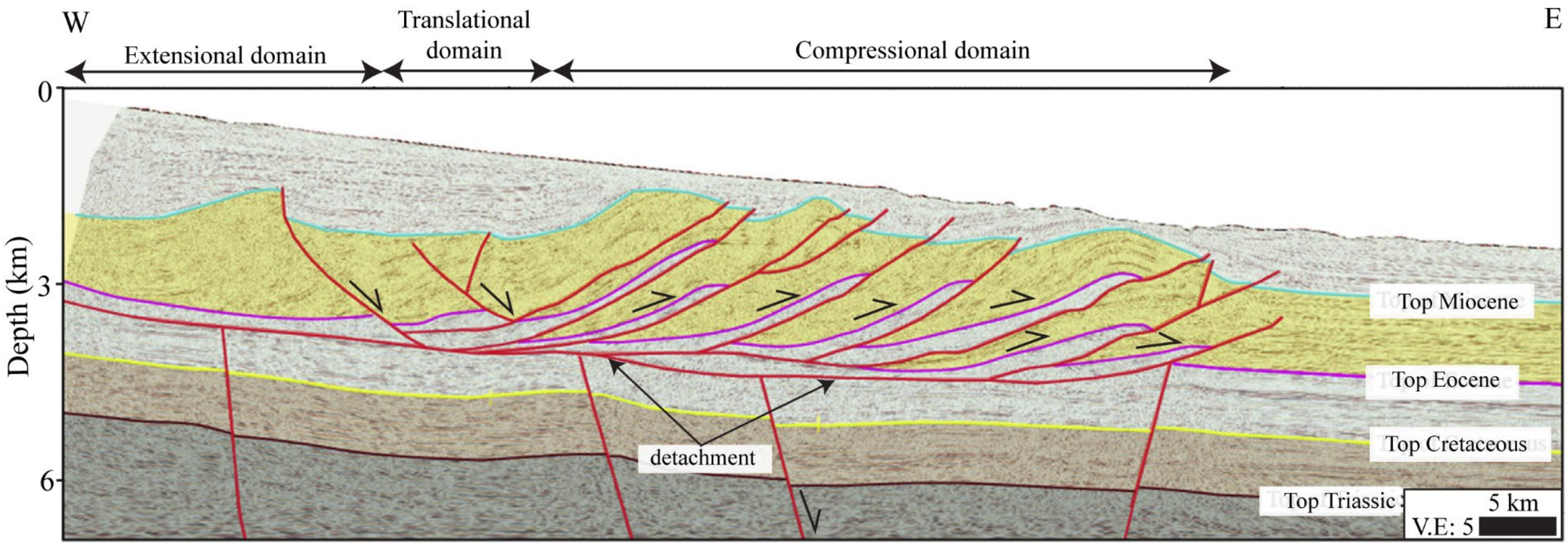

Figure 2.18: Regional, northwest-to-southeast depth cross-section through the Rovuma Basin of Mozambique (the location of the cross-section is shown on the map in Fig. 2.13). The lateral extents of the three structural zones are shown and include the updip extensional zone, a narrow transitional zone, and the downdip compressional domain. The passive margin foldbelt system of the basin has been active since the late Eocene period and detached along the top of an Eocene shale horizon (modified from Cai et al., 2020).

Hydrocarbon potential

Four source rock intervals have been reported in the Rovuma Basin: Permo-Triassic, Lower Jurassic, Lower Cretaceous, and Upper Cretaceous. Geochemical and seismic facies analysis show that a Late Jurassic source rock interval is widespread. Systematic basin modeling studies show that the timing of oil generation in the Rovuma Basin is Middle to Late Cretaceous and that gas generation is Early Paleogene to Recent (Cai et al., 2020). These observations constrain a less favorable timing for oil generation and a more favorable timing for gas accumulation. The reservoirs are Late Cretaceous sandstone-rich channel-fills and splays that developed over wide areas of the East African margin. Recent giant gas field discoveries such as Mamba, Prosperidade, Golfinho, and Coral indicate a working petroleum system with gas mature source rock in the Rovuma Basin (Zhang et al., 2017). Reservoirs of the Coral and Mamba fields are composed of high-quality 100-meter-thick sandstone units formed by high-density gravity flows and bottom currents that have distributed the sands over tens of kms along the margin (Fonnesu et al., 2020).

2.7 Discussion

2.7.1 Settings of passive margin foldbelts

Transform-passive margins vs. rifted-passive margins

Most of the passive margin foldbelts of the Gulf of Mexico, Atlantic margins, and western Indian Ocean margin can be classified as rifted-passive passive margins or transform-passive margins, which have distinctive bathymetric and structural differences (Sapin et al., 2021; Mann, 2022). Recent deeply-penetrating seismic reflection data and seismic refraction data show that orthogonally-rifted margins are highly tapered in the cross-sectional view and have broad shelves and relatively subdued bathymetric slopes in their overlying passive margin sedimentary sections. In contrast, these same studies have shown that transform margins are more truncated and have narrow shelves and relatively steep bathymetric slopes in their overlying passive margin sections.

Another category of rifted passive margins is volcanic margins characterized by broad and relatively flat shelf and slope areas underlain by thick accumulations of magmas intermixed with sedimentary rocks and seen on seismic reflection data as “seaward-dipping reflectors” or “SDRs” that can extend 100s of kms along strike (Reuber et al., 2019). A final category of margins is deltaic margins which also exhibit broad shelves and slope areas underlain by seaward-prograding, clastic sedimentary deposits.

In Figure 2.19, I summarize the bathymetric slopes of 13 PMFBs, which can be compared to these four different settings of margins: 1) rifted-passive margins, 2) transform-passive margins, 3) volcanic rifted margins, and 4) deltaic margins. Examples of PMFBs developed on rifted-passive margins and characterized by highly tapered margins in a cross-sectional view and gently sloped overlying passive margins ranging in dip angles from 1.9° to 3.4° include the following examples: (1) Perdido (bathymetric slope or alpha = 1.5); (2) Campeche (alpha = 2.2); (3) Lamu (alpha = 1.9); (5) Rovuma (alpha = 3.4) and (6) Kwanza (alpha = 2.2). This group of PMFBs exhibits wider deformation zones than the transform types, especially when salt underlies the main detachments.

Examples of PMFBs developed on transform-passive margins and characterized by more truncated margins with narrow shelves and relatively steep bathymetric slopes ranging from 1.5° to 2.3° include the following examples: 1) Mexican Ridges (alpha = 2.3); (2) Pará-Maranhão (alpha = 1.5); and (3) Barreirinhas (alpha = 2) (Fig. 2.19). This group of PMFBs exhibit more narrow deformation zones than the rifted types.

Examples of PMFBs developed on deltaic margins and characterized by broad shelves and slope areas underlain by seaward-prograding, clastic sedimentary deposits with bathymetric slopes ranging from 0.9° to 1.4° include the following examples: 1) Atwater-Mississippi (alpha = 0.9); (2) Foz do Amazonas (alpha = 1.1); and (3) Niger (alpha = 1.4) (Fig. 2.19). This group exhibits the thickest sedimentation of the four groups.

Examples of PMFBs developed on volcanic margins characterized by broader margins underlain by prograding mixed magmatic and sedimentary flows ranging in dip from 1.1° to 1.9° include the following examples: (1) Pelotas (alpha = 1.9) and (2) Orange River (alpha = 1.1).

Margin oversteepening related to orogenic events

Orogenic events contribute to the passive margin foldbelt evolution by increasing the amount of seaward tilting of the passive margin (Rowan et al., 2004; Morley et al., 2011). Denudation resulting from this uplift contributes large amounts of clastic sediment to the basin, which acts to destabilize the margin even more. This combination and interplay of the increased slope due to gravity-gliding and sediment loading due to gravity spreading results in the structures demonstrated in the regional cross-sections.

In the western Gulf of Mexico, the basement and surface slopes of the Perdido and Mexican Ridges foldbelt are controlled by the Laramide orogeny (Fitz-Díaz et al., 2018; Hudec et al., 2019) and a post-Laramide uplift event (Kenning and Mann, 2020). In the transition from the shale-based northern Mexican Ridges to the salt-based Salina del Bravo foldbelt, an updip episode of Oligo-Miocene sediment loading caused the folding of both salt-based and shale-based structures in the downdip area (Kenning and Mann (2021).

In the Campeche PMFB, the oversteepening of the basemen and salt surface was triggered by the Middle Miocene Chiapanecan orogeny (Hasan and Mann, 2021). The northeastern South American PMFB, including the Pará-Maranhão and Barreirinhas, are similarly controlled by orogenic events related to the Andean orogeny along the western margin of South America (Reis et al., 2010).

Margin oversteepening related to cratonic uplift

The influence of cratonic uplift has been proposed by previous studies for the evolution of the Kwanza PMFB. Cratonic uplift affects the PMFB in two ways: (1) by increasing basinward tilt and (2) by increasing sediment supply (Hudec and Jackson, 2004). The cratons in West Africa, including the West African Craton Congo Craton and Kalahari Craton, are considered the primary sediment sources of the large river systems that feed the offshore PMFB and have a direct influence on their evolution. Eastern African basins, including the Lamu and Rovuma, are assumed to be affected by the East African rift system. However, the eastern branch of that rift system is located almost 500 km eastward of the cratonic uplift of western Africa (Cai et al., 2020).

Margin oversteepening related to the progradation of major deltas

The Atwater-Mississippi, Foz do Amazonas, and Niger PMFBs are all strongly influenced by delta progradation and have produced wider and thicker PMFBs with gentler surface slopes (Fig. 2.19). In the Atwater-Mississippi, 4–8 km of sediment has been deposited during the Middle to Late Miocene as the result of the progradation of the Mississippi Delta (Peel et al., 1995). The Foz do Amazonas PMFB also accumulated 10 km of sediment in the Late Miocene (Reis et al., 2010). The Niger Delta is up to 12 km thick (Wu et al., 2015). The large amount of clastic sediment deposition in such a short period for each of these PMFBs dominated their evolution through the gravity-spreading process. The timing of extensional faults, folds, and thrusts in each basin coincides with the high amount of deposition resulting from delta progradation and indicates a causal relationship.

2.7.2 Controlling factors for the formation of passive margin foldbelts

The controlling factors for passive margin foldbelts have been previously divided into two end members: gravity gliding and gravity spreading (Rowan et al., 2004). Gravity gliding is the translation of a body along a detachment slope where gravitational energy is released due to this movement. In contrast, gravity spreading is defined as the vertical collapse and lateral spreading of a body of rock under its own weight. The direction and amount of detachment along the slope in a basin drive the gravity-gliding process, whereas depositional loading controls the gravity-spreading process.

The relative contribution of both controlling factors is still under debate (Brun and Fort, 2011; Rowan and Ratliff, 2012). Using forward modeling, Peel (2014) has shown that the contribution of gravity gliding has a positive linear relationship with the angle of the detachment surface. For example, with a low-angle detachment surface (4°), gravity spreading contributes 65% of the total gravitational force, whereas with a detachment angle of 8°, it is only 38% (Peel, 2014). Considering the range of detachment angles (2–7°) for the PMFB described in this chapter, it is likely that the passive margin foldbelt evolution is driven by similar combinations of slope-angle-controlled gliding and deposition-controlled spreading.

My compilation based on more deeply-penetrating seismic reflection data shows the importance of basement dip on PMFBs that can be related to their original tectonic settings that include rifted-passive margins, transform-passive margins, deltaic margins, and rifted-volcanic margins (Fig. 2.19). Categorizing the forces involved as either gravity gliding or gravity spreading is more challenging.

2.7.3 Salt- vs. shale-based detachments

Gravity-driven passive margin foldbelts are transported along either salt or shale detachments. The first-order structural style, which can range from a zone of updip extensional structures to a zone of lateral translation or even a zone of contractional structures, remains similar in all of this chapter's examples—regardless of whether salt or shale forms the detachment horizon.

In a more detailed analysis, it can be observed that some specific structural styles observed in PMFB depend on the salt vs. shale detachment type. Symmetrical detachment folds characterize gravity-driven systems associated with salt detachment. In contrast, shale-detached passive margin foldbelts are dominated by imbricate thrusts, fault-bend folds, and fault-propagation folds. The difference in structural style is likely the result of the differing rheologies of salt and shale (Oliveira et al., 2013).

For example, subsurface salt is mobile, viscous, and readily deforms to fill the cores of folds, produce large diapirs, and forms more extensive salt canopies in comparison to shale, that is relatively less mobile, viscous, and less prone to deformation. The reason for this different between salt and shale deformation is likely related to the more plastic behavior of shale that deforms only when the deviatoric stress overcomes its shear strength (Rowan et al., 2004).

The original distribution of autochthonous salt is also proposed as a control on fold geometry as described in PMFB, including the Perdido (Trudgill et al., 1999) and Campeche (Hasan and Mann, 2021). The presence of an originally thick salt layer can readily mobilize and fill the cores of detachment folds and produce gentle, symmetrical anticlines over large areas, as seen in many PMFBs in the Gulf of Mexico. In areas of a reduced and thinner salt supply, a more asymmetrical structural style is observed with tighter folds bounded by one or both sides by reverse faults (Rowan et al., 2004).

2.7.4 Structural differences: Variations in updip extension and downdip compression

The updip extensional domain of passive margin foldbelts is dominated by basinward-dipping listric normal faults associated with antithetic and landward-dipping normal faults (Figs. 2.4–2.6, 2.9a, 2.12, and 2.14). Evidence of expulsion rollovers associated with rapid sediment loading is observed in salt-controlled PMFBs such as the Atwater-Mississippi, Perdido, and Campeche (Figs. 2.4–2.5 and 2.7). The expulsion of the primary autochthonous salt results in allochthonous canopies that overlie the translational or compressional domains. These higher-level and extensive salt canopies are unique to salt-based PMFB and are not observed in shale-based PMFB. This observation is likely due to the higher mobility and lower viscosity of salt in comparison to shale (Wu and Bally, 2000).

The structural style of the downdip compressional domain depends on whether salt or shale forms the underlying detachment. The compressional domain of shale-based systems is dominated by asymmetrical and imbricated thrust systems (e.g., Foz do Amazonas, Pará-Maranhão, Barreirinhas, Pelotas, Niger Delta, Orange River, Lamu, and Rovuma). In contrast, salt-detachments such as the Atwater-Mississippi, Campeche, Perdido, and Kwanza are dominated by symmetrical and upright detached and salt-filled anticlines with fewer thrust and reverse faults.

2.7.5 Passive margin foldbelts compared within the framework of critical taper wedge theory

Bilotti and Shaw (2005), Mourgues et al. (2014), and Tesei et al. (2021) have all modeled passive margin foldbelts using critical taper wedge theory. The taper of a wedge is defined as the angle between its free surface and basal detachment. Critical taper wedge mechanics theory states that once a wedge reaches some critical taper angle, the wedge will grow self similarly as material is either added to the wedge by deposition or tectonic accretion—or removed from the wedge by erosion or tectonic erosion. At the critical taper angle, the stress overcomes the strength of the detachment layer and the thrust wedge propagates basinward (Bilotti and Shaw, 2005; Davis et al., 1983).

The taper angle in the studied passive margin foldbelts ranges from 2.1° to 9.3° (Fig. 2.19). These taper angles are lower than the taper angles of accretionary wedges at active margins, as reported by Davis et al. (1983). Evidence of propagation along a basal detachment results in a wide contractional domain in PMFB and demonstrates that these broad PMFB attained critical taper at least for a limited time interval. The reason for attaining a critical taper stage at such a low taper angle may relate to the weak basal detachment consisting of either salt or overpressured shale (Bilotti and Shaw, 2005; Tesei et al., 2021).

Steeper basement slopes and higher detachment angles in the updip extensional domain commonly result in a narrower zone of listric normal faults observed in the Mexican Ridges, Pará-Maranhão, and Lamu passive margin foldbelts (Figs. 2.6, 2.10, and 2.17). I classify two of these margins as transform-related (Mexican Ridges, Pará-Maranhão) with characteristic steeper slopes and more narrow shelves (Fig. 2.19).

More gentle basement slopes, wider shelves, and detachment angles result in wider zones of extensional deformation as observed in the rifted zones, large deltas, or volcanic rifted margins that include the Kwanza, Orange River, Pelotas, and Campeche PMFB. However, the lateral and downdip limit of the passive margin foldbelt system is also controlled by the lateral extent of the underlying shale detachment or overpressured zone and by the buttressing effect of a downdip basement, step-up fault as found in the Perdido and Campeche PMFB (Hasan and Mann, 2021).

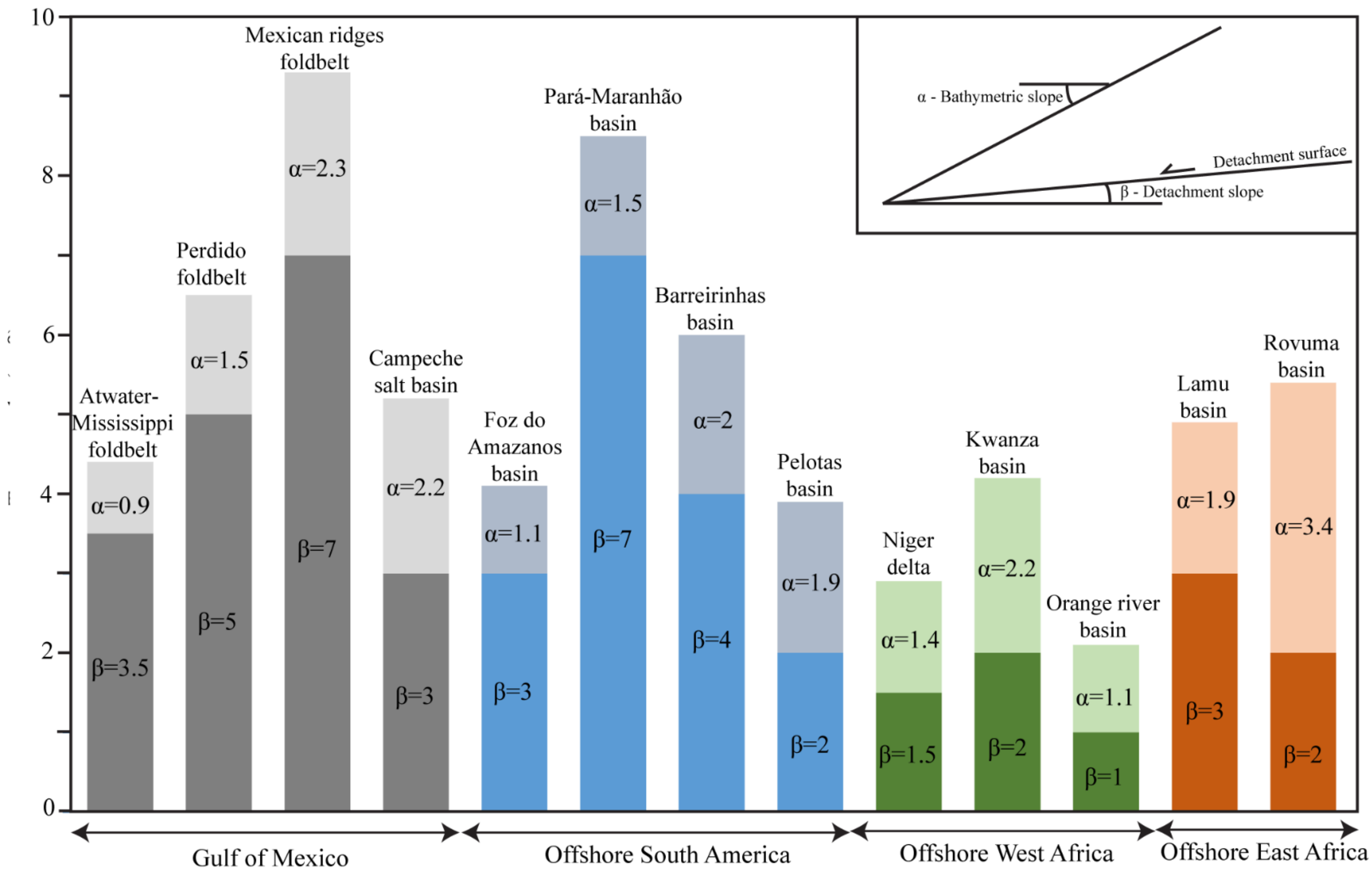

Figure 2.19: Bar chart summarizing the bathymetric slope (a), detachment slope (b), and taper angle (a+b) of each of the 13 passive margin foldbelts described in this chapter. The translational zone and relatively wide compressional domain indicate that the passive margin foldbelt system behaves as a critical taper wedge. The taper angles range from 2.1° to 9.3° and are relatively low compared with those of accretionary wedges at subduction zones with critical tapers in the range of >9° (Davis et al., 1983). The low taper angles of these PMFBs compared to accretionary prisms may reflect their detachment along zones of elevated pore-fluid pressure, as described for the Niger Delta PMFB by Bilotti and Shaw (2005).

2.7.6 Effects on sources, reservoirs, traps, and hydrocarbon maturation

Exploration interest in deepwater passive margin foldbelts increased significantly over the past decade as more and more examples of PMFB have been described using seismic data grids. The growing interest is a result of numerous geological, engineering, and economic factors including: 1) the diminishing number of undrilled onshore and nearshore structural traps, thus motivating companies to venture farther offshore; 2) the abundance of attractive undrilled large traps in deepwater passive margin foldbelts, which are known to contain a variety of play types, reservoirs, and seals; and 3) the presence of natural oil seeps indicating, in cases, multiple working petroleum systems; the availability of higher resolution wide-azimuth 2D and 3D seismic data in these structurally challenging deepwater provinces and advances in deepwater drilling technology (Morley et al., 2011).

There are many world-class examples of petroleum production from deepwater basins associated with mobile substrates formed by either salt or shale (Mann, 2022). Mobile salt or shale in a basin is attractive in the hydrocarbon exploration business as the remobilization of either can result in a variety of structural traps and seals. The presence of sandy turbidites, widespread source rocks, and abundant structural closures makes passive margin foldbelts an ideal area for offshore exploration.

Hydrocarbon exploration PMFB is much more extensive in salt-based systems than in overpressured shale detachment systems. The salt-based PMFB, such as Atwater-Mississippi, Perdido, Campeche, and Kwanza, provide the habitat for multiple, giant oil and gas discoveries (Figs. 2.3 and 2.13). Except for the productive Niger Delta and Rovuma examples, most shale-based PMFBs lack significant hydrocarbon discoveries, although many of these deepwater, shale-dominated areas remain underexplored.

2.8 Conclusions of this study

Deepwater passive margin foldbelts occur globally and play an important role in the exploration and production business for many companies, countries, and economies. These complex structural provinces have been studied for decades. The previous global reviews of the structure of PMFBs by Rowan et al. (2004) and Morley et al. (2011) focused on the mechanisms for the passive margin foldbelt systems with some key examples. Rowan et al. (2004) concluded that the main control on the variation in structural styles of PMFB was whether the detachment horizon beneath the PMFB was composed of shale with frictional strength—that produces basinward-verging thrust imbricates and associated folds—or salt—that produces symmetrical fold above a viscous salt sheet with no internal frictional strength. Rowan et al. (2004) and Morley et al. (2011) both noted that the largest control on the structural styles of deepwater foldbelts was whether the detachment was shale or salt.

Both of these previous review papers also speculated on the roles of gravity gliding (translation of a body along a detachment slope where gravitational energy is released due to this movement and driven mainly by slope angle) and gravity spreading (vertical collapse and lateral spreading of a body of rock under its own weight mainly driven by sediment loading). Both papers remained inconclusive in defining which mechanisms are dominant in any specific example of a PMFB, including those compiled in this paper.

My study includes deeply-penetration seismic reflection data collected in the nearly two decades that follow both of these review papers of Rowan et al. (2004) and Morley et al. (2011). These higher resolution data add important structure parameters for the 13 PMFBs, as compiled in Figure 2.19.

One important conclusion from my study is using this higher resolution seismic data to classify PMFBs according to their tectonic origin based on four groups: 1) rifted-passive margins, 2) transform-passive margins, 3) volcanic rifted margins, and 4) deltaic margins. Examples of PMFBs developed on rifted-passive margins and characterized by highly tapered margins in a cross-sectional view and gently sloped overlying passive margins ranging in dip angles from 1.9° to 3.4° degrees (Fig. 2.19). Examples of PMFBs developed on transform-passive margins and characterized by more truncated margins with narrow shelves and relatively steep bathymetric slopes ranging from 1.5° to 2.3° (Mexican Ridges, Pará-Maranhão, and Barreirinhas). This group of PMFBs exhibit more narrow deformation zones than the rifted types.

Examples of PMFBs developed on deltaic margins and characterized by broad shelves and slope areas underlain by seaward-prograding, clastic sedimentary deposits with bathymetric slopes ranging from 0.9° to 1.4° (Atwater-Mississippi, Foz do Amazonas, and Niger). This group exhibits the thickest sedimentation of the four groups. Examples of PMFBs developed on volcanic margins are characterized by broader margins underlain by prograding magmatic and sedimentary flows ranging in dip from 1.1° to 1.9° (Pelotas, Orange River) (Fig. 2.19).

I also recognize the importance of post-rift or transform events such as the oversteepening of the margins related to rapid sediment loading in the western GOM (Fig. 2.7), tectonic events affecting the western GOM (Fig. 2.5), and cratonic uplift as observed in western Africa (Figs. 2.15 and 2.16).

2.9 Unanswered areas for future work on the topic of the structure and origins of PMFBs

The analysis presented in this chapter and the extensive results from prior studies listed in the references section, there exists several key unsolved challenges in passive margin foldbelt research. (1) What are the dominant controls on PMFB evolution? Three key controls include fluid pressure, overburden lithology, and detachment dip, yet their relative impact on PMFB evolution remains an important research question. (2) What is the relative contribution of active and passive salt diapirism to not only the formation but also the evolution of structures observed in PMFB? (3) What are the relative contributions of gravity-gliding and gravity spreading in the development of PMFB, and how do these controls affect each of the main parts of the foldbelt? (4) Why do sequential restorations show that the amount of updip extension is typically higher than the amount of contraction? Additional geological and geophysical evidence from case studies and global synthesis studies are required to advance understanding in these principal research areas.

There are several key remaining questions that are significant for hydrocarbon exploration in passive margin foldbelts. First, how critical is the role of active deformation due to updip extension, which commonly poses a risk to seal failure? Seal failure drains reservoirs as the result of late-stage reactivation of faults (Hasan et al., 2021). Second, what is the stratigraphic location and extent of the detachment layer that can potentially act as a hydrocarbon fluid migration barrier? Third, how is reservoir quality sediment routed through the sometimes tortuous pathways of PMFB to the deeper part of these basins? Structures that deform the seafloor can limit the transport of high-quality sediment.

The following chapter is based on: Hasan, M.N., Mann, P., 2021. Structural styles and evolution of the Campeche salt basin, southern Gulf of Mexico. Marine and Petroleum Geology, v. 133, n. 105313. https://doi.org/ 10.1016/j.marpetgeo.2021.105313.

CHAPTER 3: STRUCTURAL STYLES AND EVOLUTION OF THE CAMPECHE SALT BASIN, SOUTHERN GULF OF MEXICO

3.1 Introduction

The Bajocian-early Callovian Campeche salt basin extends over 125,000 km^2 in the southern Gulf of Mexico (GOM) (Fig. 3.1). The Campeche salt basin is a less explored and drilled area of the GOM compared to the better explored sub-salt plays of the larger Louann salt basin that extends 900 km along the conjugate margin in northern GOM (Pindell et al., 2019, 2020; Kenning and Mann, 2020a) (Fig. 3.1). To this date, there have been only five deepwater wells drilled in water depths >1000 m in the Campeche salt basin (Davison, 2020). As a result, the geological history and tectonostratigraphy of the southern GOM in Mexican waters remain less understood than its northern conjugate margin in US waters.

Previous papers published on the regional geology and stratigraphy of the Campeche salt basin were based on the integration of seismic reflection, well, and regional geologic information (Padilla y Sánchez, 2007; Pindell and Miranda, 2011; Comissión Nacional de Hidrocarburos, 2015; Rowan, 2018; Hudec and Norton, 2019; Davison, 2020; Pindell et al., 2020; Shann, 2020; Sickmann and Snedden, 2020). Other studies have focused on the local structure and tectonics of the shallow-water shelfal area of Mexico (Ambrose et al., 2003; Mitra et al., 2005; Ricoy-Paramo, 2005; Gómez-Cabrera and Jackson, 2009; Hernández, 2013; Perez Gutierrez, 2013). The objective of this chapter is to present a comprehensive description and interpretation of the tectonic evolution of the Campeche salt basin using an extensive grid of 23,612 km of 2D seismic data provided by Geoex MCG. The observed salt structures of the Campeche salt basin are compared in the context of the main structural elements of a gravity-driven passive margin foldbelt: an updip extensional zone and a downdip compressional zone linked kinematically by an underlying and shallowly

Figure 3.1: Tectonic map of Mexico and the southern Gulf of Mexico basin showing the Campeche salt basin, the limit of oceanic crust (LOC), the area of late Jurassic oceanic crust, and major sedimentary basins. The white box shows the location of the more detailed map of the Campeche salt basin shown in Fig. 3.3. Map information is compiled from Witt et al. (2012a); Hudec et al. (2013); Comissión Nacional de Hidrocarburos, 2015; Nguyen and Mann (2015); Fitz-Díaz et al. (2018); Kenning and Mann (2020a,b).

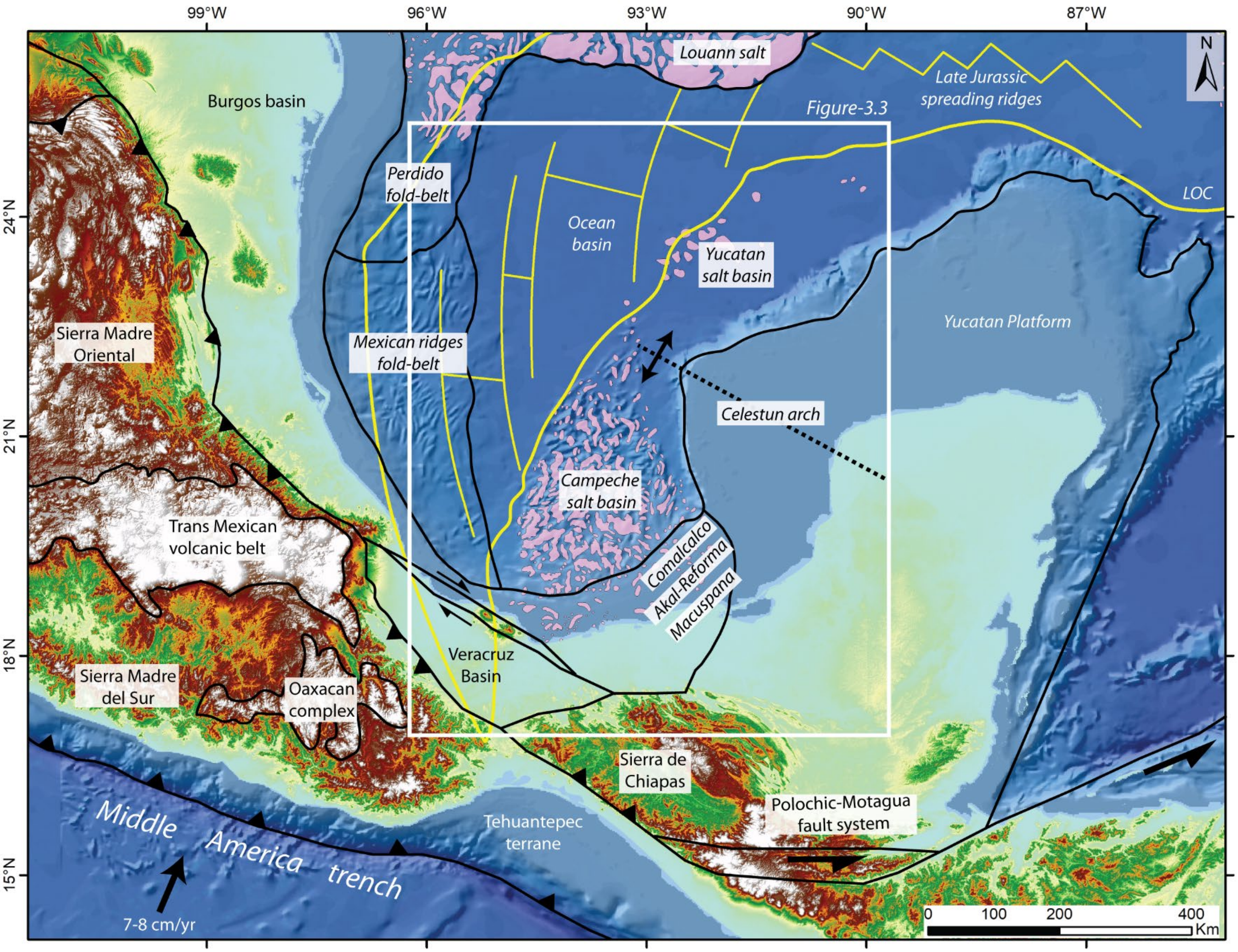
99°W
96°W
93°W
90°W
87°W
24°N
21°N
18°N
15°N
N
Louann salt
Late Jurassic spreading ridges
Figure-3.3
Burgos basin
Perdido fold-belt
Ocean basin
Yucatan salt basin
LOC
Yucatan Platform
Sierra Madre Oriental
Mexican ridges fold-belt
Celestun arch
Campeche salt basin
Trans Mexican volcanic belt
Comalcalco
Akal-Reforma
Macuspana
Veracruz Basin
Sierra Madre del Sur
Oaxacan complex
Sierra de Chiapas
Polochic-Motagua fault system
Tehuantepec terrane
Middle America trench
7-8 cm/yr
0
100
200
400
Km

dipping salt detachment surface (Rowan et al., 2004). This chapter illustrates: 1) how the variation of basement morphology reflects the northwestward dip of the base-salt topography (Pindell et al., 2015) and 2) how the salt thickness of the Campeche salt basin deformed within the passive margin foldbelt to form potential, salt-controlled, hydrocarbon traps.

3.2 Regional geological framework

3.2.1 Tectonic evolution of the Gulf of Mexico

The plate tectonic evolution of the GOM is described by previous authors as a two-phase opening, with the first phase of Triassic-middle Jurassic rifting and the second phase of late Jurassic seafloor spreading, with both phases related to the separation and counterclockwise rotation of the Yucatan continental block from the much larger, North American continental plate (Marton and Buffler, 1999; Pindell and Kennan, 2009; Hudec et al., 2013; Eddy et al., 2014; Nguyen and Mann, 2015). The late Triassic-middle Jurassic (~210-163 Ma) first phase of rifting is recorded by a broad zone of northeast-trending rifts in the northeastern and northern GOM that reflect northwest to southeast continental extension between the North and South American continents and the intervening Yucatan continental block (Pindell and Kennan, 2001; Liu et al., 2019; Steier and Mann, 2019; Erlich and Pindell, 2020).

Crustal thinning related to this broad zone of continental extension is manifested by a normal-fault-controlled rift filled with redbed-type continental sediment, overlain by a less faulted sag basin filled by evaporites of Bajocian-early Callovian ages (~170 Ma to ~165 Ma) (Rowan, 2018; Pulham et al., 2019; Hudec and Norton, 2019; Pindell et al., 2020; Kenning and Mann, 2020a) (Fig. 3.2).

During the late Jurassic and before the onset of seafloor spreading, the second rifting phase is recorded by an elongate, structural low adjacent to the area of the oldest oceanic crust (Hudec and Norton, 2019) (Fig. 3.2). This feature has been referred to as the "outer marginal trough" (Pindell et al., 2014; Curry et al., 2018; Rowan, 2018), the "outer trough" (Hudec and Norton, 2019), the "outer rift/graben" (Davison, 2020), and the "marginal rift" (Liu et al., 2019). In this chapter, this feature is referred as the "outer marginal trough."

Early continental rifting was followed by late Jurassic oceanic spreading in the central GOM that separated the southern Campeche salt basin from the Louann salt basin (Pindell, 1985; Pindell and Kennan, 2001, 2009; Eddy et al., 2014; Hudec et al., 2013; Nguyen and Mann, 2015; Steier and Mann, 2019; Lin et al., 2019; Kenning and Mann, 2020a).

3.2.2 Tectonic evolution of the Yucatan margin and Campeche salt basin

Salt basins in the Mexican sector of the GOM can be divided into Yucatan and Campeche salt basins separated by the northwest-trending Celestun basement arch (Hudec and Norton, 2019; Steier and Mann, 2019) (Fig. 3.1).

In the Campeche salt basin, a gentle northwestward tilt of the basin characterizes the late Jurassic to Cenozoic evolution (Rivera et al., 2011). It is related by Steier and Mann (2019) on the Yucatan margin to the thermal subsidence of the more distal, late Jurassic oceanic crust that underlies the central GOM (Lin et al., 2019). This gradual tilting caused downslope sliding along the Jurassic salt horizon of the Yucatan continental block and produced salt rollers of late Jurassic to Cretaceous (Pindell et al., 2014; Hudec and Norton, 2019; Steier and Mann, 2019; Kenning and Mann, 2020b).

Pulsed and shorter-lived orogenic events contributed to the northwestward tilting of the continental blocks in southeastern Mexico and the Yucatan Peninsula (Pindell and Miranda, 2011). From the late Cretaceous to middle Eocene, the Laramide orogeny-related Mexican fold and thrust belt propagated towards the northeast and deformed the onshore area of eastern Mexico (Kenning and Mann, 2020a) and the shallow-water zone of the Campeche salt basin (Horbury et al., 2003; Davison, 2020; Kenning and Mann, 2020a).

A later compressional event, the Chiapanecan orogeny, whose main deformation phase occurred during the Middle Miocene (11.6–13.8 Ma), produced folding and basinward tilting. This Middle Miocene orogeny can be linked to the shallow subduction of the Cocos plate beneath southern Mexico (Mandujano-Velazquez and Keppie, 2009; Witt et al., 2012b; Shann, 2020). The Chiapanecan orogeny formed the Akal-Reforma high (Padilla y Sánchez, 2007) with the adjacent Macuspana and Comalcalco rifts in the southern Campeche salt basin began forming in the late Middle Miocene and Pliocene, respectively (Padilla y Sánchez, 2007; Pindell and Miranda, 2011; Cruz-Mercado et al., 2012). Increased basinward gravity gliding from the late Middle Miocene to Recent along the large counter-regional faults that dip landward and expulsion rollovers contributed to downdip folding in the deepwater Campeche salt basin (Pindell and Miranda, 2011; Rivera et al., 2011).

3.2.3 Stratigraphy and basin fill of the Campeche salt basin

The Phase 1 syn-rift section and its overlying, 4-7-km-thick sag section overlies the Paleozoic basement and forms the pre-salt section of the Campeche salt basin (Fig. 3.2) (Rowan, 2018; Hudec and Norton, 2019). An extensive and thick sag basin formed in the middle Jurassic time (Lin et al., 2018; Steier and Mann, 2019). Following Phase 1 rifting, seawater - likely derived from the Pacific Ocean - filled the broad sag basin that overlay the extinct rifts during the Bajocian-early Callovian and formed the massive Louann-Campeche salt deposit as part of this extensive sag basin (Steier and Mann, 2020; Pindell et al., 2020).

The Louann salt in diapirs of the USA offshore sector is composed of almost pure halite (96–99%) and contains very few interbeds of other sedimentary rocks (Fredrich et al., 2007). Pure halite has also been cored in several shallow water wells in the Campeche salt basin (Davison, 2020). The absence of any significant clastic or carbonate interbeds within the evaporite interval supports its rapid deposition (Davison, 2020). Oxfordian aeolian sandstone - which is age and facies-wise equivalent to the Norphlet Formation in the US GOM, overlies the Bajocian salt (Godo, 2017; Steier and Mann, 2019; Snedden et al., 2020).

During the late Jurassic and Cretaceous, clastic, rift-related sedimentation transitioned upward into thick carbonate sedimentation of the passive margin that formed shallow carbonate platforms bordering the Yucatan platform (Padilla y Sánchez, 2007). Cenozoic subsurface stratigraphy is dominated by clastic sedimentation, including margin collapse sequences, large submarine channel complexes, and mass transport complexes (Sickmann and Snedden, 2020) (Fig. 3.2).

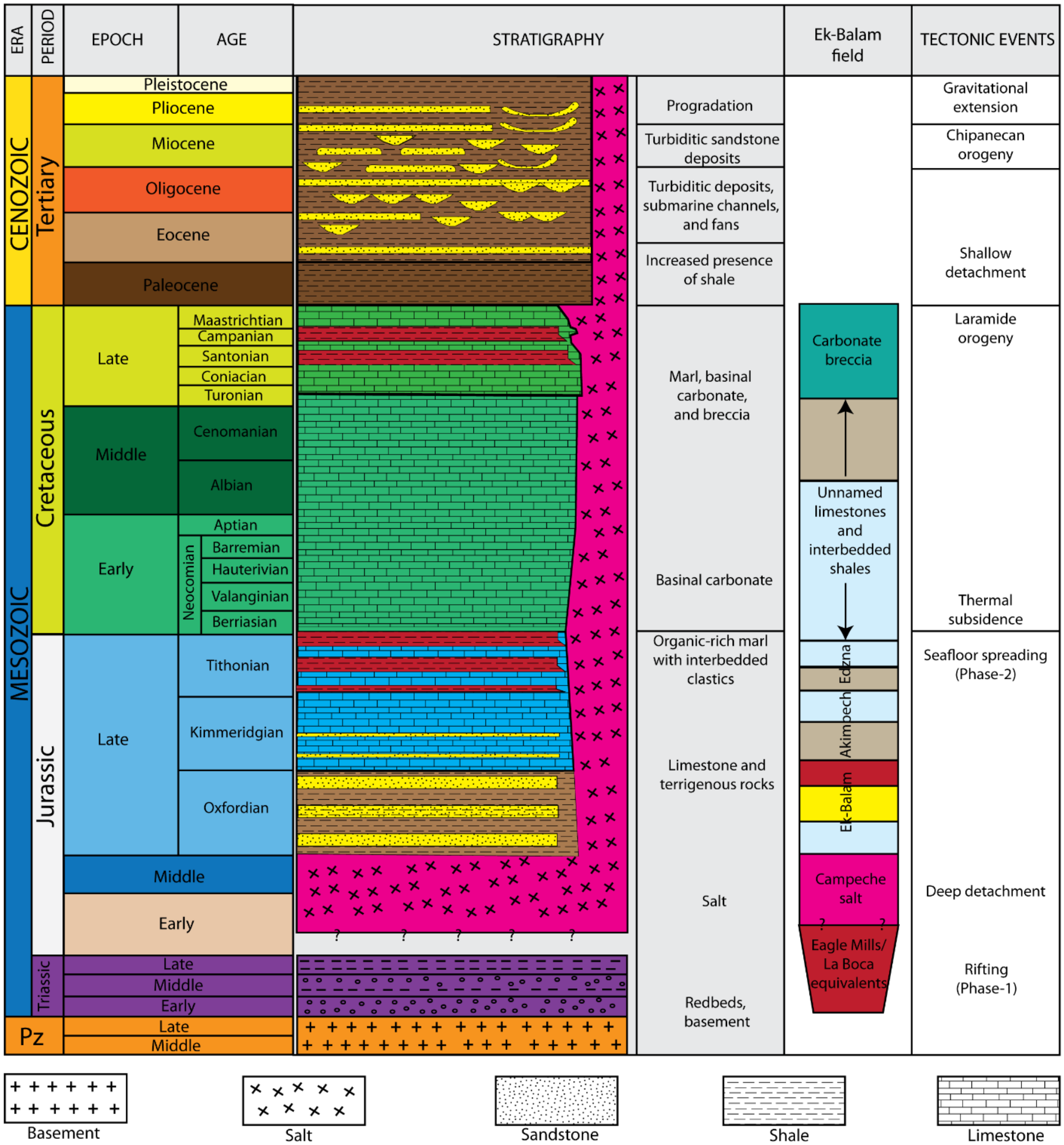

Figure 3.2: Stratigraphic column summarizing the lithologies, sedimentary facies of the Campeche salt basin and its correlation with the generalized stratigraphy of the Ek-Balam field (Steier and Mann, 2019) and the main regional tectonic events compiled from Arzate et al. (2009a); Comissión Nacional de Hidrocarburos, 2015; and Steier and Mann (2019). The location of two Ek-Balam wells is shown on the map of Fig. 3.3.

3.3 Data and methods

3.3.1 Subsurface dataset used in this study

This study uses 23,612 km of pre-stack depth migrated (PSDM) seismic reflection data from the Campeche salt basin in addition to an adjacent regional grid of 5000 km of PSDM data from the Yucatan salt basin that covers a combined area of 260,000 km^2. The datasets acquired in 2015–16 were kindly provided by Geoex MCG for this study. The 2D seismic reflection grid has a line spacing of 10 km in the Campeche salt basin and 40 km in the Yucatan salt basin. The dataset spans the shelf, slope, and basinal areas that range in water depth from 0 to 4000 m. The 2D seismic survey has long offsets (12 km) and deep recording (14s). All seismic sections are displayed with the same polarity and vertical exaggeration (V.E = 4). An increase in acoustic impedance is represented by a peak (red), and a decrease is represented by a trough (blue).

Shipborne magnetic data from the Maximus survey (Geoex MCG) was integrated with the Earth magnetic anomaly dataset (EMAG2) (Maus et al., 2009). Major tectonic features of the Campeche salt basin, including the outer marginal trough, the Celestun arch, and the Campeche magnetic anomaly, were mapped. These magnetic data were also used to estimate the depth and dip direction of the top Paleozoic basement in the basin that is not well imaged on seismic reflection lines due to the presence of the intervening salt layer (Fig. 3.1).

This study integrates interpreted seismic lines from Padilla y Sánchez (2007); Gómez-Cabrera and Jackson (2009); Comissión Nacional de Hidrocarburos, 2015; Ysaccis et al. (2018); Hudec and Norton (2019); Shann (2020); and Davison (2020) for the Campeche salt basin along with published regional seismic lines from Steier and Mann (2019); Miranda-Madrigal and Chávez-Cabello (2020); and Kenning and Mann (2020b) for the Yucatan salt basin. Age information and lithology data from Pemex (2009–2019), Hernández (2013), and six publicly accessible DSDP wells (Ewing et al., 1969; Worzel et al., 1973) for stratigraphic interpretation were incorporated. The top and base of the salt were identified by high-amplitude peaks with internal chaotic reflections interpreted as horizons of remobilized salt (Steier and Mann, 2019; Kenning and Mann, 2020b).

3.3.2 Tilt depth method for estimating the depth to top basement

The configuration of the Paleozoic basement was estimated by the tilt-depth method using Geosoft Oasis Montaj software. This method uses the tilt angle of the reduced-to-pole (RTP) transformation of the total magnetic intensity data to estimate the location and depth of magnetic sources (Salem et al., 2007).

The tilt equation is given by:

$$Z = [d\theta/dh]^{-1} \qquad \text{(Eq.1)}$$

The equation indicates that the horizontal location of the magnetic source occurs at zero tilt angle (θ) and the source depth corresponds to the horizontal distance (h) between the tilt angles of 0° to ±45° (Salem et al., 2007, 2010). Using this method, the depth to the basement (z) was determined by the negative reciprocal of the horizontal gradient ($[d\theta/dh]^{-1}$) at the zero contours of the tilt angle, as described in Blakely et al. (2016). The depth estimates from the tilt depth method were combined with observations from seismic reflection.

3.3.3 Sequential structural restoration

To quantify the amount of updip extension at and above the autochthonous salt layer in the Comalcalco rift that contributes to the downdip compression in the deepwater Campeche salt basin, a 140-km cross-section was constructed (modified from Padilla y Sánchez, 2007) that traverses the listric normal fault zone and was sequentially restored using the Petroleum Experts MOVE software. The direction of the restored cross-section (northwest-southeast) is approximately parallel to the downdip movement direction of the passive margin foldbelt. The restoration of the Campeche passive margin foldbelt followed methods described by Rowan (1993), Rowan and Ratliff (2012), and Ellis et al. (2015) (line location in Fig. 3.3 and the restoration result is shown in Fig. 3.15).

Each interval was backstripped and the underlying sedimentary layers were decompacted using the curve of Sclater and Christie (1980). The porosities and depth coefficients used in the decompaction process were estimated based on the lithologies summarized in Figure 3.2.

Following Perez Gutierrez (2013), displacement along individual faults was restored using the fault parallel flow algorithm for thrust faults and the inclined shear algorithm (60^0–85^0 shear angle) for listric normal faults. The geometries of salt bodies were allowed to change in the restoration process to account for salt movement in and out of the plane of the section. The final two steps of the restoration process were to flatten the section to a regional level using a simple shear algorithm and then to calculate the Airy isostasy (Rowan, 1993).

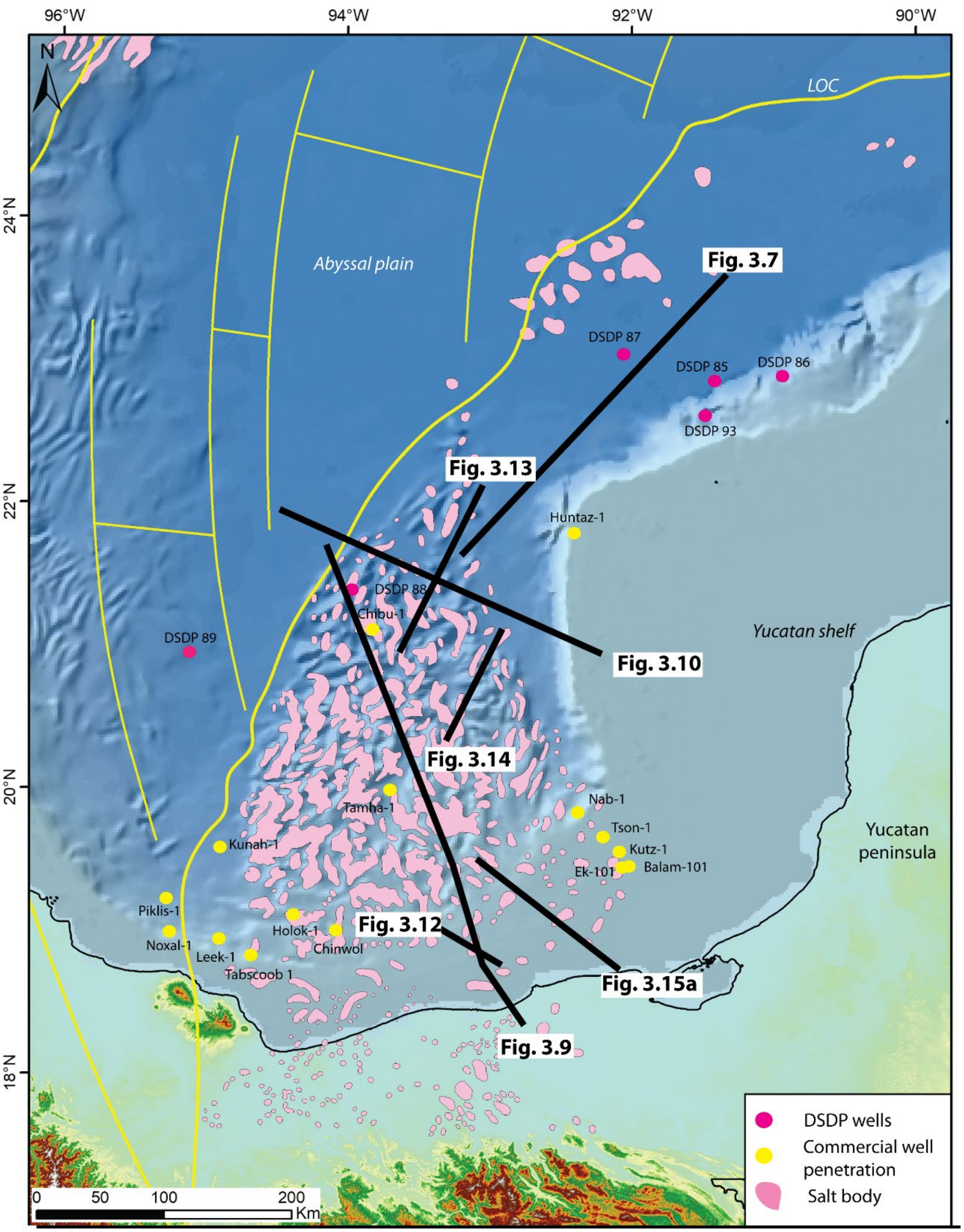

Figure 3.3: Bathymetric map of the Campeche salt basin showing the distribution of Jurassic salt diapirs (Kenning and Mann, 2020b), commercial wells (Comissión Nacional de Hidrocarburos, 2015), DSDP wells, locations of the seismic sections shown in this paper, and the location of the structurally-restored, regional cross-section across the updip part of the passive margin foldbelt (Fig. 3.15). Seismic data provided courtesy of Geoex MCG.

3.4 Late Jurassic outer marginal trough system along the Campeche margin

3.4.1 Spatial analysis of the outer marginal trough

The boundaries and prominent, elongate low of the outer marginal trough were determined from the reduced-to-pole transformation of the total magnetic field (RTP-TMI) and its tilt derivative transformation (Fig. 3.4). The regional magnetic lineaments are less pronounced on the RTP-TMI map, which likely reflects the stronger expression of the shorter wavelength magnetic anomalies (Fig. 3.4a). The RTP-TMI data was low-pass filtered to 70 km and a tilt derivative map was derived to improve the expression of the regional magnetic anomalies (Fig. 3.4b).

The outer marginal trough can be observed in the magnetic map as a 40-55-km wide by 670-km-long, negative magnetic anomaly (Fig. 3.4). The outer marginal trough runs along the entire southern GOM and its limit of oceanic crust (Pindell et al., 2016; Rowan, 2018; Hudec and Norton, 2019; Lin et al., 2019; Liu et al., 2019). The basement high that bounds the basinward edge of the outer marginal trough is characterized by a linear positive anomaly that marks the basement step-up fault adjacent to the edge of the late Jurassic oceanic crust (Pindell and Kennan, 2009; Pindell et al., 2014; Steier and Mann, 2019; Kenning and Mann, 2020b) (Fig. 3.4b).

The magnetic maps reveal two other prominent magnetic anomalies: the Campeche magnetic anomaly and the Celestun arch (Pindell et al., 2016; Steier and Mann, 2019). The Campeche magnetic anomaly is 450 km long and 150 km wide (Fig. 3.4) and extends in the north-south direction along the central area of the Campeche salt basin. The Celestun Arch is 50–80 km wide, 400 km long and strikes in a northwest-southeast direction.

Figure 3.4: a) Reduced-to-pole of total magnetic intensity (RTP-TMI) map of the southern Gulf of Mexico showing locations of the Campeche magnetic anomaly (CMA) and Celestun arch (CA) - a prominent, northwest-trending basement arch that separates the Campeche and Yucatan salt basins; b) Tilt derivative map using 70 km low pass filtered RTP-TMI data showing locations of the east-northeast-trending, Jurassic outer marginal trough, the limit of oceanic crust, and the late Jurassic oceanic crust in the central Gulf of Mexico. The 40-55-km-wide and 400-km-long outer marginal trough that forms the western border of the Campeche salt basin is inferred to mark the early onset of late Jurassic, Phase-2 oceanic spreading in the central Gulf of Mexico. Magnetic data provided courtesy of Geoex MCG and Maus et al. (2009).

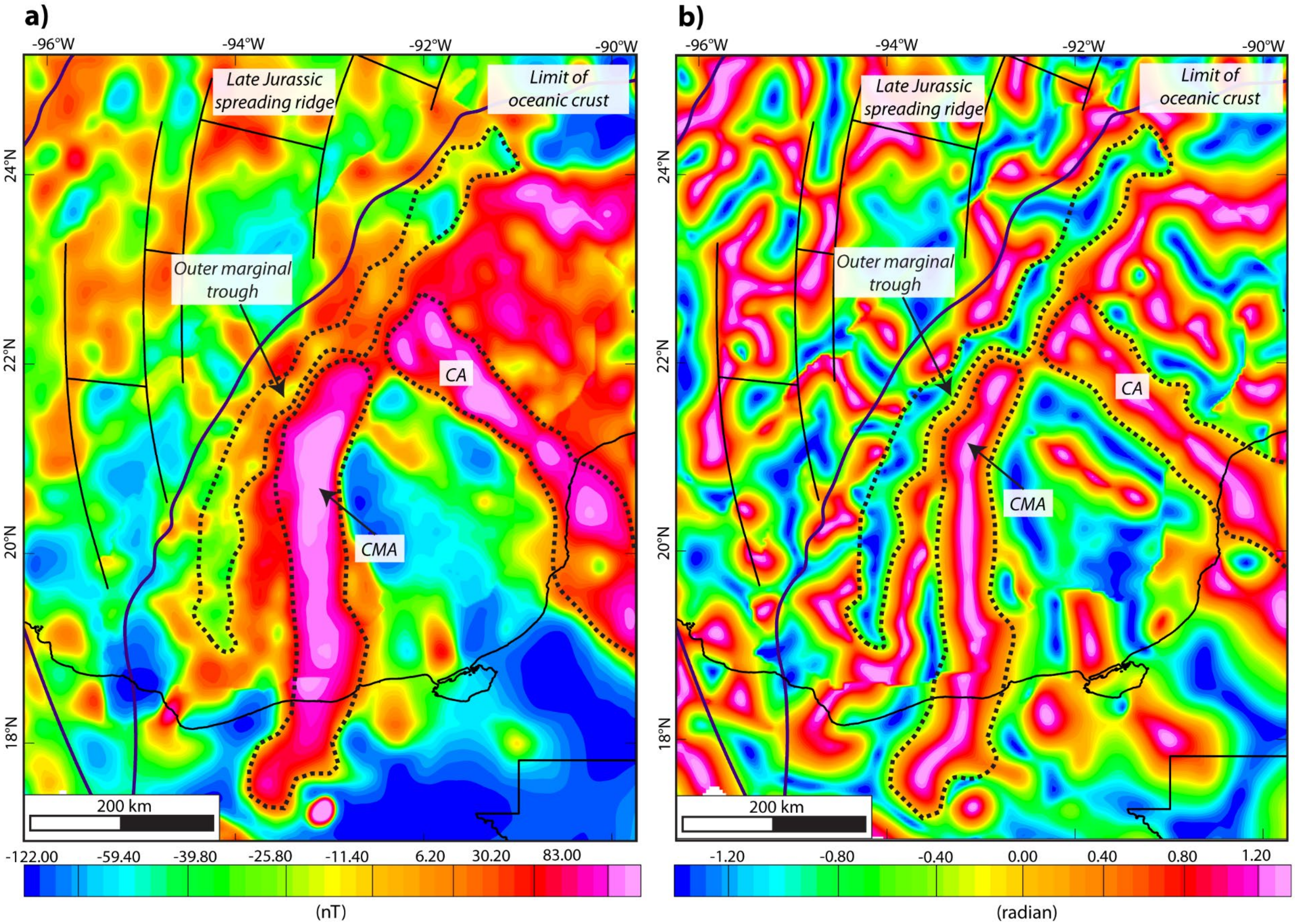

a)
b)
-96°W
-94°W
-92°W
-90°W
24°N
22°N
20°N
18°N
Late Jurassic spreading ridge
Limit of oceanic crust
Outer marginal trough
CA
CMA
200 km
-122.00
-59.40
-39.80
-25.80
-11.40
6.20
30.20
83.00
(nT)
-1.20
-0.80
-0.40
0.00
0.40
0.80
1.20
(radian)

3.4.2 Seismic reflection mapping of the outer marginal trough

The interpreted bathymetry from seismic mapping shows that the seafloor of the Campeche salt basin dips to the northwest and that the seafloor of the Yucatan salt basin dips to the west-northwest (Fig. 3.5a). The total sedimentary thickness map reveals the extent and architecture of the rift structure underlying the Campeche salt basin on the stretched/ transitional crust that flanks of the late Jurassic oceanic crust (Fig. 3.5b).

The total sediment thickness ranges from 2 to 7 km along the slope of the Yucatan carbonate platform and gradually thickens westward, where a sharp increase in total sediment thickness delineates the outer marginal trough that overlies the inferred necking domain of the continental crust (Fig. 3.5b) (Steier and Mann., 2019). The sediment thickness in the outer marginal trough is locally >15 km. Some localized variations in thickness are observed, especially in the southeastern Campeche salt basin. The southeastern corner of the Campeche salt basin shows a sudden increase in sediment thickness that delineates the basinward limit of the Comalcalco rift (Fig. 3.5b). However, the landward limit of the extensional area in the southernmost Campeche basin is limited by the coverage of the seismic grid and extends south of my seismic grid (Fig. 3.5b).

Figure 3.5: a) Bathymetric map of the study area showing the northwestward-dipping slope of the Yucatan salt basin and the west-northwestward-dipping slope of the Campeche salt basin based on the seismic grid shown by the light gray lines. The northwest-trending Celestun arch separates the two adjacent salt basins. b) Total sediment thickness from the seismic mapping of the grid shown by the light gray lines illustrates the thickest area of sedimentation along the east-northeast-trending outer marginal trough outlined by black dashes. Seismic data provided courtesy of Geoex MCG.

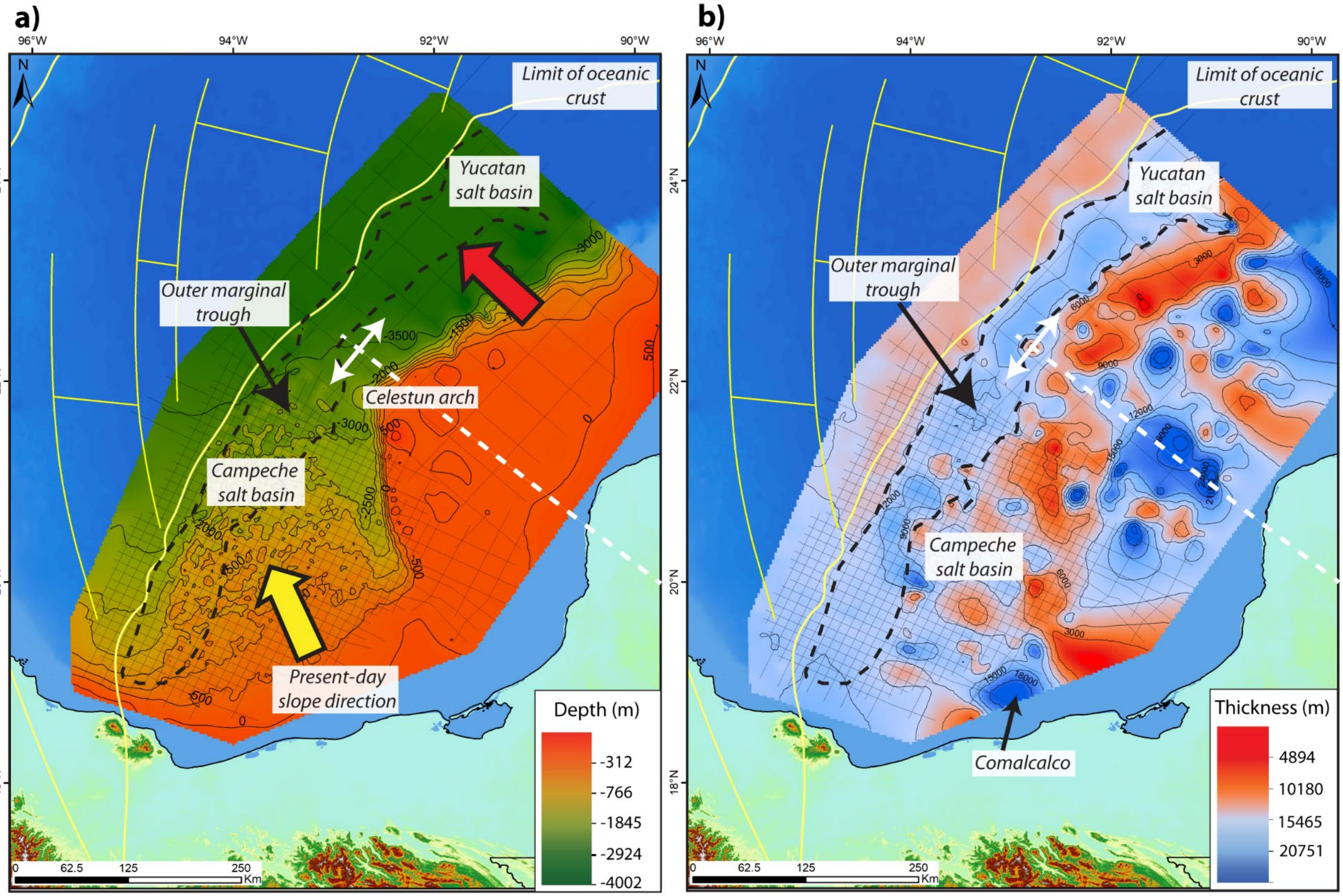

a)
Limit of oceanic crust
Yucatan salt basin
Outer marginal trough
Celestun arch
Campeche salt basin
Present-day slope direction
Depth (m)
-312
-766
-1845
-2924
-4002
b)
Limit of oceanic crust
Yucatan salt basin
Outer marginal trough
Campeche salt basin
Comalcalco
Thickness (m)
4894
10180
15465
20751

3.4.3 Distribution of allochthonous salt

As shown in Figure 3.6a, the distribution of the thickest, allochthonous salt in the Campeche salt basin coincides with the elongate outer marginal trough. This salt thick likely reflects the presence of deep salt feeders of initial greater thickness that feed the overlying allochthonous salt sheet. The depth structure maps show a more extensive secondary allochthonous salt distribution in the southern area of the Campeche salt basin. No higher allochthonous salt is present along the northwestern Campeche margin and Yucatan salt basin (Steier and Mann, 2019; Hudec and Norton, 2019).

The isopach map in Figure 3.6b shows notable thickness variations between the top of allochthonous salt and the seafloor (200–7000 m). By contrast, the thickness of the Campeche salt remains relatively uniform in the area of the distal deepwater Campeche margin. The sedimentary thickness above the allochthonous salt layer exhibits a uniform thickness of <1000 m. The top of allochthonous salt to seafloor thickness increases abruptly to 5–7 km in the depocenter of the updip Comalcalco rift (Fig. 3.6b).

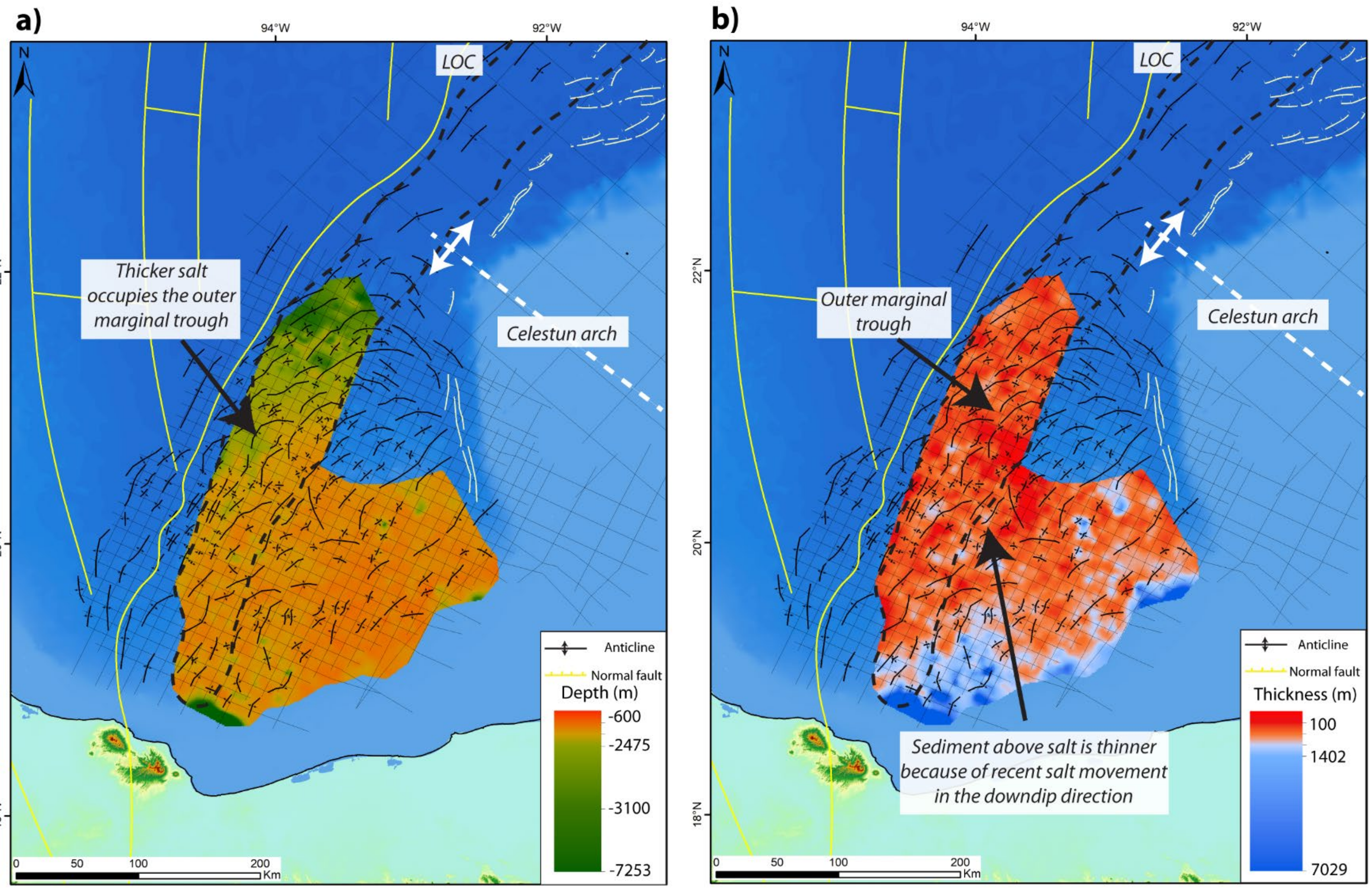

Figure 3.6: a) Distribution of allochthonous salt across the Campeche salt basin based on top allochthonous salt mapping using the seismic grid shown by the light, gray lines. The elongate, east-northeast extension of the allochthonous salt and its more extensive salt feeder systems is controlled by the thicker Jurassic salt deposition within the east-northeast-trending late Jurassic outer marginal trough. b) Isopach map showing the northward decrease in the thickness of the interval from top allochthonous salt to the seafloor from 1500 m to 200 m. Seismic data provided courtesy of Geoex MCG.

3.5 Basement architecture of the Campeche salt basin

3.5.1 Celestun arch: the boundary between Campeche and Yucatan salt basins

The boundary between the Campeche and Yucatan salt basin is a prominent, 110-km-wide by 400-m-high, northwest-trending basement arch extending to the northwest from the Yucatan platform. Steier and Mann (2019) termed this feature as the "Celestun magnetic anomaly" or "Celestun arch," which also has been observed in seismic reflection lines by Hudec and Norton (2019). Seismic images reveal the basement arch exhibits vertical relief of several hundred meters and is onlapped by pre-salt sedimentary strata, demonstrating that the arch was a positive feature before the deposition of the combined Louann-Campeche salt-filled sag basin of Bajocian-early Callovian age (Fig. 3.7). The autochthonous salt is either welded or absent directly above the Celestun arch (Fig. 3.7). At the base of the section right below the Celestun arch, a zone of bright reflectors at a depth of 16–17 km is inferred to represent the Moho of the thinned, continental crust (Fig. 3.7) (Kenning and Mann, 2020b).

The overall distribution and thickness of the Jurassic salt layer change abruptly across the Celestun arch in the northeast-southwest strike direction of two adjacent salt basins (Hudec and Norton, 2019). On the Yucatan margin, extensional growth fault systems are dominant. In contrast, large salt pillows and diapirs are more prominent on the Campeche margin (Fig. 3.7). The contrasting basin geometries control these differences between the two salt basins, with the Campeche salt basin being significantly more confined than the more uniformly dipping Yucatan salt basin. Another important difference between the two salt basins is that the salt is thicker (2–5 km) in the Campeche basin and forms salt-cored anticlines that are not observed in the Yucatan salt basin (Hudec and Norton, 2019).

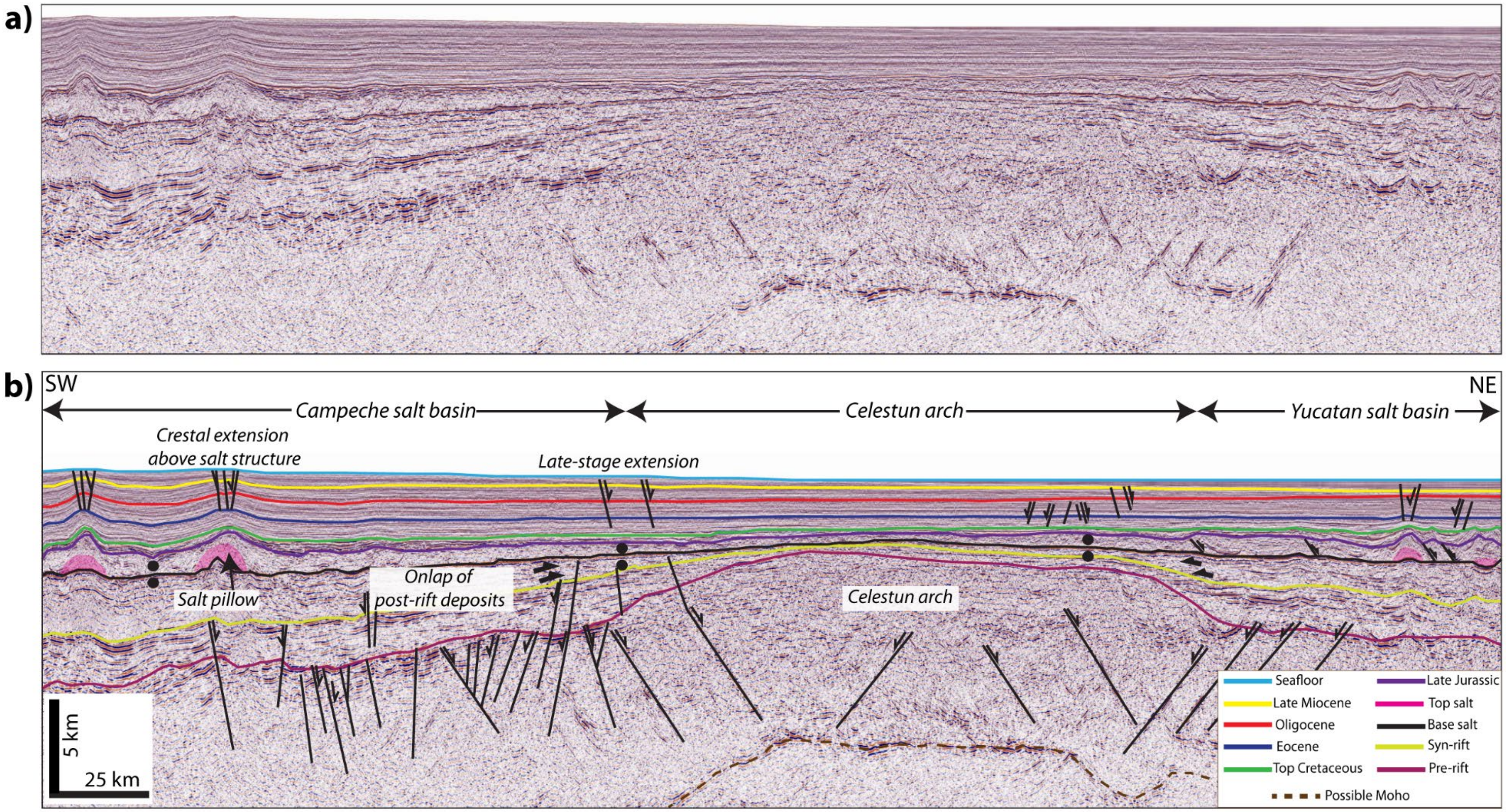

Figure 3.7: a) Uninterpreted northeast-southwest seismic across the Celestun arch (located on the map in Fig. 3.3). b) Interpreted seismic section showing the structure of the northwest-trending Celestun arch that forms a broad, structural high separating the Campeche and Yucatan salt basins (Fig. 3.4b). Differences in the two adjacent salt basins include: 1) thicker and more diapiric salt in the Campeche salt basin; 2) salt roller detachment across the broader and more planar Yucatan salt basin; 3) elongate passive margin foldbelt deformation in the more confined Campeche salt basin. Onlap of pre-salt sedimentary strata demonstrates that the arch was a positive feature prior to Bajocian-early Callovian age salt deposition. Seismic data provided courtesy of Geoex MCG

3.5.2 Basement structure and distribution of salt-associated deformation

The magnetic data allows an improved image of the basement surface and shows an excellent correlation with seismic images (Fig. 3.8a and 3.8b). The top Paleozoic basement depth ranges from 5 to 20 km west of the Yucatan carbonate platform and >15 km in depth within the 670 km outer marginal trough (Fig. 3.8a). The overall basement dip direction of the Campeche salt basin is to the north-northwest, whereas in the Yucatan salt basin, the basement dip is to the northwest (Fig. 3.8a).

Extensive northwest-dipping thrusts extend from onshore to the shelfal area of the Akal-Reforma high (Fig. 3.8a). A complex array of northeast-southwest trending normal faults of the Comalcalco and Macuspana rifts strike perpendicular to the Akal-Reforma high (Fig. 3.8a). The Macuspana normal faults dip landward, whereas the Comalcalco normal faults dip basinward (Padilla y Sánchez, 2007). These normal faults sole out on both allochthonous and autochthonous salt and transition downdip in the deeper water area into a train of folds, thrusts, anticlines, squeezed diapirs, and break-thrusts (Pindell and Miranda, 2011). The updip hingelines strike in northeast-southwest orientation, but these orientations transition to northwest-southeast as the passive margin foldbelt follows the arcuate curvature of the underlying outer marginal trough and its thicker salt detachments. The basement map reveals a continuous ridge defined by a basement step-up fault at the western limit of the outer marginal trough (Fig. 3.8a). Beyond the western salt limit and above the late Jurassic oceanic crust, a less dense group of folds with northeast-trending fold hingelines are mapped.

Figure 3.8: a) Map showing the depth to the top of the Paleozoic basement map for the Campeche salt basin based on the application of the tilt-depth magnetic method of Salem et al. (2007, 2010). The top basement map highlights the elongate shape of a 40-55-km-wide outer marginal trough as it trends to the northeast. The outer marginal trough is bounded along its western edge by a basement step-up fault that separates the structural low of the outer marginal trough from the adjacent, higher-standing area of the late Jurassic oceanic crust. Seismic data provided courtesy of Geoex MCG. b) Plot showing a good correlation between basement depth from the seismic reflection grid and the magnetic dataset.

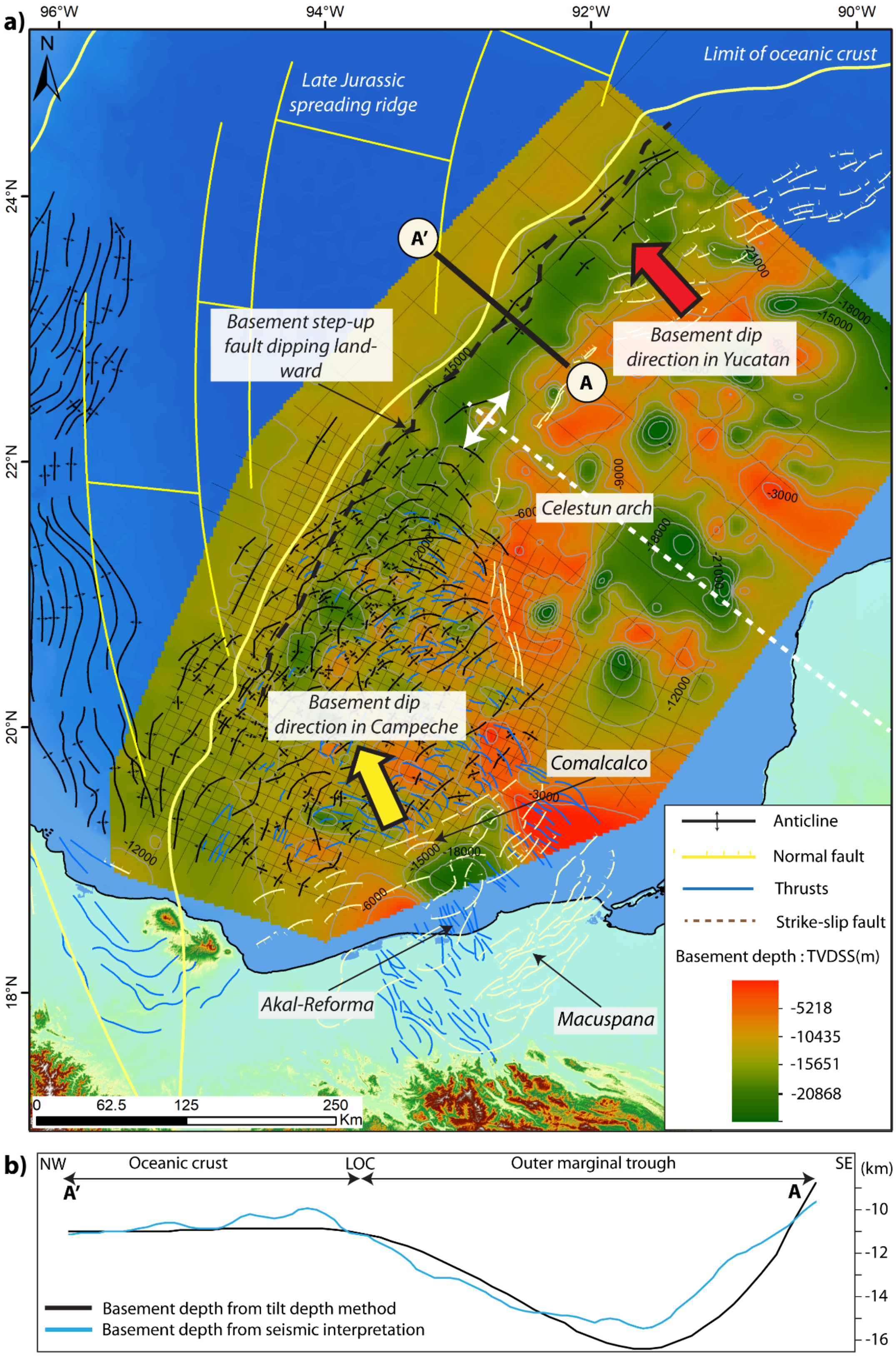
a)
96°W
94°W
92°W
90°W
24°N
22°N
20°N
18°N
N
Limit of oceanic crust
Late Jurassic spreading ridge
A'
A
Basement step-up fault dipping land-ward
Basement dip direction in Yucatan
Celestun arch
Basement dip direction in Campeche
Comalcalco
Akal-Reforma
Macuspana
Anticline
Normal fault
Thrusts
Strike-slip fault
Basement depth : TVDSS(m)
-5218
-10435
-15651
-20868
0 62.5 125 250 Km
b)
NW
SE
Oceanic crust
LOC
Outer marginal trough
(km)
-10
-12
-14
-16
Basement depth from tilt depth method
Basement depth from seismic interpretation

3.6 Regional structural trends along the Campeche margin

3.6.1 Structural provinces along northwest-southeast direction

The regional southeast-to-northwest, structural cross-section of the Campeche salt basin (Fig. 3.9) reveals two structural domains:

1) An updip area of normal faults; the upslope extensional domain includes a zone of regional listric normal faults, detaching on both allochthonous salt and autochthonous salt; rollover structures and counter-regional normal faults record extensional deformation of late Middle Miocene to Recent age.

2) A downdip area of compressional deformation is characterized by salt canopies, open salt-cored folds, salt diapirs, and break-thrusts. The allochthonous salt bodies have coalesced in the proximal part of this domain. Closely spaced upright diapirs are concentrated in the outer marginal trough area (Fig. 3.9); upright and symmetrical diapirs exhibit 6–8 km in relief and bound minibasins with 8–10 km of clastic sedimentary infill.

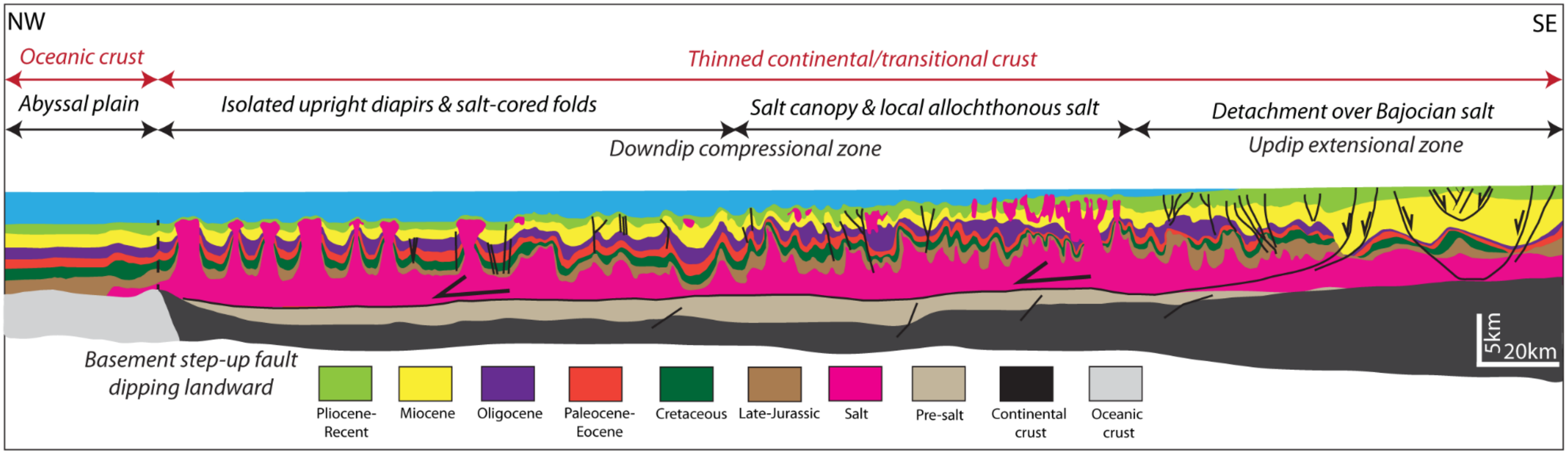

Figure 3.9: Composite southeast-to-northwest regional structural cross-section of the Campeche salt basin (located on the map in Fig. 3.3) showing the main structural provinces of the basin and the variability in deformational styles. Updip extensional zone consists of listric normal faults that detach on both allochthonous salt remobilized during the late Middle Miocene and autochthonous salt of the Bajocian-early Callovian age. The downdip contractional zone consists of salt-cored folds, thrusts, autochthonous salt diapirs, allochthonous salt canopies, and detachment folds with kink bands. The cross-section is constructed using interpretations from this study, Comissión Nacional de Hidrocarburos, 2015, and Horn et al. (2017).

3.6.2 Structural provinces in the eastern area of the Campeche basin

In contrast to the regional cross-section shown in Figure 3.9, the cross-section in Figure 3.10 traverses the northern part of the Campeche salt basin. It is oriented in a dip orientation across the margin of the Yucatan continental block (line location is shown in Fig. 3.3). Basinward of the Yucatan carbonate platform, this slope is characterized by an interval of 300–600 m thick salt rollers and normal faults rooted on a basinward-dipping, Bajocian-early Callovian to Cretaceous detachment surface (Hudec and Norton, 2019; Steier and Mann, 2019). The extent of the basin along this section is relatively narrow (50–60 km) with a more steeply northwestward dipping basement surface, in contrast to the more gently dipping basement surface shown on the cross-section in Figure 3.9. Basinward of the Yucatan carbonate platform, the base salt occurs at a depth of 10–12 km within the outer marginal trough (Fig. 3.10). Because salt is much thicker in the outer marginal trough, numerous large salt diapirs exhibit as much as 6–8 km of vertical relief.

Salt diapirism is observed throughout the Cenozoic remains active in the northern Campeche salt basin. All four diapirs shown in the section of Figure 3.10 form positive features on the seafloor with up to 500 m of relief. The development of salt diapirs is locally associated with minibasins that were accompanied by welding along the source salt layer and have resulted in the formation of turtle structures (Fig. 3.10). Prominent mass-transport complexes are present adjacent to the salt diapir (Fig. 3.11). The pre-salt rift deposits and sag sequences are relatively well imaged in this part of the basin compared to the southern Campeche margin, where the thickness of the allochthonous salt unit makes imaging more challenging.

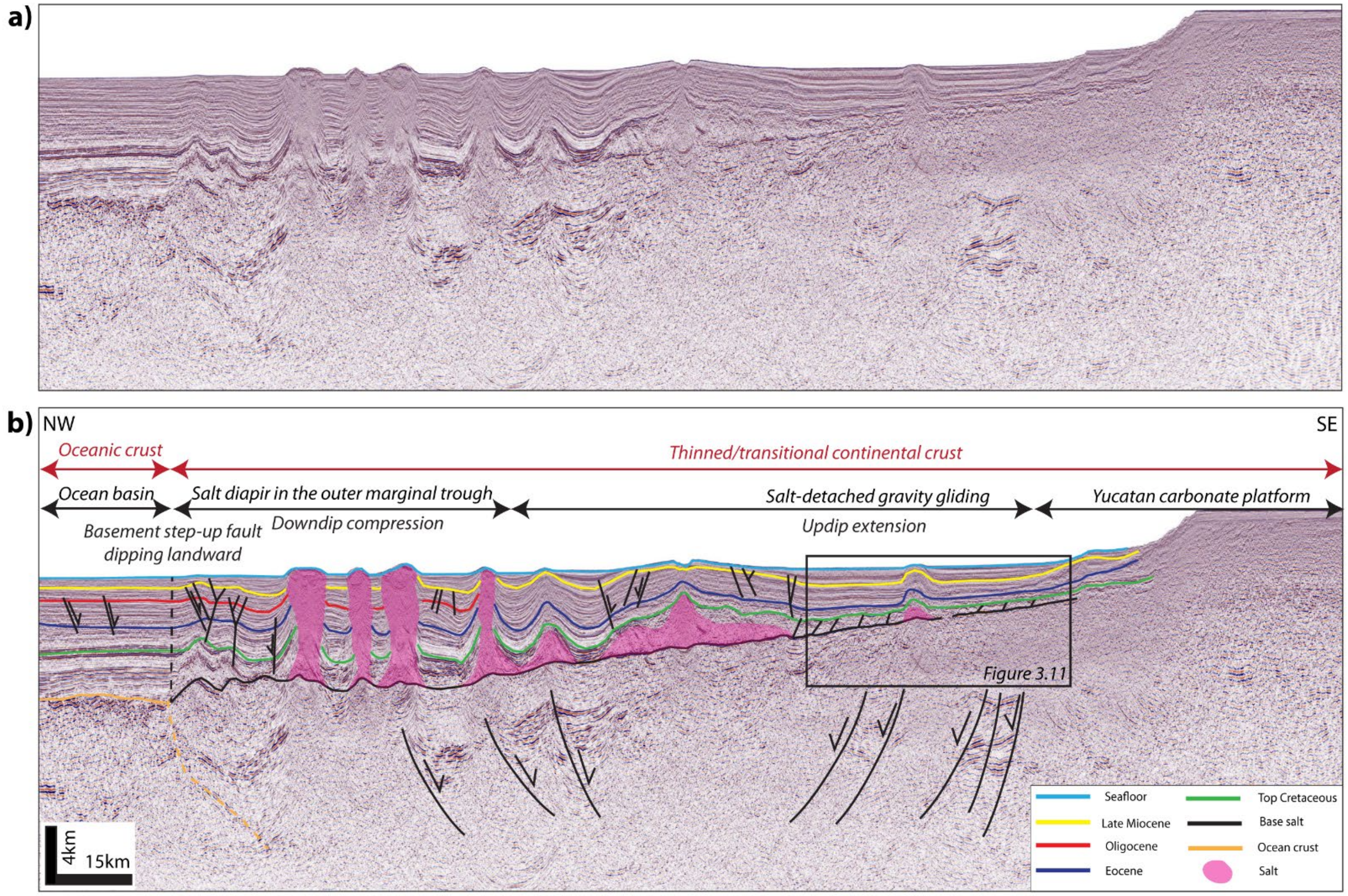

Figure 3.10: a) Uninterpreted west-northwest seismic section of the Yucatan salt basin east of the Celestun arch (located on the map in Fig. 3). b) Interpreted seismic section showing the structural variation between the updip, detached salt pillow structures, and the downdip diapiric and folds. The largest diapirs are concentrated in the basement low and mark the 40-55-km-wide outer marginal trough area adjacent to the oceanic crust. Gravitational sliding on the updip salt layer is enhanced by its steeper gradient leading upwards to the Yucatan carbonate platform. Syn-rift and post-rift sag deposits both contribute to the greater total sediment thickness in the outer marginal trough area. Seismic data provided courtesy of Geoex MCG.

3.7 Seismic profiles through updip extensional domain

3.7.1 Seismic profile through salt roller province

In the eastern part of the study area, seismic data reveal the presence of a steeply dipping extensional system characterized by salt roller structures (Figs. 3.10 and 3.11). The province encompasses approximately a 20–45 km wide area parallel to the Yucatan carbonate platform. Gravity gliding with minor slip occurs above very thin autochthonous salt where base salt is either welded or relatively small salt pillows are present (Fig. 3.11). Salt rollers and accompanying normal faults are separated by rafted Mesozoic sediments transported downslope along the basal salt detachment (Fig. 3.11).

The late Mesozoic normal fault system is truncated by a regional unconformity marking the Cretaceous-Paleogene boundary (Fig. 3.11). Sub-parallel, sub-salt continuous stratal reflections thicken in the basinward direction beneath the salt layer.

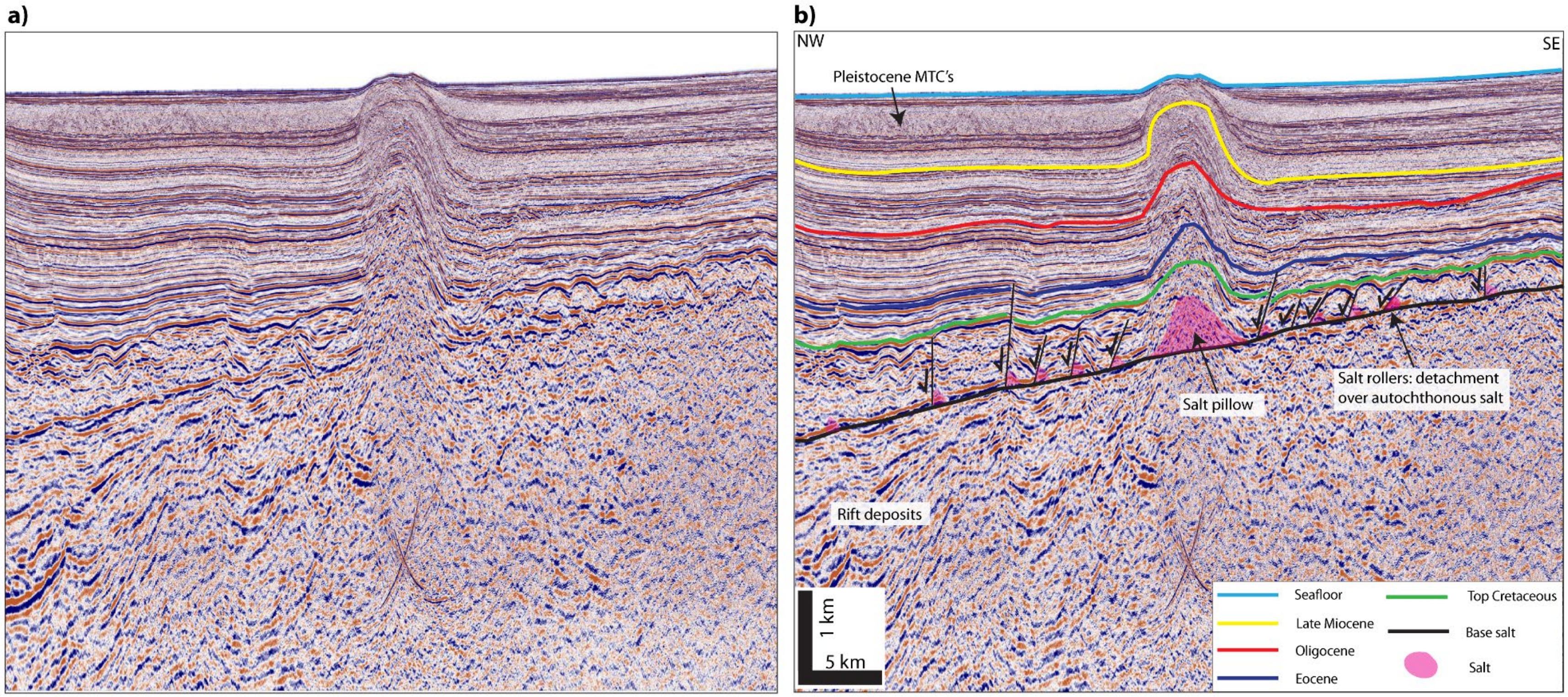

Figure 3.11: a) Uninterpreted west-northwest seismic section (location on Fig. 3.10). b) Interpreted seismic section showing the structural style of salt rollers formed on the updip, Bajocian-early Callovian to Cretaceous detachment. Gravitational sliding on the updip salt layer from the late Jurassic-Cretaceous is enhanced by updip loading by post-rift sag deposits and downdip thermal subsidence of the late Jurassic oceanic crust (Steier and Mann, 2019). Seismic data provided courtesy of Geoex MCG.

3.7.2 Seismic profile through expulsion rollover province

Counter-regional normal faults with associated expulsion rollovers occur in the Comalcalco rift that forms part of the updip extensional domain of the Campeche passive margin foldbelt (Figs. 3.1, 3.5b, and 3.12). Fault-controlled minibasins form prominent northeast-southwest trending depressions roughly parallel to the present-day coastline of southeastern Mexico (Fig. 3.12). The minibasins formed when a large clastic wedge prograde northward and loaded the salt with >4 km of Plio-Pleistocene sediments (Fig. 3.12).

Keystone (faults at the crest of salt structures) and counter-regional fault families have been described from the northern Gulf of Mexico by Rowan et al. (1999). The keystone faults include synthetic-antithetic normal faults produced by minor outer arc bending above salt rollovers. Counter-regional systems form above and ahead of where salt is expelled seaward from an allochthonous salt sheet. The lower part of the rollover anticline likely forms a salt weld, and the upper part is a normal fault with a slip in the landward direction (Fig. 3.12). Similar structures in the Macuspana rift have been reported by previous authors (Padilla y Sánchez, 2007; Pindell and Miranda, 2011).

Figure 3.12: a) Uninterpreted northwest-southeast seismic across the updip area of the Campeche salt basin (located on the map in Fig. 3.3). b) Interpreted seismic section showing the structural style of the shelfal, updip, southeastern extensional province of the Campeche salt basin deformed by listric normal faults detaching on Bajocian-early Callovian salt. Gravitational sliding on the updip salt layer is enhanced by sedimentary loading of post-rift deposits. Cretaceous and Cenozoic sag deposits are deposited in the southern shelfal area of the Campeche basin. The structural complexity in this area results from the overprint of these Neogene normal faults on the pre-existing northwest-southeast trending folds and thrusts that deformed the southern Campeche basin during the final, middle Miocene stage of the Chiapanecan orogeny (thrusts shown in blue on the map in Fig. 3.8). This middle Miocene shortening event produced crustal thickening and oversteepening of the margin that led to the formation of the late Middle Miocene-Recent passive margin foldbelt and downslope flow of the Jurassic salt layer. About 5 km of sedimentary loading in the Plio-Pleistocene led to the seaward evacuation of the salt canopies and the counter-regional normal faults that bound the Plio-Pleistocene minibasins. Seismic data provided courtesy of Geoex MCG.

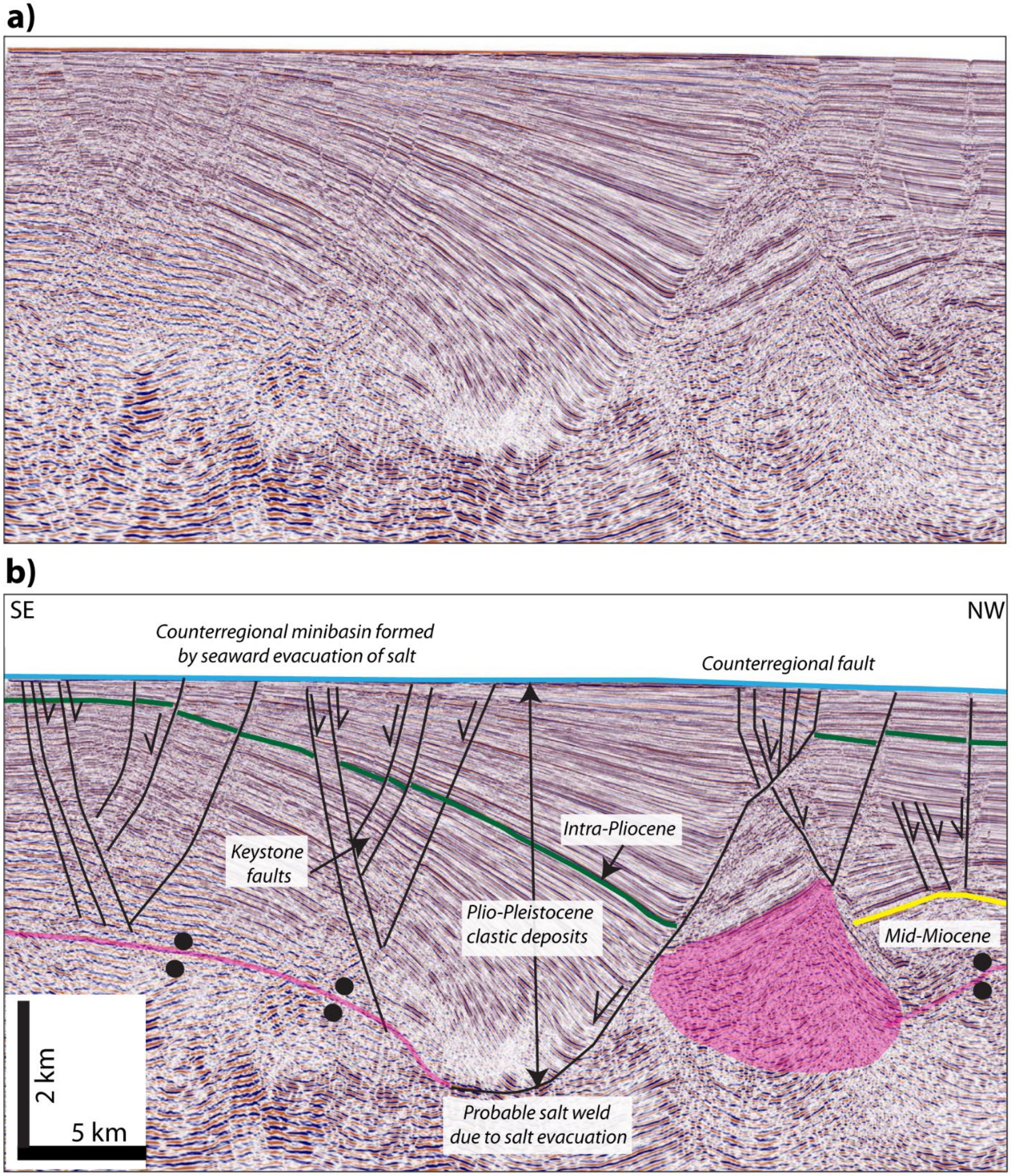
a)
b)
SE
NW
Counterregional minibasin formed by seaward evacuation of salt
Counterregional fault
Intra-Pliocene
Keystone faults
Plio-Pleistocene clastic deposits
Mid-Miocene
2 km
5 km
Probable salt weld due to salt evacuation

3.8 Seismic profiles through downdip compressional domain

3.8.1 Seismic profile through outer marginal trough

The salt-associated structural styles in the outer marginal trough are characteristic of salt-cored anticlines that consist of linear and symmetrical detachment folds. The fold profiles are generally well rounded with regular wavelengths of 5–10 km (Fig. 3.13). Synclines forming the minibasins are usually present at the same level and develop above a salt weld. Sediment thickness in the primary minibasins above the salt horizon is approximately 8–10 km.

Analysis of reflection continuity and stratal geometry reveals the growth packages in the section starting in the Eocene-Oligocene were likely produced by passive diapirism related to sediment loading that include the distal submarine fans related to Miocene to Recent Mississippi delta. Distinct wedging of sedimentary deposits with mass-transport complexes was identified in the Neogene to Recent, indicating that a major pulse of salt mobilization occurred during this time of formation of the passive margin foldbelt (Fig. 3.13).

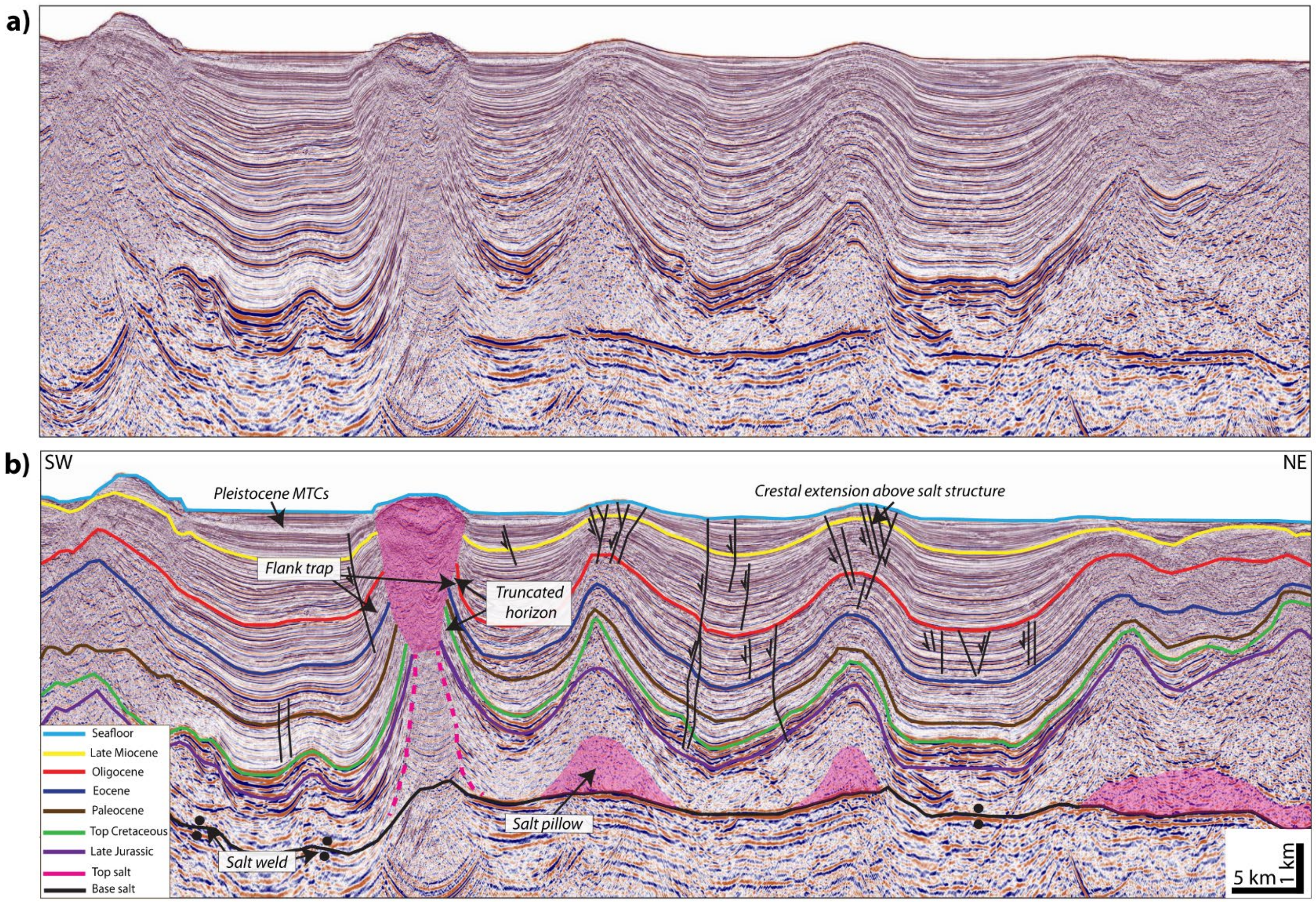

Figure 3.13: a) Uninterpreted northeast-southwest dip section across the downdip, compressional domain of the Campeche salt basin (located on the map in Fig. 3.3). b) Interpreted seismic section showing the structural style of downdip, salt-cored folds formed above the salt detachment. Outer arc stretching of the anticlinal crests is accommodated by crestal or keystone normal faults. A variety of hydrocarbon trap types are indicated in the syn-folding, Cenozoic section. Seismic data provided courtesy of Geoex MCG.

3.8.2 Along strike profile inboard of the outer marginal trough

Inboard of the outer marginal trough relative to the Yucatan carbonate platform, the structural styles are different, although their timing of deformation is synchronous. Salt-related structures in this area of the northwestern Campeche basin include tighter detachment folds with distinct kink bands in their limbs (Fig. 3.14). The observed kink bands similar to the Perdido foldbelt are difficult to interpret in some parts of the section and result from poor seismic imaging on the steeply-dipping fold flanks (Camerlo and Benson, 2006) (Fig. 3.14). From distinctive seismic facies of interpreted age horizons, some anticlines are interpreted to be cut on one or both limbs by high-angle reverse faults called “break-thrusts” by Rowan et al. (2000).

The original distribution of autochthonous salt is proposed as the main control on fold geometry as described in other areas like the Perdido foldbelt in the northwestern GOM (Trudgill et al., 1999; Rowan et al., 2000) (Fig. 3.1). The stratal geometry from seismic reflections reveals that sedimentary packages remain uniform in thickness until Middle Miocene to Recent when folding and syn-folding sedimentation initiated as a result of the Chiapanecan orogeny (Shann, 2020).

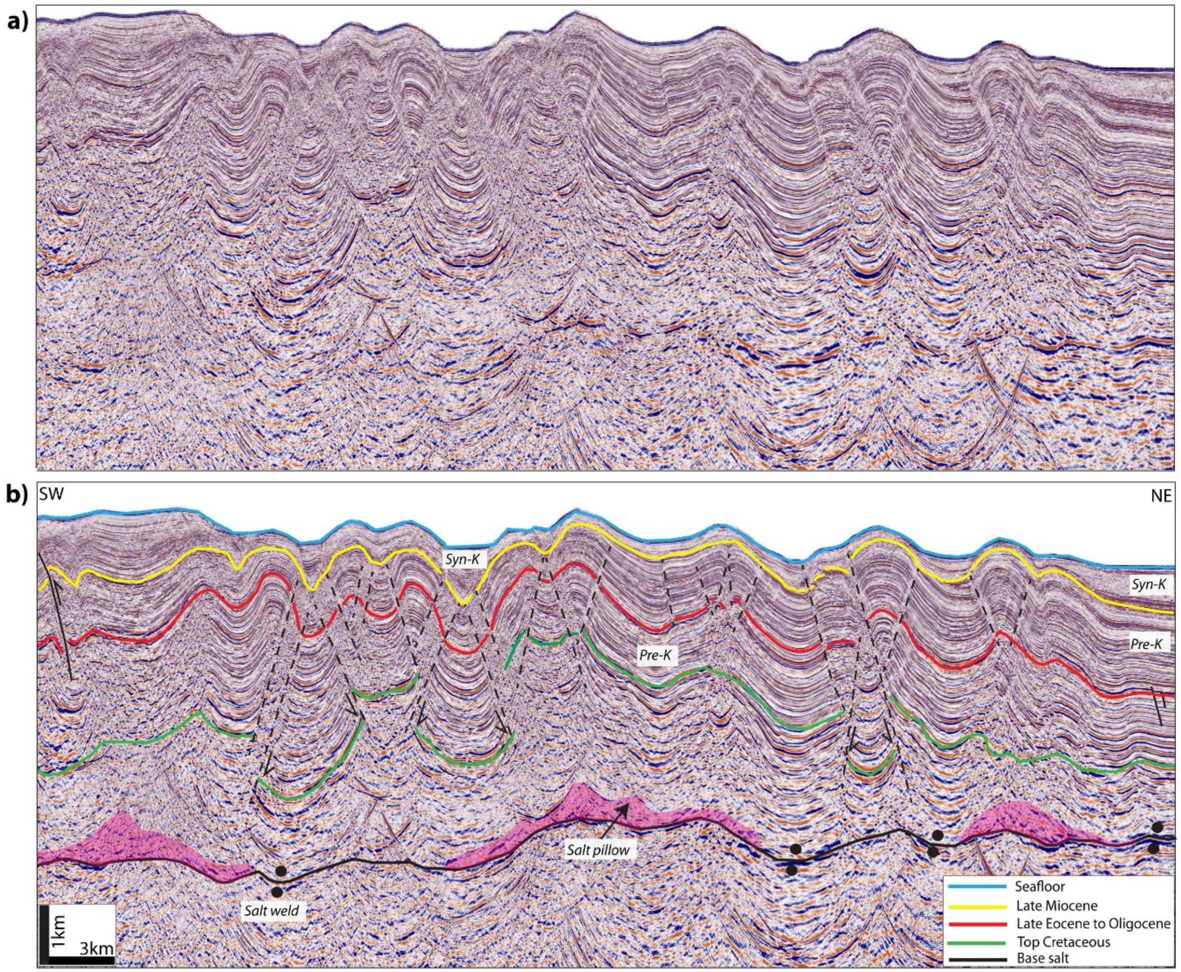

Figure 3.14: a) Uninterpreted southwest-northeast dip section across the downdip, compressional domain of the Campeche salt basin (located on the map in Fig. 3.3). b) Interpreted seismic section showing the structural style of downdip, detachment folds with kink bands formed above the autochthonous salt. The salt layer is relatively thin in this area (0.5–1 km) compared to the area of thicker salt (2–5 km) in the outer marginal trough. The thinner salt leads to a structural style of detachment folds with break-thrusts. Seismic data provided courtesy of Geoex MCG.

3.9 Structural restoration of the updip normal faults

A dip-oriented seismic profile across the updip extensional domain of the linked passive margin foldbelt shows Pliocene to Recent, listric normal faulting that separates the Comalcalco rift from the Akal- Reforma high (Fig. 3.15). These thin-skinned normal faults detach primarily on salt and are actively deforming the seafloor. Rollover anticlines associated with the listric normal faults contain up to 4–6 km of Pliocene-Recent sedimentary rocks (Fig. 3.12).

A structural restoration was carried out in four steps based on the dated stratigraphic units seen on the seismic lines (Fig. 3.15a): 1) from late Jurassic to Miocene, there was minor slip along the listric normal faults as the Comalcalco rift post-dates these stratigraphic units; in the more basinward part of the section, some thrust-bound pop-up structures of the early Cenozoic age are observed that are likely related to the Laramide orogeny; 2) listric normal faults detached on salt with approximately 10.5 km of extension in the downdip basinward direction; the timing of the slip in this step is Pliocene and follows the oversteepening of the southern margin of the Campeche salt basin due to the formation of Akal-Reforma high during the Chiapanecan orogeny; 3) a downdip extension of another 10 km in the Pleistocene to Recent, making a total downdip extension of 20.5 km across the Comalcalco rift; and 4) the accommodation created by the extension results in a marked increase in sedimentation rate around Pliocene to Recent with ~4 km of sediment deposited since 5 Ma.

Similar structures in the Macuspana rift with the extension starting in the late Middle Miocene have been reported by previous authors (Padilla y Sánchez, 2007; Pindell and Miranda, 2011). The total basinward slip of these two rifts contributed to the structures of the downdip compressional domain of the passive margin foldbelt.

Figure 3.15: a) Dip-oriented cross-section showing normal faults of the up-dip extensional domain of the Campeche salt basin. The section used is modified from a previous structural section by Padilla y Sánchez (2007). A total extension of 20.5 km in the Comalcalco rift from the Pliocene to Recent extension is estimated by sequentially restoring the section. This large magnitude of Comalcalco and Macuspana rifts is compensated by an inferred equivalent amount of downdip shortening. b) Schematic diagram showing the location of the restored section relative to the structural configuration of the Campeche salt basin modified from Bhatnagar et al. (2019). The basement step-up limiting the salt extent in the western edge and Yucatan continental margin in the east channels the downward salt flow and passive margin foldbelt.

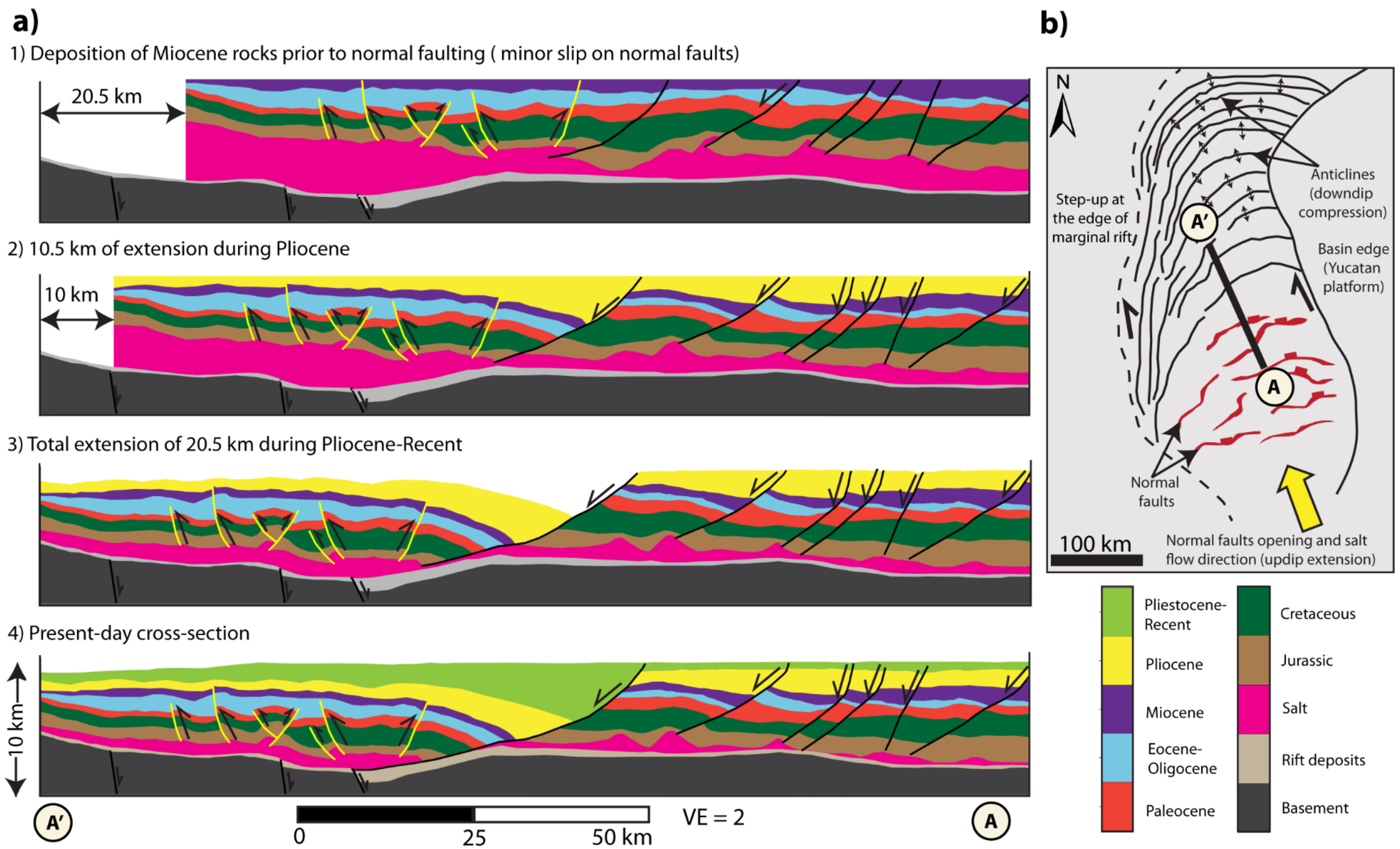

a)
1) Deposition of Miocene rocks prior to normal faulting (minor slip on normal faults)
20.5 km
2) 10.5 km of extension during Pliocene
10 km
3) Total extension of 20.5 km during Pliocene-Recent
4) Present-day cross-section
10 km
A′
0
25
50 km
VE = 2
A
b)
N
Step-up at the edge of marginal rift
Anticlines (downdip compression)
A′
Basin edge (Yucatan platform)
A
Normal faults
100 km
Normal faults opening and salt flow direction (updip extension)
Pliestocene-Recent
Pliocene
Miocene
Eocene-Oligocene
Paleocene
Cretaceous
Jurassic
Salt
Rift deposits
Basement

3.10 Discussion

3.10.1 The outer marginal trough, its control on salt distribution, and structural styles

The presence of thick autochthonous and allochthonous salt limits the ability of 2D seismic reflection data to image deeper structures in the Campeche salt basin that include the top Paleozoic basement, Triassic- Jurassic rift basins, and Cretaceous-Cenozoic post-rift basins in the Campeche salt basin and adjacent areas (Bain et al., 2019) (Fig. 3.10). The integration of potential field data and 2D seismic led me to interpret a 40-55-km wide and 400-km-long Campeche segment of the southern GOM outer marginal trough system that displays a distinctive, negative magnetic signature on the RTP-TMI and its tilt derivative map (Figs. 3.4 and 3.8).

Both autochthonous and allochthonous salt thickness is significantly higher in the outer marginal trough (7–8 km) than in more landward areas (2–3 km), which was probably controlled by salt deposition within the outer marginal trough axis (Figs. 3.9 and 3.10). Previous workers in the GOM proposed that greater thickness of autochthonous Bajocian-early Callovian salt was deposited or transported post-depositionally late in the rifting history just before the initiation of the late Jurassic oceanic spreading. This led to the elongate thick salt along the outer marginal trough (Pindell and Kennan, 2009; Hudec et al., 2013; Nguyen and Mann, 2015; Rowan, 2018). The allochthonous salt distribution also shows a distinct elongate pattern above the outer marginal trough that likely reflects deeper feeder systems that connect the allochthonous salt to an underlying body of autochthonous salt (Fig. 3.6a).

The variability of salt-related structural styles in the downdip deepwater Campeche salt basin can be explained by thickness variations in the salt layers described by Trudgill et al. (1999) for the Perdido and Mississippi fan foldbelt in the northern GOM. In the Campeche area, a similar relationship between thicker salt layers in the outer marginal trough allows the salt to flow into the cores of broad anticlines and maintain their more open, cross-sectional geometry (Fig. 3.13). In contrast, areas of thinner salt layers do not provide enough flow into the cores of anticlines and result in tighter anticlines cored with distinct kink bands, in places reverse faults (Fig. 3.14) (Rowan et al., 2000; Camerlo and Benson, 2006).

3.10.2 Kinematic evolution of the updip extension and downdip compression

The Chiapanecan orogeny (related to the shallow subduction of the Cocos plate) produced northeast-verging folds and thrusts in the area of Akal-Reforma high and shelfal area of southeastern Mexico (Fig. 3.8a) and formed a northern extension of the Chiapas foldbelt in southern Mexico (Mitra et al., 2005). After the main Middle Miocene folding phase of the Chiapanecan orogeny, the Akal-Reforma high became gravitationally unstable and extended to form the northeast-trending Macuspana and Comalcalco rift systems in the breakaway zones of the passive margin foldbelt (Pindell and Miranda, 2011). These extensional systems detach on listric normal faults that overlie the allochthonous salt. The Macuspana rift opened during the late Middle Miocene, and the Comalcalco rift opened in Pliocene, and both contributed to the fold and thrust structures within the downdip compressional domain.

My sequential restoration of the listric normal faults in the Comalcalco rift reveals that an approximately 20.5 km of extension in the basinward direction has occurred from the Pliocene to the Present age to give an average rate of displacement of 3.84 mm/yr (Fig. 3.15). To balance the total extension in the updip domain from both of these rifts, the linked downdip shortening in the passive margin foldbelt would propagate in the downdip deepwater area of the basin as documented in other well-studied passive margin foldbelts including the Perdido (Trudgill et al., 1999), Mississippi (Rowan et al., 2000), Mexican Ridges (Yarbuh and Contreras, 2017; Kenning and Mann, 2020a), and Lamu foldbelt of offshore Kenya (Cruciani and Barchi, 2016). A sequential restoration that includes the areas of the Macuspana rift and the downdip, compressional domain of the Campeche salt basin would quantitatively resolve the deformational kinematics of the entire Campeche passive margin foldbelt, but this task would require a grid of seismic data that images both the autochthonous and allochthonous salt levels.

Analysis of reflection continuity and stratal geometry reveals the presence of growth packages in the Eocene-Oligocene likely to have resulted from passive diapirism. The seismic sections along the deepwater outer marginal trough and inboard reveal a distinct syn-kinematic growth sequence of Neogene to Recent, whose age matches the timing of the updip passive margin rifts (Figs. 3.13 and 3.14). Evidence of thicker Pleistocene mass-transport complexes in the minibasins also reflects the timing of the shortening pulse due to gravitational gliding and spreading (Figs. 3.13 and 3.14). The total updip extension and passive diapirism contributed to the development of the extensive deepwater salt-associated structures (Fig. 3.15a). Due to the propagation lag and sedimentary response to tectonism, a minor delay in compression timing in the downdip area is likely. Apango et al. (2021) conclude that the deformation timing is late Miocene in the downdip deepwater western part of the study area. Differential loading from sedimentation in the Paleogene results in minor thinning of strata adjacent to the diapirs (Fig. 3.13). Extension along salt rollers from the Yucatan carbonate platform to the northwest has been previously attributed to the widening of the outer marginal trough (Rowan, 2018; Hudec and Norton, 2019).

3.10.3 Interpretation of the basin within the framework of a passive margin foldbelt

In this study, the distinctive structural styles of the Campeche salt basin (Fig. 3.9) were compared with the structural framework of a passive margin foldbelt model as described by Rowan et al. (2004).

1) A 200-km-wide, updip area of extension includes a zone of regional listric normal faults, detaching on both allochthonous salt and autochthonous salt; some rollover structures and counter-regional normal faults have formed because of extensional deformation. The Macuspana rift formed during the late Middle Miocene, and the Comalcalco rift formed during the Pliocene and were coeval with folds and thrusts of the downdip compressional domain (Padilla y Sánchez, 2007; Pindell and Miranda, 2011).

2) A 300-km-wide downdip area of compressional deformation is characterized by salt canopies, more open salt-cored folds, salt diapirs, and break-thrusts. The allochthonous salt bodies have coalesced in the proximal part of this domain. Closely spaced upright diapirs concentrated in the outer marginal trough area are observed (Fig. 3.9); the upright diapirs are 6–8 km in relief and bound minibasins with 8–10 km of Cenozoic clastic sedimentary infill.

The downdip deepwater area of the Campeche salt basin with minor allochthonous salt shows less downdip structural variability compared to the updip area of the basin. The presence of autochthonous and allochthonous salt results in a complex polygonal array of folds, thrusts, and salt canopies with highly variable orientation within the proximal compressional domain (Fig. 3.8a). Inflection areas of basement dip in the Campeche salt basin concentrate more deformation during downdip gliding of the passive margin foldbelt (Figs. 3.13 and 3.14).

Normal faults in the salt roller province just outboard of the Yucatan carbonate platform likely formed in response to the earlier, Late Jurassic to Cretaceous episodes of gravity gliding during periods of basinward tilting of the margin as the newly formed oceanic crust cooled and subsided (Figs. 3.10 and 3.11) (Hudec and Norton, 2019; Steier and Mann, 2019).

Several observations explain the cause of the oversteepening and gravitational failure of the southern edge of the Campeche salt basin during the late Middle Miocene to Recent: 1) the northeast-southwest orientation of the downdip deepwater anticlines remain active today as the folds are bathymetrically expressed on the seafloor (Fig. 3.10); 2) 20.5 km extension in the downdip direction is observed on the listric normal faults formed during the Comalcalco extension. The extension in the Comalcalco and Macuspana rifts both contribute to the downdip compression. Late Jurassic to Cretaceous extension of the salt-roller province is relatively minor and may have been accommodated by the synchronous widening of the outer marginal trough (Fig. 3.15a); 3) Stratal geometries show growth packages in the section starting in the Eocene-Oligocene that likely resulted from passive diapirism related to sedimentary loading. Late Miocene to Recent syn-tectonic growth strata and mass-transport complexes in the downdip deepwater indicate the timing of a major deformation pulse (Figs. 3.13 and 3.14); and 4) the overall northeast-east-northeast oroclinal arcuate shape of the deepwater foldbelts indicate the dominant salt flow direction is southeast to northwest (Fig. 3.15b).

However, deformations of the Campeche salt basin differs from other similar passive margin foldbelts in several aspects: 1) the extent of the translational/neutral zone of shortening is not discernible due to multiple deformation events; 2) the basement and base salt gradient is relatively low compared to similar passive margin systems (Fig. 3.9) (Cruciani and Barchi, 2016; Evans and Jackson, 2020); 3) the presence of a 2-5 km-thick salt layer results in complex allochthonous salt structures in the central area rather than a less deformed, neutral zone as observed in passive margin foldbelts (Rowan, 2004); 4) the overall shape of the passive margin domains is arcuate due to their confinement between areas of thicker continental crust of the Yucatan block to the east and buttressing by the higher-standing and salt-free oceanic crust to the west (Fig. 3.8a); and 5) an isolated and simpler passive margin system without the above mentioned features develops in the Yucatan salt basin to the east (Hudec and Norton, 2019; Steier and Mann, 2019) (Fig. 3.7).

3.10.4 Implications for hydrocarbon prospectivity

Clusters of natural sea surface seep in the Campeche salt basin occur in two areas: 1) a sub-circular, updip extensional domain in the shallow offshore area of the southern Campeche basin (Area 1 on Fig. 3.16a); and 2) the highly elongated area overlying the thicker Jurassic sedimentary section of the outer marginal trough (Area-2 on Fig. 3.16a) (Kenning and Mann, 2020b). The seeps cluster of Area 1 corresponds with the Akal-Reforma high that includes the structurally complex Cantarell and Sihil fold-thrust structures (Mitra et al., 2005), and Plio-Pleistocene gas plays in the Comalcalco and Macuspana rifts (Ambrose et al., 2003; Shann, 2020). Gas maturity in the Comalcalco and Macuspana rifts likely results from >4 km of sedimentation in the Plio-Pleistocene (Ambrose et al., 2003).

In seep Area 2 of the outer marginal trough, the total sediment thickness reaches >15 km due to the accommodation space produced during Phase 2 Gulf of Mexico opening. Deeper burial of the source rocks has driven oil generation and expulsion in the overlying Neogene minibasins (Kenning and Mann, 2020b). The thickest concentration of salt in the outer marginal trough results in kilometer-scale salt structures (Figs. 3.10 and 3.13). Combined structural and stratigraphic traps are present along the upturned strata at the flanks of the salt diapirs (Kenning and Mann, 2020b) (Fig. 3.16c). Salt pillow structures along the inner flanks of the outer marginal trough create structural traps with four-way closures in both Mesozoic and Cenozoic sections (Fig. 3.16b). However, the late Middle Miocene to Recent passive-margin system focusing on Area 2 can also indicate likely seal failures due to active deformation indicated by the presence of natural seeps (Fig. 3.16a).

In the oceanic part of the southern GOM, anticlinal structures create Paleocene to Eocene shale-cored closures, and late Jurassic source rocks occupy the gas window as the result of thick, Cenozoic sedimentation (Apango et al., 2021) (Fig. 3.16d). Updip-salt rollers provide potential three-way fault traps above the primary salt detachment surface (Fig. 3.16e). High-amplitude reflections above salt-rollers were inferred to be Norphlet-equivalent sandstones that are producing in the US GOM and charged by overlying Oxfordian source intervals (Steier and Mann, 2019). The presence of aeolian deposits in the Campeche basin has been locally confirmed by Snedden et al. (2020) after studying the facies of Jurassic sandstone in cores from the Balam and Ek wells (Fig. 3.3). These authors conclude that the aeolian Norphlet facies of Mexico had a different source area from the better-studied Norphlet Formation of the eastern GOM and that the two Norphlet areas may not have formed a continuous aeolian dune field as proposed by Steier and Mann (2019).

Figure 3.16: a) Map showing the clustering of natural oil seeps observed at the sea surface (yellow circles) in the east-northeast-trending outer marginal trough (Area 2) and sub-circular Akal-Reforma, Macuspana, and Comalcalco areas (Area 1) illustrated in Fig. 3.15. Sources of the natural seep data include: Saunders et al. (2016), Mendelssohn et al. (2017), and Kenning and Mann (2020b); b) Example of a direct hydrocarbon indicator with high-amplitude in Cretaceous rocks within a structural closure above a salt pillow; c) Example of multiple, potential traps beneath an overhang area formed by a large salt diapir; d) Example of a direct hydrocarbon indicator with a flat spot above a four-way closure above a shale detachment, and e) Salt rollers with potential Norphlet reservoirs upturned along normal faults. Seismic data provided courtesy of Geoex MCG.

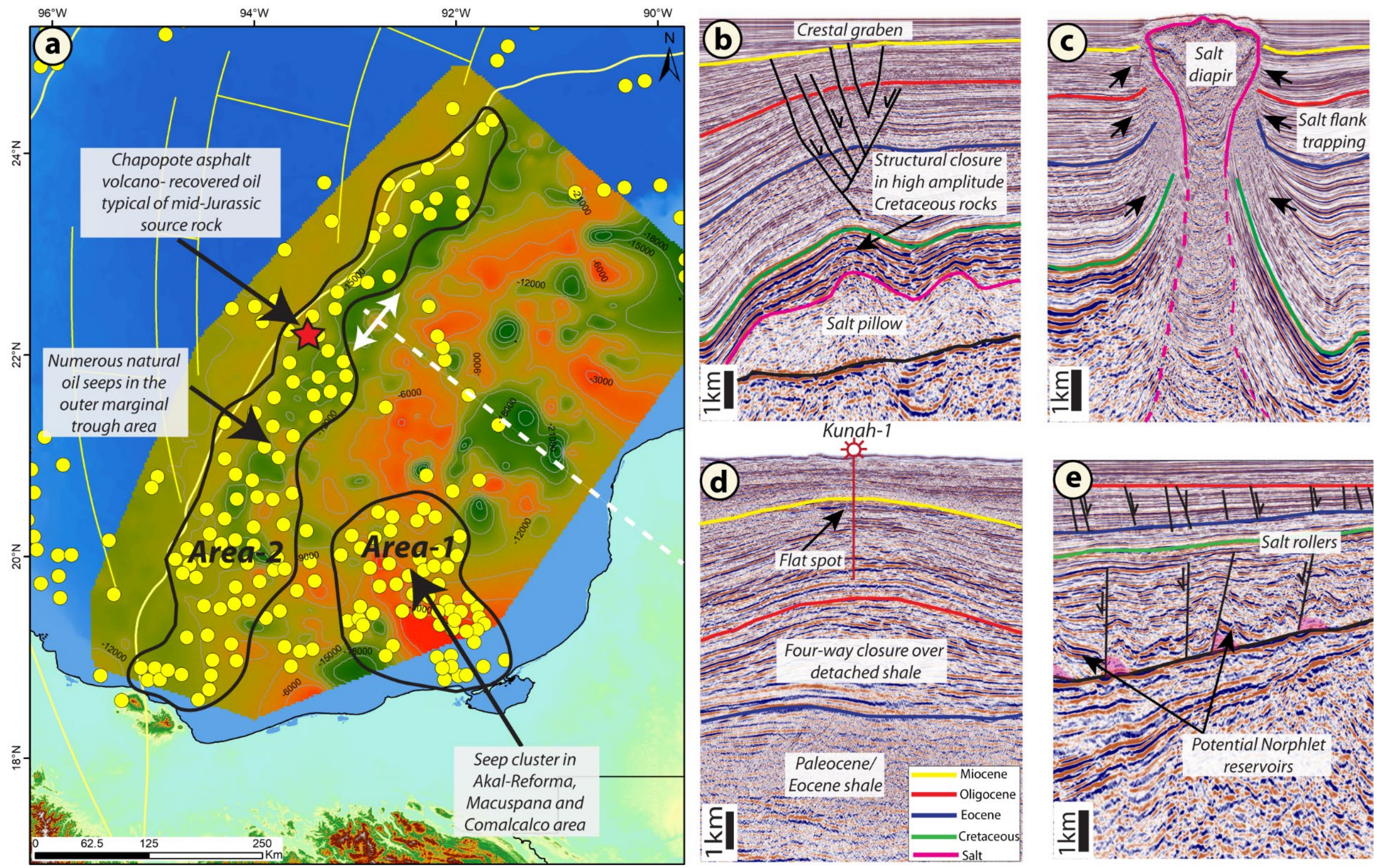

96°W
94°W
92°W
90°W
24°N
22°N
20°N
18°N
a
N
Chapopote asphalt volcano- recovered oil typical of mid-Jurassic source rock
Numerous natural oil seeps in the outer marginal trough area
Area-2
Area-1
Seep cluster in Akal-Reforma, Macuspana and Comalcalco area
0 62.5 125 250 Km
b
Crestal graben
Structural closure in high amplitude Cretaceous rocks
Salt pillow
1km
c
Salt diapir
Salt flank trapping
1km
Kunah-1
d
Flat spot
Four-way closure over detached shale
Paleocene/ Eocene shale
1km
Miocene
Oligocene
Eocene
Cretaceous
Salt
e
Salt rollers
Potential Norphlet reservoirs
1km

3.11 Conclusions

Tilt-derivative magnetic mapping was used to delineate the top of the Paleozoic basement beneath the Campeche salt basin and reveals a 40- 55-km wide and 400 km long outer marginal trough that formed during the onset of Phase 2 GOM rifting and presently localizes the thickest accumulation of Bajocian-early Callovian salt (Figs. 3.4 and 3.8). The elongated basement depression of the outer marginal trough is bounded on its western edge by a faulted basement high along the late Jurassic oceanic crust that acted as a western barrier to channel the Middle Miocene to Recent basinward salt flow and passive margin foldbelt along the north-northeast-trending outer marginal trough (Figs. 3.8 and 3.15b).

The greater salt thickness (2–5 km) in the outer marginal trough results in the present-day elongate pattern of allochthonous salt and its control on the salt-feeder systems that are inferred to underlie the outer marginal trough (Fig. 3.6a). The 2–5 km thickness of salt in the outer marginal trough results in salt-cored anticlines. In more updip areas, the structural style includes detachment folds with distinctive kink bands developed within a much thinner salt layer (Figs. 3.10, 3.13, and 3.14). Analogous structural styles of salt-rich-diapiric and salt-poor detachment fold with kink bands and break thrusts have been described from the hydrocarbon-rich Perdido passive margin foldbelt of the northwestern US GOM (Trudgill et al., 1999; Rowan et al., 2000).

The main folding phase of the Chiapanecan orogeny in the Middle Miocene oversteepened the margin forming the Akal-Reforma. Updip extension of the Macuspana and Comalcalco rifts began in the late Middle Miocene and Pliocene, respectively. During the extension, the downdip Campeche salt basin evolved as a thin-skinned, gravity-driven system that was confined over a distance of 500 km in a broad arc to the north-northeast along a 40-55 km-wide, structural low defined by the basement high along the basinward edge of the outer marginal trough and the more elevated areas of the late Jurassic oceanic crust to the west and Yucatan continental margin to the east. Late Middle Miocene initiation of the Campeche passive margin foldbelt is attributed to compression related to the Chiapanecan orogeny that previous workers have attributed to the shallow subduction of the Cocos plate along the Pacific margin of southwestern Mexico. Deformation prior to the late Middle Miocene resulted from passive diapirism, Laramide orogeny, and Chiapanecan orogeny. This confined passive margin foldbelt differs significantly in its structural style from the unconfined, downdip, gravitational salt off the Yucatan margin to the northeast that has been described by previous workers.

The confined, Campeche passive margin foldbelt consists of a downdip, compressional domain linked along a Callovian-Bajocian and Cretaceous detachment to an updip, extensional domain. The basinward translation of sedimentary rocks on the underlying salt detachment resulted from the northwestward tilting of the basin initiated during the thermal subsidence of late Jurassic oceanic crust, the crustal shortening and thickening during the Paleogene Laramide orogeny, and the middle Miocene Chiapanecan orogeny (Figs. 3.8 and 3.15a).

Structural variations of the Campeche passive margin foldbelt can be divided into: 1) a 200-km-wide, updip extensional zone of listric normal faults that detach on both allochthonous salt remobilized during the late Middle Miocene and autochthonous salt of Bajocian-early Callovian age and 2) 300-km-wide, downdip contractional zone of salt-cored folds, thrusts, autochthonous salt diapirs, allochthonous salt canopy, and detachment folds with kink bands.

The presence of natural, sea-surface oil seeps identified by previous workers in the outer marginal trough and the updip extensional domain provide evidence for a working hydrocarbon system in the basin - but also indicate likely seal failures along active faults (Fig. 3.16a). A wide variety of structural traps associated with salt diapirs, salt pillows, inverted turtle-back minibasins, and salt rollers are linked in some cases to direct hydrocarbon indicators and are described throughout the basin (Figs. 3.10 and 3.16). Improved seismic imaging will likely lead to a better definition of sub-salt and pre-salt plays.

The following chapter is based on: Hasan, M.N., Pepper, A., Mann, P., 2022. Basin-scale estimates of thermal stress and expelled petroleums from Mesozoic-Cenozoic source rocks, southern Gulf of Mexico. Marine and Petroleum Geology, n. 105995. https://doi.org/10.1016/j.marpetgeo.2022.105995

CHAPTER 4: BASIN-SCALE ESTIMATES OF THERMAL STRESS AND EXPELLED PETROLEUM FROM MESOZOIC-CENOZOIC POTENTIAL SOURCE ROCKS, SOUTHERN GULF OF MEXICO

4.1 Introduction

The deepwater southern Gulf of Mexico (GOM) includes the Yucatan and Campeche salt basins that remain two of the larger and least explored areas of the GOM basin when compared to the much better-explored Louann salt basin along the northern conjugate margin of the GOM (Hudec et al., 2013; Davison and Cunha, 2017; Hudec and Norton, 2019; Pindell et al., 2020; Kenning and Mann, 2020a) (Figs. 4.1 and 4.2). Petroleum exploration along the deepwater southern Gulf of Mexico increased after the deregulation and opening of exploration block acquisition to international oil companies in 2015 (Yúnez and Chapa, 2017). At the end of 2021, less than fifteen (15) deepwater wells were drilled by international companies in water depths >500 m (Shann, 2020). With so few wells, the geological history and petroleum prospectivity of the southern GOM in Mexican waters remain far less understood than the deepwater areas of its US conjugate margin (Weimer et al., 2017; Snedden and Galloway, 2019).

The regional distribution and maturity of prolific, Upper Jurassic to lowermost Cretaceous-age source rocks is a crucial element for the petroleum productivity of the GOM (Weimer et al., 2017). Previous papers on the maturity modeling of source rocks in the southern GOM have focused on local areas of the Mexican margins of the southern GOM (Arzate et al., 2009a, b; Santamaria-Orozco, 2000; Kenning and Mann, 2020b; Apango et al., 2021).

To better understand the petroleum expulsion potential in the Campeche and Yucatan salt basin, I present: 1) basin-wide and map-based thermal stress modeling of the four potential source

Figure 4.1: Tectonic map of the southern Gulf of Mexico highlighting the Campeche salt basin, Yucatan salt basin, the limit of oceanic crust (LOC), extinct late Jurassic spreading ridges and fracture zones, outer marginal trough (OMT), and major sedimentary basins. Structural and tectonic elements are compiled from Witt et al. (2012a); Comissión Nacional de Hidrocarburos (2015); Nguyen and Mann (2015); Fitz-Díaz et al. (2018); Kenning and Mann (2020b); and Hasan and Mann (2021). The white rectangle shows the limit of Figure 4.2.

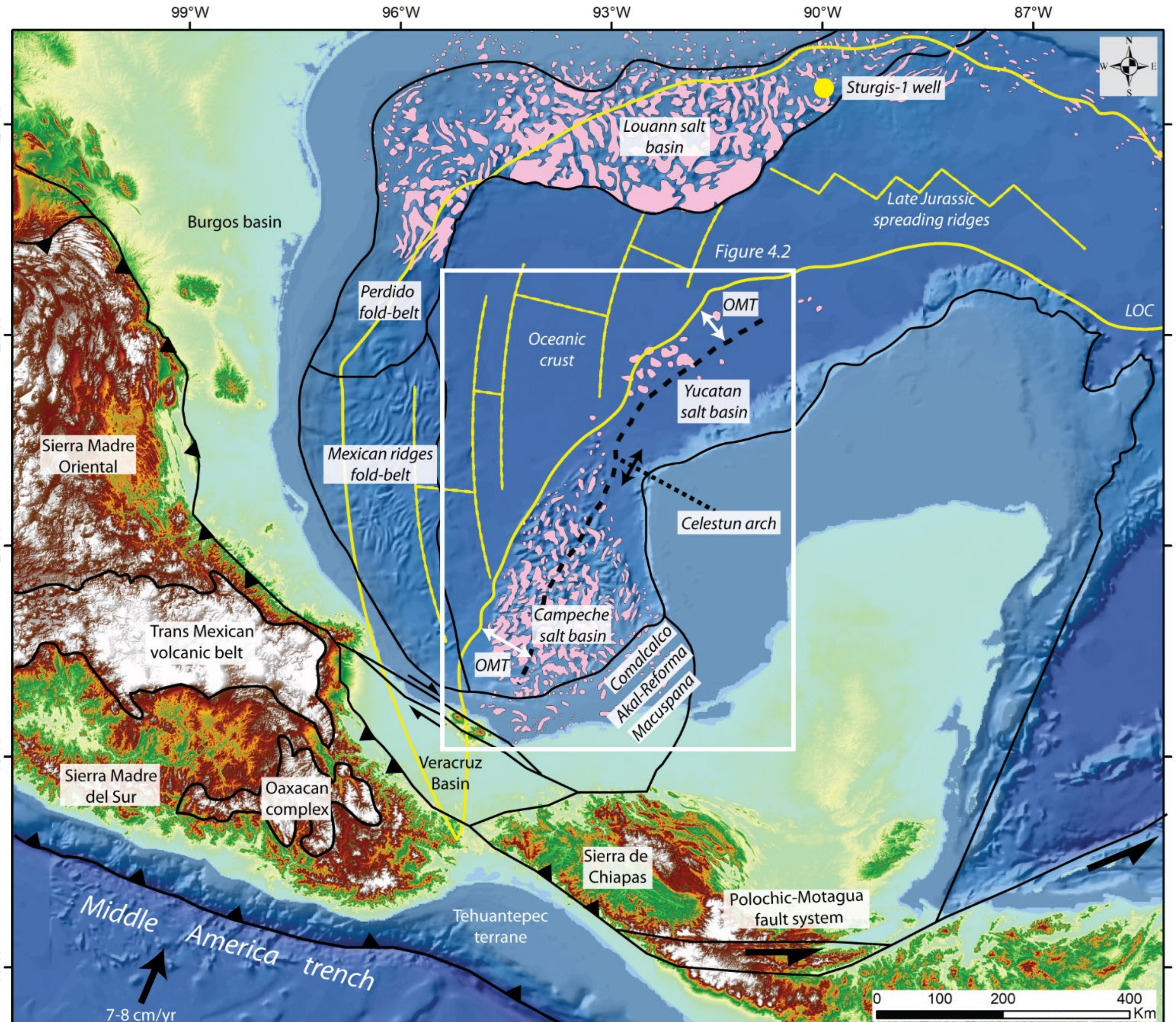

99°W
96°W
93°W
90°W
87°W
27°N
24°N
21°N
18°N
15°N
Sturgis-1 well
Louann salt basin
Late Jurassic spreading ridges
Burgos basin
Figure 4.2
Perdido fold-belt
OMT
LOC
Oceanic crust
Yucatan salt basin
Sierra Madre Oriental
Mexican ridges fold-belt
Celestun arch
Campeche salt basin
Trans Mexican volcanic belt
OMT
Comalcalco
Akal-Reforma
Macuspana
Veracruz Basin
Sierra Madre del Sur
Oaxacan complex
Sierra de Chiapas
Polochic-Motagua fault system
Middle America trench
Tehuantepec terrane
7-8 cm/yr
0 100 200 400 Km

intervals (Oxfordian, Tithonian-centered, Cenomanian-Turonian, lower Miocene); 2) sensitivity analysis of the thermal stress modeling scenarios; and 3) estimated expelled petroleum yields from Oxfordian and Tithonian-centered source intervals identified in previous studies (Santamaria-Orozco, 2000; Arzate et al., 2009a, b; Kenning and Mann, 2020b; Apango et al., 2021).

4.2 Geologic setting of the Campeche and Yucatan salt basins

The GOM basin evolved during a two-phase opening that included an initial, northwest-to-southeast rifting phase during the Triassic-middle Jurassic and a second phase of north-to-south oceanic spreading during the late Jurassic (Marton and Buffler, 1999; Pindell and Kennan, 2009; Hudec et al., 2013; Eddy et al., 2014; Nguyen and Mann, 2015). Following Phase 1 rifting (~210-163 Ma), seawater filled the broad sag basin that overlay the extinct, Phase 1 rifts during the Bajocian-early Callovian. Repeated periods of seawater evaporation formed the massive salt deposit within a single salt basin (Nguyen and Mann, 2015; Steier and Mann, 2019; Pindell et al., 2020).

The progressive, counterclockwise rotation of the Yucatan continental block formed an area of late Jurassic, post-salt oceanic crust in the deep, central part of the GOM. This area of late Jurassic oceanic crust separated the southern Campeche-Yucatan salt basin in the Mexican Gulf of Mexico from the Louann salt basin in the US northern Gulf of Mexico (Fig. 4.1).

During the earliest part of the late Jurassic and prior to the onset of seafloor spreading, the second north-south rifting phase is recorded by an elongate, rift that formed across the central GOM. This "outer marginal trough" is found bounding both the northern and southern margins of the GOM in the Campeche-Yucatan salt basin (Hasan and Mann, 2021; Rowan, 2022; Mann, 2022).

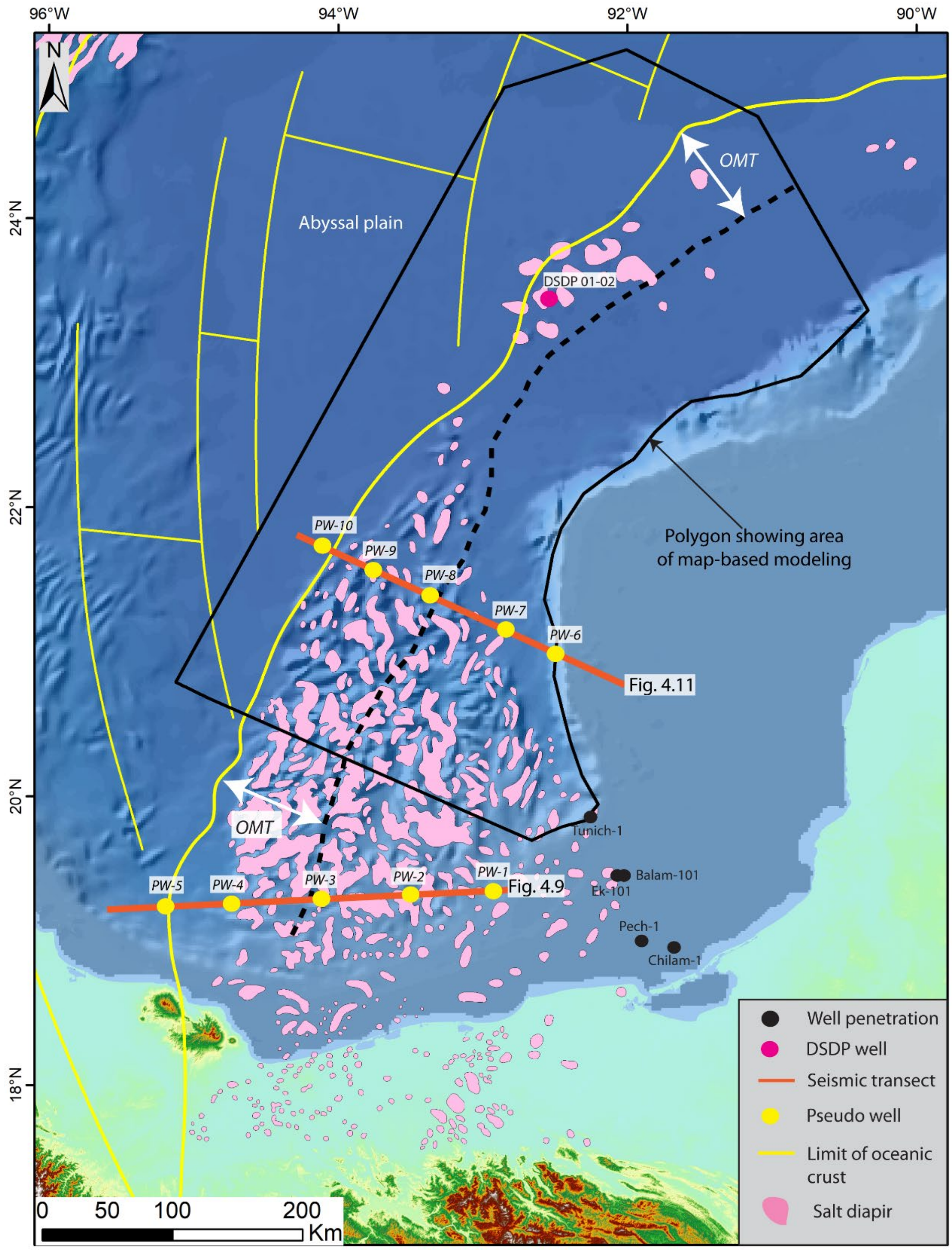

Figure 4.2: Bathymetric map of the Campeche salt basin showing the distribution of Jurassic salt diapirs from Kenning and Mann (2020b), location of the wells used for temperature calibration, location of the pseudo-wells, and the cross-sections (Figs. 4.9 and 4.11) shown in this chapter. The black polygon shows the area of three-dimensional maturity modeling. Seismic data was provided courtesy of Geoex MCG.

In the Campeche and Yucatan salt basin, a northwestward tilt of the entire southern margin of the GOM basin was produced by thermal subsidence of the oceanic crust and characterized the late Jurassic to Cenozoic history of the northern and southern passive margins (Rivera et al., 2011; Steier and Mann, 2019). This gradual and thermally-driven tilting caused downslope and northward sliding along the Jurassic salt horizon of the Yucatan continental block (Hudec and Norton, 2019; Steier and Mann, 2019; Kenning and Mann, 2020b).

The middle Miocene Chiapanecan orogeny was initiated by the shallow subduction of the Cocos plate along the Pacific margin of Mexico (Villagomez et al., 2022). This orogenic event oversteepened the margins of the southwestern Gulf of Mexico and produced updip extension along the northeast-trending Macuspana and Comalcalco rift systems and downdip compression in deeper water areas (Pindell and Miranda, 2011; Hasan and Mann, 2021; Hasan and Mann, 2022; Villagomez et al., 2022).

4.3 Methodology and input parameters

4.3.1 Subsurface dataset used in this study

This study uses a 23,612 km grid of 2D, pre-stack depth migrated (PSDM) seismic reflection data covering approximately 260,000 km^2 along the Campeche and Yucatan margin. These data were kindly provided by Geoex MCG for my use in this study and were also used as part of a previously published mapping study (Hasan et al., 2021).

The 2D seismic reflection grid has a line spacing of 10 km in the Campeche salt basin and 40 km in the Yucatan salt basin. The dataset has long offsets (12 km) and record lengths (14 seconds). The seismic dataset spans the shelf, slope, and basinal areas that range in water depth between -500 m to -3,800 m across the deepwater study area. I also used high-resolution shipborne gravity data from the same survey and its tilt derivative to define the limit of the late Jurassic oceanic crust, which is one of the primary inputs in my basin modeling.

4.3.2 Stratigraphy and seismic facies

Because of a paucity of access to industry wells, this study relies on seismic-facies based horizon interpretation (Fig. 4.3). I integrated age and lithology information from Pemex (2009-2019), Hernández (2013) and interpreted seismic lines from published literature (Padilla y Sánchez, 2007; Gómez-Cabrera and Jackson, 2009; Comissión Nacional de Hidrocarburos, 2015; Hudec and Norton, 2019, Steier and Mann, 2019; Kenning and Mann, 2020b).

The top and base of the salt were identified by high-amplitude peaks that bound a zone of remobilized salt characterized by chaotic reflectors (Fig. 4.3) (Hudec and Norton, 2019). The uppermost Jurassic and Cretaceous are characterized by their high-amplitude reflection character in a peak-trough-peak configuration that has been recognized across the southwestern GOM (Kenning and Mann, 2020b). Although age constraints for the Paleogene sequence are approximate, the late Miocene angular unconformity related to Chiapanecan orogeny can also be mapped throughout the study area (Hasan and Mann, 2021).

The integrated 1D and map-based thermal models are based on estimated ages of horizons interpreted using the regional grid of seismic dataset. The average lithological proportion of the mapped intervals was simplified to avoid introducing complexity in the models in the absence of well control (Fig. 4.3). Default values for the basin modeling software (Genesis and Trinity) were used for thermal conductivity and for the compaction parameters of formation lithologies.

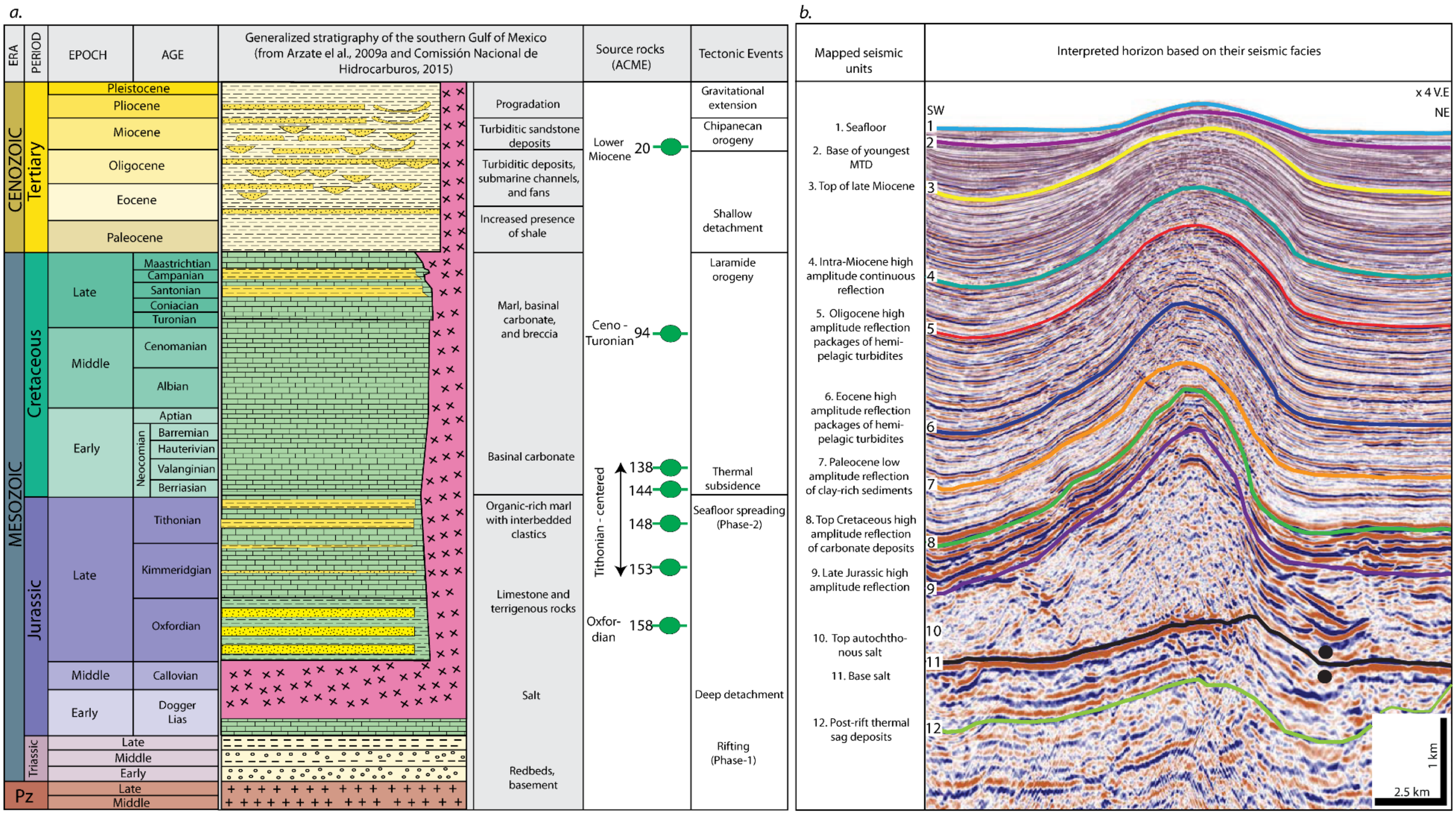

Figure 4.3: a) Generalized stratigraphic column summarizing the lithologies and known source intervals with their acme ages in millions of years for the southern Gulf of Mexico. Tectonic events are compiled from Arzate et al. (2009a); and Comisión Nacional de Hidrocarburos (2015). b) Seismic to stratigraphic age correlation that was used in this study for mapping major horizons. Age assignment for this less-drilled area was estimated based on interpreted seismic lines from Comisión Nacional de Hidrocarburos (2015); Hudec and Norton (2019); Steier and Mann (2019); and Kenning and Mann (2020b). Seismic data were provided courtesy of Geoex MCG.

4.3.3 Lithospheric and crustal structure of the Gulf of Mexico

The tilt derivative map of the gravity data was used as an edge detector of lateral crustal changes (Ibraheem et al., 2019) to define major geologic boundaries in the study area. The tilt derivative map reveals the limit of the oceanic crust (LOC), Campeche escarpment, Chiapas foldbelt, and extinct spreading ridges and fracture zones in late Jurassic oceanic crust in the central GOM (Fig. 4.4a). A pronounced, regional lineament marks the limit of oceanic crust and its abrupt east-west change in thickness with the adjacent continental crust. Smaller gravity anomalies within the deepwater Campeche and Yucatan salt basins are inferred to be salt bodies (Fig. 4.4a).

The crustal thickness map of the study area is derived from gravity inversion that is constrained by previous seismic refraction studies (Liu, 2021). The thickness of the crust varies from 6 km to 40 km (Fig. 4.4b). Three distinct crustal domains can be identified from this crustal thickness map: 1) oceanic crust in central GOM, the boundary of which was defined from the tilt derivative map (Fig. 4.4a), has a crustal thickness of ~8 km; 2) thinned transitional crust in the landward direction shows an increased crustal thickness to 10-25 km; and 3) relatively less deformed continental crust is observed beneath the Yucatan carbonate platform with a thickness of 20-36 km (Fig. 4.4b).

Depth to the base lithosphere map shows a constant depth of 85 km beneath the oceanic crust that increases in a linear manner in the landward direction with the thickness of the continental crust (Fig. 4.4c). The map was taken from a GOM-wide proprietary study of This !s Petroleum Systems LLC that iteratively fits temperature data of several wells to derive the base lithosphere depth and keeps other known parameters constant (personal communication, This !s Petroleum Systems LLC; Pepper et al., 2021).

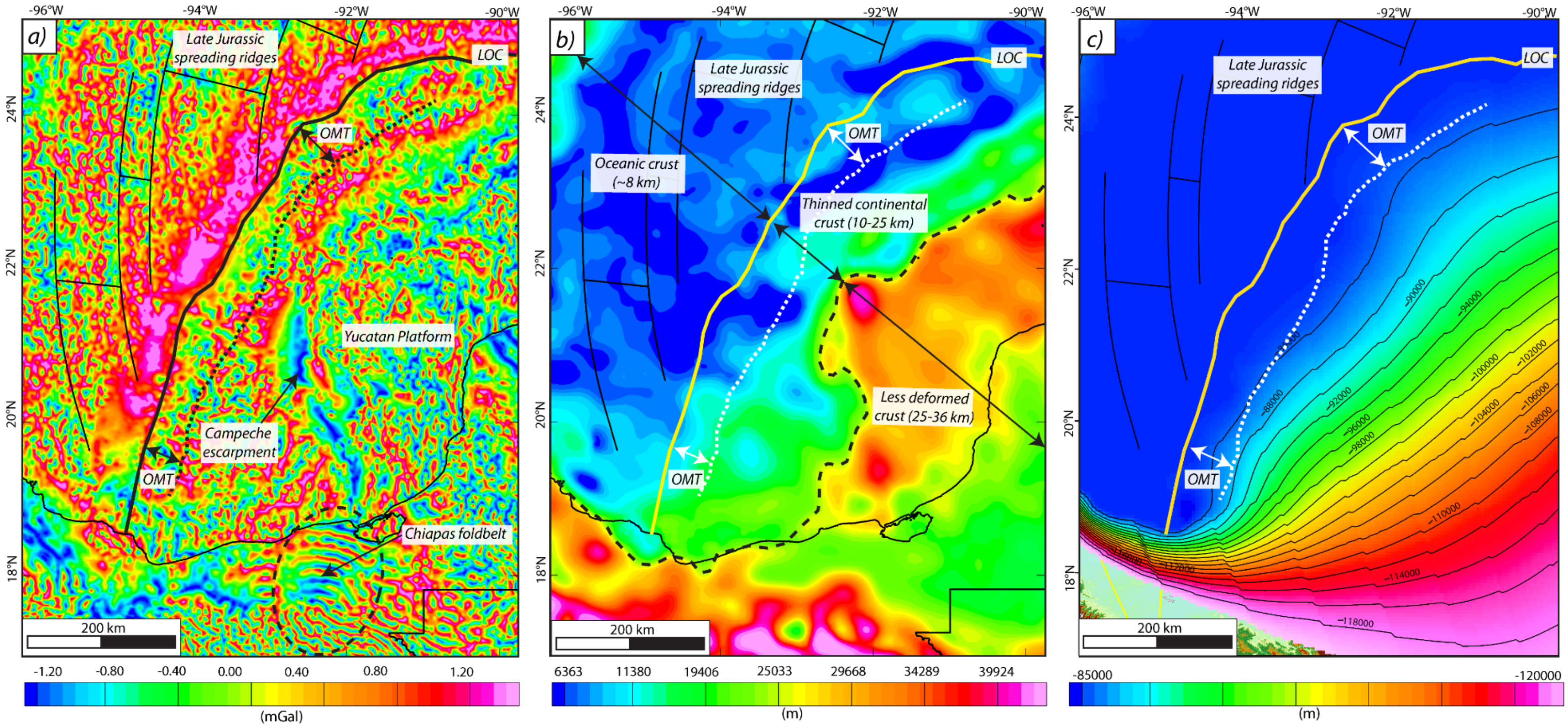

Figure 4.4: a) Tilt derivative map of Bouguer gravity showing the location of the limit of oceanic crust (shipborne gravity data was provided courtesy of Geoex MCG.). The boundary between the two types of crust is identified by the sharp change in gravity signal that reflects the density variations between the two types of crust. b) Crustal thickness map of the southern Gulf of Mexico derived from 3D gravity structural inversion (from Liu 2021). c) Map of the base lithosphere defined by the 1330 °C isotherm (Turcotte and Schubert 2002) that was used as a boundary condition for the thermal modeling. OMT is the outer marginal trough that borders the late Jurassic oceanic crust.

4.3.4 Source rocks of the conjugate margins of the GOM

The Tithonian-centered source rocks are considered as the primary source of petroleum in the deepwater southern GOM, with the Oxfordian as a secondary source (Arzate et al., 2009a, b). Using 86-rock samples from 28 cores in 13 wells from the Cantarell oil field, Santamaria-Orozco (2000) was able to identify the Tithonian (gross thickness of 200 m) and Oxfordian (gross thickness of 100 m) source intervals. The Ceno-Turonian interval is interpreted to be present by some authors but mostly in the onshore part of the Gulf of Mexico (Teerman et al., 2010; Weimer et al., 2017).

Using oil geochemical studies from the southern Gulf of Mexico that were mainly sulfur vs. API gravity (Guzman-Vega and Mello, 1999; Santamaria-Orozco, 2000), I was able to identify four oil families and their organofacies (Pepper and Corvi, 1995). Oil families-1, 2, and 3 follow a trend of high sulfur in heavy oils that decreases with lighter API and originate from clay-poor organofacies-A source rocks (Fig. 4.5). The Jurassic and Cretaceous source rocks that generate oil families 1, 2, and 3 are associated with marine, clay-poor and carbonate depositional environments.

A poorly defined source interval of lower Miocene age is present in the Comalcalco and Macuspana extensional fault systems and depocenters (Guzman-Vega and Mello, 1999), where up to 4 km of clastic sediment was deposited since the Miocene (Hasan and Mann, 2021). Oil family-4 of proposed lower Miocene origin shows low sulfur incorporation indicating a clay-rich organofacies-B source rock (Fig. 4.5). The lower Miocene source rocks generating these oils were deposited in a marine siliciclastic setting.

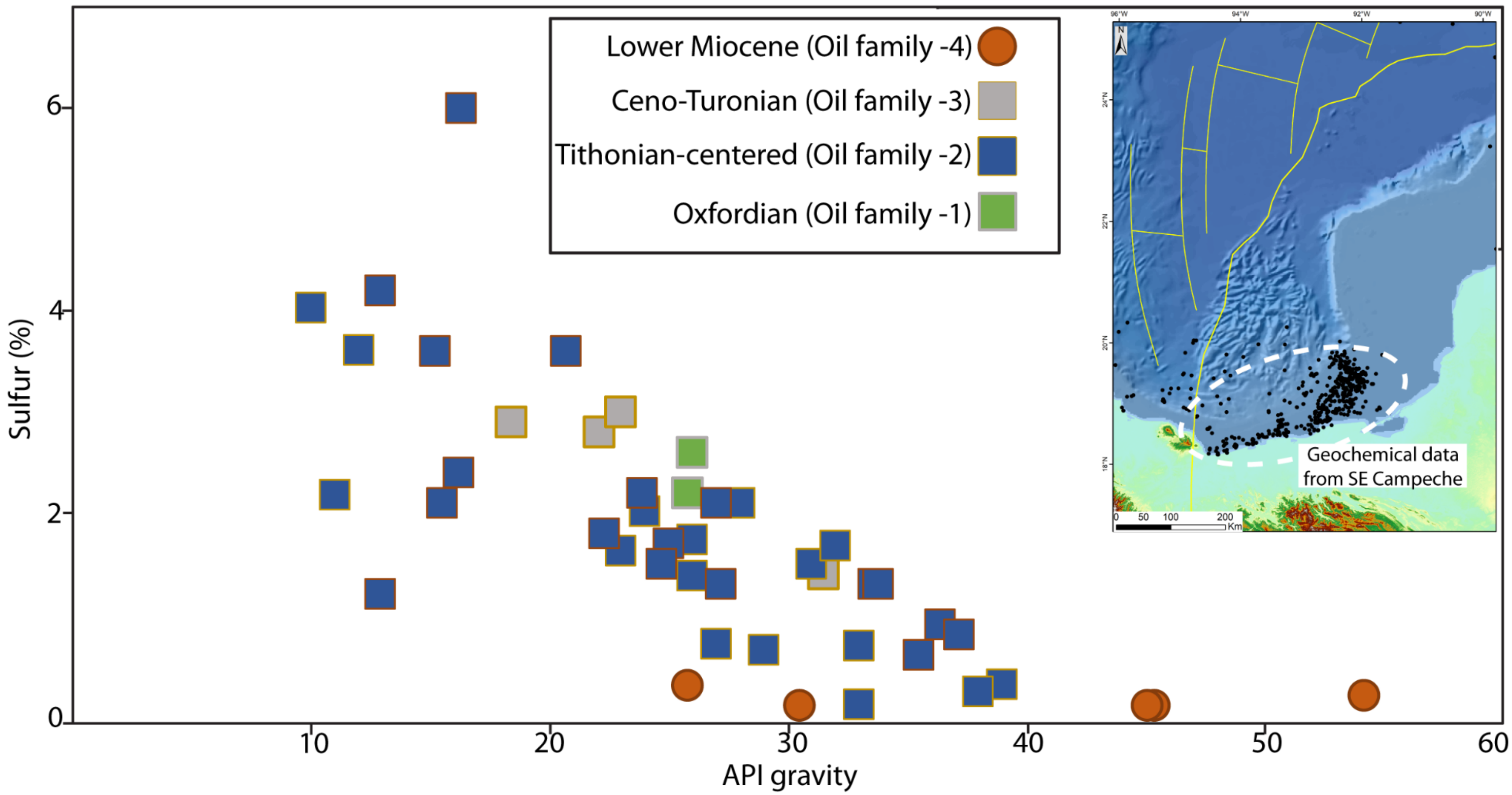

Figure 4.5: Correlation between sulfur content and API gravity of oil samples in the southern Gulf of Mexico (data collected from Guzman-Vega and Mello 1999; Santamaria-Orozco, 2000). Oil families-1, 2, and 3 show an initial high sulfur-API gradient: sulfur is high in low maturity heavy oils fluids. It decreases with lighter oils generated from clay-poor, organofacies-A source rocks (Pepper and Corvi, 1995). Oil family-4 of lower Miocene age shows low sulfur incorporation at all levels of API that is typical of clay-rich organofacies-B source rocks (Pepper and Corvi, 1995).

For these intervals, source rock facies may not necessarily be present uniformly across the entire basin, especially where lateral facies variations are observed (Arzate et al., 2009a). The Oxfordian - and especially the Tithonian-centered source rocks - are generally assumed to be widespread across the deepwater southern Gulf of Mexico. However, the late Jurassic separation of the Louann salt body in the northern US GOM and its conjugate Campeche-Yucatan salt body in the southern Mexican GOM progressively reduces their thickness and eventually leads to non-deposition of these five acmes, with the older acmes absent over a wider area (Pepper and Pindell, 2017). Only the Valanginian and younger acmes are predicted to cover the entire area of the late Jurassic oceanic crust.

Using a basin-wide framework of biostratigraphically correlated organofacies depositional acmes (where the acme age is expressed in Ma), eight (8) candidate source rocks in the southern Gulf of Mexico include the following acmes: 1) A158 (late Oxfordian); 2) A153 (Kimmeridgian); 3) A148 (Tithonian); 4) A144 (Berriasian/Portlandian); 5) A138 (Valanginian), 6) A95 (Cenomanian), 7) A93 (Turonian), and 8) A20 (lower Miocene) (Pepper et al., 2020).

As the difference in depth and modeled thermal stress between individual acmes is small, I amalgamated acmes into groups to keep the modeling relatively simple. I model four (4) mid-point chronostratigraphic surfaces to estimate the thermal stress in my study area: 1) Oxfordian - 158 Ma; 2) Tithonian-centered - 145.5 Ma (average age of Acmes 153, 148, 144, 138); 3) Ceno-Turonian - 94 Ma (average age of Acmes 95, 93); and 4) lower Miocene (20 Ma).

4.3.5 Temperature calibration and boundary conditions

Kerogen maturation and other kinetic organic geochemical reactions are driven by a time-temperature integral. Throughout this paper, I use the concept ‘Thermal stress’ to describe this.

Thermal stress is the standard temperature (T_2), which a source rock must attain at a standardized heating rate of 2 °C/Myr in order to achieve approximately the same extent of kerogen degradation as when heated to temperature Tx at rate a_x in a sedimentary basin (equation 1). Conversion of the real basin temperature Tx at heating rate a_x to the standard temperature (or thermal stress) supports the comparison of the consequences of the thermal exposure of rocks across geological ages and basin settings. The procedure of correcting Tx to the standard temperature (T_2) follows from Pepper and Corvi (1995).

$$T_2 = Tx - 15°C.\log10\ (a_x/(2\ °C/Myr)) \ldots\ldots..(1)$$

The Genesis and Trinity modeling packages from Zetaware, Inc. were used to model source rock thermal stress in the study area. Initially, three calibration wells (Chilam-1, Pech-1, and Tunich-1) with known lithologies (Arzate 2009a, b) and crustal thickness (Fig. 4.4b) were used to estimate the radiogenic heat production per unit area of crust in the study area (Fig. 4.6). I created an additional temperature dataset with an 8% uplift (Waples, 2004) because Arzate (2009a, b) did not specify whether their data were corrected for the cooling effect of drilling mud.

I applied a lower boundary condition with a fixed temperature of 1330 °C at the base lithosphere (Fig. 4.4c) (Turcotte and Schubert 2002) and ran the model in transient mode to allow for the effects of rapid sedimentation. Radiogenic heat production (RHP) from the oceanic crust is assumed to be zero (Allen and Allen, 2013) and the RHP of the crust thickness at each calibration well location (0.6 microW/m^3 at Tunich-1, 0.65 microW/m^3 at Pech-1, and 0.57 microW/m^3 at Chilam-1) was inverted by matching the temperature data. I then used the calibrated average RHP (0.6 microW/m^3) from these three calibration wells to model ten pseudo-well locations along two cross-sections representing the structural variation of the basin. The locations of the ten (10) pseudo-wells are shown in Figure 4.2.

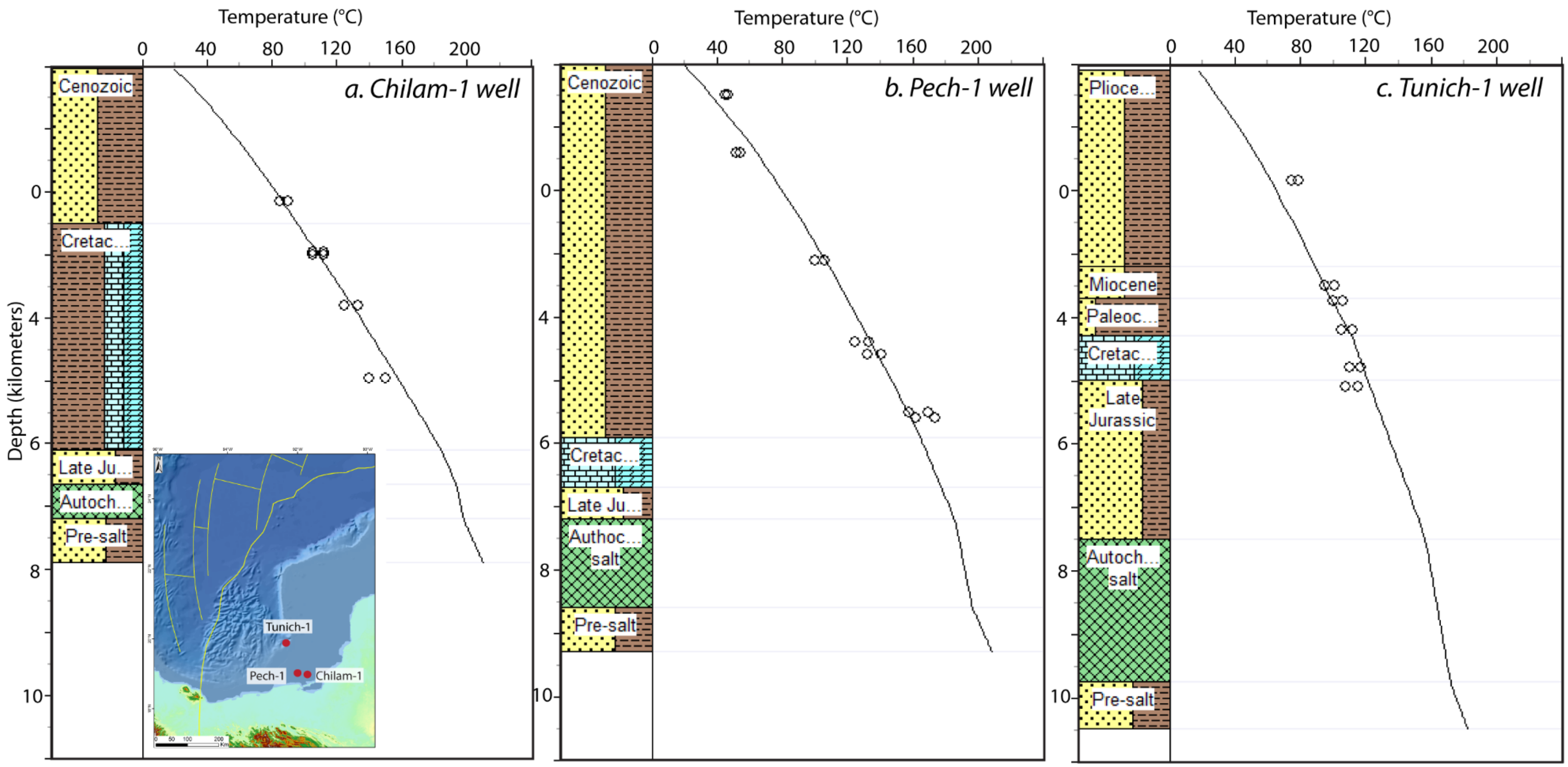

Figure 4.6: a) Temperature-depth graphs showing measured and modeled geothermal gradients of a) Chilam-1 well, b) Pech-1 well, and c) Tunich-1 well. The geothermal gradient is relatively higher in Chilam-1 compared to Pech-1 and Tunich-1. The measured temperatures are extracted from Arzate (2009a, b), who did not document whether these temperatures were corrected for the cooling effect of drilling mud

A compilation of sediment surface temperature vs. water depth from the entire Gulf of Mexico reveals a polynomial relationship used in the modeling (equation 2) (Fig. 4.7a). Water depths greater than 1300 m show a constant surface temperature of 4.3 °C. Nagihara et al. (1996) also reported an average seafloor temperature of 4 °C in the deepwater area of the northern Gulf of Mexico.

I estimated the paleo-water depths at calibration and pseudo-well locations and extrapolated the present-day water depth back through time by flattening the tectonic subsidence curve derived from 1D Genesis models for the last 70 Ma. Paleo-seafloor temperatures were then predicted through time according to paleo-bathymetry.

$$\text{Seafloor temperature, } Y = -1.7651\text{E-}09X^3 + 1.4098\text{E-}05X^2 - 2.7452\text{E-}02X + 2.0000\text{E+}01 \quad \ldots\ldots\ldots(2)$$

Where, X = water depth in m

The Trinity basin modeling package (Zetaware Inc.) was used for the map-based modeling of the study area delimited by the polygon on the map in Figure 4.2. I restricted my modeling to the northern two-thirds of the study area as the presence of thick autochthonous and allochthonous salt limits the ability to map deeper structures in the southern Campeche salt using 2D seismic data (Kenning and Mann, 2020b; Hasan and Mann, 2021).

Regionally-mapped structural surfaces and their associated isopach maps were imported in the Trinity software (Fig. 4.8). From the interpreted horizons, source rock depths were calculated for previously discussed interval average ages (Oxfordian – 158 Ma, Tithonian-centered – 145.5 Ma, Ceno-Turonian – 94 Ma, and lower Miocene – 20 Ma).

To extrapolate 1D models through empirical relationships to map-based model, a temperature curve was fitted to a pseudo-well with no salt and no radiogenic heat (PW #5) and was then applied to the four source rock surfaces as a base case. At this stage, the resulting models do not incorporate the effect of any transient event and lateral variation of heat flow controlling parameters, which is introduced next in my workflow.

I derived temperature reference curves (at PW #5) and then made associated scalar maps for three key geologic controls: 1) transient effect of high Pliocene to Recent sedimentation (equation 3, Fig. 4.7b); 2) radiogenic heat generation from the varying thickness of continental crust (equation 4, Fig. 4.7c); and 3) temperature anomaly due to high conductivity and varying thickness of salt (equation 5).

A temperature scalar map essentially captures the lateral variation of each of these geologic controls (e.g., crust thickness, salt thickness) from the location of the reference curve (PW # 5 in this case). Each scalar map was then sequentially applied to the source rock maps to produce the temperature maps (Y2).

$Y = 1.05527 - 2.35519e^{-005X}$; X = Pliocene to Recent sediment thickness……………(3)

$Y_1 = Y \times 0.09034X^{0.0377}$; X = continental crust thickness..………..(4)

Modeled temperature, $Y_2 = Y_1 + 0.004564652X$; X = salt thickness………….(5)

The convention is that thermal stress levels required for petroleum generation and expulsion are defined as the temperature at a constant heating rate of 2 °C Ma^{-1} (Pepper and Corvi, 1995). For this reason, I corrected for the effect of the locally slower heating rate (1.44 °C Ma^{-1}) by adding a correction to the modeled temperature to derive the standard thermal stress (STS) maps of each of the four source horizons.

Heat flow associated with rifting during the Triassic and Middle Jurassic does not appear to impact maturities: the Mesozoic sediments were much too shallow to generate petroleum during this period - even at the higher, rift-related heat flows (Kenning and Mann, 2020b).

I also generated an alternative set of standard thermal stress (STS) maps based by laterally decreasing the radiogenic heat production per unit thickness of continental crust toward oceanic crust, as I recognize that the composition of the crust is unlikely to be constant everywhere and that basaltic intrusion likely increases in the greatly-extended transitional crust in the direction of oceanic crust (Fig. 4.7d). A linear scalar function was used (equation 6) instead of equation 4, to keep all other functions the same.

$Y1 = 0.7867X^{0.0522}$; X = continental crust thickness...………..(6)

Figure 4.7: a) Empirical relationship between water depth and seafloor temperature to determine present-day and paleo-seafloor temperature. b) Temperature scalar to include the transient effect of Pliocene to Recent sedimentation. c) Temperature scalar to include the radiogenic heat effect per unit thickness of continental crust. d) Alternative function to test the model of decreasing radiogenic heat toward the oceanic crust.

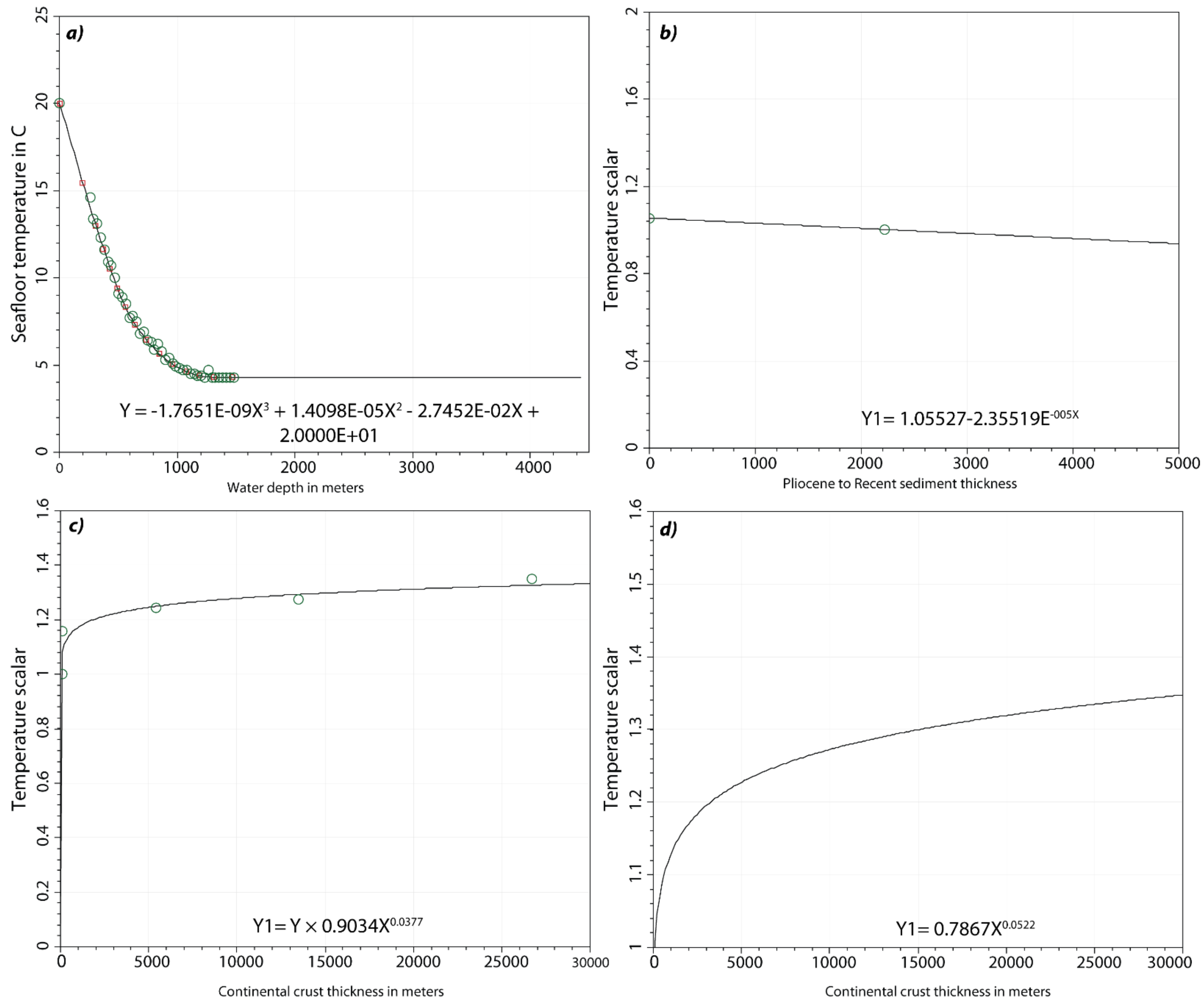
a)
Seafloor temperature in C
Water depth in meters
Y = -1.7651E-09X3 + 1.4098E-05X2 - 2.7452E-02X + 2.0000E+01
b)
Temperature scalar
Pliocene to Recent sediment thickness
Y1= 1.05527-2.35519E-005X
c)
Temperature scalar
Continental crust thickness in meters
Y1= Y × 0.9034X0.0377
d)
Temperature scalar
Continental crust thickness in meters
Y1= 0.7867X0.0522

4.4 Regional depositional trends

Regional-scale mapping of post-salt sedimentary sequences allows us to characterize the chronostratigraphic changes in depositional patterns (Fig. 4.8). The post-salt Jurassic thins towards the east, where this interval pinches out against the base of the Yucatan shelf edge (Fig. 4.8a). The isopach map shows that the post-salt Jurassic sequence is thicker (~3000 m) in the salt minibasins and is very thin above salt diapirs, indicating an earlier phase of the salt movement (Kenning and Mann, 2020b).

At a regional scale, Cretaceous and early Cenozoic can be observed thinning from west to east. Sediment thickness in these sequences reaches over 2000 m in the oceanic crust and was likely influenced by an influx of clastic sediments related to the uplift and erosion of the Late Cretaceous-Eocene Laramide orogenic belt of southern and central Mexico (Kenning and Mann, 2020b) (Figs. 4.8b and c). Middle Eocene to Oligocene depositional trends thicken toward the depositional lobe emanating from the Veracruz fan. Thicker deposits are present towards the west, where sediment thickens over 3000 m (Hasan and Mann, 2021) (Fig. 4.8d).

In the Miocene, clastic sediment deposition increased evenly with contributions from the Mississippi fan in the north, the Veracruz fan in the southwest, and fans related to the Chiapanecan orogeny to the southeast, with the Chiapanecan orogeny contributing the greatest volume of clastic sediments throughout the mapped area (Hasan and Mann; 2021; Villagomez et al., 2022) (Fig. 4.8e).

A significant shift in the depositional axis becomes apparent within the Neogene sequence, with the most abundant sedimentation occurring in the deepwater area to the northeast and thinning onto the margin towards the southwest (Fig. 4.8f).

Figure 4.8: a) Isopach thickness map for the interval from the top of salt to the top Jurassic showing the area of early salt diapir in the outer marginal trough. b) Isopach thickness map for the interval from top Jurassic to top Cretaceous unconformity showing early salt withdrawal basins in the Campeche salt basin. c) Isopach thickness map for the interval from top Cretaceous unconformity to middle Eocene showing thickening in the west related to submarine fans derived from the onshore Laramide orogeny. d) Isopach thickness map for the interval from middle Eocene to top Oligocene showing the initiation of Veracruz fan. e) Isopach thickness map for the interval from top Oligocene to top Miocene showing clastic sediment input from the Veracruz fan from southern Mexico and the Mississippi fan from the south-central USA. f) Isopach thickness map for the interval from the top Miocene to the seafloor showing thickening in the Yucatan basin that reflects increased clastic sediment input from the Veracruz and Mississippi fans.

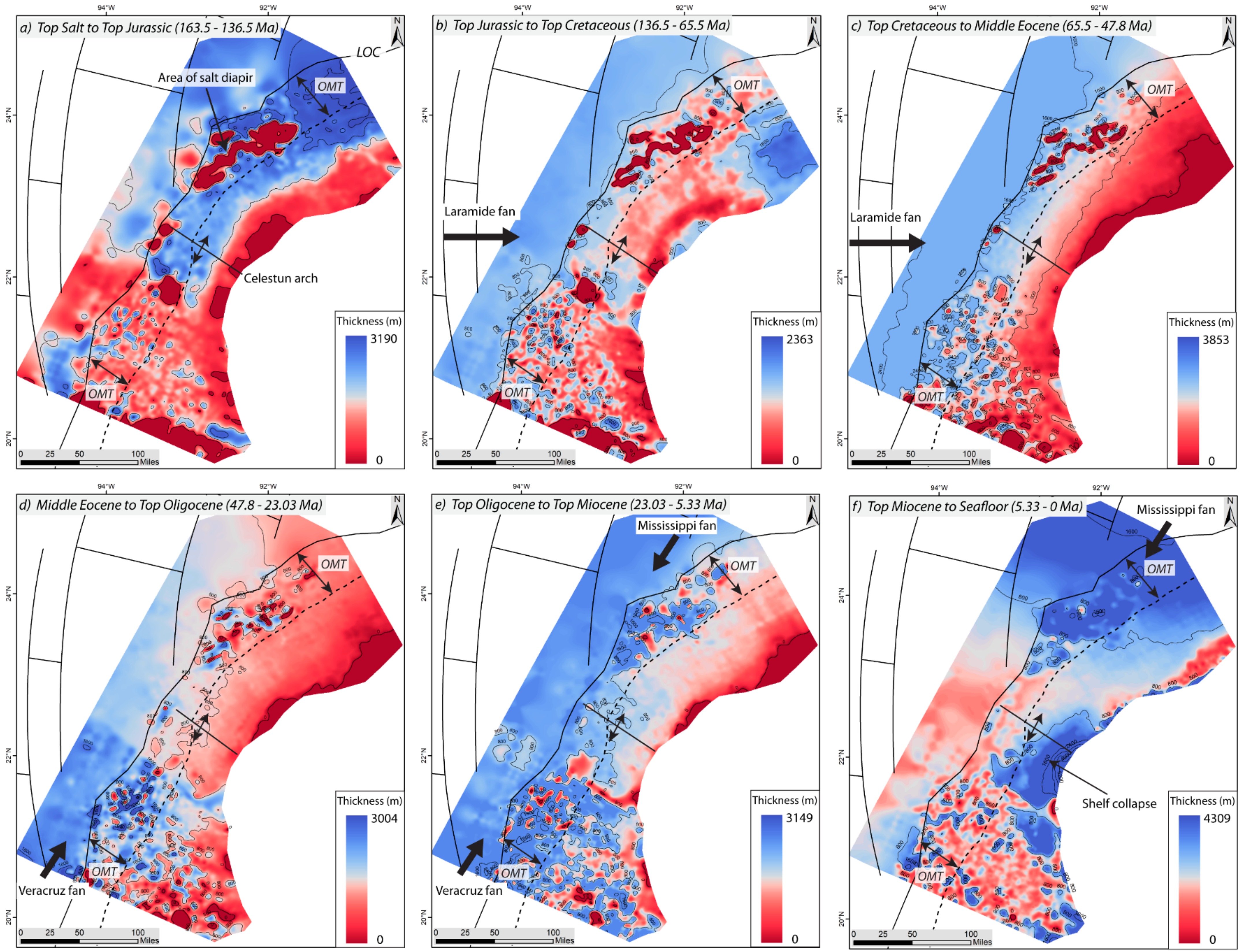

a) Top Salt to Top Jurassic (163.5 - 136.5 Ma)
LOC
Area of salt diapir
OMT
Celestun arch
OMT
Thickness (m)
3190
0
b) Top Jurassic to Top Cretaceous (136.5 - 65.5 Ma)
OMT
Laramide fan
OMT
Thickness (m)
2363
0
c) Top Cretaceous to Middle Eocene (65.5 - 47.8 Ma)
OMT
Laramide fan
OMT
Thickness (m)
3853
0
d) Middle Eocene to Top Oligocene (47.8 - 23.03 Ma)
OMT
OMT
Veracruz fan
Thickness (m)
3004
0
e) Top Oligocene to Top Miocene (23.03 - 5.33 Ma)
Mississippi fan
OMT
OMT
Veracruz fan
Thickness (m)
3149
0
f) Top Miocene to Seafloor (5.33 - 0 Ma)
Mississippi fan
OMT
Shelf collapse
OMT
Thickness (m)
4309
0
94°W
92°W
24°N
22°N
20°N
0 25 50 100 Miles

4.5 1D burial and thermal histories

4.5.1 1D modeling along southern Campeche salt basin

The regional east-west structural cross-section of the southern Campeche salt basin (line location is shown in Fig. 4.2) shows a variety of salt-related structures from the upper slope to the ocean basin (Shann, 2020) (Fig. 4.9). The continent-ocean boundary limits the extent of both allochthonous and autochthonous salt (Fig. 4.9). Contractional structures include both salt-cored anticlines and thrusted folds. Most of the structures root at the autochthonous level, although some have shallower detachment levels. Multiple deformational pulses associated with the Laramide and Chiapanecan orogenies that occurred during the Late Cretaceous through Cenozoic periods resulted in complex structures in the southern part of the Campeche salt basin (Villagomez et al., 2020) (Fig. 4.9).

I performed 1D burial and thermal history modeling on five pseudo-well locations to better understand the source rock thermal stress variation along this dip-directed cross-section. Pseudo-wells 1-4 are in the thinned continental crust, and pseudo-well 5 is in the oceanic crust (Fig. 4.9). Cenozoic clastic sedimentation during the Oligocene and Miocene are the largest contributor to the total sediment thickness.

In all pseudo-well locations along this cross-section, the primary organofacies A of the Tithonian-centered source rocks are predicted to begin oil expulsion (100 °C STS) during middle Oligocene-middle Miocene and to remain in the oil window during most of the Neogene period (Fig. 4.10).

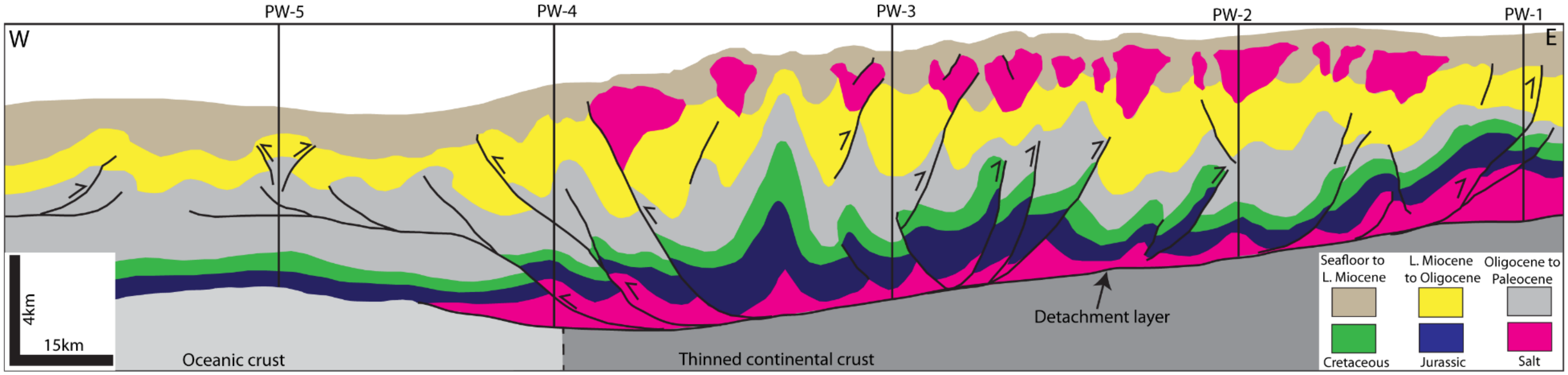

Figure 4.9: East-west regional structural cross-section of the southern Campeche salt basin (cross-section is located on the map in Fig. 4.2) showing abundant salt minibasins, normal faults, allochthonous salt bodies, and sub-canopy structures in the updip area underlain by thinned continental crust that transition downdip into thrust detachments in Paleocene-Eocene shales that are underlain by late Jurassic oceanic crust (modified from Shann, 2020). Locations of modeled pseudo-wells PW-1 through to PW-5 are shown along this cross-section.

Pseudo well-1 overlies continental crust and shows present-day thermal stress of 120 °C STS for Upper Jurassic source rocks (Fig. 4.10a). Pseudo well-2 above continental crust shows an increase in thermal stress due to thicker overburden (Fig. 4.10b). Pseudo well-3 is proximal to the outer marginal trough (OMT) and shows present-day thermal stress of 200 °C STS for Upper Jurassic source rocks (Fig. 4.10c). Pseudo well-4 in the OMT has the thickest sedimentary overburden along the transect (Fig. 4.10d).

Pseudo well-5 overlies the oceanic crust and shows decreasing thermal stress (Fig. 4.10e). The present-day maturity of these source rocks is in the gas window (>145 °C). The Ceno-Turonian source rock starts expulsion during the middle-late Miocene, and the lower Miocene source rock does not anywhere reach the threshold thermal stress temperature of ~110 °C that is required to expel hydrocarbons (Fig. 4.10).

Figure 4.10: 1D burial and thermal history modeling results of the five pseudo-wells shown in Fig. 4.9 in the southern Campeche basin. a) Pseudo well-1 in the continental crust shows present-day thermal stress of 120 °C STS for Upper Jurassic source rocks. b) Pseudo well-2 in the continental crust shows an increase in thermal stress due to thicker overburden. c) Pseudo well-3 is proximal to the outer marginal trough (OMT) and shows present-day thermal stress of 200 °C STS for Upper Jurassic source rocks. d) Pseudo well-4 is in the OMT has the thickest sedimentary overburden along the transect. e) Pseudo well-5 overlies the oceanic crust and shows decreasing thermal stress. Cenozoic sedimentation during the Oligocene and Miocene contributes most to the total sediment thickness. Paleo-water depths were calculated using present-day water depth and tectonic subsidence curves were derived using Genesis software.

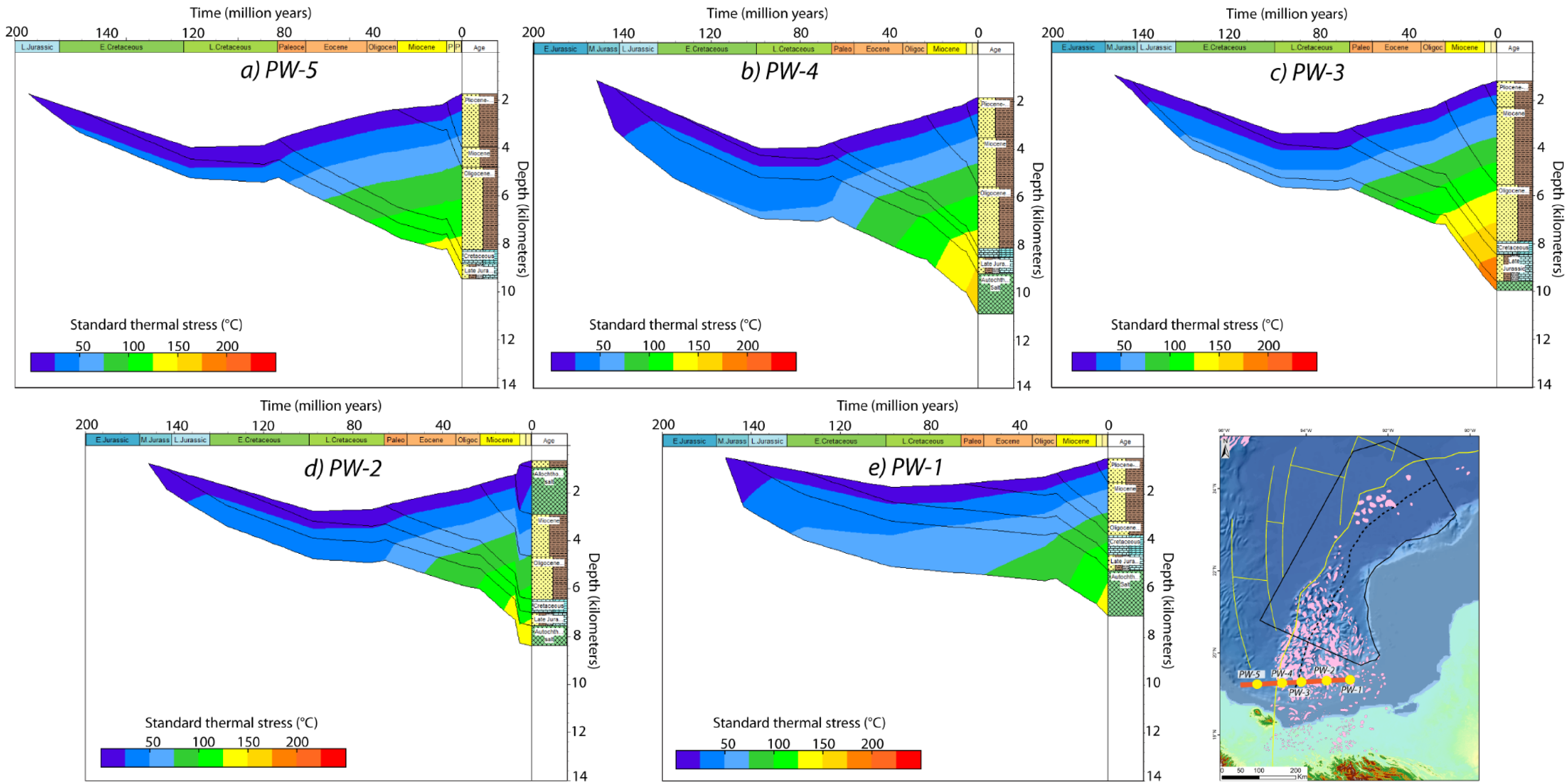

a) PW-5
b) PW-4
c) PW-3
d) PW-2
e) PW-1
Time (million years)
Depth (kilometers)
Standard thermal stress (°C)
50 100 150 200

4.5.2 1D modeling along northern Campeche salt basin

The cross-section in Figure 4.11 traverses the northern part of the Campeche salt basin and is oriented in a dip orientation across the margin of the Yucatan continental block (line location is shown in Fig. 4.2). The extent of the basin along this section is relatively narrow (~100 km) with a more steeply northwestward dipping margin, in contrast to the more gentle dips seen on the previous regional seismic section shown in Figure 4.9.

Basinward of the Yucatan carbonate platform, the base salt occurs at a depth of 6-7 km from the seafloor within the outer marginal trough (Fig. 4.11). Because salt is much thicker in the outer marginal trough, numerous large salt diapirs intrude the overlying sedimentary section and exhibit as much as 6-8 km of vertical relief. The development of salt diapirs is locally associated with minibasins that were accompanied by welding along the source salt layer and have resulted in the formation of turtle structures (Fig. 4.11). The pre-salt rift deposits and sag sequences are relatively well imaged in this part of the basin compared to the southern Campeche margin, where allochthonous salt units make seismic imaging more challenging (Fig. 4.9).

In this cross-section, pseudo-wells 6-9 overlie thinned continental crust, and pseudo-well 10 overlies oceanic crust. Total sediment thickness increases in the basinward direction (up to 11 km in pseudo well 8 and 9). Pseudo-wells 6 and 7 in the updip extensional domain have considerably thinner overburden and consequently, the primary Upper Jurassic source rocks do not reach the required thermal stress level for expulsion.

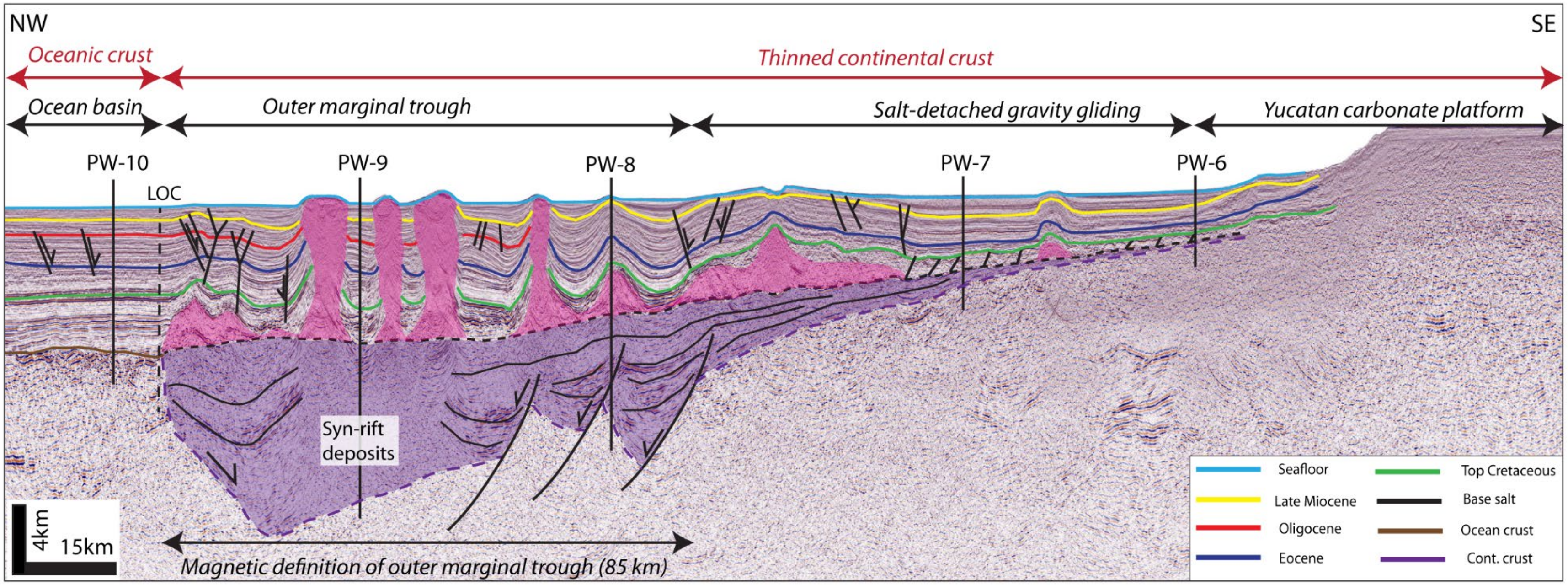

Figure 4.11: Interpreted seismic section (located on the map in Fig. 4.2) showing the updip, detached salt pillow structures, and the downdip folds and salt diapirs. The largest diapirs are concentrated above the outer marginal trough area adjacent to the oceanic crust. The 85-km-width of the outer marginal trough was defined by using magnetic data that is described in detail by Hasan and Mann (2021). Gravitational sliding on the updip salt layer is enhanced by the steeper gradient of the top basement surface in the area of the Yucatan carbonate platform. Syn-rift and post-rift sag deposits both contribute to the greater total sediment thickness in the outer marginal trough area. Modeled pseudo-well locations along this cross-section are shown. Seismic data provided courtesy of Geoex MCG.

For pseudo-wells 8 and 10, the model predicts that the primary Upper Jurassic source rocks (Oxfordian and Tithonian-centered) expel oil at 100 °C STS during the middle Oligocene and early Miocene. The present-day maturity of the Jurassic source rocks is in the gas window (>145 °C STS). Pseudo-well 9 in the outer marginal trough reaches higher thermal stress than pseudo-well 8 and 10 due to higher overburden thickness. The Ceno-Turonian source rock starts expulsion during the middle-late Miocene, and the lower Miocene source rock does not reach the required thermal stress to expel (Fig. 4.12).

Figure 4.12: 1D burial and thermal history modeling results of the five pseudo-wells shown in Fig. 4.11. a) Pseudo well-6 is adjacent to the 3-km-thick, Yucatan carbonate platform. b) Pseudo well-7 in the most distal area of rifted, continental crust shows a relative increase in thermal stress due to its thicker, sedimentary overburden. c) Pseudo well-8 is at the margin of the outer marginal trough and has the greatest sedimentary overburden (~11 km). d) Pseudo well-9 is located above the outer marginal trough and shows present-day thermal stress of 160 °C STS for Upper Jurassic source rocks. e) Pseudo well-10 in the oceanic crust shows lower present-day thermal stress than pseudo-well 8 and 9.

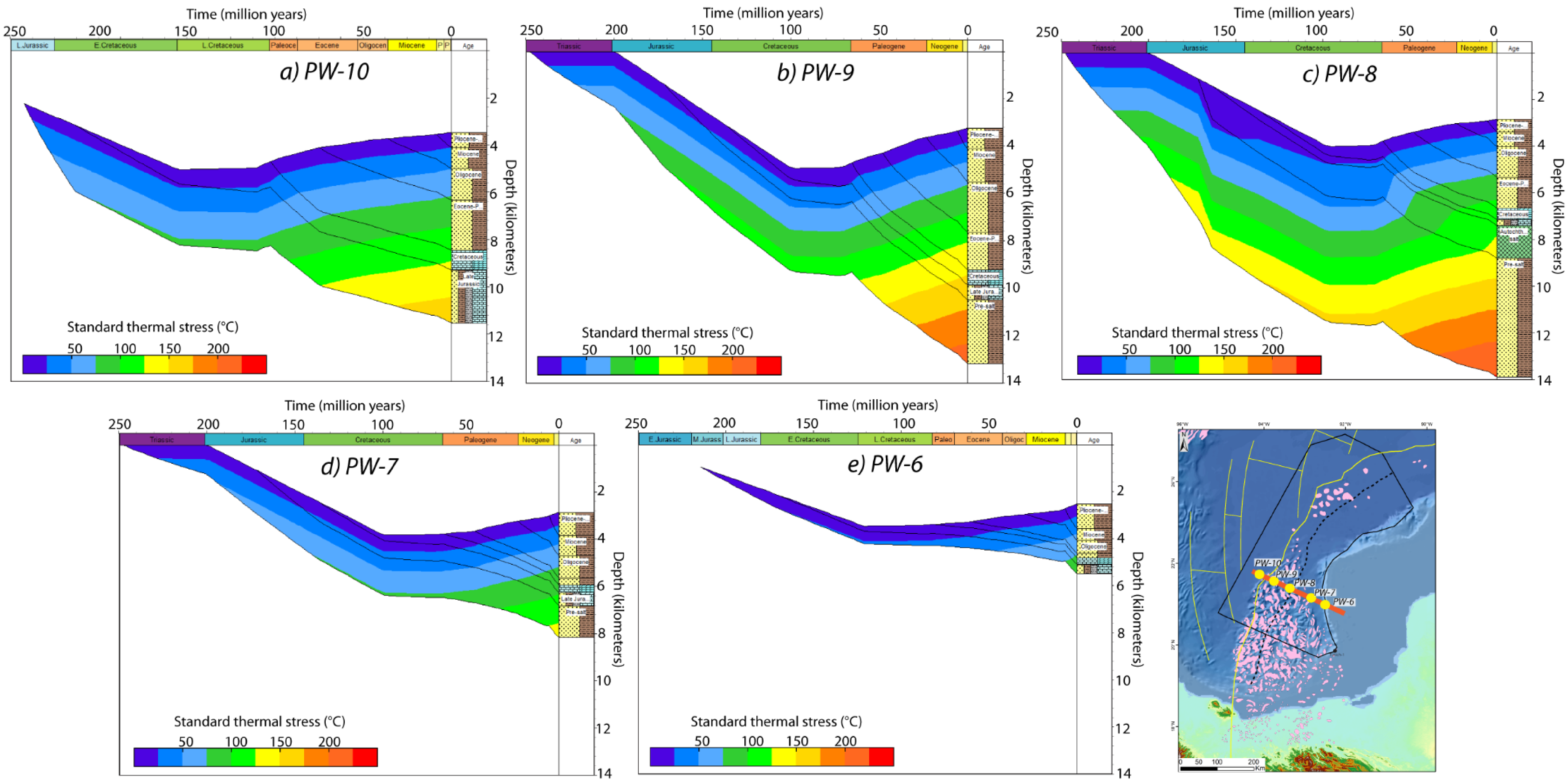
Time (million years)
a) PW-10
b) PW-9
c) PW-8
d) PW-7
e) PW-6
Depth (kilometers)
Standard thermal stress (°C)
50 100 150 200
L.Jurassic
E.Cretaceous
L.Cretaceous
Paleoce
Eocene
Oligocen
Miocene
Triassic
Jurassic
Cretaceous
Paleogene
Neogene
Age
PW-10
PW-9
PW-8
PW-7
PW-6

4.6 Map-based standard thermal stress modeling

4.6.1 Scenario-1: Constant radiogenic heat production per unit area of continental crust

In scenario-1, STS maps based on constant radiogenic heat production (RHP) per unit thickness of continental crust were created for Oxfordian, Tithonian-centered, Ceno-Turonian, and lower Miocene ages.

The Oxfordian is predicted to be within the present-day dry gas window (>165 °C STS) for the minibasins of the outer marginal trough that extend parallel to the limit of the oceanic crust (Fig. 4.13a). A similar trend of STS is observed for the Tithonian-centered (>160 °C STS) and Ceno-Turonian (>150 °C STS) source intervals where there is also a sharp change in thermal stress trend at the inner edge of the outer marginal trough (Figs. 4.13b-c). Kenning and Mann (2020b) also reported similar thermal maturity of the Yucatan salt basin.

In this part of the study area, where many salt diapirs are present, the effects of salt thermal conductivity can be observed where maturity contours are displaced by the salt bodies (Figs. 4.13a-c). Inboard of the outer marginal trough, in the mid-slope part of the basin, all three Mesozoic source intervals are in the present-day oil window (100-145 °C STS). However, towards the Yucatan carbonate platform, source rocks become immature.

In the western part of the study area, above the oceanic crust, source rocks are less mature than in the outer marginal trough due to less burial thickness and the absence of radiogenic heat contribution from the crust. Hypothetical, lower Miocene source rocks are immature (50-75 °C STS) throughout the modeled area (Fig. 4.13d).

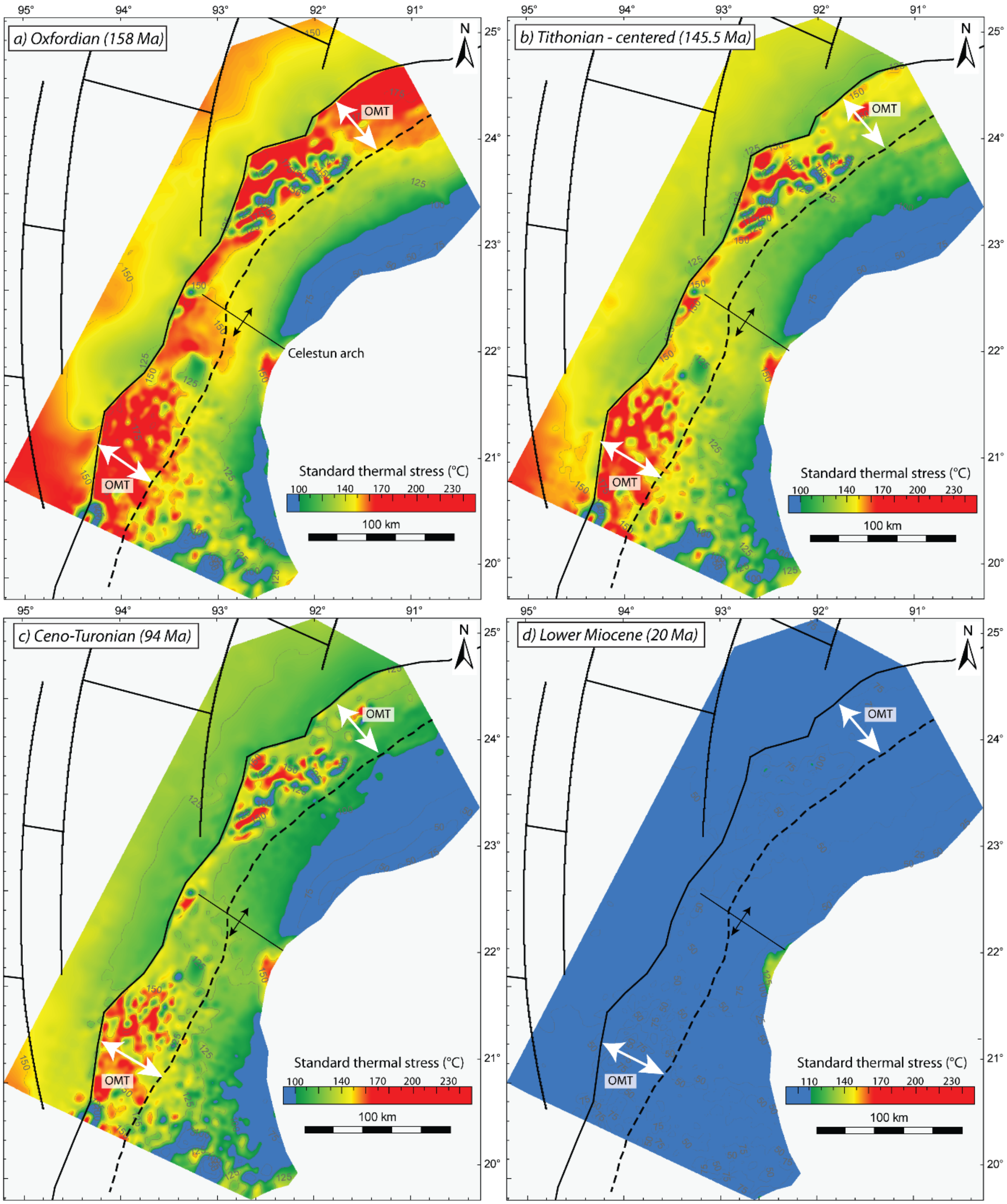

Figure 4.13: Standard thermal stress (STS) maps based on constant radiogenic heat production (RHP) per unit thickness of continental crust. RHP from the oceanic crust is assumed to be zero (Allen and Allen, 2013). a) STS map for the Oxfordian source interval. b) STS map for the Tithonian-centered source interval. c) STS map for the Ceno-Turonian source interval. d) STS map for the lower Miocene source interval.

4.6.2 Scenario -2: Laterally varying radiogenic heat production per unit thickness of continental crust

Previous crustal modeling of the Gulf of Mexico and similar rifted margins shows that basaltic input increases towards the continent-ocean transition (Rowan, 2018). An alternative set of STS maps based on decreasing RHP per unit thickness of continental crust were created for Oxfordian, Tithonian-centered, Ceno-Turonian, and lower Miocene ages. The Oxfordian, Tithonian-centered, and Ceno-Turonian are predicted to be in the present-day dry gas window (>165 °C STS), gas-condensate window (>145 °C STS), and late oil window (<145 °C STS), respectively, within the deeper minibasins of the outer marginal trough (Figs. 4.14a-c).

Inboard of the outer marginal trough, the thermal stress of all three Mesozoic source intervals decreases in a linear manner in the eastwardly direction of the Yucatan carbonate platform (Figs. 4.14a-c). Lower Miocene source rocks are immature (50-75 °C STS) throughout the modeled area (Fig. 4.14d).

Given the lack of temperature data in the modeled area, scenario testing offers a simple alternative approach to help define the degree of variability of thermal stress. Subsequent petroleum expulsion and fluid viscosity analysis are based on this model, which I propose is the most reasonable, geologic interpretation. Nevertheless, the thermal stress variations between these two sets of models are minor, as described above (<5 °C). It is possible to imagine other basement RHP scenarios, such as one end-member being that the entire transitional crust is basaltic in nature and that the crust in the whole study area has zero RHP. I propose that this end-member scenario is unlikely and is not discussed further.

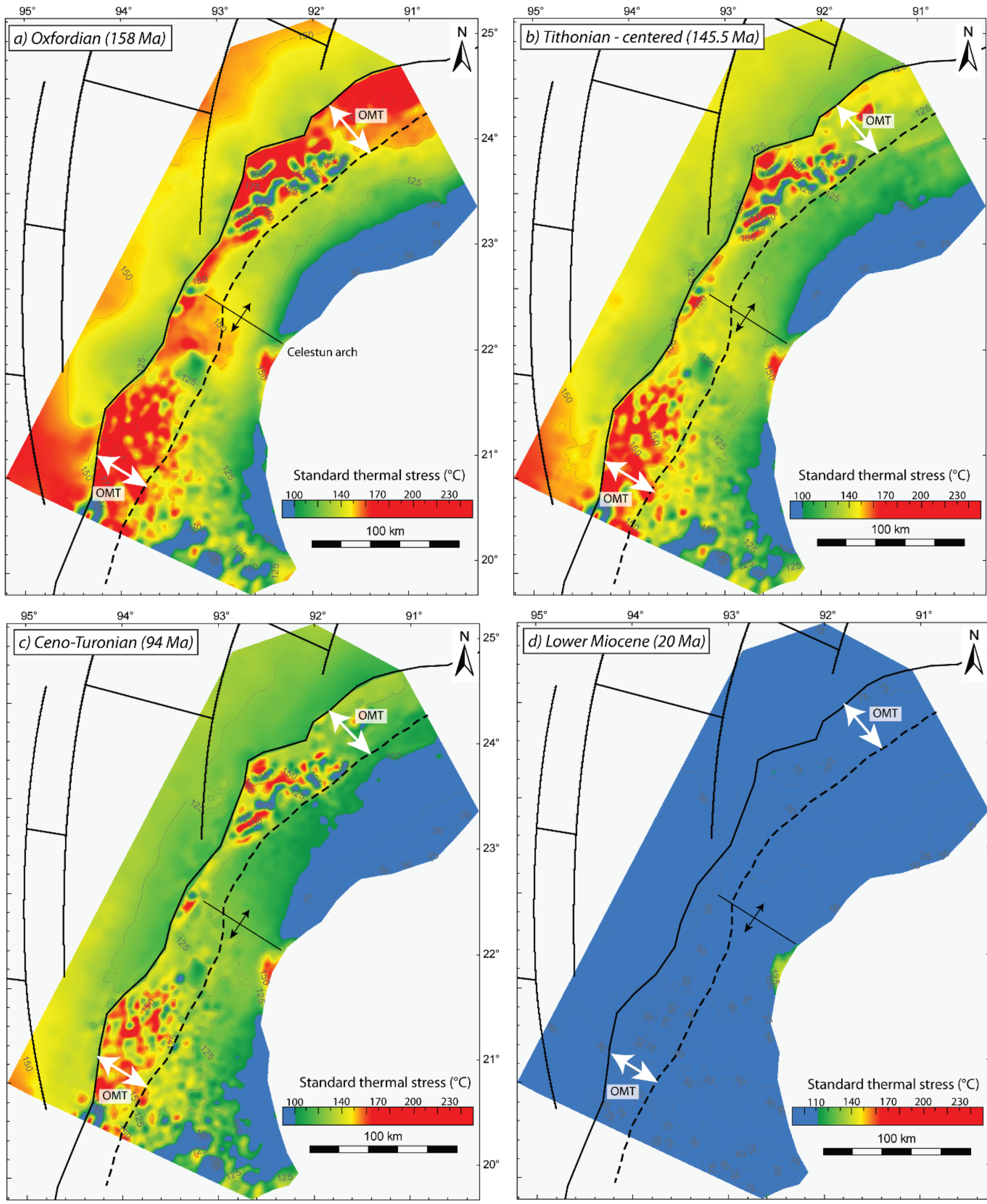

Figure 4.14: STS maps based on decreasing RHP per unit thickness of continental crust toward the direction of oceanic crust. A linear scalar function was derived assuming basaltic input increases toward the oceanic crust with a resulting RHP decrease. a) STS map for the Oxfordian source interval. b) STS map for the Tithonian source interval. c) STS map for the Ceno-Turonian source interval. d) STS map for the lower Miocene source interval.

4.7 Estimation of expelled petroleum

4.7.1 Calculating ultimate expellable potential

To evaluate the initial expulsion potential of the source rocks in the study area, I estimate the ultimate expellable potential (UEP) that is sub-divided into an oil potential (UEO) and a gas potential (UEG) for the Sturgis-1 well on the northern conjugate margin of the GOM (located on the map in Fig. 4.1). Ultimate expellable potential represents the cumulative masses of oil and gas that can be expelled upon complete maturation of the source rock (Pepper and Roller, 2021).

There is no publicly-available information from wells penetrating the primary Upper Jurassic source rocks in the southern Gulf of Mexico. Because both margins are conjugates during the period of Triassic-Jurassic rifting, I use the Sturgis-1 well from the conjugate margin in the northern GOM to estimate the ultimate expellable potential. The relationship between standard thermal stress and cumulative petroleum expelled from the Sturgis-1 well (Fig. 4.15) was then applied to the variable radiogenic heat production model (Figs. 4.14a, b).

I estimated the expelled petroleum in my area only for the Oxfordian and Tithonian-centered source intervals for three reasons: 1) the Sturgis-1 well does not encounter any good quality source rock of Ceno-Turonian and lower Miocene age; 2) the Ceno-Turonian interval is interpreted to be present mostly in the onshore part of the Gulf of Mexico (Teerman et al., 2010; Weimer et al., 2017); and 3) the lower Miocene source rock is inferred to be present only in the Comalcalco and Macuspana extensional system that is located outside of modeling area (Guzman-Vega and Mello, 1999).

The Sturgis-1 well log documents the Oxfordian (50.56 m) and Tithonian-centered (132.51 m) source interval and reveals similar source qualities with high hydrogen index (avg. 615) and organic carbon (avg. 4.4%). Each sample interval in the bar chart represents the half-thickness between adjacent samples, with the per sample ultimate expellable oil (UEO) in green, the ultimate expellable gas (UEG) in red, and the UEP being the sum of the two stacked bars in million barrels of oil equivalent (BOE) per square kilometer (Fig. 4.15).

The total interval UEP, UEO, and UEG are integrated across the whole ~183-m interval, corresponding to the maximum cumulative expelled yields that can be read from the cumulative expulsion versus thermal stress chart; UEO is 68.78 million bbl of oil/km^2, and UEG is 19.19 million BOE/km^2. UEP is the sum of the two: 87.98 million BOE/km^2. The UEP contribution from the Oxfordian and Tithonian-centered intervals are ~24% and ~76%, respectively (Fig. 4.15).

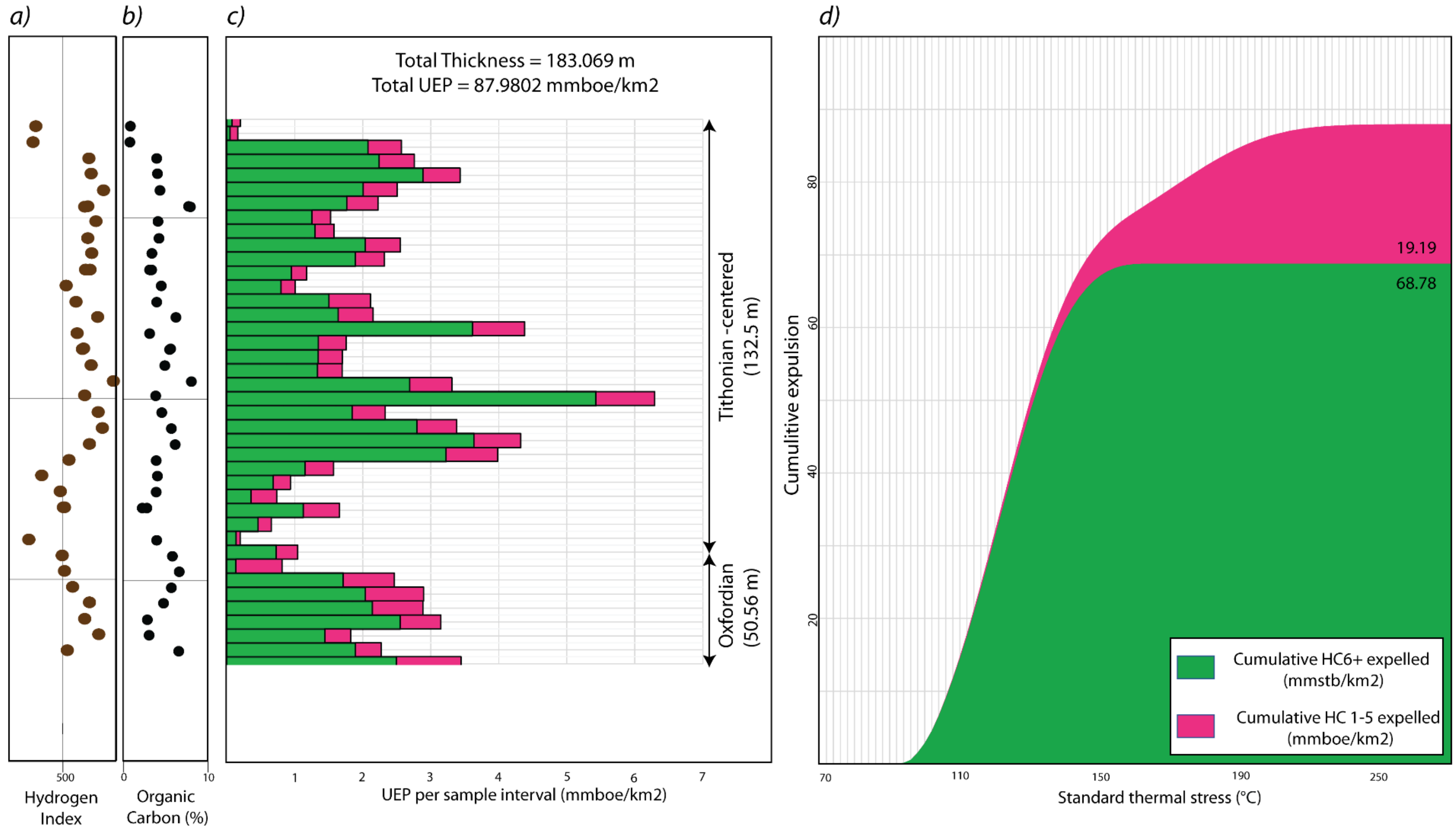

Figure 4.15: a) Depth vs. hydrogen index plot of good quality source rocks of the Oxfordian and Tithonian-centered source interval of the Sturgis-1 well digitized from BOEM (2021) (hydrogen index avg. 615). b) Percentage of organic carbon (avg. 4.4%). c) Estimate of Ultimate expellable potential (UEP). Each sample interval in the bar chart represents the half-thickness between adjacent samples, with the per sample ultimate expellable oil (UEO) in green, the ultimate expellable gas (UEG) in red, with the UEP representing the sum of the two stacked bars in million barrels of oil equivalent (BOE) per square kilometer. d) Cumulative expulsion versus thermal stress chart; UEO is 68.78 million bbl of oil/km^2, and UEG is 19.19 million mmstb/km^2. UEP is the sum of the two: 87.98 million BOE/km^2.

4.7.2 Petroleum expelled from Oxfordian and Tithonian-centered source intervals

Figure 4.16 shows the modeled expelled oil (Fig. 4.16a), expelled gas (Fig. 4.16b), and combined expelled oil and gas (Fig. 4.16c) maps for the Oxfordian source interval. The amount of expelled oil, gas, and total petroleum reaches a maximum of 15, 5, and 20 million bbl of oil equivalent [BOE]/km^2, respectively, within the outer marginal trough.

In the deeper minibasin areas of the outer marginal trough, Oxfordian source rocks have expelled all their oil potential, as the cumulative oil expulsion vs. temperature curve starts flattening (Fig. 4.15). The maximum oil charge is limited to 15 million bbl of oil/km^2. As the thermal stress reaches approximately 175 °C in the outer marginal trough for the Oxfordian source interval, cumulative gas accumulation has not yet reached its maximum potential.

Similarly, Figure 17 shows the modeled expelled oil (Fig. 4.17a), expelled gas (Fig. 4.17b), and combined expelled oil and gas (Fig. 4.17c) maps for the Tithonian-centered source interval, which is the primary source rock in the basin. The UEP contribution from the Tithonian-centered interval is ~76% of the total generation, as shown in Figure 4.15.

The amount of expelled oil, gas, and total petroleum reaches a maximum of 53, 10, and 63 million bbl of oil equivalent [BOE]/km^2, respectively, in the outer marginal trough. As the thermal stress reaches approximately 160 °C in the outer marginal trough for the Tithonian-centered source interval, cumulative oil accumulation has reached its maximum potential (53 million bbl of oil/km^2) while gas remains beneath maximum potential. Similar to the thermal stress map, cumulative expulsion from both Oxfordian and Tithonian-centered source intervals decreases linearly towards the east in the direction of the Yucatan carbonate platform (Figs. 4.16 and 4.17). For the estimation of expelled oil and gas, I assume a constant source rock thickness across the entire map-based modeling area, but lateral variation is likely.

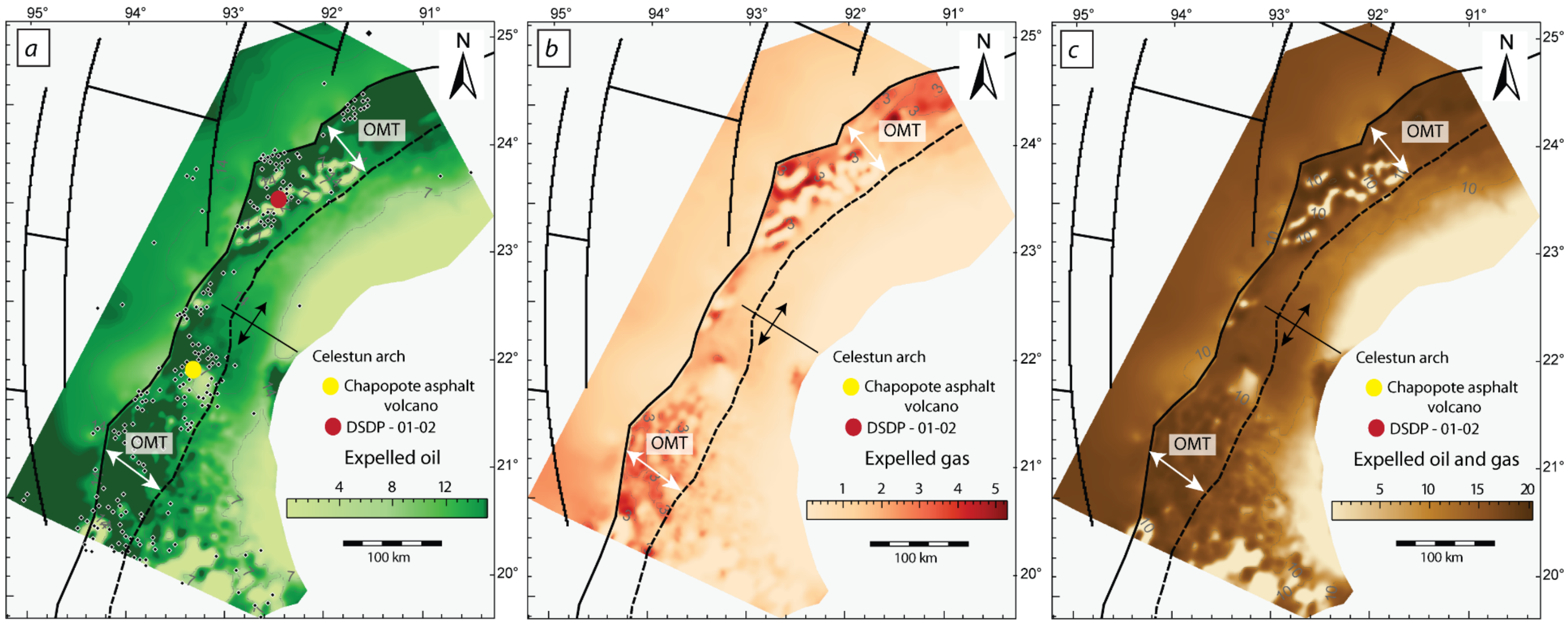

Figure 4.16: a) Map of expelled oil for the Oxfordian source interval. b) Map of expelled gas for the Oxfordian source interval. c) Map of expelled oil and gas for the Oxfordian source interval. Maps were generated using the ultimate expellable potential log of Sturgis-1 well from the conjugate rifted margin in the northeastern US Gulf of Mexico and the STS model derived from variable radiogenic heat production of continental crust (Fig. 4.14a). The amount of expelled oil, gas, and total petroleum reaches 15, 5, and 20 million bbl of oil equivalent [BOE]/km^2, respectively, in the outer marginal trough (OMT). Black dots in Fig. 4.16a show the locations of natural oil seeps compiled from Saunders et al. (2016) that support my model predictions of an active petroleum system.

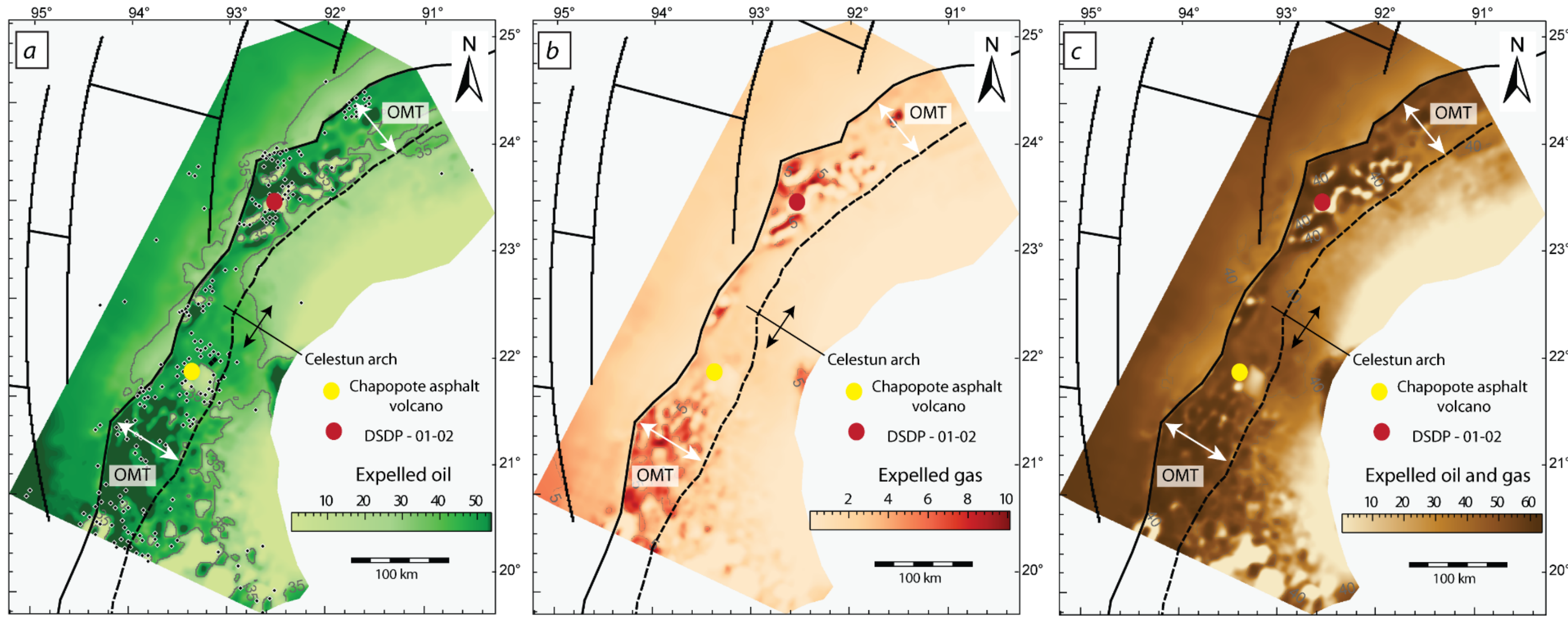

Figure 4.17: a) Map of expelled oil for the Tithonian-centered source interval. b) Map of expelled gas for the Tithonian-centered source interval. c) Map of expelled oil and gas for the Tithonian-centered source interval. Maps were generated using the ultimate expellable potential log of Sturgis-1 well from the conjugate rifted margin in the northeastern US Gulf of Mexico and the STS model derived from variable radiogenic heat production of continental crust (Fig. 4.14b). The amount of expelled oil, gas, and total petroleum reach 53, 10, and 63 million bbl of oil equivalent [BOE]/km^2, respectively, in the outer marginal trough (OMT) of the southern Gulf of Mexico. Black dots in Fig. 4.17a show the locations of natural oil seeps compiled from Saunders et al. (2016) that supports my model predictions of an active petroleum system.

4.7.3 Expelled fluid viscosity prediction

Petroleum system modeling can be used to predict in-situ petroleum fluid properties based on source rock organofacies and generation kinetics. In this study, I show the lateral variation of instantaneous fluid viscosity of the petroleum generated from Oxfordian and Tithonian-centered source intervals using KinEx software (Fig. 4.18). In KinEx, these predictions are based on empirical relationships between organofacies, gas-oil ratio (GOR), pressure, temperature, and fluid viscosity measured in oil samples obtained from different basins worldwide.

Based on my model output, the viscosity has an initial steep inverse relationship with thermal stress that flattens around ~130 °C STS. In the minibasins within the outer marginal trough, the expelled petroleum viscosity is low (~0.1 cP). Cracking of heavier molecules due to higher thermal stress results in less viscous petroleum, increases the GOR dramatically, and is manifested by the increasing API gravity of the oil fraction. In agreement with the relationship to thermal stress explained above, instantaneous fluid viscosity from both Oxfordian and Tithonian-centered source intervals increases linearly in the eastward direction of the Yucatan carbonate platform.

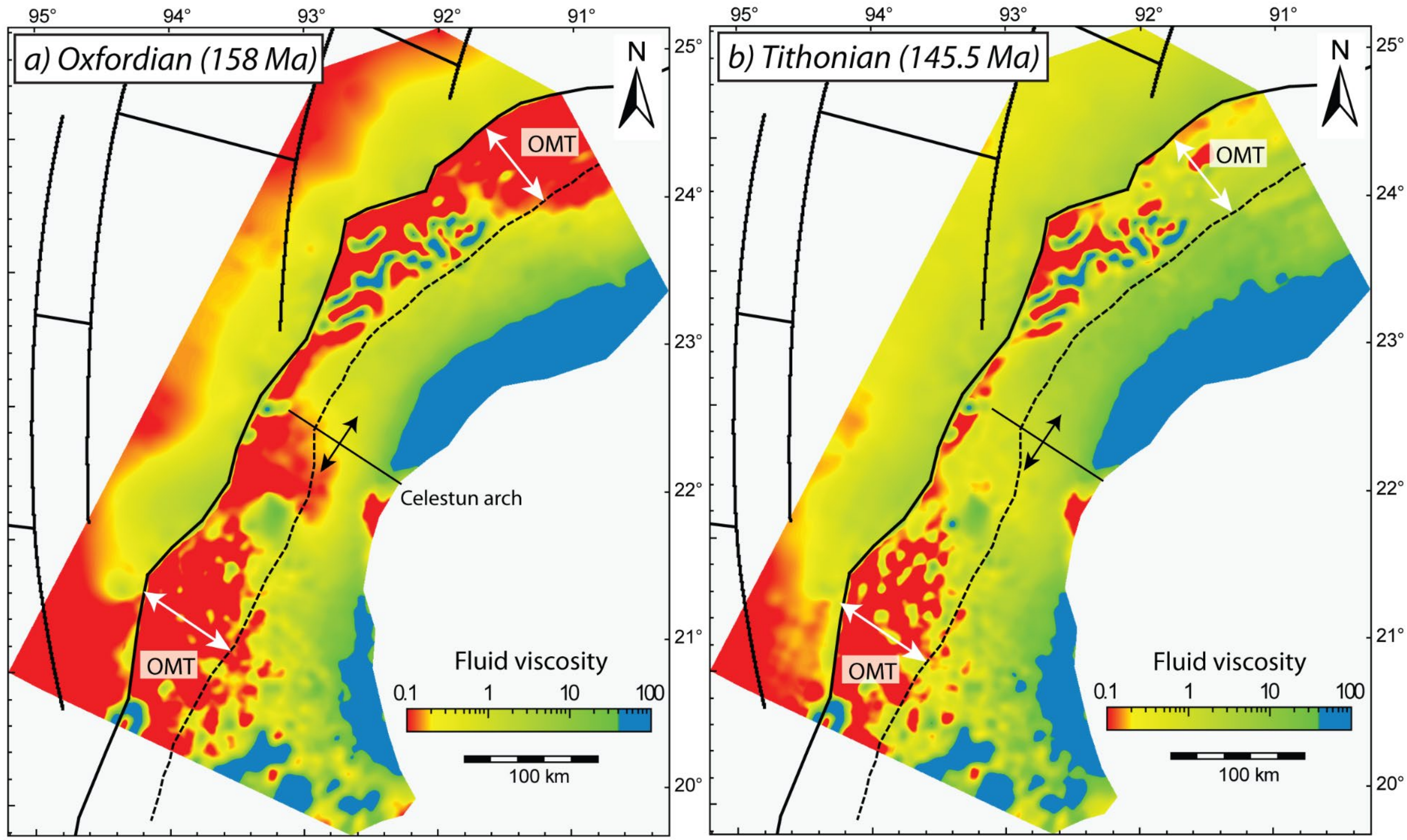

Figure 4.18: a) Expelled instantaneous petroleum fluid viscosity map of the Oxfordian source interval. b) Expelled instantaneous petroleum fluid viscosity map of the Tithonian-centered source interval. Modeled viscosity is relatively low (~0.1-1 cP) for the petroleum generated in the minibasin kitchens of the outer marginal trough (OMT).

4.8 Discussion

4.8.1 Quantitative thermal stress and expelled petroleum modeling

Thermal stress modeling predicting accurate subsurface temperature in the southern Gulf of Mexico requires consideration of three key factors: 1) differences in crustal type and thickness from east to west (thinned continental crust, hyperextended continental crust with possible mantle or lower crust exhumation, and oceanic crust); 2) these crustal types control the total radiogenic heat production and influence heat flow in the overlying sedimentary sequence; 3) disruption of isotherms around salt bodies due to differing thermal conductivity of salt (4.5 °C per kilometer of salt thickness in my models); and 4) transient effect of rapid sedimentation of the Plio-Pleistocene sediments especially in the south-eastern Comalcalco, Macuspana fault systems and depocenters (Hasan and Mann, 2021).

Small differences might arise from accounting for the thermal dependence of the salt conductivity on temperature and salt geometry evolution through time (Davison and Cunha, 2017). Because the Trinity basin modeling software does not take into account lateral variations of heat flow and salt geometry through time, some errors might arise in the calculation of source rock maturity around the edges of large salt bodies.

My study of integrated thermal stress modeling incorporating crustal parameters (Fig. 4.4) yields a bottom-up petroleum system evaluation of the Campeche and Yucatan salt basin. The workflow to reach this conclusion included: 1) crustal surfaces based on detailed 2D and 3D geophysical analysis (Hasan and Mann, 2021); 2) calibration of well temperature data; 3) paleo-bathymetry; 4) paleo-surface temperature; 5) incorporation of transient and anomalous heat effect in the modeling; and 6) testing geology-based alternative scenarios. This integrated workflow enhances our understanding of the thermal stress of a study area that is structurally complex with many controls on variation in subsurface temperature.

A complete understanding of the potential source intervals in a basin requires a quantitative estimate of the amount of expelled petroleum. I use the ultimate expellable potential (UEP) workflow described by Pepper and Roller (2021). The layer-by-layer calculation of source intervals from available geochemical or petrophysical-log derived value rather than pre-averaging takes vertical stratigraphic heterogeneity and pattern of expulsion potential into account. Although for the estimation of expelled oil and gas, I assume constant source rock thickness across the entire map-based modeling area, lateral variation is more than likely.

4.8.2 Evaluation of thermal stress and expelled petroleum trends

The Oxfordian and Tithonian-centered source interval is predicted to have reached dry gas and gas-condensate in the outer marginal trough based on my preferred thermal modeling from variable RHP per unit area of continental crust (Fig. 4.14). Deeper burial (>7 km) of the source rocks has driven petroleum generation and expulsion in the overlying Neogene minibasins (Kenning and Mann, 2020b). Although the present-day maturity of the Upper Jurassic source rocks remains in the dry gas and gas-condensate window, there is likely a time lag (10-20 Ma) between petroleum expulsion and the charging of reservoirs (Pepper and Yu, 1995).

He and Murray (2020) report representative maturity models in the northern Gulf of Mexico, with the Tithonian interval reaching the oil expulsion window between 10 to 20 million years ago. Only in the last 5 million years did the ‘oil front’ arrive in the Miocene and Pliocene reservoirs, with the later-expelled gas remaining deep in the basin. First, to calibrate with the modeling, the ratio of carbon isotopes and elemental composition of the hydrocarbon is determined to find the thermal stress and burial depth at which the hydrocarbon was generated. Then using a generalized percolation rate of petroleum through sedimentary rocks, an estimate of the migration “lag time” can be calculated (Liu et al., 2020).

Clusters of natural sea surface seeps in the Campeche and Yucatan salt basin observed in the outer marginal trough help explain a similar phenomenon (Saunders et al., 2016). Drilling at DSDP Site 2 in 1968 recovered oil-stained caprock from above one of the salt diapirs (Watkins and Buffler 1996) (Fig. 4.2). Further south, oil was recovered from an asphalt volcano ("Chapopote asphalt volcano") at the inner edge of the outer marginal trough (Naehr et al., 2009).

The abundance of evidence of petroleum occurrence indicates a working petroleum system within the outer marginal trough of the Campeche and Yucatan salt basin. Far fewer oil seeps are located up-dip, where source rock maturities are anticipated to be lower or immature.

My analysis shows that the Tithonian-centered and Oxfordian source rocks expelled petroleum in the outer marginal trough of the basin is 20 million bbl and 63 million bbl of oil equivalent [BOE]/km^2, respectively. The Tithonian-centered source interval contributes 76% of the total Upper Jurassic expelled petroleum. The source beds can be regarded as "world-class," with expelled petroleum value attaining such a high value. Because the primary source intervals in the study area are situated beneath the thick Cenozoic clastic deposits, the petroleum system requires several kilometers of vertical migration to charge the Neogene reservoirs (Pepper and Yu, 1995).

4.8.3 Petroleum system time chart and petroleum prospectivity

The main elements of the petroleum systems for the outer marginal trough are summarized in a petroleum system event chart (Fig. 4.19a). Mesozoic source rocks of organofacies-A remain in the oil window during late Paleogene to early Neogene time. Speculative source rocks of the lower Miocene age do not expel any petroleum into the deepwater Campeche and Yucatan salt basins. Other than discoveries in the south-eastern part of the study area (e.g., Cantarell, Sihil field), the majority of the recent discoveries are from Miocene reservoirs, especially in the deepwater Campeche salt basin (Shann, 2020).

Combined structural and stratigraphic traps are present along the upturned strata at the flanks of the salt diapirs (Kenning and Mann, 2020b) (Fig. 4.19b). Salt pillow structures along the inner flanks of the outer marginal trough create structural traps with four-way closures in both Mesozoic and Cenozoic sections. Anticlinal structures create Paleocene to Eocene shale-cored closures in the oceanic part of the southern GOM (Kenning and Mann, 2020b). Updip-salt rollers provide potential three-way fault traps above the primary salt detachment surface (Fig. 4.9). High-amplitude reflections above salt-rollers are inferred to be Norphlet-equivalent sandstone producing in the US GOM that is charged by overlying Oxfordian source intervals (Steier and Mann, 2019; Snedden et al., 2020).

The trap formation timing in the deepwater Campeche and Yucatan began in the Chiapanecan orogeny during the middle to late Miocene, although deformation continues to the present as the result of large-scale passive margin gravity sliding. The late Middle Miocene to Recent passive-margin system focusing on the outer marginal trough results in a 300-km-wide zone of downdip shortening expressed on folds, imbricate thrusts, and diapirs (Hasan and Mann, 2021).

Figure 4.19: a) Petroleum systems chart for the study area of the southern Gulf of Mexico summarizing the major tectonic events, petroleum system elements, and the predicted thermal stress of source rocks. b) Schematic cross-section based on the seismic line in Figure 4.11 showing hydrocarbon trap types observed in the seismic grid from the southern Gulf of Mexico. Four-way and three-way structural closures are commonly associated with salt diapirs, salt pillows, and allochthonous salt bodies with salt shown in pink.

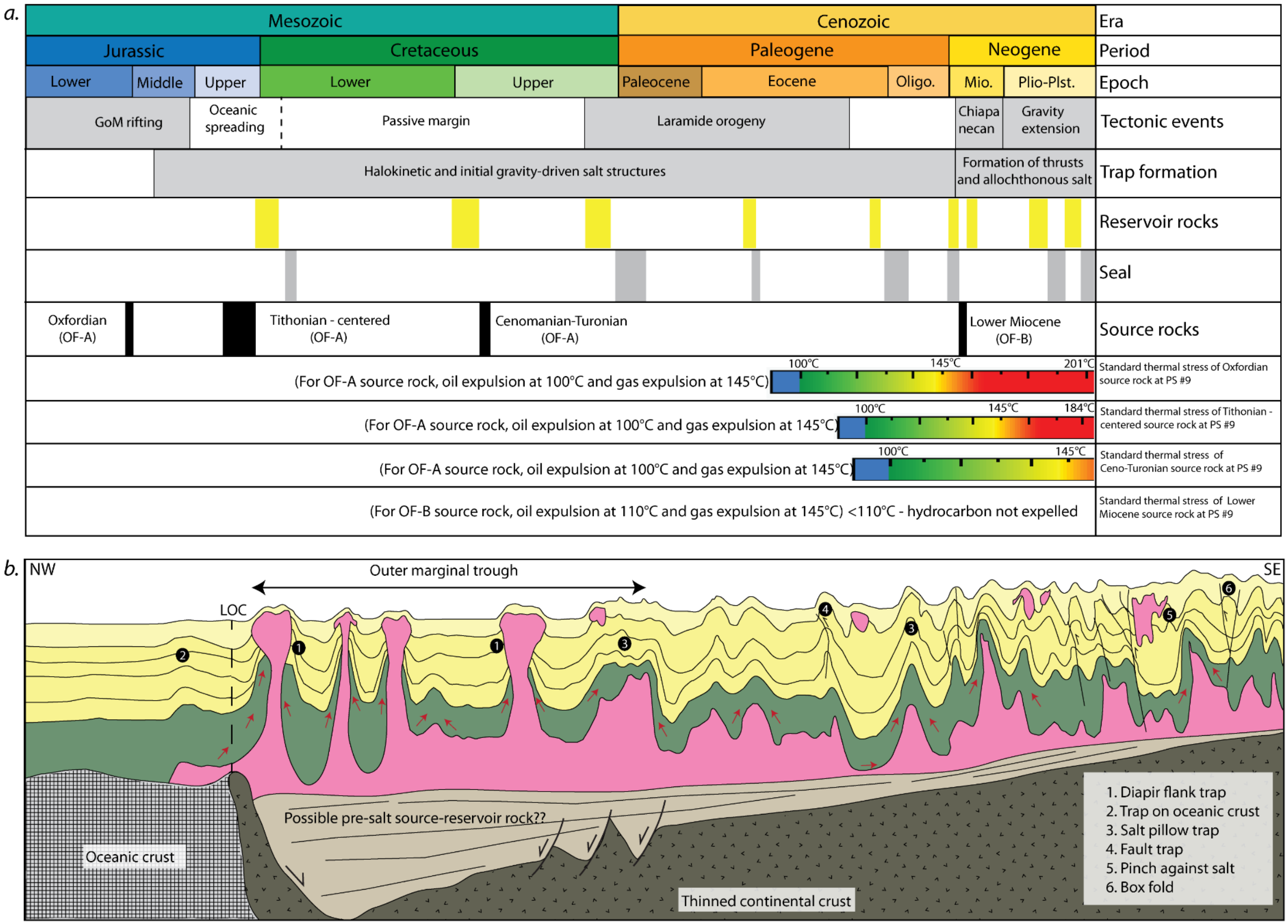

a.
Mesozoic
Cenozoic
Era
Jurassic
Cretaceous
Paleogene
Neogene
Period
Lower
Middle
Upper
Lower
Upper
Paleocene
Eocene
Oligo.
Mio.
Plio-Plst.
Epoch
GoM rifting
Oceanic spreading
Passive margin
Laramide orogeny
Chiapanecan
Gravity extension
Tectonic events
Halokinetic and initial gravity-driven salt structures
Formation of thrusts and allochthonous salt
Trap formation
Reservoir rocks
Seal
Oxfordian (OF-A)
Tithonian - centered (OF-A)
Cenomanian-Turonian (OF-A)
Lower Miocene (OF-B)
Source rocks
(For OF-A source rock, oil expulsion at 100°C and gas expulsion at 145°C)
100°C
145°C
201°C
Standard thermal stress of Oxfordian source rock at PS #9
(For OF-A source rock, oil expulsion at 100°C and gas expulsion at 145°C)
100°C
145°C
184°C
Standard thermal stress of Tithonian - centered source rock at PS #9
(For OF-A source rock, oil expulsion at 100°C and gas expulsion at 145°C)
100°C
145°C
Standard thermal stress of Ceno-Turonian source rock at PS #9
(For OF-B source rock, oil expulsion at 110°C and gas expulsion at 145°C) <110°C - hydrocarbon not expelled
Standard thermal stress of Lower Miocene source rock at PS #9
b.
NW
SE
Outer marginal trough
LOC
Possible pre-salt source-reservoir rock??
Oceanic crust
Thinned continental crust
1. Diapir flank trap
2. Trap on oceanic crust
3. Salt pillow trap
4. Fault trap
5. Pinch against salt
6. Box fold

4.9 Conclusions

The Oxfordian and Tithonian-centered source intervals reached dry gas and gas-condensate expulsion levels in the outer marginal trough based on my preferred thermal model. These source rocks were previously in the oil window from the late Paleogene to early Neogene.

Ultimate expellable potential (UEP) based quantitative estimation of expelled petroleum from the Tithonian-centered source expelled up to 63 million bbl of oil equivalent [BOE]/km^2 and that the Oxfordian source interval expelled up to 20 million bbl of oil equivalent [BOE]/km^2. The Tithonian source interval contributes 76% of the total Upper Jurassic-lower Cretaceous expelled petroleum in the southern Gulf of Mexico. The predicted instantaneous petroleum viscosity ranges from very high at the present-day kitchen edge to very low (~0.1 cP) in the gas-condensate window.

Various combined structural and stratigraphic traps are present in the study area that include: diapir flank traps, four-way anticlinal closures associated with Bajocian-Callovian salt and Paleogene shale, and three-way fault closures. Based on my proposed basin model, I predict that these traps are charged by petroleum expelled by the late Jurassic source rocks from the late Paleogene to early Neogene. The 'lag time' required for vertical migration observed in the northern Gulf of Mexico explains why this earlier-expelled low maturity oil is seeping at the sea surface today from the charged, subsurface traps, I predict.

My study shows that the Campeche and Yucatan salt basin hosts multiple high-quality expulsion-mature source rocks.

The following chapter is based on: Hasan, M.N., Mann, P., 2022. Controls of tectonic evolution on source rock thermal maturity of the Moroccan salt basin. Basin Research (in review).

CHAPTER 5: CONTROLS OF TECTONIC EVOLUTION ON SOURCE ROCK THERMAL MATURITY OF THE MOROCCAN SALT BASIN

5.1 Introduction

The Moroccan rifted-passive margin of the Central Atlantic Ocean extends ~3500 km from the Straits of Gibraltar to the northern border of Mauritania (Tari et al., 2013) (Figs. 5.1 and 5.2). This margin forms the conjugate rifted margin for much of the eastern margin of the USA and Maritime Canada (Schettino and Turco, 2011). Hydrocarbon exploration of the offshore Morocco margin over the past few decades has resulted in a series of unsuccessful shelf, slope, and deepwater wells that tested Early Cretaceous-Cenozoic clastic rocks and Jurassic carbonate rocks from the late 1960s through the early 2000s (Pichel et al., 2019; Galhom et al., 2022). While the offshore Atlantic margin of Morocco remains a frontier area that lacks significant hydrocarbon exploration, data compilations by Davison (2005) and Neumaier et al. (2018) show that a working petroleum systems based on Mesozoic source rocks exist along the 3500-km-long Moroccan Atlantic margin (Davison, 2005; Neumaier et al., 2018).

Previous papers published on the regional geology, stratigraphy, salt tectonics, and source rock thermal maturity modeling of the offshore Moroccan margin include studies of seismic refraction data (Klingelhoefer et al., 2016), integrate seismic reflection, refraction, well, and regional geologic information (Davison, 2005; Tari and Jabour, 2013; Klingelhoefer et al., 2016; Neumaier et al., 2018; Galhom et al., 2022; Uranga et al., 2022). Studies focusing on source rock presence (Sachse et al., 2012) and maturity (Neumaier et al., 2018, Galhom et al., 2022) in offshore Morocco are limited and cover local areas with 1D thermal maturity modeling. With the recent hydrocarbon discoveries (Venus and Graff) in offshore Namibia primarily sourced from Cretaceous source rocks (Hedley et al., 2022), a key remaining question is whether the same source interval is mature in the offshore Moroccan margin or not. A map-based modeling for the margin that is not yet done can unravel the answer to that question, which is the primary objective of this chapter.

In this chapter, I present a comprehensive and bottom-up description and interpretation of: a) the crustal structure of the offshore Moroccan salt basin using spatial analysis of gravity dataset, 2D gravity models using publicly available free-air satellite gravity field data from Sandwell et al. (2014); b) controls of regional tectonic events on the source rock thermal maturity using previous results from both deepwater and shelfal wells; and c) hydrocarbon sweet spots in the study area, integrating various geophysical dataset and modeling workflows. For this study, I used a ~8474 line-km grid of 2D, pre-stack depth migration (PSDM), seismic reflection dataset along with potential field data (Fig. 5.3).

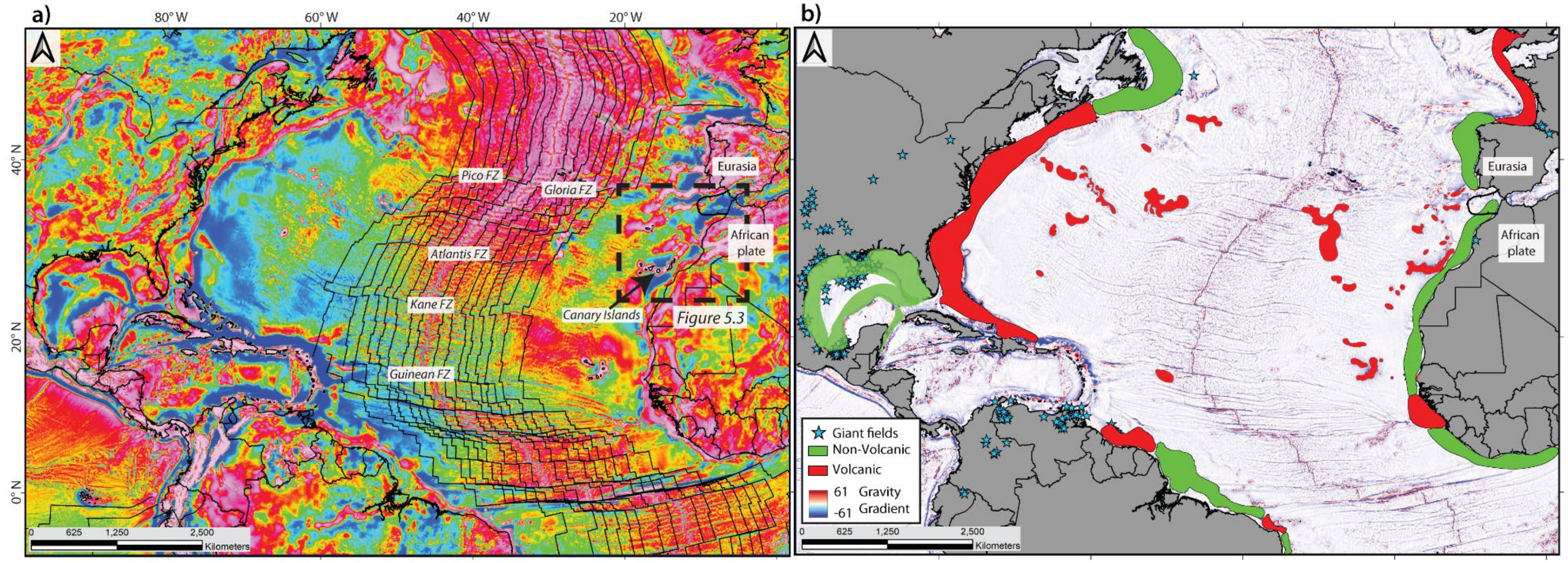

Figure 5.1: a) Free-air gravity anomaly map from Sandwell et al. (2014) showing the oceanic crustal spreading fabric and fracture zones of the Central Atlantic. The dotted black box shows the location of the more detailed map of the study area shown in Fig. 5.3. b) Compilation of volcanic (red polygons) and non-volcanic margins (green polygons) of the Mesozoic rifted margins of the Gulf of Mexico and circum-Atlantic margins from Mann (2022). Basemap is vertical gradient gravity (VGG) of Sandwell et al. (2014).

Figure 5.2: Early Jurassic to Early Miocene plate reconstructions of northern Africa, the Mediterranean Sea, and the Central Atlantic Ocean modified from Schettino and Turco (2011). a) Early Jurassic (~185 Ma) plate reconstruction showing the breakup of Pangea with continental rifts opening in a northwest-to-southeast direction as shown by the double-headed arrows; box shows the study area of northern Morocco shown in Fig. 5.3. b) Early Cretaceous (~147 Ma) plate reconstruction showing the northwest-to-southeast oblique opening of the central Atlantic and the failed rift in the northern part of the continental African plate that will be inverted in the Cenozoic as the Atlas Mountains. c) Late Cretaceous (~67 Ma) showing the northwestward movement of the African plate toward the Iberian margin of Eurasia as shown by the white arrow that is related to the opening of the South Atlantic ocean. d) Early Miocene (~20 Ma) reconstruction showing the tectonic inversion of the failed continental rift in Morocco to form the High Atlas and Anti-Atlas elongate mountain belts formed as the result of continued northwestward Africa-Eurasia convergence as shown by the white arrow.

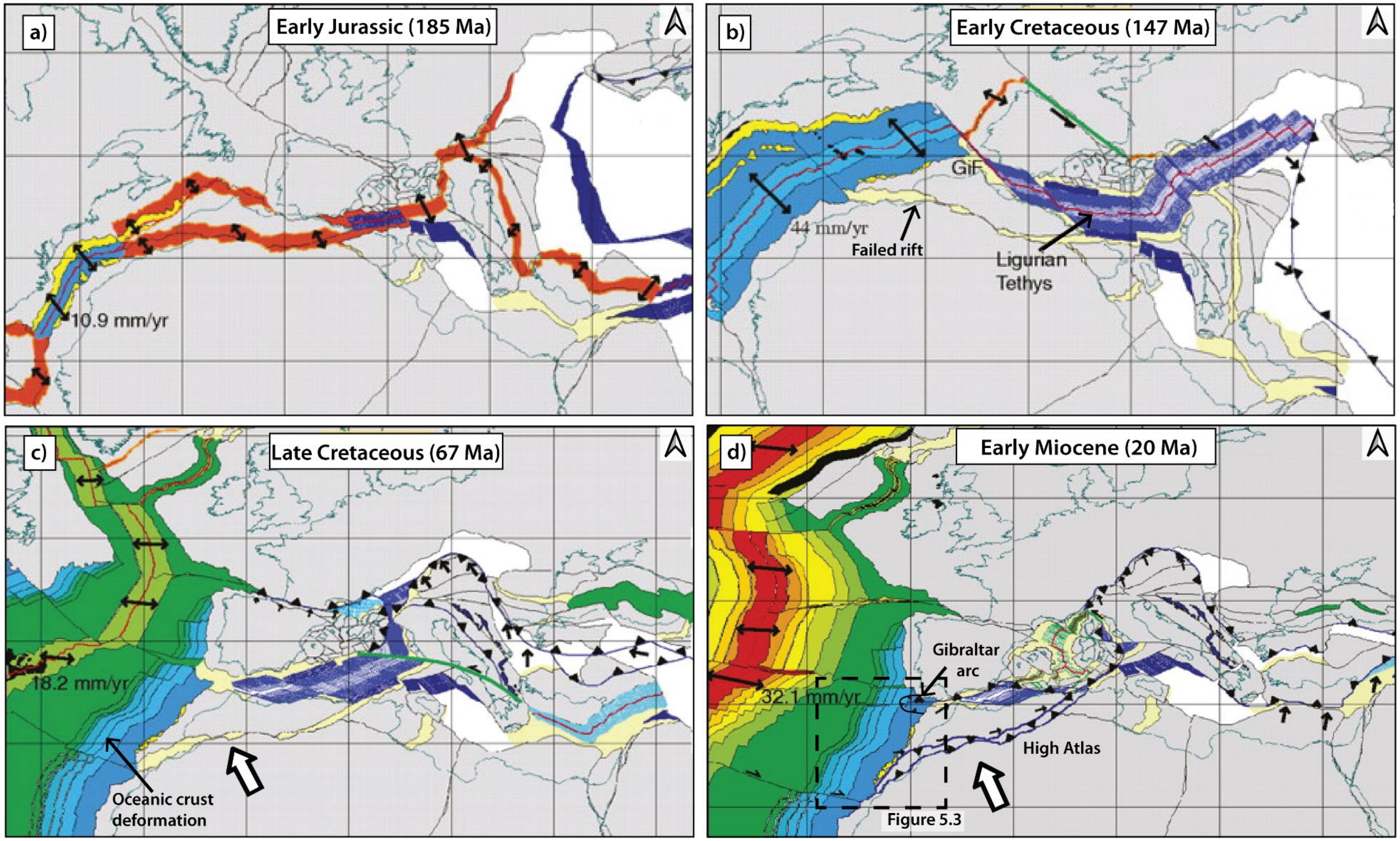
a)
Early Jurassic (185 Ma)
10.9 mm/yr
b)
Early Cretaceous (147 Ma)
GiF
44 mm/yr
Failed rift
Ligurian
Tethys
c)
Late Cretaceous (67 Ma)
18.2 mm/yr
Oceanic crust
deformation
d)
Early Miocene (20 Ma)
Gibraltar
arc
32.1 mm/yr
High Atlas
Figure 5.3

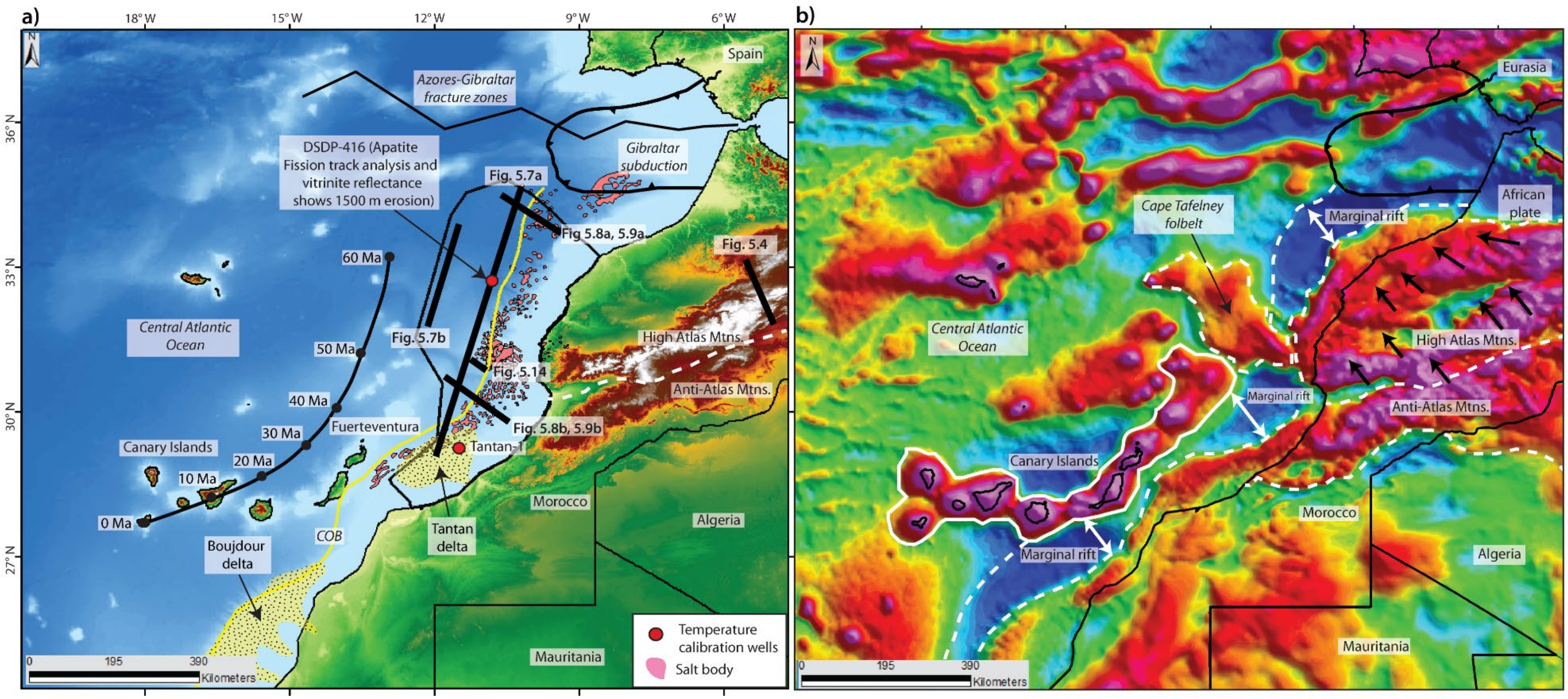

Figure 5.3: a) Topographic map of northwestern Africa showing the location of the seismic lines, IODP and oil exploration wells, distribution of Jurassic salt bodies in pink, and the continent-ocean boundary shown as the yellow line. b) Free-air gravity map revealing the major tectonic features: the 50-80-km-wide marginal rift that parallels the continent-oceanic boundary, the Canary Islands hotspot track, Cape Tafelney foldbelt, and the High Atlas and Anti-Atlas mountains. Black arrows show the GPS displacement vectors with Iberia (Eurasia) as a fixed reference frame, as compiled by Gutscher et al. (2012).

5.2 Regional geologic framework

5.2.1 Tectonic evolution of the margin

Early Jurassic to Early Miocene plate reconstructions of the study area modified from Schettino and Turco (2011) are summarized in Figure 5.2. Northwest-southeast-directed rifting between the Moroccan Atlantic margin and its North American conjugate began in the Late Triassic and was manifested by the widespread development of grabens and half-grabens filled with clastic red beds on both conjugate margins (Davison, 2005) (Fig. 5.4). Triassic-Jurassic rifting occurred along north-northeast-trending zones of structural weakness defined by the late Paleozoic Hercynian orogenic trends (Hafid et al., 2008) (Figs. 5.2a and 5.4). Fed by marine incursions from the Tethys Ocean east of present-day Morocco, the major Jurassic salt province formed as a syn- to post-rift sag sequence along the marginal rift of the northern margin of Morocco with the salt body thinning to the south (Tari and Jabour, 2013) (Figs. 5.3a, 5.4, and 5.5).

Klingelhoefer et al. (2009) used refraction profiles to identify an un-rifted continental crust with a thickness of 30-35 km that occupies the narrow shelf area of Morocco. In the deeper water areas, crustal thinning is manifested by a 5-7-km-thick, transitional continental crust, known as the "marginal rift" (Miller, 2021) (Fig. 5.3b). The marginal rift structure is characterized by a prominent, elongated gravity low that is inferred to represent the relatively deeper crystalline basement with a higher density than the adjacent rift flanks (Fig. 5.3b). The width of the marginal rift structure can be measured as 50-80-km-wide and includes a 750-km long negative anomaly along the northern Moroccan rifted-passive margin that reflects the continent-ocean boundary (Fig. 5.3b).

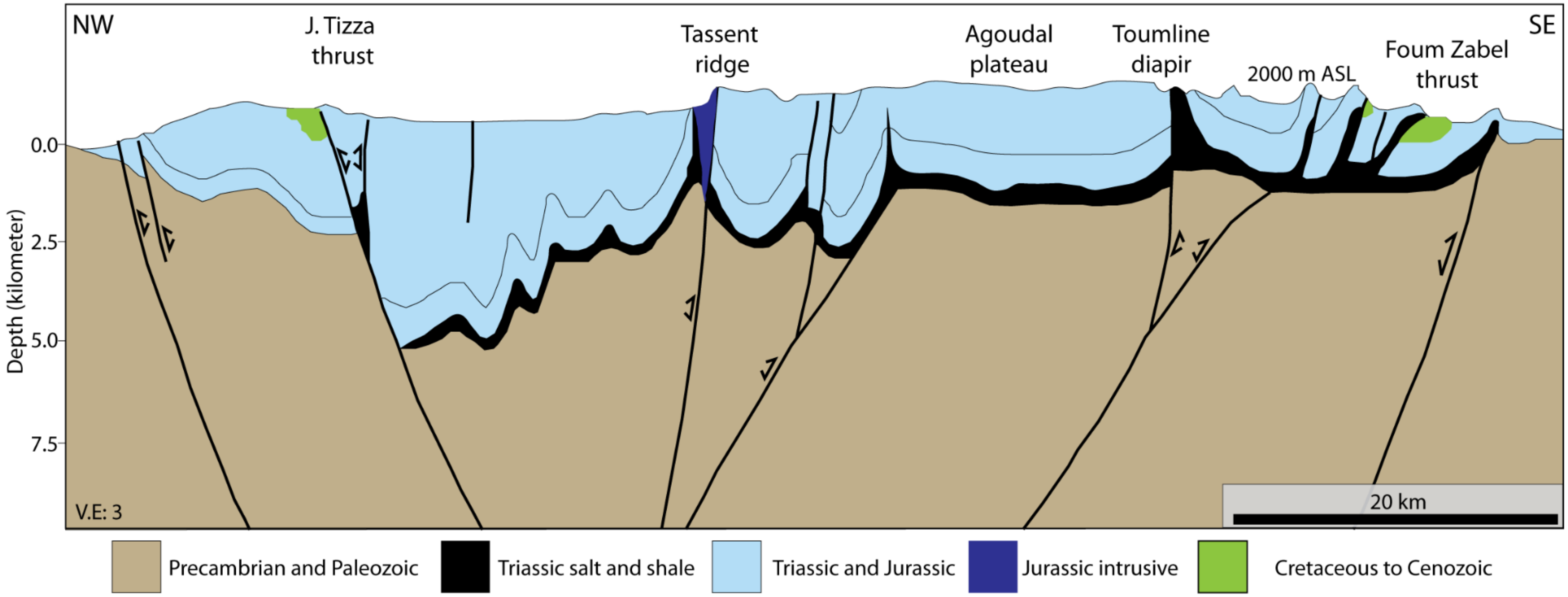

Figure 5.4: Northwest-to-southeast geologic structural cross-sections across the central High Atlas Mountains (modified from Babault et al., 2013). The cross-section is based on field data combined with gravity modeling. The post-rift Cretaceous and Cenozoic sedimentary rock that once covered this entire area were removed by erosion during the late Cretaceous to Recent Atlas orogeny that was produced by the period of northwest-to-southeast plate convergence shown on the plate reconstructions in Fig. 5.3.

Figure 5.5: Generalized stratigraphic column summarizing the lithologies, sedimentary facies, unconformities, and major tectonic events. Tectonic events are modified from Davison (2005) and Galhom et al. (2022). The period of plate convergence shown in the map view on Figs. 5.3c and 5.3d occurred during the late Cretaceous and Cenozoic and led to a broad area of uplift and erosion of the Moroccan margin that included the uplift of the High Atlas Mountains.

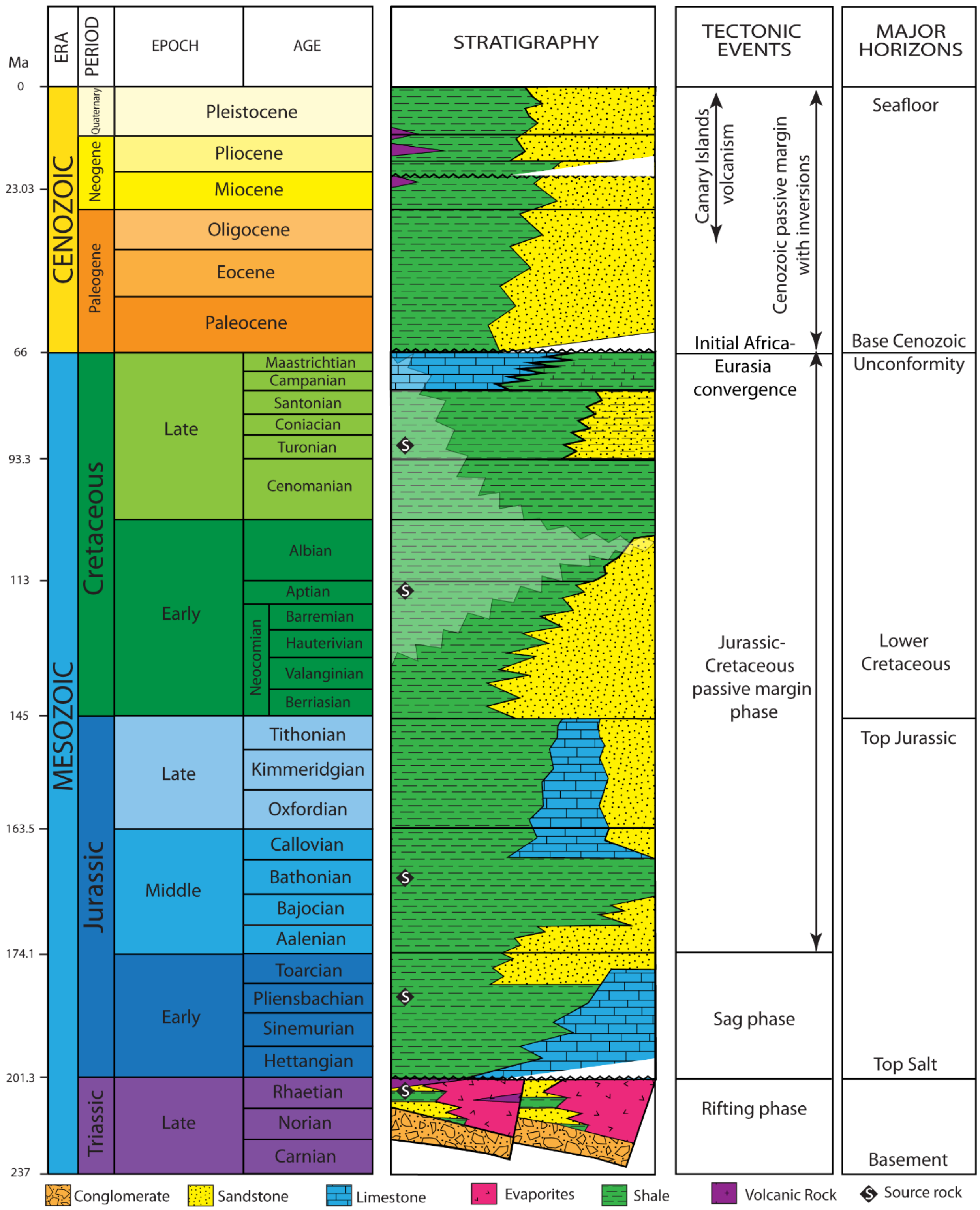

Ma
ERA
PERIOD
EPOCH
AGE
STRATIGRAPHY
TECTONIC EVENTS
MAJOR HORIZONS
0
23.03
66
93.3
113
145
163.5
174.1
201.3
237
CENOZOIC
MESOZOIC
Quaternary
Neogene
Paleogene
Cretaceous
Jurassic
Triassic
Pleistocene
Pliocene
Miocene
Oligocene
Eocene
Paleocene
Late
Early
Late
Middle
Early
Late
Maastrichtian
Campanian
Santonian
Coniacian
Turonian
Cenomanian
Albian
Aptian
Neocomian
Barremian
Hauterivian
Valanginian
Berriasian
Tithonian
Kimmeridgian
Oxfordian
Callovian
Bathonian
Bajocian
Aalenian
Toarcian
Pliensbachian
Sinemurian
Hettangian
Rhaetian
Norian
Carnian
Canary Islands volcanism
Cenozoic passive margin with inversions
Initial Africa-Eurasia convergence
Jurassic-Cretaceous passive margin phase
Sag phase
Rifting phase
Seafloor
Base Cenozoic Unconformity
Lower Cretaceous
Top Jurassic
Top Salt
Basement
Conglomerate
Sandstone
Limestone
Evaporites
Shale
Volcanic Rock
Source rock

The transition from continental rifting to the formation of oceanic crust at a spreading ridge was initiated during the Middle Jurassic at ~185 Ma (Wenke et al., 2014; Schettino and Turco, 2011) (Figs. 5.2b and 5.5). Following the Mesozoic rift phase, the Atlantic margin of Morocco became a passive margin characterized by an overlying section of thick carbonate and clastic rocks (Davison, 2005) (Fig. 5.5). During the latest Cretaceous and through the Cenozoic, the rifted passive margin of Morocco underwent northwest-southeast, regional compression related to Late Cretaceous – Cenozoic continental collision between Africa and Europe (Atlasic orogeny) that was produced by the relative northward motion of the African plate toward Iberian margin and Eurasia (Bosworth et al., 1999; Guiraud et al., 2005; Serpelloni et al., 2007; Schettino and Turco, 2011; Dehler and Welford, 2013; Neumaier et al., 2018) (Figs. 5.2c and 5.5).

The northern regions of Morocco were affected by several episodes of uplift and erosion related to this long-lived and widespread orogeny that continues till present-day (Fig. 5.2d). The deformed belts within the continental crust include Anti-Atlas Mountains composed of late Paleozoic rocks and the inverted Triassic-Jurassic rifts as the High Atlas that expose redbeds, evaporites, and shallow marine sedimentary rocks (Davison, 2005) (Figs. 5.2d, 5.4, and 5.5). Exhumation history of the Atlas Mountains using Jurassic intrusives yields apatite fission track ages a peak uplift and cooling age of Campanian (~80 Ma). Constraints from (U–Th)/He of plutonic rocks in the High Atlas Mountains suggests that these were intruded at 50 Ma and experienced a slow cooling and uplift trend after their intrusion (Barbero et al., 2007; Domenech et al., 2016) (Fig. 5.4). A large, east-west trenching arch in the oceanic crust of offshore Morocco marked the gravity high seen on Figure 5.3a, called the Cape Tafelney foldbelt is also proposed to be linked to the same Atlasic orogenic event and forms the offshore extension of the High Atlas Mountains (Hafid et al., 2000; Benabdellouahed et al., 2017).

These Cenozoic tectonic events related to regional plate convergence between African and Eurasia with northwest-south compressional effects have affected the source rock presence, distribution, and especially the burial thickness that controls the source rock thermal maturity in both the offshore rifted-continental margin and the area with oceanic crust (Powney et al., 2020).

5.2.2 Stratigraphy, basin fill, and major unconformity

The amount of syn-rift clastic sediment deposits along the Moroccan Atlantic margin was variable and controlled by the rift basin morphology. The thickness of syn-rift, terrigenous, clastic sediments along the northern Moroccan margin is around 900 m (Davison and Dailly, 2010; ONHYM, 2019). Salt was deposited within the marginal rift along a narrow rifted margin formed during the syn-rift to the post-rift stage (Uranga et al., 2022). The distribution of evaporite deposits is observed to be thicker in the northern Moroccan margin (Tari and Jabour, 2013). This could result from either diachronous salt deposition or a synchronous salt deposition during the opening of the Morocco-Nova Scotia conjugate margins that youngs to the north (Schettino and Turco, 2011). The presence of salt in the northern basins controls the characteristic structural style in the northern part of the Moroccan marginal rift with areas of salt diapirism and salt walls. The salt structural styles are dominated by expulsion roll-overs driven by progradational loading triggering basinward salt withdrawal due to the westward termination of the onland High Atlas Mountains (Uranga et al., 2022) (Fig. 5.3b).

The post-rift, passive margin of Morocco was initiated with the formation of a massive Jurassic carbonate reef and shelf facies (Davison, 2005) (Fig. 5.5). As a result of major sea-level regression, a humid climate, and continental sediments transported along a major river system from the African continent during the Early Cretaceous, a 1-4 km thick section of continental to marine deltaic sediments was deposited as the Tantan delta in the study area (Wynn et al., 2002; Galhom et al., 2022) (Fig. 5.3a). The overlying Cenozoic sedimentary section consists of thin, marine chalk in the study area due to the low influx of clastic sediments during this period.

A significant erosion event (Base Cenozoic unconformity) related to northwest-to-southeast convergence between Africa and Eurasia affected the study area that was documented in the DSDP-416 well, where approximately 1500 m of the section was eroded in the Late Cretaceous period (Boutefeu et al., 1980) (Fig. 5.6). DSDP-416 well shows that the overlying sediments of the unconformity are Eocene in age. A time gap of 30 to 40 million years can be observed in the depositional hiatus (Fig. 5.6). The break in vitrinite reflectance value attests to a period of widespread uplift and erosion. The vitrinite reflectance at the Late Cretaceous period is significantly higher than would be expected if the section is currently at its maximum depth of burial and maximum temperature (Fig. 5.6).

A similar stratigraphic age gap and erosion (800-1500 m) are reported in DSDP-415 and 370 wells (Powney et al., 2020). Galhom et al., 2022 also reported a 1400 m erosion of Hauterivian age in the DSDP-397 well, approximately 800 km south of the DSDP-416 well, indicating the unconformity affects the entire intervening area between the Tarfaya-Dakhla basin in southern Morocco studied by Galhom et al. (2022) and my study area edging to the north in northern Morocco (Fig. 5.3a). The timing of the erosion corresponds to the first shortening in the Atlas system in response to the onset of convergence between Africa and Eurasia (Figs. 5.3c and 5.3d).

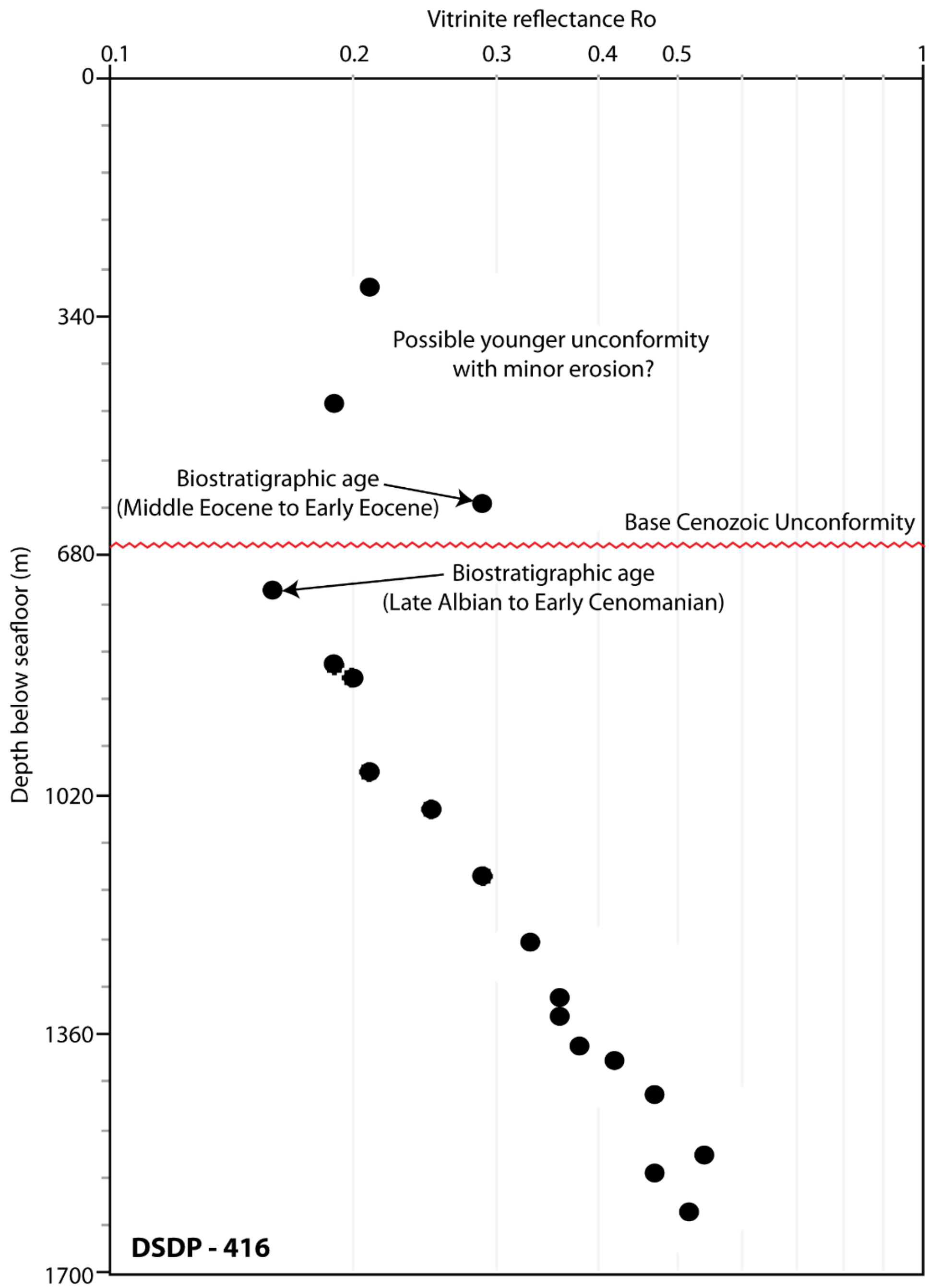

Figure 5.6: Measured vitrinite reflectance from the well at DSDP Site 416 that is located on the map in Fig. 5.3a showing the discontinuity at the Base Cenozoic unconformity produced by 1500 m of late Cretaceous erosion due to Africa-Eurasia convergence (Boutefeu et al., 1980). Other nearby DSDP boreholes also show a time gap of 30 to 40 million years (Paleocene to Mid-Late Cretaceous) with the erosion of 800-1600 m, possibly by the mass-transport complexes that formed during the first pulse of the Atlas orogenic shortening. Slope front erosion by deep-sea currents was proposed by Galhom et al. (2022) as the mechanism for the coeval erosional event in southern Morocco based on observations from DSDP site 397.

5.2.3 Source rocks of the northern Moroccan margin

There is a lack of source rock information in offshore northern Morocco because exploratory wells are few and are widely separated. Early exploration activities in the Moroccan Atlantic margin included the drilling expeditions by the Deep Sea Drilling Project (DSDP) that penetrated and cored Cenozoic, Late Cretaceous, and Early Cretaceous sections (Boutefeu et al., 1980).

Direct evidence of source rocks in the deepwater areas of the distal, rifted domain comes from DSDP information and outcrops of the Mesozoic, rift-related sedimentary section in the basal complex of Fuerteventura, Canary Islands that overlies the continent-ocean boundary as shown in Figure 5.3a. Geochemical analysis of Middle and Early Jurassic sedimentary samples from Fuerteventura showed a richness in their organic content (Geo Expro, 2019; Powney et al., 2020). Restricted carbonate-rich source rocks (Organofacies A) were interpreted for these Jurassic source rocks, which are commonly spatially discontinuous and likely to be found in the isolated deep-minibasins throughout the salt basin.

Late Jurassic source rocks are assumed to be the main source of hydrocarbons in producing fields of conjugate Nova Scotia shelf. However, source rocks of this age interval have not been reported in onshore or offshore Morocco (Olsson et al., 2018; Beicip-Franlab, 2019). Mudstone and siltstone interbedded in Early Cretaceous turbidite sequences cored in the well DSDP Site 416 contain organic matter of predominantly continental origin (Deroo et al. 1980) with low organic content and low hydrogen indices. The Late Cretaceous rocks of onshore Morocco contain thermally immature organic matter (Sachse et al., 2011; Sachse et al., 2012). Cenozoic source rocks in onshore and offshore Morocco are poorly documented and immature, where sampled (Neumaier et al., 2018). A case can be made for a possible pre-salt syn-rift source rock in half grabens of the Triassic age that are locally proven as mature in onshore Morocco (Becip-Franlab, 2019).

Using the information of previous studies focusing on source rocks of onshore and offshore Morocco, five (5) candidate source rocks in the Moroccan salt basin were modeled in this study: 1) Late Cretaceous (Turonian: 89-87 Ma); 2) Early Cretaceous (Aptian: 115-112 Ma); 3) Middle Jurassic (Bathonian: 168-166 Ma); 4) Early Jurassic (Plienbachian: 184-183 Ma); and 5) Triassic (Rhaetian: 200 Ma) (Table-5.1). Notably, all the source rock layers implemented in the model are not necessarily present along the entire study area.

Table 5.1: Table summarizing the potential Mesozoic source rocks of the northern Moroccan margin, their age, total organic carbon (TOC) content, hydrogen index (HI), and organofacies compiled by Becip-Franlab (2019). Thermal maturity kinetics is driven by burial history and source rock organofacies. TOC and HI are shown for comparison purposes only.

Potential source rocks	Stage	Age (MY)	TOC (%)	HI (mg/g)	Organofacies
Late Cretaceous	Turonian	89-87	3	600	OF-A
Early Cretaceous	Aptian	115-112	2	300	OF-A
Middle Jurassic	Bathonian	168-166	3	600	OF-A
Early Jurassic	Pliensbachian	184-183	3	450	OF-A
Triassic	Rhaetian	200	3	500	OF-B

5.3 Data and methods

This study primarily uses a ~8474 line-km grid of 2D, pre-stack depth migration (PSDM) seismic reflection data that covers an area of approximately 163,100 km² along the offshore northern Moroccan margin. Seismic mapping of the major horizons and source rock intervals was carried out using this seismic grid. The seismic dataset spans the shelf, slope, and basinal areas that range in water depth between 0 m to -5,200 m. The datasets were processed in 2017 and were kindly provided by Geoex MCG for this study.

Free-air satellite gravity field data (Sandwell et al., 2014) were used for 2D gravity modeling to better understand the thicknesses and boundaries between crustal types. Satellite gravity was also used for mapping the lateral extent of major tectonic structures, such as the continent-ocean boundary and the marginal rift that flanks the oceanic crust (Fig. 5.3b).

Two 2D gravity models were created by Miller (2021) along the most representative dip lines, covering the thicker salt basin in the south and the thinner salt basin in the north. Oasis Montaj software was used by Miller (2021) to create layers based on seismic reflection lines to compare the observed and calculated gravity values along the modeled dip-lines. The error between the observed and calculated gravity values was measured by generating the root-mean-square error. To better constrain the gravity models, Miller (2021) integrated refraction data from Contrucci et al. (2004), Klingelhoefer et al., 2009; Wenke et al., 2014; Klingelhoefer et al., 2016; Biari et al., 2017 and density values from Jiménez-Munt et al., 2011.

For initial thermal maturity modeling, two calibration wells with known lithology and borehole temperature were used to: a) calibrate the geothermal gradient in the different crustal domains (Tantan-1 in the marginal rift and DSDP-416 in the oceanic crust 450 km to the north of the Tantan-1 well and b) evaluate the petroleum generation potential in these 1D locations. The measured geothermal gradient in the marginal rift is 29 °C/km in the marginal rift at the Tantan-1 well and 23 °C/km in the oceanic crust at DSDP Site 416. Heat flow is slightly cooler in the oceanic crust because of the absence of radiogenic heat generated from the continental crust (Allen and Allen, 2013). Even though we mention geothermal gradient as a constant value (23 °C/km), it is not a univariate function. Geothermal gradient can vary depending on the rock type at specific stratigraphic intervals. For example, potassium, uranium, and thorium-rich shales will auto-generate additional heat from the radiogenic decay of those elements. The algorithm of the modeling software that I used for the study (Genesis) will fit the trend line based on the individual lithologies provided from the stratigraphic section if there is no additional temperature calibration provided. This is the function that provided the observed curvature of the trend line shown on the bottom half of the curve in DSDP site 416 calibration.

The Trinity basin modeling package (Zetaware Inc.) was used for the map-based modeling of the study area delimited by the polygon on the map shown in the map in Figure 5.3. 1D models were scaled to map-based models using temperature scalar maps to incorporate the lateral variation of heating due to key geologic controls such as paleo water depth and salt thickness.

5.4 Structural trends along the Moroccan salt basin

5.4.1 Regional seismic profiles through oceanic crust

A 175-km long reflection seismic section oriented in the strike direction reveals the crustal and sedimentary character of the transition from full-thickness continental crust, to thinned continental crust underlying the marginal rift, to Jurassic oceanic crust in the Central Atlantic Ocean (Fig. 5.7a). From south-southwest to the north-northeast, this line - which was previously interpreted by (Powney et al., 2020) - shows: a) full-thickness (30-40 km) continental crust; b) thinned, continental crust of the marginal rift overlain by 1-4-km autochthonous salt deposits where salt diapirism is concentrated in the area of the thickest salt within the marginal rift; and c) 5-6-km-thick Jurassic oceanic crust with prominent half-grabens in the fractures zones related to Atlantic opening.

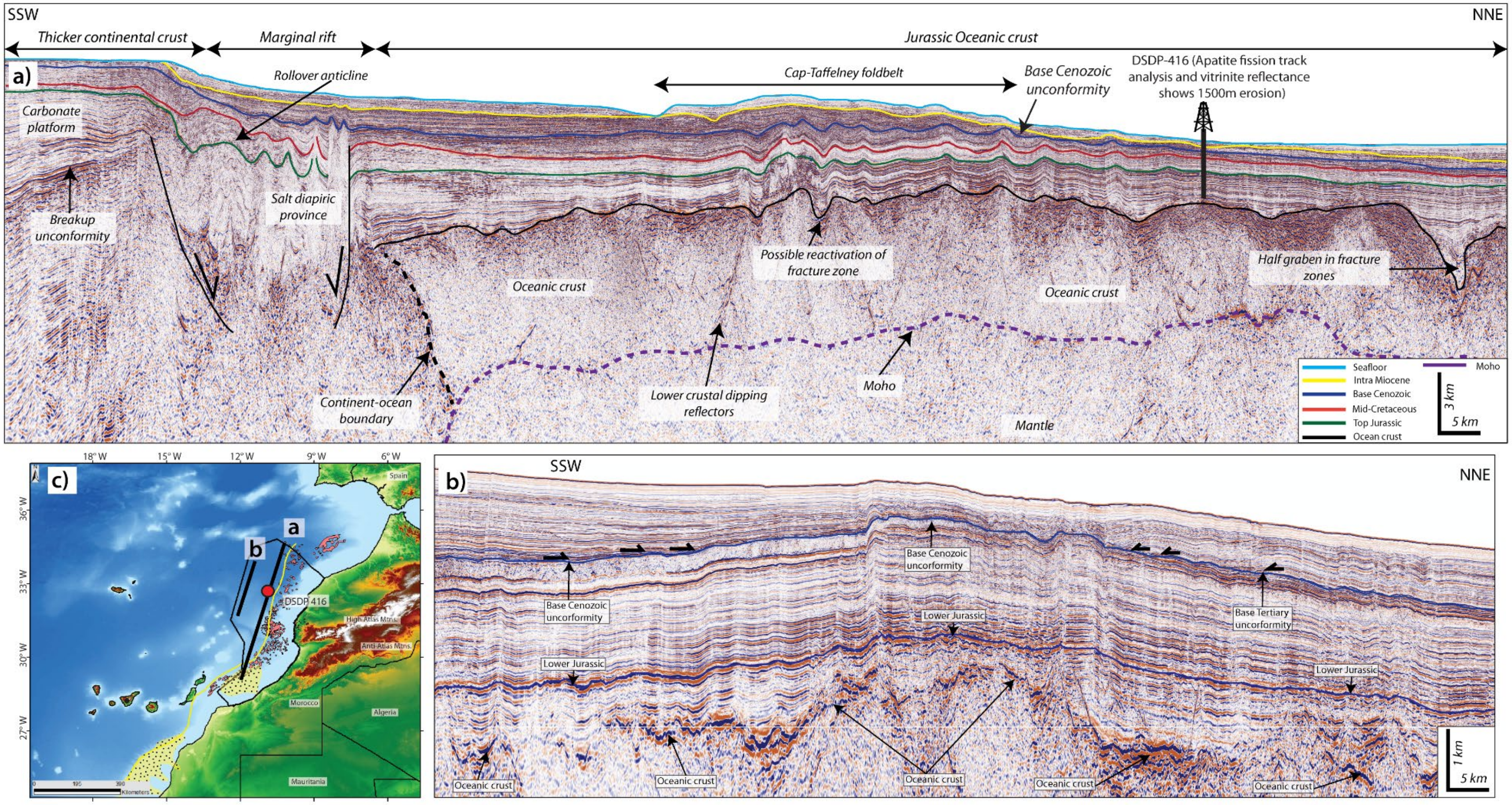

Figure 5.7: a) Interpreted regional seismic line showing the major tectonic elements of the margin, including the Jurassic carbonate platform, salt basin, oceanic crustal deformation of the Cape Tafelney foldbelt, and normal oceanic crust with its underlying reflection marking the base of the oceanic crust (Moho). Reactivation of oceanic fracture zones near the elevated crest of the Cape Tafelney anticline. b) Zoomed seismic line showing the reflection termination associated with Base Cenozoic unconformity. The age of the unconformity and interpreted horizons were constrained from the biostratigraphic report of the DSDP-416 borehole. c) Inset map shows the location of the two seismic lines shown. Seismic data provided courtesy of Geoex MCG.

A “step-up fault” with a distinct reflection shown as a dotted line in Figure 5.7a marks the transition between the necked zone of the thinned continental crust and the adjacent oceanic crust of the Late Jurassic age. Landward of the necking domain, a prominent roll-over anticlinal structure can be observed along this faulted boundary of the marginal rift.

A zoomed-up seismic line in Figure 5.7b shows the truncation of the Base Cenozoic unconformity and folding of the oceanic crust expressed as the Cape-Tafelney foldbelt. A 500-700 m thick package of mass transport complexes can be overserved beneath the unconformity (Fig. 5.7b). The age of the hiatus at the unconformity and interpreted horizons were constrained as (Late Cretaceous to Eocene) from the biostratigraphy report of the DSDP-416 borehole (Powney et al., 2020).

5.4.2 Regional seismic profiles through marginal rift

Two northwest-southeast dip-oriented seismic lines are shown in Figure 5.8 to reflect the structural style and the variability of the crustal structure of the marginal rift. The 75-km long northern seismic section shown in Figure 5.8a covers an area of relatively thinner salt and shows a variety of salt-associated structures. Tilted blocks along listric, normal faults mark the transition between the necked zone of continental crust and the full-thickness continental crust that underlies the modern coastline of Morocco. The necked domain of thinned, continental crust is dominated by diapiric salt structures, some of which are presently active, as seen from their elevations and seafloor deformation. Jurassic to present sediment thickness in the marginal rift ranges 4-6-km in this domain, higher than the adjacent full-thickness continental crust and oceanic crustal domain. The thickening in slope due to Early Cretaceous deltaic deposition is not observed along this part of the margin (Fig. 5.8a).

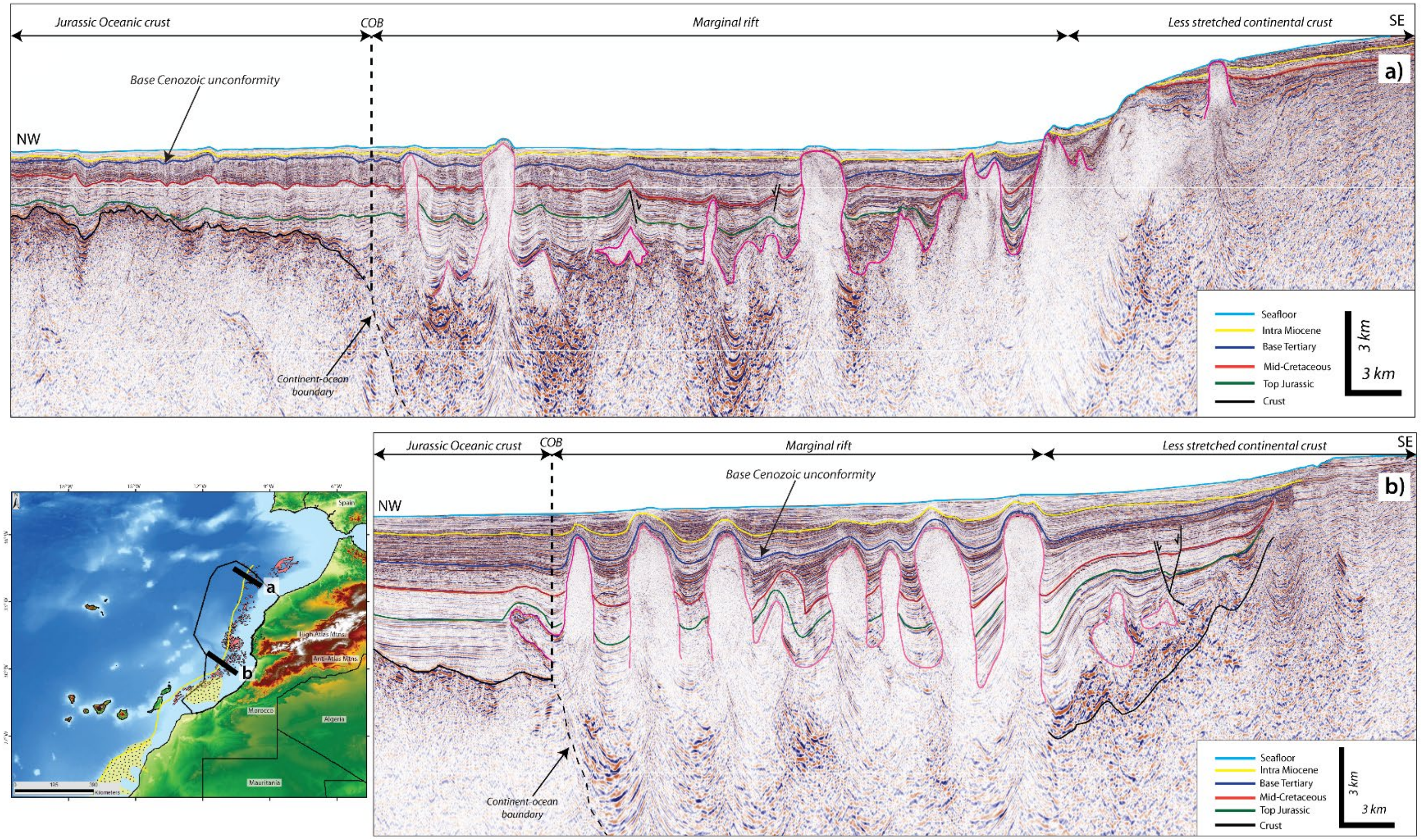

Figure 5.8: a) Interpreted dip-oriented seismic line from the northern part of the Moroccan marginal rift located on the inset map showing a wider and less inverted marginal rift with a more deeply buried salt layer. b) Interpreted dip-oriented seismic line from the southern part of the marginal rift showing a narrower and more elevated and inverted marginal rift with more pronounced diapirism. Although the transition from continental crust to oceanic crust is discernible from the seismic lines, neither the thickness of the oceanic crust nor the thinned, continental crust beneath the Moroccan marginal rift is interpretable from the seismic reflection data alone and requires gravity modeling to estimate the top and base of the two crustal types. Seismic data provided courtesy of Geoex MCG.

The interpreted 55-km long dip-oriented seismic line from the southern part of the study area covers the relatively thicker and more elevated part of the salt basin that I interpret as its higher degree of tectonic inversion (Fig. 5.8b). The slope area of the margin has 2-3 km of Jurassic sedimentary rocks associated with the progradation of the Tantan delta of the Early Jurassic age. Some smaller salt bodies in the updip slope can be interpreted based on their massive or chaotic reflection patterns.

Large-scale salt diapiric structures dominate the entire marginal rift area along this seismic section. The continent-ocean boundary approximately defines the basinward extent of the presence of salt bodies. A basement step-up fault marks the continent-ocean boundary between the necked zone of the thinned continental crust and the adjacent oceanic crust. Although the continent-ocean boundary is discernible from the seismic reflection pattern, the thickness of the crust is not interpretable (Fig. 5.8b).

5.5 2D gravity modeling along the Moroccan marginal rift

Because the available seismic reflection lines cannot penetrate through the thick salt cover, two 2D gravity modeling along the same dip-oriented lines shown in Figure 5.8 were performed by Miller (2021) to better infer the deeper crustal structure and thickness. Reflection seismic interpretations were used as the base for different sedimentary stratigraphic units and refraction data were integrated into the gravity model to provide improved constraints on the crustal structure.

The 2D gravity modeling in both models reveals the southeast-to-northwest transition from the full-thickness continental crust (30-40 km) to thinned, transitional crust (6-10 km) and to oceanic crust underlying the deepwater area (6-7 km) (Figs. 5.9a, b). The necked domain of thinned continental crust shows 5-6 km thickness and is filled by evaporites or clastic rocks. The structure varies in the thinned continental crustal domain due to full- and half-grabens. Through modeling, Miller (2021) defined the density contrast between the upper and lower crust. The 2D gravity models (Fig. 5.9) reveal that the continental-oceanic boundary aligns well with the marginal rift interpretation as seen on the free-air gravity map (Fig. 5.3b). The observed and calculated gravity values in these models show an excellent fit with a root mean square error of <10.

Figure 5.9: Gravity models along the 2D seismic reflection lines shown in Fig. 5.8 and their respective graphical comparison of observed free-air gravity values to the calculated gravity values. Multi-layer crustal and stratigraphic cross-section with assigned model densities is shown. The location of the line of sections of the two models are shown in Fig. 5.3. a) This model located in the northern part of the study area shows a transition from full thickness continental crust (38 km) in the east to a thinned continental crust of 8 km thickness that underlies the marginal rift. b) A similar crustal morphology and thickness are observed in this model compared to model shown in Fig. 5.9a, with a notable increase in the presence of salt diapirs and thickness. I attribute this change to the more pronounced inversion of the basin seen in Fig. 5.9b, which is in an east-west alignment with the uplift of the onland High Atlas Mountains and the offshore Cape Tafelney foldbelt

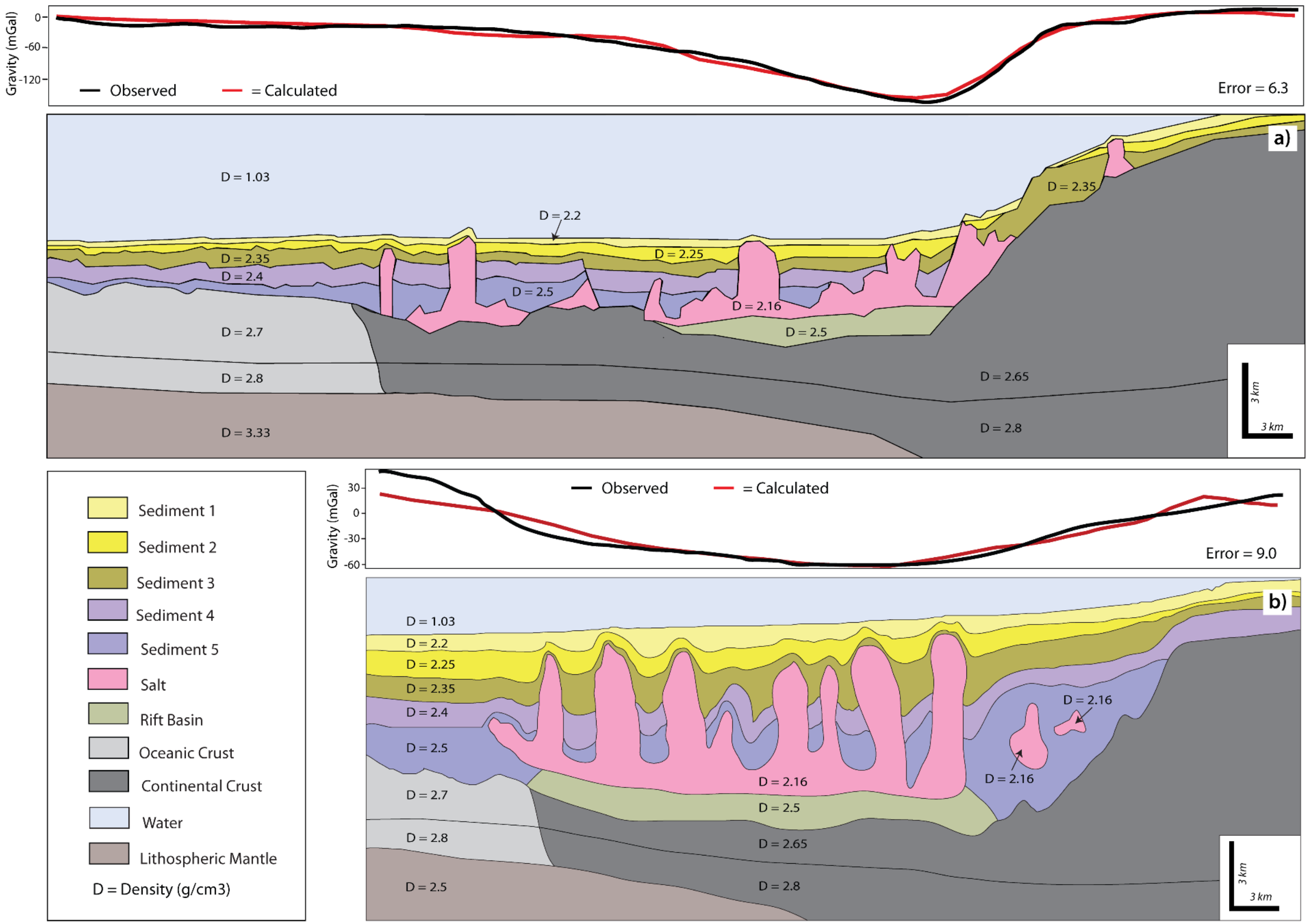

Gravity (mGal)
0
-60
-120
Observed
= Calculated
Error = 6.3
a)
D = 1.03
D = 2.2
D = 2.35
D = 2.25
D = 2.35
D = 2.4
D = 2.5
D = 2.16
D = 2.5
D = 2.7
D = 2.8
D = 2.65
D = 3.33
D = 2.8
3 km
3 km
Sediment 1
Sediment 2
Sediment 3
Sediment 4
Sediment 5
Salt
Rift Basin
Oceanic Crust
Continental Crust
Water
Lithospheric Mantle
D = Density (g/cm3)
Gravity (mGal)
30
0
-30
-60
Observed
= Calculated
Error = 9.0
b)
D = 1.03
D = 2.2
D = 2.25
D = 2.35
D = 2.4
D = 2.5
D = 2.16
D = 2.16
D = 2.16
D = 2.5
D = 2.7
D = 2.8
D = 2.65
D = 2.5
D = 2.8
3 km
3 km

5.6 Thermal maturity modeling results

5.6.1 Variation of geothermal gradients in different crustal domains

Two borehole locations with known lithologies and temperature gradients were used to calibrate the geothermal gradient in different tectonic domains in the study area (Fig. 5.10). The measured temperatures were extracted from well information compiled by Beicip-Franlab (2019). The Tantan-1 well was used to derive the geothermal gradient in the marginal rift area with a transitional crustal thickness of 5-6 km and DSDP-416 for the oceanic crust (Fig. 5.10).

I added an 8% upward uncertainty with the measured temperature as the Beicip-Franlab (2019) report did not document whether they were corrected for the cooling effect of drilling mud. The measured geothermal gradient in the marginal rift is 29 °C/km in marginal rift and 23 °C/km in the oceanic crust. Heat flow is slightly cooler in the oceanic crust because of the absence of radiogenic heat generated from the continental crust (Allen and Allen, 2013).

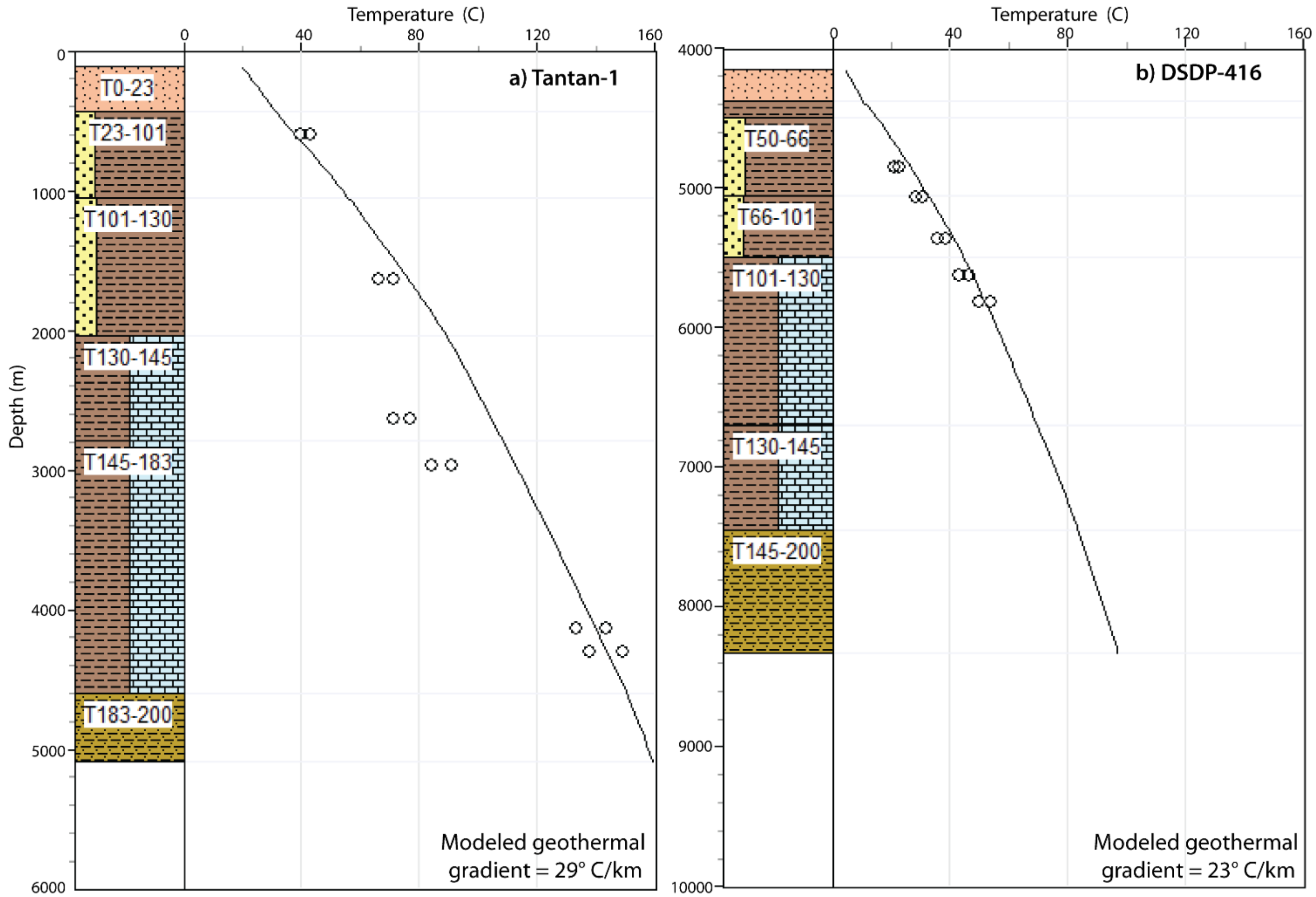

Figure 5.10: Temperature-depth graph showing measured and modeled geothermal gradients of a) Tantan-1 well and b) DSDP 416 well located on the map in Fig. 5.3a. The geothermal gradient is relatively higher in the Tantan-1 well than in the well at Site DSDP-416 as the result of additional radiogenic heat generated from the continental crust and the relatively colder Mesozoic oceanic crust, which lacks radiogenic heat. The absence of deeper temperature measurements at the drilling log at site DSDP-416 will increase the uncertainty of the geothermal gradient in the oceanic crust. The measured temperatures are extracted from the report by Beicip-Franlab (2019), which did not contain any documentation of the cooling effect of drilling mud. For this reason, I have added an uncertainty range represented by the adjacent dots.

5.6.2 1D burial and thermal histories

Thermal maturity modeling for the Tantan-1 well located in the southern part of the marginal rift shows that: 1) the Triassic and Jurassic source interval occupies the present-day late oil to gas window (140-150 °C) and 2) the Cretaceous source interval is either presently immature or occupies the early oil expulsion window (110 °C). The Jurassic source rocks entered the oil window early in the Early Cretaceous period and had ample geologic time to migrate into the younger Cretaceous and Cenozoic reservoir rocks. The potential Early and Late Cretaceous source rocks remained immature in the marginal rift, as shown in this study (Fig. 5.11a).

Thermal maturity modeling at the DSDP-416 well location shows that the Jurassic section is presently in a temperature range of 75-100 °C and immature for petroleum generation. Similarly, the relatively younger source rocks of Cretaceous age remain immature (<50 °C) (Fig. 5.11b). Lower thermal maturity above the oceanic crust results from a combination of Late Cretaceous tectonic uplift event and the cooling effect of the oceanic crust that underlies the deepwater areas (Fig. 5.11b).

Figure 5.11: Comparison of the 1D burial and thermal history modeling results from a) the Tantan-1 well and b) the DSDP-416 well. Due to high overburden sediment thickness and radiogenic heat source in the thinned, continental crust underlying the Tantan-1 well, Jurassic source rocks are in the present-day oil window (100-150 °C). In contrast, in DSDP-416, Jurassic source rocks remain immature (> 100 °C). Label over lithology patterns indicates the age span of each stratigraphic unit in millions of years.

a) Tantan-1

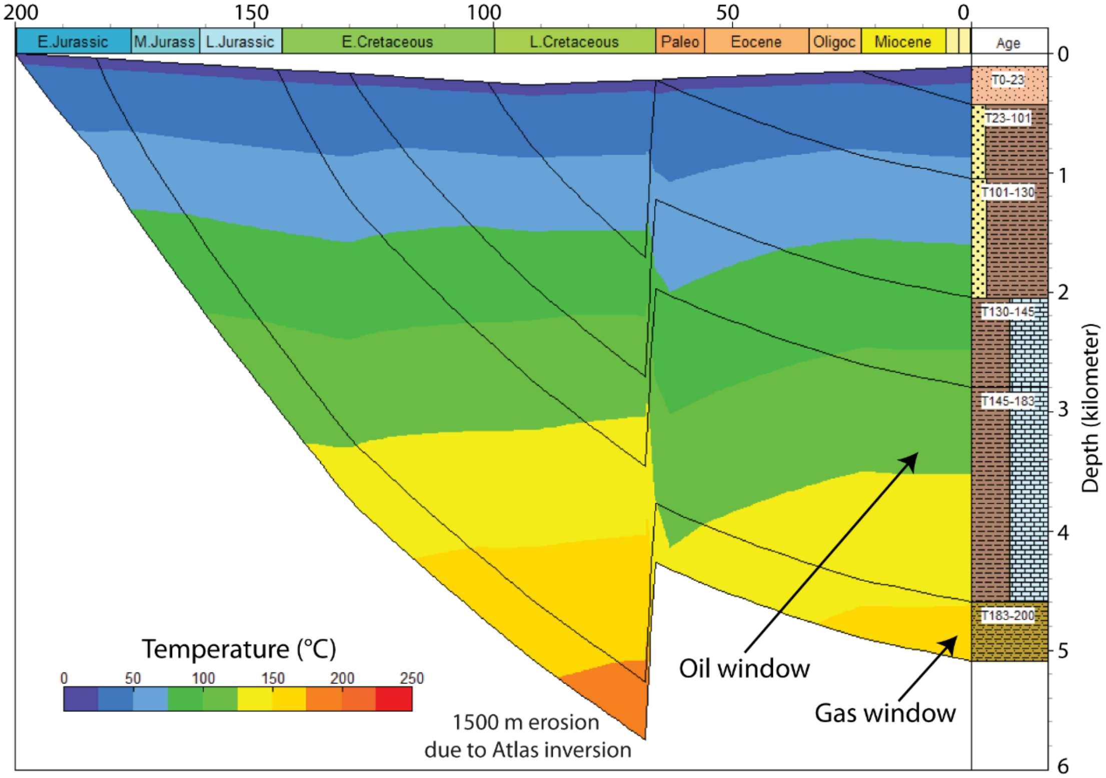

b) DSDP-416

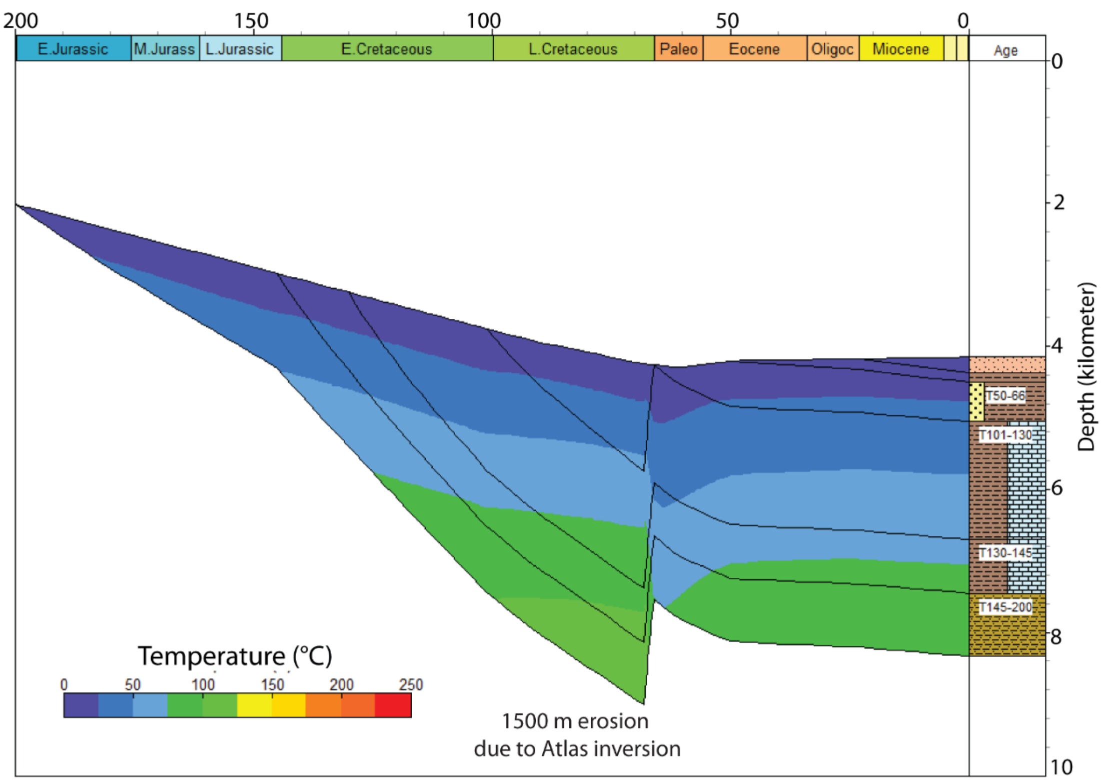

5.6.3 Regional maturity trends predicted by map-based modeling

In Figure 5.12, present-day thermal maturity maps were created for 1) Late Cretaceous (Turonian: 89-87 Ma); 2) Early Cretaceous (Aptian: 115-112 Ma); 3) Middle Jurassic (Bathonian: 168-166 Ma); 4) Early Jurassic (Plienbachian: 184-183 Ma); and 5) Triassic (Rhaetian: 200 Ma) source intervals. This map-based approach takes into account thermal maturity variations related to the crustal type and thickness, paleo-water depth, and Jurassic salt thickness.

The Late Cretaceous source rock is predicted to be immature (> 100 °C) in the study area. Early Cretaceous rock is predicted to be immature in the northern part of the marginal rift with early oil window maturity (100-120 °C) in the salt-related minibasins. A similar thermal maturity trend is observed for the modeled Jurassic source intervals. Thermal maturity maps show (100 °C – 150 °C) in the southern marginal rift area. In contrast, the northern part of the marginal rift remains the most extensive area of immaturity with the exception of a few isolated minibasins. The Triassic thermal maturity map shows gas maturity (> 150 °C) in the southern marginal rift and oil window (100 °C – 150 °C) in the north. Oceanic crust generally shows source rocks immaturity in all modeled intervals with some isolated patches of early oil window.

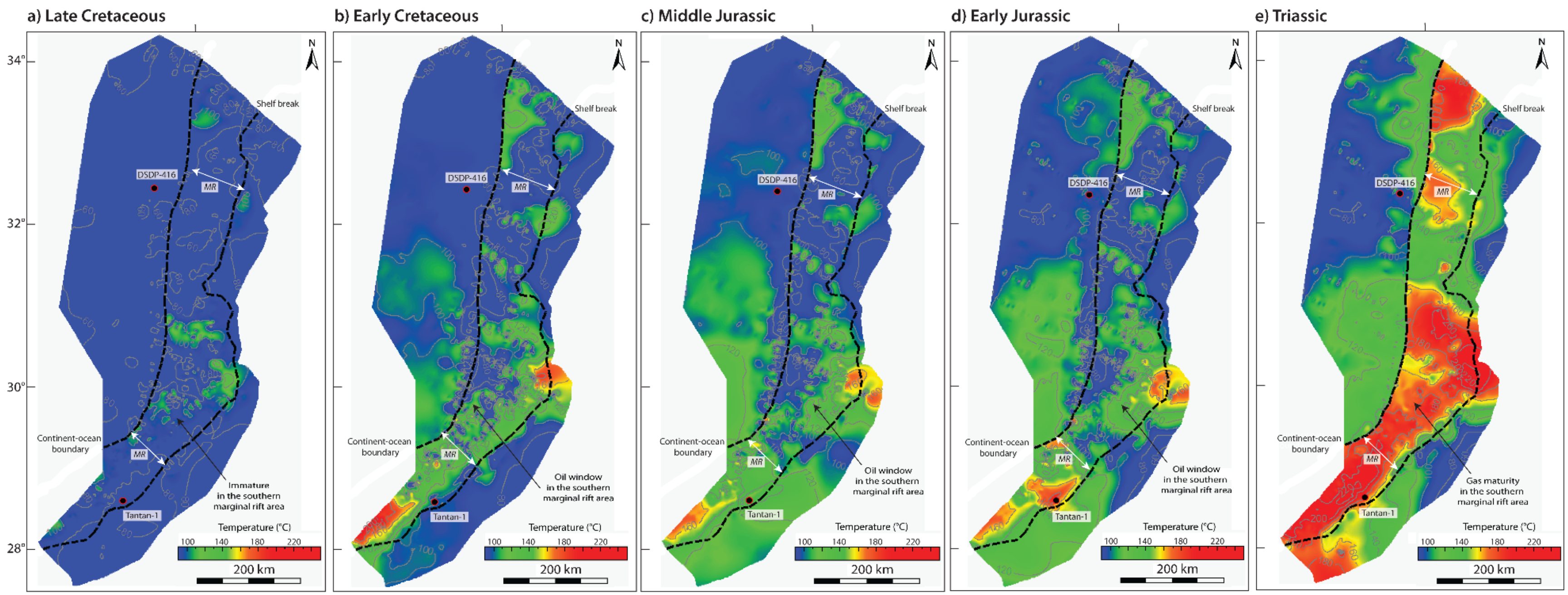

Figure 5.12: Comparison of thermal maturity maps of the potential source rock intervals in the northern Moroccan margin. a) Late Cretaceous/Base Cenozoic source rock; b) Early Cretaceous source rock; c) Middle Jurassic source rock; d) Early Jurassic source rock; and e) Triassic source rock. Late Cretaceous/Base Cenozoic and Early Cretaceous thermal maturity maps show immaturity (>100 °C) for source rocks of this age range in the study area. Middle Jurassic and Early Jurassic thermal maturity maps show oil window (100 °C – 150 °C) in the area of the southern Moroccan marginal rift. The Triassic thermal maturity map shows gas maturity (> 150 °C) for source rocks of this age in the southern marginal rift and an oil window (100 °C – 150 °C) in the northern marginal rift. All modeling scenarios show that source rocks that overlie oceanic crust remain immature due to no input from radiogenic heating.

5.7 Discussion

5.7.1 Modeling parameters and uncertainties

The bottom-up study of integrated thermal maturity modeling incorporates crustal parameters from refraction studies and gravity modeling with interpretation of a seismic reflection grid to yield a petroleum system evaluation of the offshore Moroccan salt basin. Thermal maturity modeling provides accurate subsurface temperature offshore Moroccan margin when three factors are taken into consideration: 1) differences in crustal type and thickness from east to west (full-thickness continental crust, thinned continental crust, hyperextended transitional crust, and oceanic crust); 2) the control of continental to oceanic crustal types to the total radiogenic heat production that influences heat flow in the overlying sedimentary sequence; and 3) disruption of isotherms around salt bodies due to differing thermal conductivity of salt.

Small differences might arise from accounting for the thermal dependence of the salt conductivity on temperature and salt geometry evolution through time (Davison and Cunha, 2017). Because Trinity does not take into account lateral variations of heat flow and salt geometry through time, some errors might arise in calculating source rock maturity around the edges of large salt bodies.

A 1500 m of eroded sedimentary section is modeled in both of these 1D and subsequent map-based models because the Base Cenozoic unconformity is extensive across the entire study area based on four main observations: a) termination of seismic reflections along an unconformity surface on the regional seismic grid (Fig. 5.7); b) the break in vitrinite reflectance in DSDP-416 as shown in Figure 5.6; c) similar erosion (800-1500 m) is reported in DSDP-415 and 370 wells from vitrinite reflectance and apatite fission track analysis (Powney et al., 2020); and d) Galhom et al. (2022) also reported a 1400 m erosion of Hauterivian age in DSDP-397 well, approximately

800 km south of DSDP-416. Although multiple scenarios can be modeled based on the estimated ranges for the thickness of the eroded section, the linked changes in thermal maturity remain relatively minor.

5.7.2 Maturation history and hydrocarbon sweetspots

Predicted source rock maturation and generation vary laterally through the offshore Moroccan margin (Fig. 5.12). My modeling predicted favorable source rock thermal maturity in the southern 400 km of the marginal rift area as a zone of mature Early Jurassic source rocks (Fig. 5.13c). In addition to control of the type and thickness of crust, change in stratigraphic thickness and localized tectonic events control the lateral variation of maturity.

A significant erosion event (Base Cenozoic unconformity) affected the entire study area as documented in the DSDP-416 well (Fig. 5.6). The Base Cenozoic unconformity erodes approximately 800-1500 m of sediment in the study area, making the Cenozoic overburden relatively thin. The vitrinite reflectance at the Late Cretaceous period is significantly higher than would be expected if the section is currently at its maximum depth of burial and maximum temperature (Fig. 5.6). The Late Cretaceous timing corresponds to the initial shortening in the Atlas system in response to the onset of convergence between Africa and Eurasia (Schettino and Turco, 2011; Neumaier et al., 2018). Previous workers have identified three pulses of inversion, but the Base Cenozoic corresponds to the most prominent period of inversion along the southern margin of Morocco (Galhom et al., 2022).

A prior Early Cretaceous depositional event changes the maturity in the southern portion of the marginal rift. As a result of major sea-level regression and massive continental sediments supply from the African continent during the Lower Cretaceous, a 1-4 km thick section of continental to marine deltaic sediments was deposited as Tantan delta in that area (Fig. 5.3a). Considering the higher geothermal gradient of 29 °C in the transitional continental crust, that extra overburden was enough to mature the Jurassic source rocks in that area.

A compilation of existing exploration drilling results shown in Figure 5.13b matches the predictions based on my modeling results shown in Figure 5.12. The subsurface penetrations with hydrocarbon shows are located south of the Cape Tafelney trend and within the Early Cretaceous depocenter of the Tantan delta. Almost no well penetrations with hydrocarbon shows are located in the northern portion of the marginal rift, where I predict a lack of maturity for the Jurassic source rocks (Fig. 5.13b).

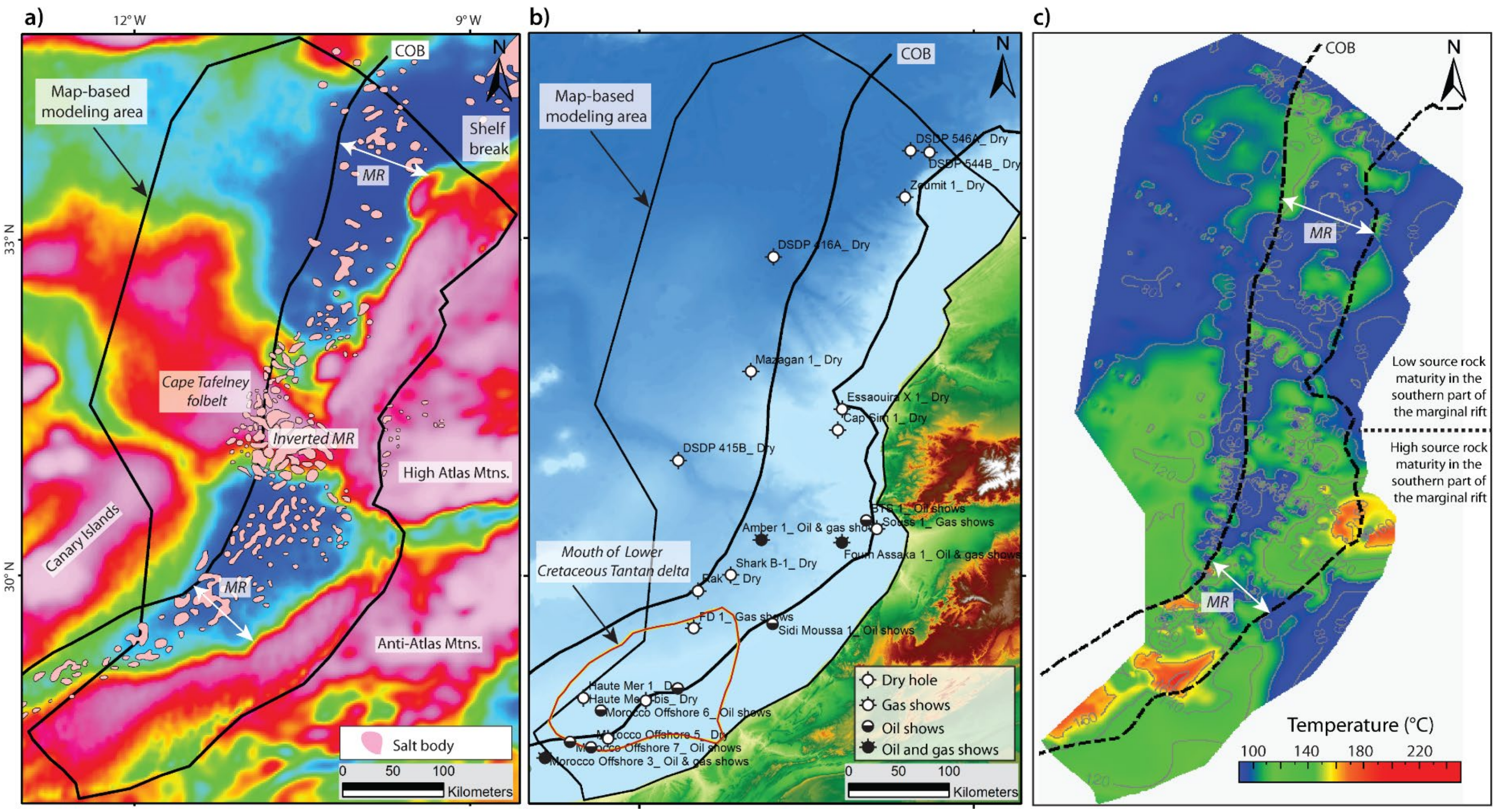

Figure 5.13: a) Free-air gravity map outlining the 50-80-km-wide Moroccan marginal rift that parallels the continent-oceanic boundary and coastline of present-day Morocco. Also seen on the gravity image are the High Atlas and Anti-Atlas mountains, an inverted Triassic-Jurassic rift, and the collinear Cape Tafelney anticline, as seen on the seismic lines in Figs. 5.7a and 5.7b. b) Topographic and bathymetric map showing the location of existing drilling locations in the study area of the Moroccan marginal rift and their status as producing wells, wells with shows, or dry holes. c) Thermal maturity map based on my 1-D thermal maturity modeling of the proven Lower Jurassic source rock in the offshore Moroccan margin. My prediction of thermal maturity shows southern marginal rift area is mature for hydrocarbon generation in contrast to the northern area that remains immature. A clear correlation can be observed between the maturity prediction from the 1-D basin model and oil and gas, assuming all hydrocarbons are based on Jurassic source rocks.

5.7.3 Example of trapping styles and patterns of hydrocarbon migration

Potential trapping structures in this area include thrust-faulted strata above salt pillows in addition to associated faulting and folding of the overlying Cenozoic section. Combined structural and stratigraphic traps are present along the upturned strata at the flanks of the salt diapirs (Fig. 5.14). Both broad and subtle anticlinal structures associated with salt pillow structures in the marginal rift create structural traps with four-way closures.

High-amplitude reflections above primary Jurassic salt are considered carbonates likely with high reservoir potential. Updip-pinch out with gentle folding of Mesozoic carbonates provide potential three-way fault traps. Timing of trap formation versus hydrocarbon expulsion is assumed not to be a significant issue, with peak expulsion occurring right after trap formation during the Cenozoic. However, it is not clear if expulsion continued into the Cenozoic when recent salt movements could provide a risk of breaching some of the earlier-formed trapping structures (Kenning and Mann, 2020b).

Significant normal faulting throughout the stratigraphic section and permeable carrier beds likely provide efficient vertical migration pathways from local kitchen areas, as shown by the arrows in Figure 5.14. Minimal lateral, long-distance is required to provide hydrocarbon charge. Substantial variation in burial depth on either side of some structural features could also result in individual traps being charged by a mixture of different fluid types produced from source rocks at variable levels of thermal maturity (Hasan and Mann, 2021).

Triassic lacustrine source rocks would likely be required for favorable hydrocarbon prospectivity in the pre-salt section, as the relative structural and stratigraphic positions make it unlikely that post-salt source rocks could have charged the pre-salt system (Kenning and Mann, 2020b). If pre-salt, Triassic source rocks are present along the deepwater Moroccan margin, my modeling predicts mature gas or overmaturity across significant areas (Fig. 5.12e). Numerous thick-skinned rift-related normal faults would provide excellent migration routes and trapping structures in the form of tilted fault blocks, particularly in the deeper syn-rift section if effective source and reservoir rocks are present at this depth (Fig. 5.14). Pre-salt source intervals may also charge the Cenozoic reservoir through the salt window (where salt is welded).

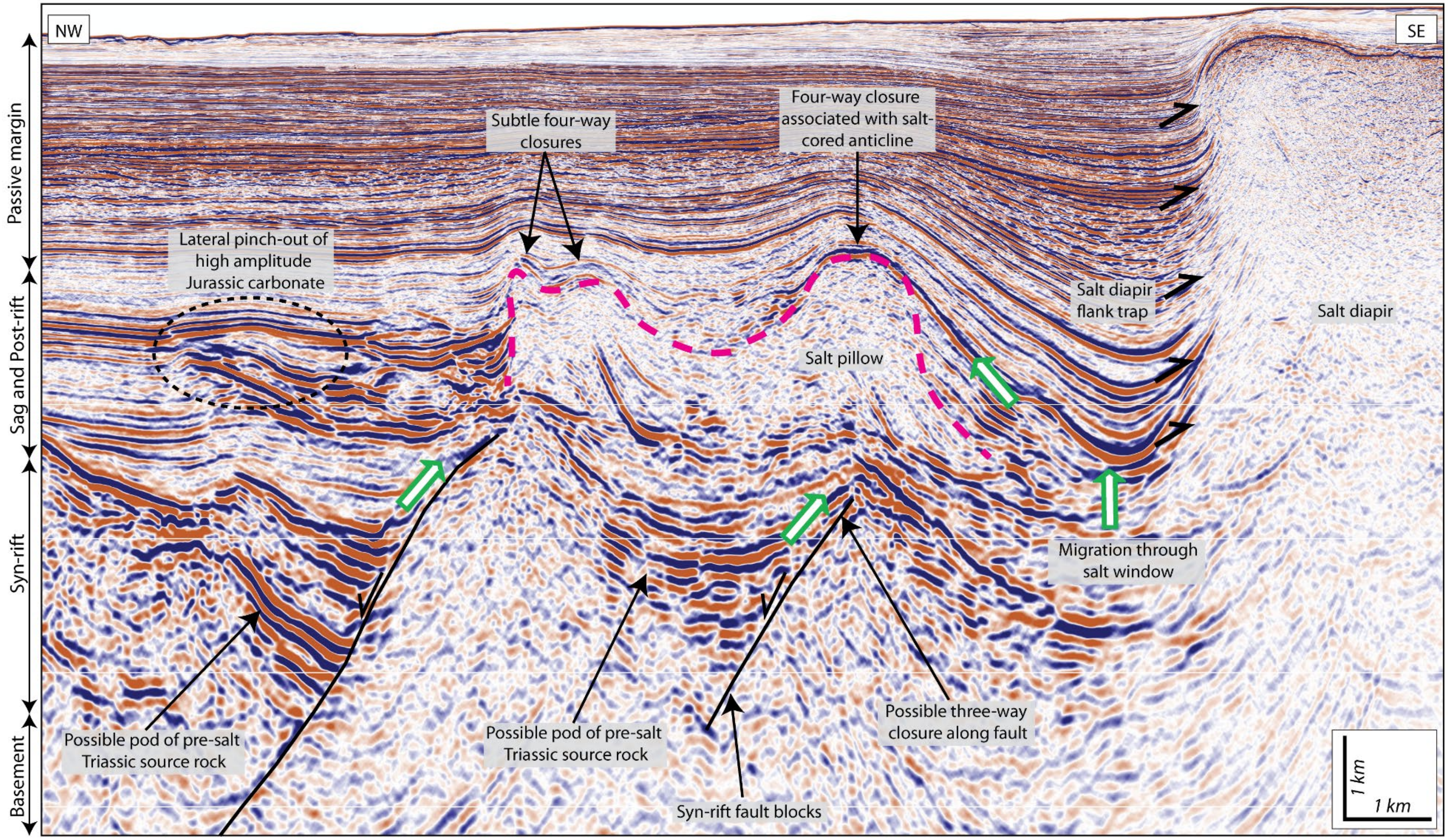

Figure 5.14: Seismic reflection line located on the map in Fig. 5.3a shows various undrilled and potential hydrocarbon trap types with their inferred migration pathways in the study area. Four-way and three-way structural closures are commonly associated with salt diapirs and salt pillows, shown by the pink dotted line.

5.7.4 Petroleum system time chart

The main elements of the petroleum systems for the marginal rift are summarized in a petroleum system event chart (Fig. 5.15). The trap formation timing in deepwater northern Morocco primarily formed as inverted structures during the Cenozoic period as the result of the Atlasic orogeny (Figs. 5.3c, d). Some initial halokinetic and gravity-driven salt structures are reported but not the primary mechanism for forming the structures (Hafid, 2000; Uranga et al., 2022).

Reservoir presence is a critical risk factor in the deepwater exploration of the Moroccan Atlantic margin. Regional evidence shows that the Early Cretaceous sequences are significantly more sand-prone in the deepwater than the overlying Late Cretaceous and Cenozoic strata (Davison, 2005). However, there might still be a case for uneven reservoir distribution within the Late Cretaceous sequence due to the syn-depositional growth of some of these salt-related structures (Tari et al., 2013). The limited siliciclastic sediment supply during the entire Cenozoic to Upper Cretaceous was caused by the prevailing dry climate and lack of major river systems (Tari and Jabour, 2013).

The Cretaceous interval remains immature in the study area. The proven Early Jurassic source rock enters the expulsion window early in Lower Cretaceous and transitions to the gas window in Cenozoic. Speculative Triassic source rock is overmature in the study area. Even though the trap formation is after the source rocks pass the oil window, the 'lag time' required for vertical migration can explain both oil and gas shows in the drilled wells. Speculative Triassic source rock has begun peak hydrocarbon expulsion as early as the Early Cretaceous, before the formation of most post-salt structures.

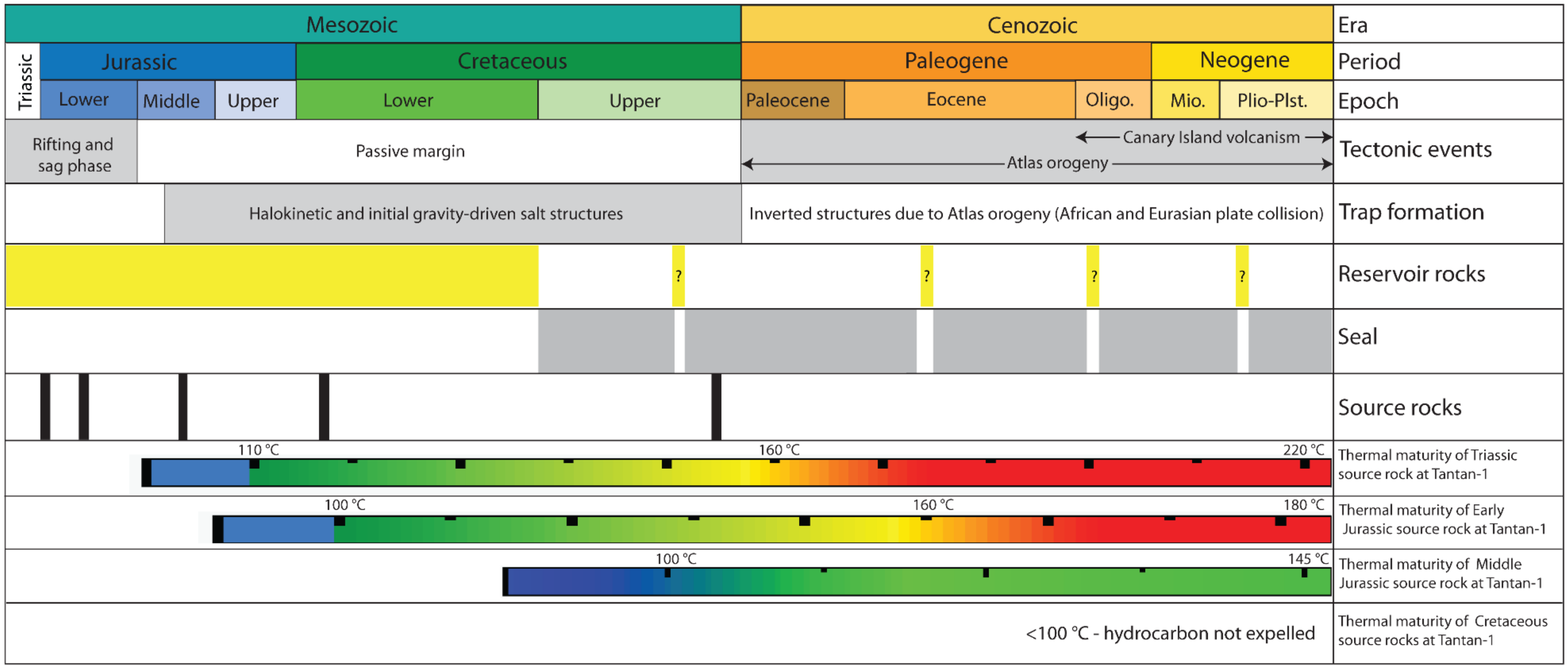

Figure 5.15: Petroleum systems chart for the study area of offshore Morocco showing tectonic events, petroleum system elements, and the predicted thermal maturity of source rocks. The Late Cretaceous-Cenozoic uplift event related to the North Africa-Eurasia convergence during this period elevated the early and Cretaceous and Cenozoic source rocks to the point that none reached maturity. While also uplifted by the same event, the Jurassic source rocks were deeply buried enough before this uplift event that these source rocks reached maturity.

5.8 Conclusions

Integrated gravity and seismic data analysis reveals the structure of the 50-80-km-wide Moroccan marginal rift of the Triassic-Jurassic ages that overlies the necked zone of the rifted continental margin; this rift structure contains 2-3 km of salt and clastic sedimentary rocks of the Jurassic age.

The geothermal gradient in the marginal rift is 29 °C and in the oceanic crust is 23 °C. Radiogenic heat due to the granitic composition of continental crust causes a higher geothermal gradient. The absence of radiogenic heat in the oceanic crust results in relatively lower geothermal gradients and can explain the immaturity of source rocks in these deepwater areas.

Jurassic source rocks are mature in the southern 400 km of the marginal rift for petroleum generation. In contrast, Cretaceous source rocks remain immature or were eroded during a tectonic uplift event related to the Atlasic orogeny caused the northwest-to-southeast convergence between Africa and Eurasia during the Late Cretaceous. Maturity is higher in the southern part of the study area due to the deposition of the Lower Cretaceous delta and the deposition of a 1-4 km of additional overburden thickness.

BIBLIOGRAPHY

Adegoke, O.S., Oyebamiji, A.S., Edet, J.J., Osterloff, P.L., Ulu, O.K., 2017. Geology of the Niger Delta Basin. In: Adegoke, O.S., Oyebamiji, A.S., Edet, J.J., Osterloff, P.L., Ulu, O.K. (Eds.), *Cenozoic Foraminifera and Calcareous Nannofossil Biostratigraphy of the Niger Delta*, Amsterdam, Netherlands, Elsevier, p. 25-66.

Allen, P.A., Allen, J.R., 2013. Basin Analysis: Principles and Application to Petroleum Play Assessment (3rd Edition), Wiley-Blackwell, Oxford, 632 p.

Ambrose, W.A., Wawrzyniec, T.F., Fouad, K., Talukdar, S.C., Jones, R.H., Jennette, D.C., Holtz, M.H., Sakurai, S., Dutton, S.P., Dunlap, D.B., Guevara, E.H., Meneses- Rocha, J., Lugo, J., Aguilera, L., Berlanga, J., Miranda, L., Morales, J.R., Rojas, R., Solís, H., 2003. Geologic framework of upper Miocene and Pliocene gas plays of the Macuspana Basin, southeastern Mexico. Am. Assoc. Petrol. Geol. Bull., v. 87, p. 1411–1435.

Apango, F., Snedden, J.W., Daigle, H., Yurchenko, I.A., 2021. Analysis of hydrocarbon underfilled and water-filled Miocene deep-water reservoirs, eastern Mexico offshore. Mar. Petrol. Geol., v. 131, n. 105158.

Arzate, S.O., Moguel, C.R., López, M.M., Flores, M.F., 2009a. Basin modeling of the Upper Jurassic petroleum systems (Tithonian and Oxfordian) in the Akalan-Chilam area of the Campeche sound in the southern Gulf of Mexico. In: Bartolini, C., Roman Ramos, J.R. (Eds), *Petroleum Systems in the Southern Gulf of Mexico*. AAPG Memoir, v. 90, p. 285–313.

Arzate, S.O., Esteban, S.M., Cuauhtémoc, R.M., Joel, R.R., Edgar, B.R., Sergio, H., Alejandro, C., 2009b. Two-dimensional and three-dimensional numerical simulation of petroleum systems approaching the deep-water Gulf of Mexico (Kayab Area, Campeche Sound, Mexico): Definition of thermally mature and prospective areas. In: Bartolini, C., Roman Ramos, J.R. (Eds), *Petroleum Systems in the Southern Gulf of Mexico*. AAPG Memoir, v. 90, p. 117–136.

Babault, J., Teixell, A., Struth, L., Van Den Driessche, J., Arboleya, M.L., Tesón, E., 2013. Shortening, structural relief and drainage evolution in inverted rifts: insights from the Atlas Mountains, the eastern Cordillera of Colombia and the Pyrenees. In M. Nemcok, A. Mora, and J. W. Cosgrove (Eds.), *Thick-skin-dominated Orogens: From Initial Inversion to Full Accretion.* Geol. Soc. London. Spec. Publ. v. 377, p. 141–158.

Bain, J., Kegel, J., O'Reilly, C., 2019. Crustal interpretation by gravity, magnetics, and seismic data over the Gulf of Mexico. Gulf Coast Assoc. Geol. Soc. Trans., v. 69, p. 319–331.

Barbero, L., Teixell, A., Arboleya, M.-L., Río, P.D.., Reiners, P.W. and Bougadir, B., 2007. Jurassic-to-present thermal history of the central High Atlas (Morocco) assessed by low-temperature thermochronology. Terra Nova, v. 19, p. 58-64.

Beicip-Franlab., 2019. Thermal and maturity modeling of Nova Scotia and northern Morocco conjugate margins. p. 33. Accessed on September 22, 2022. https://oera.ca/sites/default/files/2020-03/Chapter5_Basin_Modelling_FINAL.pdf.

Benabdellouahed, M., Klingelhoefer, F., Gutscher, M.A., Rabineau, M., Biari, Y., Hafid, M., Duarte, J.C., Schnabel, M., Baltzer, A., Pedoja, K., Le Roy, P., Reichert, C., Sahabi, M., 2017. Recent uplift of the Atlantic Atlas (offshore West Morocco): Tectonic arch and submarine terraces, Tectonophysics, v. 706–707, p. 46-58.

Bhatnagar, P., Verma, S., Bianco, R., 2019. Characterization of mass transport deposits using seismic attributes: Upper Leonard Formation, Permian Basin. Interpretation, v. 7, p. 19-32.

Biari, Y., Klingelhoefer, F., Sahabi, M., Funck, T., Benabdellouahed, M., Schnabel, M., Reichert, C., Gutscher, M.-A., Bronner, A., Austin, J. A., 2017. Opening of the central Atlantic Ocean: implications for geometric rifting and asymmetric initial seafloor spreading after continental breakup, Tectonics, v. 36, p. 1129–1150.

Bilotti, F., Shaw, J.H., 2005. Deep-water Niger Delta fold and thrust belt modeled as a critical-taper wedge: The influence of elevated basal fluid pressure on structural styles. Am. Assoc. Pet. Geol. Bull., v. 89, p. 1475–1491.

Blakely, R.J., Connard, G.G., Curto, J.B., 2016. Tilt derivative made easy. Energy Geosci, p. 3–6. Accessed on July 15, 2022. https://www.scribd.com/document/435796395/Tilt-Derivative-Made-Easy-07-2016.

BOEM, 2021. Geographic mapping data in digital format. Accessed on September 5, 2022. https://www.data.boem.gov/Main/Mapping.aspx.

Bosworth, W., Guiraud, R., Kessler, L.G., 1999. Late Cretaceous (ca. 84 Ma) compressive deformation of the stable platform of northeast Africa (Egypt): far-field stress effects of the "Santonian event" and origin of the Syrian arc deformation belt, Geology, v. 27 (7), p. 633–636.

Bouroullec, R., Weimer, P., 2017. Geometry and kinematics of Neogene allochthonous salt systems in the Mississippi Canyon, Atwater Valley, western Lloyd Ridge, and western DeSoto Canyon protraction areas, northern deepwater Gulf of Mexico. Am. Assoc. Pet. Geol. Bull., v. 101, p. 1003–1034.

Bouroullec, R., Weimer, P., Serrano, O., 2017. Petroleum geology of the Mississippi Canyon, Atwater Valley, western DeSoto Canyon, and western Lloyd Ridge protraction areas, northern deepwater Gulf of Mexico: Traps, reservoirs, and tectonostratigraphic evolution. Am. Assoc. Pet. Geol. Bull., v. 101, p. 1073–1108.

Boutefeu, A., Leplat, P., Somers, Y., 1980. Preliminary results of petrographic and electron-spin-resonance studies of organic matter from Deep Sea Drilling Project Sites 370 and 416. Accessed on October 11, 2022. http://deepseadrilling.org/50/volume/dsdp50_19.pdf.

Brownfield, M.E., 2016. Assessment of undiscovered oil and gas resources of the Orange River Coastal Province, Southwest Africa. In: Brownfield, M.E. (Ed.), *Geologic Assessment of Undiscovered Hydrocarbon Resources of Sub-Saharan Africa*. U.S. Geological Survey Digital Data Series, v. 69–GG, p. 14.

Brun, J.P., Fort, X., 2011. Salt tectonics at passive margins: Geology versus models. Mar. Pet. Geol., v. 28, p. 1123–1145.

Cai, J., He, Y., Liang, J., Qiu, C., Zhang, C., 2020. Differential deformation of gravity-driven deepwater fold-and-thrust belts along the passive continental margin of East Africa and their impact on petroleum migration and accumulation. Mar. Pet. Geol., v. 112, n. 104053.

Camerlo, R.H., Benson, E.F., 2006. Geometric and seismic interpretation of the Perdido fold belt: Northwestern deep-water Gulf of Mexico. Am. Assoc. Pet. Geol. Bull., v. 90, p. 363–386.

CBTH database compilation, 2020. CBTH phase V atlas and database compilation.

Ceraldi, T.S., Hodgkinson, R., Backe, G., 2017. The petroleum geology of the West Africa margin: an introduction, In: Ceraldi, T.S., Hodgkinson, R., Backe, G., (Eds.), *The Petroleum Geology of the West Africa Margin,* Geol. Soc. Spec. Publ., v. 438, p. 1–6.

Comissión Nacional de Hidrocarburos, 2015. Saline Basin - petroleum geological synthesis. p. 1–47. Accessed on July 15, 2022. https://rondasmexico.gob.mx/media/1557/geological-atlas-cs.pdf.

Conti, B., Perinotto, J.A.D.J., Veroslavsky, G., Castillo, M.G., de Santa Ana, H., Soto, M., Morales, E., 2017. Speculative petroleum systems of the southern Pelotas Basin, offshore Uruguay. Mar. Pet. Geol., v. 83, p. 1–25.

Contreras, J., Z€uhlke, R., Bowman, S., Bechst€adt, T., 2010. Seismic stratigraphy and subsidence analysis of the southern Brazilian margin (Campos, Santos and Pelotas basins). Mar. Pet. Geol., v. 27, p. 1952–1980.

Contrucci, I., Klingelhöfer, F., Perrot, J., Bartolome, R., Gutscher, M. A., Sahabi, M., Rehault, J. P., 2004. The crustal structure of the NW Moroccan continental margin from wide-angle and reflection seismic data, Geophysical Journal International, v. 159, p. 117-128.

Corredor, F., Shaw, J.H., Bilotti, F., 2005. Structural styles in deepwater fold-and-thrust belts of the Niger Delta. Am. Assoc. Pet. Geol. Bull., v. 89, p. 753– 780.

Cruciani, F., Barchi, M.R., 2016. The Lamu Basin deepwater fold-and-thrust belt: an example of a margin-scale, gravity-driven thrust belt along the continental passive margin of East Africa. Tectonics, v. 35, p. 491–510.

Cruciani, F., Barchi, M.R., Koyi, H.A., Porreca, M., 2017. Kinematic evolution of a regional-scale gravity-driven deepwater fold-and-thrust belt: The Lamu Basin case-history (East Africa). Tectonophysics, v. 712–713, p. 30–44.

Cruz-Mercado, M.A., Flores-Zamora, J.C., León-Ramírez, R., López-Céspedes, H.G., Peterson-Rodríguez, R.H., Reyes-Tovar, E., Sánchez-Rivera, R., Barrera-González, D., 2012. Salt provinces in the Mexican portion of the Gulf of Mexico – structural characterization and evolutionary model. Gulf Coast Assoc. Geol. Soc. Trans., v. 61, p. 93–103.

Curry, M.E., Peel, F.J., Hudec, M.R., Norton, I.O., 2018. Extensional models for the development of passive-margin salt basins, with application to the Gulf of Mexico. Basin Res., v. 30, p. 1180–1199.

da Cruz, C.A., Severiano Ribeiro, H.J.P., da Silva, E.B., 2021. Exploratory plays of the Foz do Amazonas Basin, NW portion, in deep and ultra-deep waters, Brazilian equatorial margin. J. South Am. Earth Sci., v. 111, n. 103475.

Da Silva Pellegrini, B., Ribeiro, H.J.P.S., 2018. Exploratory plays of Pará-Maranhão and Barreirinhas basins in deep and ultra-deep waters, Brazilian Equatorial Margin. Braz. J. Geol., v. 48, p. 485–502.

Davis, D., Suppe, J., Dahlen, F.A., 1983. Mechanics of fold-and-thrust belts and accretionary wedges. J. Geophys. Res. Solid Earth, v. 88, p. 1153–1172.

Davison, I., 2005. Central Atlantic margin basins of northwest Africa: geology and hydrocarbon potential (Morocco to Guinea). Journal of African Earth Sciences, v. 43, p. 254-274.

Davison, I., 2020. Salt tectonics in the Sureste basin, SE Mexico: Some implications for hydrocarbon exploration. In: Davison, I., Hull, J.N.F., Pindell, J. (Eds.), *The Basins, Orogens and Evolution of the Southern Gulf of Mexico and Northern Caribbean*. Geol. Soc., London, Spec. Pub., v. 504, p. 345–359.

Davison, I., Cunha, T.A., 2017. Allochthonous salt sheet growth: Thermal implications for source rock maturation in the deepwater Burgos Basin and Perdido Fold Belt, Mexico, Interpretation, v. 5, p. 1-141.

Davison, I., Dailly, P., 2010. Salt tectonics in the Cap Boujdour area, Aaiun Basin, NW Africa, Mar. Pet. Geol., v. 27, p. 435–441.

de Vera, J., Granado, P., McClay, K., 2010. Structural evolution of the Orange Basin gravity-driven system, offshore Namibia. Mar. Pet. Geol., v. 27, p. 223–237.

Dehler, S.A., Welford, J.K., 2013. Variations in rifting style and structure of the Scotian Margin, Atlantic Canada, from 3D gravity inversion. In: Mohriak, W.U., Danforth, A., Post, P.J., Brown, D.E., Tari, G.C., Nemčok, M., Sinha, S.T. (Eds.), *Conjugate Divergent Margins*, Geol. Soc. Spec. Publ., v. 369, p. 289-300.

Deroo, G., Herbin, J.P., Roucache, J., Tissot, B., 1980. Organic geochemistry of some Lower Cretaceous shales from Deep Sea Drilling Project Site 416, eastern North Atlantic. In: Stout, L.N., Worstell, P. et al. (Eds.), *Leg 50 of the Cruises of the Drilling Vessel Glomar Challenger,* *Funchal, Madeira Islands to Funchal, Madeira Islands*: *Initial Reports of the Deep Sea Drilling Project*. United States Government Printing Office, Washington, DC, v. 50, p. 429–435.

Domènech, M., Teixell, A., and Stockli, D. F., 2016. Magnitude of rift-related burial and orogenic contraction in the Marrakech High Atlas revealed by zircon (U-Th)/He thermochronology and thermal modeling, Tectonics, v. 35, p. 2609– 2635.

Eddy, D.R., Van Avendonk, H.J.A., Christeson, G.L., Norton, I.O., Karner, G.D., Johnson, C.A., Snedden, J.W., 2014. Deep crustal structure of the northeastern Gulf of Mexico: implications for rift evolution and seafloor spreading. J. Geophys. Res. Solid Earth, v. 119, p. 6802–6822.

Ellis, J., Macaulay, E., Anderson, H., 2015. The structural restoration of salt; global case studies of best practice workflows. AAPG search and discovery article #90216. Accessed on July 15, 2022. http://www.searchanddiscovery.com/abstracts/html/2015/90216ace/abstracts/2103063.htm.

Erlich, R.N., Pindell, J., 2020. Crustal origin of the West Florida Terrane, and detrital zircon provenance and development of accommodation during initial rifting of the southeastern Gulf of Mexico and western Bahamas. In: Davison, I., Hull, J.N.L., Pindell, J. (Eds.), *The Basins, Orogens and Evolution of the Southern Gulf of Mexico and Northern Caribbean*, Geol. Soc. London Spec. Publ, v. 504, p. 77-118.

Evans, S.L., Jackson, C.A.L., 2020. Base-salt relief controls salt-related deformation in the outer Kwanza Basin, offshore Angola. Basin Res., v. 32, p. 668–687.

Ewing, M., Worzel, J.L., Beall, O., Berggren, W.A., Bukry, D., Burk, C.A., Fischer, A.G., Pessagno Jr., E.A., 1969. Initial reports of the deep sea drilling project. Deep Sea Drilling Project Reports and Publications, v. 1, p. 1–672.

Fiduk, J.C., Weimer, P., Trudgill, B.D., Rowan, M.G., Gale, P.E., Phair, R.L., Korn, B.E., Roberts, G.R., Gafford, W.T., Lowe, R.S., Queffelec, T.A., 1999. The Perdido fold belt, northwestern deep Gulf of Mexico, part 2: Seismic stratigraphy and petroleum systems. Am. Assoc. Pet. Geol. Bull., v. 83, p. 578–612.

Fitz-Díaz, E., Lawton, T.F., Juárez-Arriaga, E., Chávez-Cabello, G., 2018. The Cretaceous-Paleogene Mexican orogen: Structure, basin development, magmatism and tectonics. Earth-Science Rev., v. 183, p. 56–84.

Fonnesu, M., Palermo, D., Galbiati, M., Marchesini, M., Bonamini, E., Bendias, D., 2020. A new world-class deep-water play-type, deposited by the syn-depositional interaction of turbidity flows and bottom currents: The giant Eocene Coral field in northern Mozambique. Mar. Pet. Geol., v. 111, p. 179–201.

Fredrich, J.T., Fossum, A.F., Hickman, R.J., 2007. Mineralogy of deep-water Gulf of Mexico salt formations and implications for constitutive behavior. J. Petrol. Sci. Eng., v. 57, p. 354–374.

Galhom, T., Mann, P., Rudolph, K., 2022. Jurassic-Recent structure, stratigraphy, and basin modeling of the rifted-passive margin of the Tarfaya-Dakhla basin of southern Morocco, Mar. Pet. Geol., n. 105626.

GEBCO, 2020. GEBCO 2020 Bathymetric Grid. Accessed on July 15, 2022. https://www.gebco.net/.

Geo Expro, 2013. The Pelotas Basin oil province revealed, v. 10(4). Accessed on July 15, 2022. https://www.geoexpro.com/articles/2013/12/the-pelotas-basin-oil-province-revealed.

Geo Expro, 2019. Morocco Atlantic offshore: new data, new insights. p. 64-68. Accessed on September 22, 2022. https://archives.datapages.com/data/geo-expro-magazine/016/016003/pdfs/64.pdf.

Godo, T., 2017. The Appomattox Field: Norphlet Aeolian Sand Dune Reservoirs in the Deep-Water Gulf of Mexico. In: Merrill, R.K., Sternbach, C.A. (Eds.), *Giant Fields of the Decade 2000-2010*, AAPG Memoir, v. 113, p. 29–54.

Gómez-Cabrera, P.T., Jackson, M.P.A., 2009. Regional Neogene salt tectonics in the offshore Salina del Istmo Basin, Southeastern Mexico. In: Bartolini, C., Román-Ramos, J.R. (Eds.), *Petroleum Systems in the Southern Gulf of Mexico*. AAPG Memoir, v. 90, p. 1-28.

Granado, P., De Vera, J., McClay, K., 2009. Tectonostratigraphic evolution of the Orange Basin, SW Africa. Trab. Geol., v. 29, p. 321–328.

Grando, G., Schleder, Z., Shackleton, R., Seed, G., Buddin, T., McClay, K., Borraccini, F., 2009. 3D structural evolution of the salt controlled Frampton Anticline, Atwater Valley foldbelt, deep water Gulf of Mexico. AAPG search and discovery article #50161, p. 128. Accessed on July 15, 2022. http://www.searchanddiscovery.com/documents/2009/50161grando/ndx_grando.pdf.

Greenhalgh, J., Borsato, R., Mathew, F., Duncan-Jones, G., Pimenta, I., Marques da Silva, J., Narciso da Silva, L., 2012. Petroleum plays and prospectivity in the Kwanza and Benguela Basins offshore Angola. AAPG Search and Discovery Article #10443, p. 7. Accessed on July 15, 2022. http://www.searchanddiscovery.com/documents/2012/10443greenhalgh/ndx_greenhalgh.pdf.

Guiraud, R., Bosworth, W., Thierry, J., A. Delplanque, A., 2005. Phanerozoic geological evolution of northern and Central Africa: an overview, Journal of African Earth Sciences, v. 43, p. 83-143.

Gutscher, M.A., Dominguez, S., Westbrook, G.K., Le Roy, P., Rosas, F., Duarte, J.C., Terrinha, P., Miranda, J.M., Graindorge, D., Gailler, A., Sallarès, V., Bartolomé, R., 2012. The Gibraltar subduction: a decade of new geophysical data, Tectonophysics, v. 574, p. 72-91.

Guzman-Vega, M. A., Mello, M. R., 1999. Origin of oil in the Sureste Basin, Mexico. Am. Assoc. Petrol. Geol. Bull., v. 83 (7), p. 1068-1095.

Hafid, M., 2000. Triassic–early Liassic extensional systems and their Tertiary inversion, Essaouira Basin (Morocco). Mar. Petrol. Geol., v. 17, p. 409–429.

Hasan, M.N., and Mann, P., 2021. Structural styles and evolution of the Campeche salt basin, southern Gulf of Mexico. Mar. Petrol. Geol., v. 133, n. 105313.

Hasan, M.N., Mann, P., 2022. Deepwater passive margin foldbelts. In: Rotzien, J., Yeilding, C., Sears, R., Hernández-Molina, F.J., Catuneanu, O., (Eds.), *Deepwater Sedimentary Systems: Science, Discovery, and Applications*, Elsevier, p. 119-147.

Hasan, M.N., Pepper, A., Mann, P., 2022. Basin-scale estimates of thermal stress and expelled petroleums from Mesozoic-Cenozoic source rocks, southern Gulf of Mexico. Marine and Petroleum Geology, n. 105995.

Hasan, M.N., Potter-McIntyre, S., Tedesco, S., 2021. Wrench faulting and trap breaching: a case study of the Kizler North Field, Lyon County, Kansas, USA. Midcontinent Geoscience, v. 2, p. 1–14.

Hasan, M.N., 2019. Reservoir characterization of the Kizler North field, Lyon Co., Kansas, USA, Unpublished MS Thesis, Southern Illinois University at Carbondale, 120 p.

He, Z., Murray, A., 2020. Migration loss, lag and fractionation: Implications for fluid properties and charge risk. AAPG Annual Conference and Exhibition, September 2020, Houston, TX. Accessed on July 15, 2022.
https://www.researchgate.net/publication/351516104_Migration_Loss_Lag_and_Fractionation_Implications_for_Fluid_Properties_and_Charge_Risk.

Hedley, R., Intawong, A., Winter, F., Sibeya, V., 2021. Hydrocarbon play concepts in the Orange Basin in light of the Venus and Graff oil discoveries. First Break, v. 40, p. 91-95.

Hernández, H.S., 2013. Stratigraphic characterization and evolution of a mid-Tertiary age deep water system, Holok area, SW Gulf of Mexico, Unpublished PhD Dissertation, University of Aberdeen, 250 p.

Horbury, A.D., Hall, S., Francisco, G.P., Dioniso, R.F., Armando, R.F., Patricia, O.G., Martín, M.M., Guillermo, Q.R., 2003. Tectonic sequence stratigraphy of the western margin of the Gulf of Mexico in the late Mesozoic and Cenozoic: less passive than previously imagined: circum-gulf of Mexico and Caribbean hydrocarbon habitats, basin formation and plate tectonics. In: Bartolini, C., Buffler, R.T., Blickwede, J.F. (Eds.), *The Circum-Gulf of Mexico and the Caribbean: Hydrocarbon Habitats, Basin Formation and Plate Tectonics*. AAPG Memoir, v. 79, p. 184–245.

Horn, B.W., Hartwing, A., Faw, J., Novianti, I., Goswami, A., McGrail, A., 2017. Refining exploration opportunities in Mexico. Geo Expro, v. 14 (1), p. 66–68.
https://www.geoexpro.com/articles/2013/12/the-pelotas-basin-oil-province-revealed.

Hudec, M.R., Dooley, T.P., Peel, F.J., Soto, J.I., 2019. Controls on the evolution of passive-margin salt basins: Structure and evolution of the Salina del Bravo region, northeastern Mexico. GSA Bull., v. 132(5-6), p. 997–1012.

Hudec, M.R., Jackson, M.P.A., 2002. Structural segmentation, inversion, and salt tectonics on a passive margin: Evolution of the inner Kwanza Basin, Angola. GSA Bull., v. 114, p. 1222–1244.

Hudec, M.R., Jackson, M.P.A., 2004. Regional restoration across the Kwanza Basin, Angola: salt tectonics triggered by repeated uplift of a metastable passive margin. Am. Assoc. Pet. Geol. Bull., v. 88, p. 971–990.

Hudec, M.R., Norton, I.O., 2019. Upper Jurassic structure and evolution of the Yucatán and Campeche subbasins, southern Gulf of Mexico. Am. Assoc. Petrol. Geol. Bull., v. 103, p. 1133–1151.

Hudec, Michael R., Norton, I.O., Jackson, M.P.A., Peel, F.J., 2013. Jurassic evolution of the Gulf of Mexico salt basin. Am. Assoc. Petrol. Geol. Bull., v. 97, p. 1683–1710.

Ibraheem, I.M., Haggag, M., Tezkan, B., 2019. Edge detectors as structural imaging tools using aeromagnetic data: A case study of Sohag area, Egypt. Geosciences, v. 9, n. 5, p. 211.

Jiménez-Munt, I., Fernàndez, M., Vergés, J., Garcia-Castellanos, D., Fullea, J., Pérez-Gussinyé, M., Afonso, J.C., 2011. Decoupled crust-mantle accommodation of Africa-Eurasia convergence in the NW Moroccan margin, Journal of Geophysical Research, v. 116, p. B08403.

Kenning, J.J., Mann, P., 2020a. Control of structural style by large, Paleogene, mass transport deposits in the Mexican Ridges fold-belt and Salina del Bravo, western Gulf of Mexico. Mar. Pet. Geol., v. 115, n. 104254.

Kenning, J.J., Mann, P., 2020b. Regional thermal maturity modelling of hydrocarbons along the deepwater Yucatan margin, southern Gulf of Mexico. In: Davison, I., Hull, J.N.L., Pindell, J. (Eds.), *The Basins, Orogens and Evolution of the Southern Gulf of Mexico and Northern Caribbean*. Geol. Soc. London, Spec. Publ., v. 504, p. 203-231.

Klingelhoefer, F., Biari, Y., Sahabi, M., Aslanian, D., Schnabel, M., Matias, L., and Austin, J. A., 2016. Crustal structure variations along the NW-African continental margin: a comparison of new and existing models from wide-angle and reflection seismic data. Tectonophysics, v. 674. p. 227-252.

Klingelhoefer, F., Labails, C., Cosquer, E., Rouzo, S., Geli, L., Aslanian, D., Olivet, J.-L., Sahabi, M., Nouze, H., Unternehr, P., 2009. Crustal structure of the southwest-Moroccan margin from wide-angle and reflection seismic data (the DAKHLA experiment) part A: wide-angle seismic models, Tectonophysics, v. 468, p. 83-97.

Krueger, A., Gilbert, E., 2009. Deepwater fold-thrust belts: Not all the beasts are equal. AAPG Search and Discovery article #30085, p. 1–6. Accessed on October 26, 2022. https://www.searchanddiscovery.com/documents/2009/30085krueger/images/krueger.

Lin, P., Bird, D., Mann, P., 2019. Crustal structure of an extinct, late Jurassic-to-earliest Cretaceous spreading center and its adjacent oceanic crust in the eastern Gulf of Mexico. Mar. Geophys. Res., v. 40, p. 395–428.

Liu, J.-P., Pan, X., Ma, J., Tian, Z., Chen, Y., Wan, L., 2008. Petroleum geology and resources in West Africa: An overview. Pet. Explor. Dev., v. 35, p. 378–384.

Liu, X., Kang, Y., Li, J., Chen, Z., Ji, A., Xu, H., 2020. Percolation characteristics and fluid movability analysis in tight sandstone oil reservoirs. ACS Omega, v. 105(24), p. 14316-14323.

Liu, M., 2021. Rift evolution and crustal structure of the Gulf of Mexico basin from integration of multiple geological and geophysical datasets, Unpublished PhD dissertation, University of Houston, 227 p.

Liu, M., Filina, I., Mann, P., 2019. Crustal structure of Mesozoic rifting in the northeastern Gulf of Mexico from integration of seismic and potential fields data. Interpretation, v. 7, p. 857–867.

Mahanjane, E.S., Franke, D., 2014. The Rovuma Delta deepwater fold-and-thrust belt, offshore Mozambique. Tectonophysics, v. 614, p. 91–99.

Mandujano-Velazquez, J.J., Keppie, J.D., 2009. Middle Miocene Chiapas fold and thrust belt of Mexico: A result of collision of the tehuantepec transform/ridge with the Middle America trench. In: Murphy, J.B., Keppie, J.D., Hynes, A.J. (Eds.), *Ancient Orogens and Modern Analogues*. Geol. Soc. London, Spec. Publ., v. 327, p. 55–69.

Mann, P., 2022. Crustal structure and tectonostratigraphy of rifted-passive margins with applications for hydrocarbon exploration. In: Rotzien, J., Yeilding, C., Sears, R., Hernandez-Molina, J., Catuneanu, O. (Eds.), *Deepwater Sedimentary Systems: Science, Discovery, and Applications*, Elsevier, p. 83-117.

Marton, G.L., Buffler, R.T., 1999. Jurassic-early Cretaceous tectono-paleogeographic evolution of the southeastern Gulf of Mexico basin. In: Mann, P. (Ed.), *Sedimentary Basins of the World*. Elsevier, v. 4, p. 63–91.

Maus, S., Barckhausen, U., Berkenbosch, H., Bournas, N., Brozena, J., Childers, V., Dostaler, F., Fairhead, J.D., Finn, C., von Frese, R.R.B., Gaina, C., Golynsky, S., Kucks, R., Lühr, H., Milligan, P., Mogren, S., Müller, R.D., Olesen, O., Pilkington, M., Saltus, R., Schreckenberger, B., Thébault, E., Caratori Tontini, F., 2009. EMAG2: A 2–arc min resolution Earth magnetic anomaly grid compiled from satellite, airborne, and marine magnetic measurements. G-cubed, v. 10, p. Q08005.

Mendelssohn, I.A., Byrnes, M.R., Kneib, R.T., Vittor, B.A., 2017. Habitats and biota of the Gulf of Mexico: Before the Deepwater Horizon oil spill, v. 868. Springer, New York, NY.

Miller, B., 2021. Tectonic evolution of the Late Cretaceous-Cenozoic Lesser Antilles subduction system and the Mesozoic-Recent rifted-passive margin of northern Morocco using an integration of geologic, seismic reflection, and gravity data. Unpublished MS thesis, University of Houston, 147 p.

Miranda-Madrigal, E., Chávez-Cabello, G., 2020. Regional geological analysis of the southern deep Gulf of Mexico and northern Yucatán Shelf. In: Davison, I., Hull, J.N.L., Pindell, J. (Eds.), *The Basins, Orogens and Evolution of the Southern Gulf of Mexico and Northern Caribbean*, Geol. Soc. London, Spec. Publ., v. 504, p. 183-202.

Mitra, S., Figueroa, G.C., Garcia, J.H., Alvarado, A.M., 2005. Three-dimensional structural model of the Cantarell and Sihil structures, Campeche bay, Mexico. Am. Assoc. Petrol. Geol. Bull., v. 89, p. 1–26.

Morley, C.K., King, R., Hillis, R., Tingay, M., Backe, G., 2011. Deepwater fold and thrust belt classification, tectonics, structure and hydrocarbon prospectivity: A review. Earth Sci. Rev., v. 104, p. 41–91.

Mourgues, R., Lacoste, A., Garibaldi, C., 2014. The Coulomb critical taper theory applied to gravitational instabilities. J. Geophys. Res. Solid Earth, v. 119, p. 754–765.

Naehr, T. H., Birgel, D., Bohrmann, G., MacDonald, I. R., Kasten, S., 2009. Biogeochemical controls on authigenic carbonate formation at the Chapopote "asphalt volcano", Bay of Campeche. Chemical Geology, v. 266, p. 390-402.

Nagihara, S., Sclater, J. G., Phillips, J. D., Behrens, E. W., Lewis, T., Lawver, L. A., Nakamura, Y., Garcia-Abdeslem, J., Maxwell, A. E., 1996. Heat flow in the western abyssal plain of the Gulf of Mexico: Implications for thermal evolution of the old oceanic lithosphere. J. Geophys. Res. Solid Earth, v. 101 (B2), p. 2895-2913.

Neumaier, M., Littke, R., Back, S., Kukla, P., Schnabel, M., Reichert, C., 2018. Hydrocarbon charge assessment of frontier basins: A case study of the oceanic crust of the Moroccan Atlantic margin, Petroleum Geoscience, v. 25(2), p. 151–168.

Nguyen, L.C., Mann, P., 2015. Gravity and magnetic constraints on the Jurassic opening of the oceanic Gulf of Mexico and the location and tectonic history of the Western Main transform fault along the eastern continental margin of Mexico. Interpretation, v. 4, p. 23-33.

Oliveira, M.J.R., Santarem, P., Moraes, A., Zalán, P.V., Caldeira, J.L., Tanaka, A., Trosdtorf Jr, I., 2013. Linked extensional-compressional tectonics in gravitational systems in the Equatorial Margin of Brazil. In: Gao, D. (Ed.), *Tectonics and Sedimentation*. AAPG Memoir, v. 100, p. 159-178.

Olson, C.J., Becker, J.J., Sandwell, D.T., 2016. SRTM15_PLUS: Data fusion of shuttle radar topography mission (SRTM) land topography with measured and estimated seafloor topography

(NCEI Accession 0150537). NOAA National Centers for Environmental Information, Dataset. Accessed on October 26, 2022. https://accession.nodc.noaa.gov/0150537.

Olsson, H., Gulbrandsen, S., Fowler, M., Webb, J., 2018. Jurassic oils and source rocks of northern Morocco, p. 183. Accessed on September 22, 2022. https://oera.ca/sites/default/files/202005/Geochemistry%20of%20the%20Morocco%20Conjugate%20Margin%20Final%20Report%20-%20Part1.pdf.

ONHYM, 2019. Opportunities for hydrocarbons exploration and production in Morocco, Boujdour handout. AAPG International Conference and Exhibition, 19-22 May, 2019, San Antonio, USA.

Padilla y Sánchez, R.J., 2007. Evolución geológica del sureste Mexicano desde el Mesozoico al presente en el contexto regional del Golfo de México. Boletín la Soc. Geológica Mex., v. 59, p. 19–42.

Peel, F.J., 2014. The engines of gravity-driven movement on passive margins: Quantifying the relative contribution of spreading vs. gravity sliding mechanisms. Tectonophysics, v. 633, p. 126–142.

Peel, F.J., Travis, C.J., Hossack, J.R., 1995. Genetic structural provinces and salt tectonics of the Cenozoic offshore U.S. Gulf of Mexico: a preliminary analysis. In: Jackson, M.P.A., Roberts, D.G., Snelson, S. (Eds.), *Salt Tectonics: A Global Perspective*. AAPG Memoir, v. 65, p. 153-175.

Pemex, 2009-2019. Hydrocarbons reserves of Mexico. Accessed on October 26, 2020. https://www.pemex.com/en/ investors/publications/Paginas/hydrocarbon-evaluations.aspx.

Pepper, A S., Bugti, N., Heister, L., O'Leary, J., Laigle, J-M., Roller, E., Stalnaker, J., Mann, P., Pascoe, R, 2021. Outcrop to basin center thermal evolution of the US Gulf of Mexico Basin, IMAGE (SEG/AAPG) International Meeting for Applied Geoscience & Energy, September 26 - October 1, Denver, Colorado, USA.

Pepper, A. S., Corvi, P.J., 1995. Simple kinetic models of petroleum formation, part I: oil and gas generation from kerogen. Mar. Petrol. Geol., v. 12, p. 291–319.

Pepper, A. S., Heister, A., Pradono, M.M., 2020. The "missing source rocks" of the Gulf of Mexico mega-basin. AAPG Virtual Research Symposium: Mexican Basins - Advancing the Understanding of Mexico's Geology and Petroleum Potential. Accessed on July 15, 2022. https://www.aapg.org/videos/webinar/lacr/articleid/59060/the-missing-source-rocks-of-the-gulf-of-mexico-mega-basin.

Pepper, A. S., Pindell, J., 2017, Implications of early Gulf of Mexico tectonic history for distribution of Upper Jurassic to mid Cretaceous source rocks in deep water exploration areas of the US and Mexico. AAPG Annual Conference and Exhibition, Houston, Texas, April 2–5, 2017. Accessed on July 15, 2022. http://www.searchanddiscovery.com/abstracts/html/2017/90291ace/abstracts/2612188.html.

Pepper, A. S., Yu, Z., 1995. Influence of an inclined salt sheet on petroleum emplacement in the Pompano field area, offshore Gulf of Mexico Basin, In: M. P. A. Jackson and M. R. Hudec, (Eds.), *Salt, Sediment and Petroleums*: GCSSEPM Foundation 16th Annual Research Conference, Houston, Texas, December 3–6, 1995, p. 197–205.

Pepper, A., Roller, E., 2021. Ultimate expellable potentials of source rocks from selected super basins: What does "world class" look like? Am. Assoc. Pet. Geol. Bull., v. 105, p. 1069–1097.

Perez Gutierrez, C.M., 2013. Structural kinematics and salt evolution in the "KUZAM" area; offshore southeast Gulf of Mexico: Implications for petroleum prospectivity. Unpublished MS thesis, Colorado School of Mines, p. 210.

Pichel, L.M., Huuse, M., Redfern, J., Finch, E., 2019. The influence of base-salt relief, rift topography and regional events on salt tectonics offshore Morocco. Mar. Petrol. Geol., v. 103, p. 87-113.

Pindell, J., 1985. Alleghenian reconstruction and subsequent evolution of the Gulf of Mexico, Bahamas, and Proto-Caribbean. Tectonics, v. 4, p. 1–39.

Pindell, J., Graham, R., Horn, B., 2014. Rapid outer marginal collapse at the rift to drift transition of passive margin evolution, with a Gulf of Mexico case study. Basin Res., v. 26, p. 701–725.

Pindell, J., Miranda C.E., Cerón, A, Hernandez, L., 2016. Aeromagnetic map constrain Jurassic–early Cretaceous synrift, break up, and rotational seafloor spreading history in the Gulf of Mexico, Mesozoic of the Gulf rim and beyond: New progress in science and exploration of the Gulf of Mexico basin. In: Lowery, C.M., Snedden, J.W., Rosen, N.C. (Eds.), 35th Annual Gulf Coast Section SEPM Foundation Perkins-Rosen Research Conference. GCSSEPM Foundation, Houston, TX, USA, p. 123–153.

Pindell, J., Miranda, E., 2011. Linked kinematic histories of the Macuspana, Akal-Reforma, Comalcalco, and deepwater Campeche Basin tectonic elements, southern Gulf of Mexico. Gulf Coast Assoc. Geol. Soc. Trans., v. 61, p. 353–361.

Pindell, J., Radovich, B., Haire, E., Howard, D., Goswami, A., Dinc, G., Horn, B., 2015. Structure maps of the top-rift unconformity/oceanic crust and top Cretaceous surfaces, and the Oxfordian rift-drift reconstruction, Gulf of Mexico. Gulf Coast Assoc. Geol. Soc. Trans., v. 65, p. 821–831.

Pindell, J., Villagómez, D., Horn, B.W., Garza, R.M., 2019. Middle Jurassic tectonic models for the Gulf of Mexico in light of new Bajocian Ages for proximal margin salt deposition. 37th Annual GCSSEPM Foundation Perkins-Rosen Research Conference, Houston, TX, USA, p. 11.

Pindell, J., Weber, B., Hale-Erlich, W., Cossey, S., Bitter, M., Molina Garza, R., Graham, R., Erlich, R.N., 2020. Strontium isotope dating of evaporites and the breakup of the Gulf of Mexico and proto–Caribbean seaway. In: Uwe, C., Martens, R., Molina Garza, S. (Eds.), *Southern and Central Mexico: Basement Framework, Tectonic Evolution, and Provenance of Mesozoic–Cenozoic Basins*. Geological Society of America Special Papers, v. 546, p. 309-329.

Pindell, J.L., Kennan, L., 2001. Kinematic evolution of the Gulf of Mexico and Caribbean. Gulf Coast Section SEPM 21st Annual Research Conference, Dec 2-5, Society for Sedimentary Geology (SEPM), Houston Texas, p. 193–220.

Pindell, J.L., Kennan, L., 2009. Tectonic evolution of the Gulf of Mexico, Caribbean and northern South America in the mantle reference frame: An update. In: James, K.H., Lorente, M.A., Pindell, J. (Eds.), *The Origin and Evolution of the Caribbean Plate*, Geol. Soc. London, Spec. Publ., v. 328, p. 1–55.

Powney, M., Bray, R., Lawrence, S., 2020. New play based on a "Deep-basin" Jurassic petroleum system offshore Atlantic Morocco, Geo Expro. Accessed on July 15, 2022. https://www.geoexpro.com/articles/2020/06/new-plays-based-on-a-deep-basin-jurassic-petroleum-system-offshore-atlantic-morocco.

Pulham, A.J., Peel, F.J., Delph, B., Nicholson, T., Wu, J., 2019. The age of the Louann salt; insights from historic isotopic analyses in salt stocks from the onshore interior salt basins of the northern Gulf of Mexico. 37th Annual GCSSEPM Foundation Perkins-Rosen Research Conference, Houston, TX, USA, p. 64–66.

Reis, A.T., Araújo, E., Silva, C.G., Cruz, A.M., Gorini, C., Droz, L., Migeon, S., Perovano, R., King, I., Bache, F., 2016. Effects of a regional decollement level for gravity tectonics on late Neogene to recent large-scale slope instabilities in the Foz do Amazonas Basin, Brazil. Mar. Pet. Geol., v. 75, p. 29–52.

Reis, A.T., Perovano, R., Silva, C.G., Vendeville, B.C., Araújo, E., Gorini, C., Oliveira, V., 2010. Two-scale gravitational collapse in the Amazon Fan: A coupled system of gravity tectonics and mass-transport processes. J. Geol. Soc. Lond., v. 167, p. 593–604.

Reuber, K., Mann, P., 2019. Control of Precambrian-to-Paleozoic orogenic trends on along-strike variations in early Cretaceous continental rifts of the South Atlantic Ocean. Interpretation, v. 7, p. SH45-SH69.

Ricoy-Paramo, V., 2005. 3D Seismic characterisation of the Cantarell Field, Campeche Basin, Mexico. Unpublished PhD Dissertation. Cardiff University, 424 p.

Rivera, R.S., Ángel, M., Mercado, C., Tovar, E.R., Gilberto, H., Céspedes, L., Heberto, R., Rodríguez, P., Carlos, J., Zamora, F., Ramirez, R.L., González, D.B., 2011. Tectonic evolution of the South Gulf Salt Province in the Gulf of Mexico. Gulf Coast Assoc. Geol. Soc. Trans., v. 61, p. 421–427.

Rowan, M.G., 1993. A systematic technique for the sequential restoration of salt structures. Tectonophysics, v. 228, p. 331–348.

Rowan, M.G., 2018. The South Atlantic and Gulf of Mexico salt basins: Crustal thinning, subsidence and accommodation for salt and pre-salt strata. In: McClay, K.R., Hammerstein, J.A.

(Eds.), *Passive Margins: Tectonics, Sedimentation and Magmatism*. Geol. Soc. London, Spec. Publ., v. 476, p. 333.

Rowan, M.G., 2020. Salt- and shale-detached gravity-driven failure of continental margins. In: Scarselli, N., Adam, J., Chiarella, D., Roberts, D.G., Bally, A.W. (Eds.), *Regional Geology and Tectonics (Second Edition)*. Elsevier, v. 1, p. 205–234.

Rowan, M.G., 2022. The ocean-continent transition of late syn-rift salt basins: Extension and evaporite deposition in the southern Gulf of Mexico and global analogs. In: Koeberl, C., Claeys, P., Montanari, A. (Eds.), *From the Guajira desert to the Apennines, and from Mediterranean microplates to the Mexican killer asteroid*. Geol. Soc. London, Spec. Publ., v. 557.

Rowan, M.G., Jackson, M.P.A., Trudgill, B.D., 1999. Salt-related fault families and fault welds in the northern Gulf of Mexico. Am. Assoc. Petrol. Geol. Bull., v. 83, p. 1454–1484.

Rowan, M.G., Peel, F.J., Vendeville, B.C., 2004. Gravity-driven fold belts on passive margins. In: McClay, K.R. (Ed.), *Thrust Tectonics and Hydrocarbon Systems*. AAPG Memoir, v. 82, p. 157–182.

Rowan, M.G., Ratliff, R.A., 2012. Cross-section restoration of salt-related deformation: best practices and potential pitfalls. J. Struct. Geol., v. 41, p. 24–37.

Rowan, M.G., Trudgill, B.D., Carl Fiduk, J., 2000. Deep-water, salt-cored foldbelts: Lessons from the Mississippi fan and Perdido foldbelts, northern Gulf of Mexico. In: Mohriak, W., Taiwani, M. (Eds.), *Atlantic Rifts and Continental Margins*, Geophysical Monograph Series, v. 115, p. 173-191.

Sachse, V.F., Littke, R., Heim, S., Kluth, O., Schober, J., Boutib, L., Jabour, H., Perssen, F., Sindern, S., 2011. Petroleum source rocks of the Tarfaya Basin and adjacent areas, Morocco. Org. Geochem., v. 42, p. 209-227.

Sachse, V.F., Littke, R., Jabour, H., Schümann, T., Kluth, O., 2012. Late Cretaceous (late Turonian, Coniacian and Santonian) petroleum source rocks as part of an OAE, Tarfaya basin, Morocco. Mar. Petrol. Geol., v. 29, p. 35-49.

Salem, A., Williams, S., Fairhead, J.D., Ravat, D., Smith, R., 2007. Tilt-depth method: A simple depth estimation method using first-order magnetic derivatives. Lead. Edge, v. 26, p. 1502–1505.

Salem, A., Williams, S., Samson, E., Fairhead, D., Ravat, D., Blakely, R.J., 2010. Sedimentary basins reconnaissance using the magnetic tilt-depth method. Explor. Geophys., v. 41, p. 198–209.

Salomón-Mora, L.E., Aranda-Garcia, M., Román-Ramos, J.R., 2009. Contractional Growth Faulting in the Mexican Ridges. In: Bartolini, C., Román-Ramos, J.R. (Eds.), *Petroleum Systems in the Southern Gulf of Mexico*. AAPG Memoir, v. 90, p. 93–115.

Salomón-Mora, L.E., Cruz-Mercado, M., Alsop, I., Archer, S., 2011. Tectonics, structure and hydrocarbon potential of the Mexican Ridges Fold Belt, western Gulf of Mexico. Gulf Coast Assoc. Geol. Soc. Trans., v. 61, p. 403–419.

Sandwell, D.T., Muller, R.D., Smith, W.H.F., Garcia, E., Francis, R., 2014. New global marine gravity model from CryoSat-2 and Jason-1 reveals buried tectonic structure. Science, v. 346, p. 65–67.

Santamaria-Orozco, D. M., 2000. Organic geochemistry of Tithonian source rock and associated oils from the Sonda de Campeche, Mexico. Unpublished PhD dissertation, University of Aachen, Germany, 190 p.

Sapin, F., Ringenbach, J.-C., Clerc, C., 2021. Rifted margins classification and forcing parameters. Sci. Rep., v. 11, p. 8199.

Saunders, M., Geiger, L., Rodriguez, K., Hargreaves, P., 2016. The delineation of pre-salt license blocks in the deep offshore Campeche-Yucatan Basin. AAPG search and discovery article #10867, p. 599–604. Accessed on July 15, 2022. https://www.searchanddiscovery.com/pdfz/documents/2016/10867saunders/ndx_saunders.pdf.html.

Schettino, A., Turco, E., 2011. Tectonic history of the western Tethys since the Late Triassic. GSA Bulletin, v. 123 (1-2), p. 89–105.

Sclater, J.G., Christie, P.A.F., 1980. Continental stretching: An explanation of the post- Mid-Cretaceous subsidence of the central North Sea Basin. J. Geophys. Res. Solid Earth, v. 85, p. 3711–3739.

Serpelloni, E., Vannucci, G., Pondrelli, S., Argnani, A., Casula, G., Anzidei, M., Baldi, P., Gasperini, P., 2007. Kinematics of the Western Africa–Eurasia plate boundary from focal mechanisms and GPS data. Geophysical Journal International, v. 169 (3), p. 1180-1200.

Shann, M.V., 2020. The Sureste Basin of Mexico: Its framework, future oil exploration opportunities and key challenges ahead. In: Davison, I., Hull, J.N. L., Pindell, J. (Eds.), *The Basins, Orogens and Evolution of the Southern Gulf of Mexico and Northern Caribbean*. Geol. Soc. London, Spec. Publ., v. 504. p. 119-146.

Sickmann, Z.T., Snedden, J.W., 2020. Neogene to recent evolution of the Southern Gulf of Mexico basin: tectonic controls on deep-water sediment dispersal systems. Basin Res., v. 33(2), p. 1240–1265.

Snedden, J.W., Galloway, W.E., 2019. The Gulf of Mexico Sedimentary Basin: Depositional Evolution and Petroleum Applications, Cambridge University Press, p. 326.

Snedden, J.W., Stockli, D.F., Norton, I.O., 2020. Palaeogeographical reconstruction and provenance of Oxfordian aeolian sandstone reservoirs in Mexico offshore areas: comparison to the

Norphlet aeolian system of the northern Gulf of Mexico. In: Davison, I., Hull, J.N.L., Pindell, J. (Eds.), *The Basins, Orogens and Evolution of the Southern Gulf of Mexico and Northern Caribbean*. Geol. Soc. London, Spec. Publ., v. 504, p. 233-253.

Steele, D., Ejedawe, J., Adeogba, T., Grant, C., Filbrandt, J., Ganz, H., 2009. Geological framework of Nigeria linked shelf extension and deepwater thrustbelts. AAPG Hedberg Conference, October 4–9, Tirrenia, Italy.

Steier, A., Mann, P., 2019. Late Mesozoic gravity sliding and Oxfordian hydrocarbon reservoir potential of the northern Yucatan margin. Mar. Petrol. Geol., v. 103, p. 681–701.

Stica, J.M., Zalán, P.V., Ferrari, A.L., 2014. The evolution of rifting on the volcanic margin of the Pelotas Basin and the contextualization of the Paraná-Etendeka LIP in the separation of Gondwana in the South Atlantic. Mar. Pet. Geol., v. 50, p. 1–21.

Strozyk, F., Back, S., Kukla, P.A., 2017. Comparison of the rift and post-rift architecture of conjugated salt and salt-free basins offshore Brazil and Angola/ Namibia, South Atlantic. Tectonophysics, v. 716, p. 204–224.

Tari, G., H. Jabour, H., 2013. Salt tectonics along the Atlantic margin of Morocco. In: Mohriak, W.U., Danforth, A., Post, P.J., Brown, D.E., Tari, G.C., Nemčok, M., Sinha, S.T. (Eds.), *Conjugate Divergent Margins*, Geol. Soc. Spec. Publ., v. 369, p. 337-353.

Teerman, S. C., Howe, R. W., Hwang, R., and Lytton, R., 2010. A deepwater Gulf of Mexico source rock penetration: Applications to Mesozoic source rocks and depositional systems. AAPG Annual Convention and Exhibition, New Orleans, Louisiana, April 11–14. Accessed on July 15, 2022.
http://www.searchanddiscovery.com/pdfz/abstracts/pdf/2010/annual/abstracts/ndx_teerman.pdf.html.

Tesei, T., Cruciani, F., Barchi, M.R., 2021. Gravity-driven deepwater fold-and-thrust belts as critical Coulomb wedges: Model limitations and the role of friction vs. fluid pressure. J. Struct. Geol., v. 153, n. 104451.

Trudgill, B.D., Rowan, M.G., Fiduk, J.C., Weimer, P., Gale, P.E., Korn, B.E., Phair, R.L., Gafford, W.T., Roberts, G.R., Dobbs, S.W., 1999. The Perdido Fold Belt, northwestern deep Gulf of Mexico, part 1: Structural geometry, evolution and regional implications. Am. Assoc. Pet. Geol. Bull., v. 83, p. 1320–1336.

Turcotte, D., Schubert, G., 2002. Geodynamics (2nd ed.): Cambridge University Press. p. 848.

Uranga, R.M., Ferrer, O., Zamora, G., Munoz, J.A., Rowan, M.G., 2022. Salt tectonics of the offshore Tarfaya Basin, Moroccan Atlantic margin, Mar. Petrol. Geol., v. 138, n. 105521.

Villagómez, D., Steffensen, C., Pindell, J., Molina-Garza, R.S., Gray, G., O'Sullivan, P., Stockli, D., Spikings, R., 2022. Tectono-sedimentary evolution of Southern Mexico. Implications for

Cretaceous and younger source-to-sink systems in the Mexican foreland basins and the Gulf of Mexico. Earth-Science Reviews, vol. 231, n. 104066.

Waples, D. W., Pacheco, J., Vera, A., 2004. A method for correcting log-derived temperatures in deep wells, calibrated in the Gulf of Mexico. Petroleum Geoscience, v. 10 (3), p. 239-245.

Watkins, J.S., Buffler, R.T., 1996. Gulf of Mexico deepwater frontier exploration potential. In: O. Jones, and R.L. Freed, eds., *Structural framework of the northern Gulf of Mexico*: Trans. Gulf Coast Assoc. Geol. Soc., p. 79-92.

Weimer, P., Bouroullec, Adson, J., Cossey, S. P. J., 2017. An overview of the petroleum systems of the northern deepwater Gulf of Mexico. . Am. Assoc. Pet. Geol. Bull., v. 101 (7), p. 941-993.

Wenke, A., 2014. Sequence stratigraphy and basin analysis of the Tarfaya-Laâyoune basins Morocco, on-and offshore Morocco, Unpublished PhD dissertation, University of Heidelberg, 191 p.

Witt, C., Brichau, S., Carter, A., 2012a. New constraints on the origin of the Sierra Madre de Chiapas (south Mexico) from sediment provenance and apatite thermochronometry. Tectonics, v. 31, p. TC6001.

Witt, C., Rangin, C., Andreani, L., Olaez, N., Martinez, J., 2012b. The transpressive left lateral Sierra Madre de Chiapas and its buried front in the Tabasco plain (southern Mexico). J. Geol. Soc., v. 169, p. 143-155.

Worzel, J.L., Bryant, W., Beall Jr., A.O.R., Capo, R., Dickinson, K., Foreman, H.P., Laury, R., McNeely, B.W., Smith, L.A., 1973. Initial reports of the deep sea drilling project v. 10. Deep Sea Drilling Project Reports and Publications, p. 1–748.

Wu, J.E., McClay, K., Frankowicz, E., 2015. Niger Delta gravity-driven deformation above the relict chain and Charcot oceanic fracture zones, Gulf of Guinea: Insights from analogue models. Mar. Pet. Geol., v. 65, p. 43–62.

Wu, S., Bally, A.W., 2000. Slope tectonics: Comparisons and contrasts of structural styles of salt and shale tectonics on the northern Gulf of Mexico with shale tectonics of offshore Nigeria in Gulf of Guinea. In: Mohriak, W., Talwani, M. (Eds.), *Atlantic Rifts and Continental Margins*. American Geophysical Union Geophysical Monograph, v. 115, p. 151–172.

Wynn, R., Weaver, P., Douglas, M., Stow, D., 2002. Turbidite depositional architecture across three interconnected deep-water basins on the north-west African margin. Sedimentology, v. 49(4), p. 669-695.

Yarbuh, I., Contreras, J., 2017. The interplay between deformation, erosion and sedimentation in the deep-water Mexican Ridges foldbelt, western Gulf of Mexico basin. Basin Res., v. 29, p. 446–464.

Yarbuh, I., González-Fernández, A., Spelz-Madero, R.M., Negrete-Aranda, R., Contreras, J., 2018. Development of detachment folds in the Mexican Ridges Foldbelt, Western Gulf of Mexico Basin. Tectonics, v. 37, p. 2013–2028.

Ysaccis, R., Snyder, F., Lyon, K., Hernandez, J., Mikhaltsev, M., Villarroel, S., El- Toukhy, M., Rowan, M.G., 2018. Unraveling the impact of salt tectonics on the hydrocarbon potential of southern Mexico offshore. European Association of Geoscientists & Engineers, v. 2018, p. 1–5.

Yúnez, A.I., Chapa, F.F., 2017. Oil risk contracts, business conduct and performance patterns: data panel analysis. Contaduría y Adm., v. 62, p. 1538–1552.

Zhang, G.C., Qu, H.J., Zhao, C., Zhang, F.L., Zhao, Z., 2017. Giant discoveries of oil and gas exploration in global deepwaters in 40 years and the prospect of exploration. Nat. Gas Geosci., v. 28, p. 1447–1477.

Zhang, J., Wu, S., Hu, G., Yue, D., Xu, Z., Chen, C., Zhang, K., Wang, J., Wen, S., 2021. Role of shale deformation in the structural development of a deepwater gravitational system in the Niger Delta. Tectonics, v. 40, p. 1-33.